NTNU
Norwegian University of
Science and Technology

CLIQ Based Quench Protection of 16 [T] Nb3Sn Block-Coil Dipole Magnets for a Future Circular Collider

Jonas Blomberg Ghini

Master of Energy and Environmental Engineering
Submission date: September 2015
Supervisor: Ole-Morten Midtgård, ELKRAFT
Co-supervisor: Arjan Peter Verweij, CERN
Emmanuele Ravaioli, CERN

Norwegian University of Science and Technology
Department of Electric Power Engineering

CLIQ Based Quench Protection of 16 [T] Nb_3Sn Block–Coil Dipole Magnets for a Future Circular Collider

Jonas Blomberg Ghini

September 21, 2015

Abstract

Protection of large high–field, high–energy accelerator magnets is very challenging with current technology. To avoid damage to the magnet coil by local or global overheating, the maximum temperature in the hot–spot of the magnet coil must be kept under certain levels depending on the materials used in the coil construction. The current state of the art technology seems unable to do so.

A novel protection system for large superconducting magnets based on generating Inter Filament Coupling Loss through current oscillations in the magnet circuit is applied and simulated successfully for the Nb_3Sn block–coil dipole magnet intended for use in a 100 [TeV] Future Circular Collider.

The proposed protection system is able to keep the maximum temperature of the magnet coil during a quench below 350 [K] at nominal operating conditions, system parameters and geometry, and is shown to achieve a maximum temperature in the coil hot–spot as low as 260 [K] for the optimal protection system configuration.

Several variations on the nominal coil geometry have been investigated, showing that an increase in inductance is detrimental while a reduction is beneficial from the point of view of the new protection system.

Among the variations investigated are a graded coil and a coil with a larger aperture than the nominal geometry. The graded coil is found the most difficult to protect, while the larger aperture coil variant is the easiest to protect, with regards to the hot–spot temperature.

A large parameter space has been investigated, and the most influential parameters are found to alter the hot–spot temperature by 50 [K], while the least influential by 10 [K] when moving away from their respective nominal values. Most influential are the electrical configuration of the protection system, the non–Copper content of the superconducting strands and the coil geometry. Least influential are the residual resistivity ratio and filament twist pitch.

Taking the internal voltages to ground in the coil during application of the new protection system into account, the graded coil must be discarded completely, as turn–to-turn voltages can reach several hundred volt. The reduced inductance variants, therein the larger aperture one, proves the optimal also with respect to voltage: the turn–to–turn voltages are kept well below 100 [V], while the inter–layer voltage, critical for the application of the new protection system, only barely exceeds 1 [kV].

Acronyms

BCS	Bardeen–Cooper–Schrieffer
BICC	Boundary Induced Coupling Currents
CERN	European Organisation for Nuclear Research
CL	Crossed–Layer CLIQ configuration
CLIQ	Coupling–Loss Induced Quench protection system
CtoB	Coil–to–bore
CtoC	Coil–to–collar
FCC	Future Circular Collider
HL–LHC	High Luminosity LHC
HTS	High Temperature Superconductivity
HVDC	High–Voltage Direct Current
IFCC	Inter Filament Coupling Currents
IFCL	Inter Filament Coupling Loss
IL	Inter–layer
ISCC	Inter Strand Coupling Currents
ISCL	Inter Strand Coupling Loss
LARP	Large Hadron Collider (LHC) Accelerator Research Program
LBNL	Lawrence Berkeley National Laboratory
LEDET	Lumped–Element Dynamic Electro–Thermal model
LHC	Large Hadron Collider
LL	Layer–Layer CLIQ configuration
LLrev	Layer–Layer Reverse CLIQ configuration
LTS	Low Temperature Superconductivity
Mid	Midplane
PC	Persistent Currents
PP	Pole–Pole CLIQ configuration
QH	Quench Heaters

RRR	Residual Resistivity Ratio
SC	Superconductor, Superconductivity, Superconducting
TALES	Transient Analysis with Lumped Elements in Superconductors
TtoT	Turn–to–turn

Preface

This report has been written based on work done during the spring and summer of 2015, in the magnet protection group at CERN.

Special thanks must be extended to Michal Maciejewski and Emmanuele Ravaioli, both at CERN, without whose immediate contribution I would not have understood any of the results I present, nor would I have them in the first place. Further thanks are also extended to supervisors Ole–Morten Midtgård, at NTNU, and Arjan Peter Verweij, at CERN; even my thesis title would have been a mess, if it had ever existed, without their guidance and belief in the project.

Bergljot Tjønn has provided invaluable and tireless aid proofreading my jumbled words, and for that I am very thankful.

Frida Blomberg Håvardstun has my gratitude for her support in difficult times.

Finally, my family; Nina and Fred Blomberg–Carlsen, Luca Ghini, Ingeborg Iolanda Blomberg Ghini and Matteo Blomberg Ghini have my thanks for both taking an interest, showing support and being understanding during my long hours of work.

Contents

Chapter 1

Superconducting Magnets

This, first, chapter, I will use to present the desire for high–energy accelerators, the need these create for strong dipole magnets and how impossibly shortcoming regular conducting materials are for such a task.

I then describe the theory of superconductivity semi–quantitatively in order to justify the existence of a critical surface for a superconducting material.

The following will point out first the need to divide the material into thin, twisted, filaments to avoid flux jumps; then, it becomes apparent that cables of twisted filaments will experience transient losses under changing magnetic fields.

Finally, the chapter describes the operational challenge of protecting the magnet during a quench.

1.1 Large Particle Accelerators

The approach chosen for peering into the deepest realm of the physical world is perhaps a childish one in its intuitive and principal ease — take two rocks, hurl them at each other, let them collide and look at the pieces that fall out. In 1929 Ernest O. Lawrence invented the first Cyclotron; the machine accelerates ions in an outwardly growing spiral between the poles of a dipole magnet, and extracts the ions for collision with a stationary target once the design energy is reached. The design demands that the ions stay non–relativistic, and, thus, have a maximum energy around 15 [MeV] [1, p. 14].

The Synchrocyclotron, built in 1957, was European Organisation for Nuclear Research (CERN)'s first particle accelerator. In this machine, the accelerating electrical field has varying frequency, and so, the stringent non–relativistic limit of the classical Cyclotron is relieved — the CERN Synchrocyclotron reached 600 [MeV] [1, p. 15][2].

1959 saw the commissioning of the Proton Synchrotron at CERN. Designed for an energy of 28 [GeV], such a machine synchronises the magnetic bending field with the momentum of the particle beam and the electric accelerating field with the revolution frequency of the beam so as to keep the particle in a stationary orbit with continuous acceleration [1, p. 58–59].

When colliding with a stationary target large fractions of the energy are lost in the momentum transfer — it became necessary to device a way to collide accelerated particles head on in order to keep all the energy available for particle generation; this way many more things would fall out, available for study, from colliding the rocks. The Intersecting Storage

Rings, finished in 1971, at CERN was the first hadron collider using two intersecting storage rings, reaching a center–of–mass energy of 62 [GeV] [1, p. 12–14].

From here machines are built for 200, 600 and 2000 [GeV], finally reaching the LHC at 14 [TeV], with plans for a Future Circular Collider (FCC) with 100 [TeV] collision energy [3–5].

1.1.1 Coil Cross Section of Dipole Magnets

All circular colliders rely on dipole bending magnets to give the particle beam a stationary orbit to follow, and in order to obtain the dipole field necessary, current conductors are arranged in different ways around the bore/aperture of the beam pipe. Figure 1.1 shows the coil cross section of a magnet able to produce a perfectly uniform dipole field everywhere in the aperture. This is done by intersecting two cylinders carrying the same magnitude current density, but in opposing directions. The field can be expressed as such [6, p. 28],

$$B_x(x,y) = \frac{\mu_0 J}{2}(r_1 \sin\theta_1 - r_2 \sin\theta_2) = 0, \quad [\mathrm{T}] \quad (1.1)$$

$$B_y(x,y) = \frac{\mu_0 J}{2}(-r_1 \cos\theta_1 + r_2 \cos\theta_2) = -\frac{\mu_0 J s}{2}, \quad [\mathrm{T}] \quad (1.2)$$

where s is the eccentricity[1].

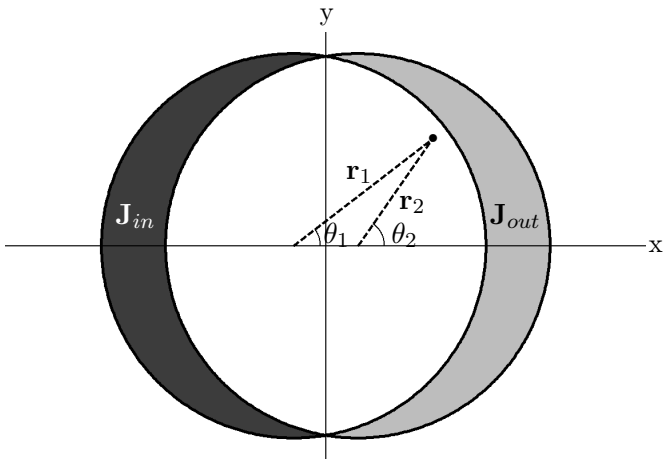

Figure 1.1: Cross–section of coil producing ideally uniform transverse dipole field[6, p. 28].

The current distribution that will give such a field can be determined quantitatively quite easily by considering the coil as a cylindrical shell with zero winding thickness (only a surface), of radius R, much like the setup in figure 1.1, but with only one of the two circles. The field inside and outside this coil will then be given as[7, p. 154],

$$\mathbf{H}_{inside} = H_0(\sin\theta\hat{\mathbf{r}} + \cos\theta\hat{\boldsymbol{\theta}}), \quad [\mathrm{A\,m^{-1}}] \quad (1.3)$$

$$\mathbf{H}_{outside} = H_0\left(\frac{R}{r}\right)^2(\sin\theta\hat{\mathbf{r}} - \cos\theta\hat{\boldsymbol{\theta}}), \quad [\mathrm{A\,m^{-1}}] \quad (1.4)$$

where $\hat{\mathbf{r}}$ and $\hat{\boldsymbol{\theta}}$ are the unit vectors in the respective directions.

Looking at the boundary between the inside and outside fields, at a radius R — that is, at the surface carrying the current — the regular expressions for boundary conditions between

[1] The amount of displacement between the two centres of the cylinders.

magnetic fields given by equations 1.3 and 1.4 give a current density[7, p. 156],

$$\begin{aligned} \mathbf{J}_{surface} &= \hat{\mathbf{r}} \times (\mathbf{H}_{outside} - \mathbf{H}_{inside}) \\ &= \hat{\mathbf{r}} \times -2H_0 \cos\theta\hat{\boldsymbol{\theta}} \\ &= -2H_0 \cos\theta\hat{\mathbf{z}}, \end{aligned} \qquad [\mathrm{A\,m^{-2}}] \quad (1.5)$$

where $\hat{\mathbf{z}}$ is the unit vector along the axis of the magnet/coil.

If, instead of a varying surface current density, which would require separate powering of each turn, one varies the thickness of the shell of current carrying material one is back to the eccentric cylinders, and the conclusion is that a configuration so that the current density is proportional to $\cos\theta$ will give the desired dipole field.

In real magnets there is no possibility to follow a perfect $\cos\theta$ proportionality for the current, and so approximations must be made[6, p. 32][1, p. 589]. This is done by a combination of current blocks and current shells/layers as shown in figure 1.2.

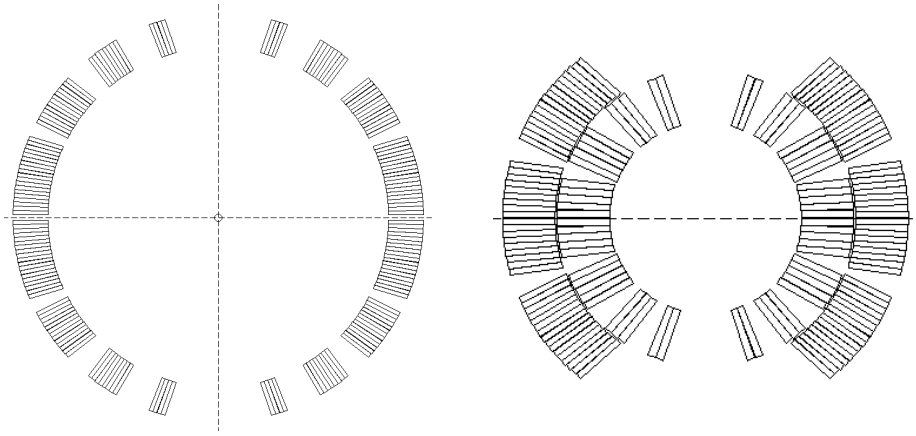

(a) D1 magnet geometry, used to bring together and then separate the counter rotating proton beams on either ends of the interaction points of the LHC [8].

(b) MB magnet geometry, main dipole magnet in the LHC [9].

Figure 1.2: Examples of practical coil geometries.

The dipole geometry investigated in this thesis is of a very different design that the more typical approaches shown in figure 1.2. An example of the block–coil dipole magnet geometry is shown in figure 1.3. This geometry is discussed in–depth in chapter 3.

1.1.2 Coil Track

Finally, once the cross–section of the coil is determined, it will be wound into a magnet coil, shown as in figure 1.4a. Figure 1.4b shows how the actual coil geometry is preserved through the curved ends of the LHC dipoles.

The finished coil is then placed inside a steel collar, then an iron yoke. The collar is primarily for mechanical purposes, while the iron yoke acts as a cold mass and to improve the aperture field strength [1, p. 589–591]. This whole assembly is then inserted into the cryostat; the chamber housing the magnet as a whole, with electric power, helium cooling lines and vacuum system.

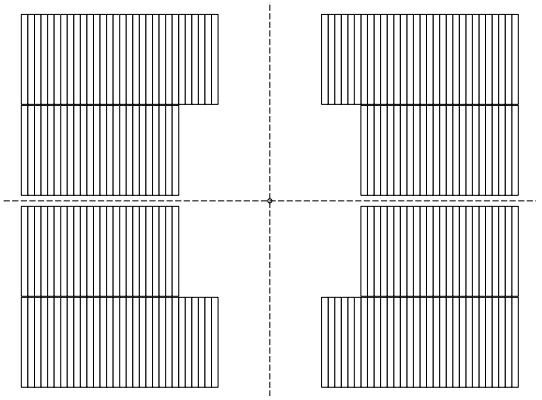

Figure 1.3: HD2 magnet geometry, proposed for use as the main dipole magnet in a 100 [TeV] hadron collider [3].

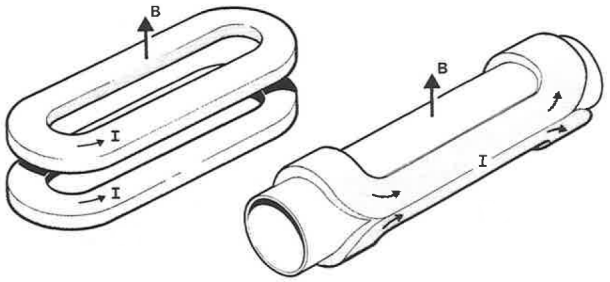

(a) Two ways to wind a coil in order to keep the cross–section necessary for a dipole field, as well as giving access to the aperture of the coil. Left winding is called a race track coil, and the right is called a curved saddle coil [6, p. 27].

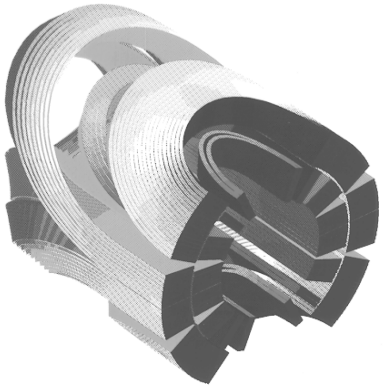

(b) 3D representation of the bend at the end of a LHC dipole [10, p. 28].

1.1.3 Beam Rigidity and Current Requirement

In an accelerator, the charged beam has a certain momentum related to its kinetic energy; this momentum means that it takes a certain force to keep the beam on a given path. From Newton's, Faraday's and Lorentz' laws of forces an expression for this *beam rigidity* is found as [1, p. 1],

$$B\rho = \frac{P}{e}, \qquad [\mathrm{T\,m}] \quad (1.6)$$

where B [T] is the magnetic field along the trajectory, ρ [m^{-1}] is the bending radius of the trajectory, P [$\mathrm{kg\,m\,s}^{-1}$] is the momentum of the individual particles in the beam and e [C] is the elementary charge.

By expressing the momentum in units of [$\mathrm{GeV\,c}^{-1}$], where [c] is the speed of light in [$\mathrm{m\,s}^{-1}$], the magnetic field necessary to keep the beam bending around a given trajectory is found as,

$$B = \frac{P}{\rho \mathrm{c}}, \qquad [\mathrm{T}] \quad (1.7)$$

Inserting the LHC design energy, 7000 [$\mathrm{GeV\,c}^{-1}$], and radius $27000/2\pi$ [m], the required

field is,

$$B = \frac{7000 \cdot 10^9[\text{eV}]1.602 \cdot 10^{-19}[\text{J eV}^{-1}]}{\frac{27000}{2\pi}[\text{m}]3 \cdot 10^8[\text{m s}^{-1}]1.602 \cdot 10^{-19}[\text{A s}]} = \frac{7000 \cdot 10^9[\text{kg m}^2\,\text{s}^{-2}]}{4300[\text{m}]3 \cdot 10^8[\text{m s}^{-1}][\text{A s}]} = 5.43[\text{T}]$$

Now, as it turns out, not every meter of an accelerator can be used to bend the beam; the actual acceleration needs to be done, the collision experiments need space, huge amounts of beam diagnostics and control systems need space, beam optics and collimation also take large parts of the total length — the final effective length of the machine usable for bending is typically about 66% of the total length. This means that the magnetic field must be even higher — 8.2 [T] is needed to bend the beam around the LHC.

The magnetic energy stored in such a field is tremendous; with the LHC dipoles as an example, having an aperture of 27 [mm] [11, sec. 7.1.2], the regular expression for magnetic energy density gives [12, eq. 16.16][7, p. 157],

$$\frac{\pi r^2 B^2}{\mu_0} = \frac{\pi(27 \cdot 10^{-3}[\text{m}])^2(8.2[\text{T}])^2}{4\pi \cdot 10^{-7}[\text{H m}^{-1}]} = 122.5, \qquad [\text{kJ m}^{-1}] \quad (1.8)$$

In the LHC dipoles there are two poles, one upper and one lower, and they are 14.3 [m] long [11, tab. 7.5]. This gives a total energy of 7 [MJ]. From the same table, the total inductance of the dipoles are also given, as 98.7 [mH]; with the expression for magnetic energy stored in an inductor, this gives a necessary transport current,

$$\begin{aligned} \frac{1}{2}L_{\text{eq}}I^2 &= 7 \cdot 10^6[\text{J}] \\ I &= \sqrt{\frac{2 \cdot 7 \cdot 10^6[\text{J}]}{L_{\text{eq}}[\text{H}]}} = 11850, \end{aligned} \qquad [\text{A}] \quad (1.9)$$

With the cross sectional area of the conductors in the dipoles, 21 [mm^2] [11, tab. 7.1], this gives an average current density of 560 [A mm^{-2}].

The HVDC link between Norway and the Netherlands, operating at 900 [kV] with a capacity of 700 [MW] will have an average current density at peak power of about 1 [A mm^{-2}] [13], while typical current densities in copper, generally, do not exceed a few tens of [A mm^{-2}], depending on application [14].

Taking, then, once again, into consideration equation 1.6, and that the beam energy of the proposed Future Circular Collider is 50 [TeV], with a circumference of 100 [km], the field required is about 16 [T]. Assuming a dipole magnet with the same characteristics as the current LHC magnets, simply with a higher current, the density will, then, be about 1000 [A mm^{-2}]. It should be abundantly clear that no normally encountered conducting material is even remotely capable of carrying such currents. The only possible solution is to use a *superconducting* material.

1.2 Superconductivity

Superconductivity is, as the name of the phenomenon suggests, known as a property in certain materials under which the resistivity of said material vanishes completely[2]. This observation

[2]Or more precisely, the resistivity is so low that persistent currents can flow with decays so small that after a year of continuous flow, the current was still the same, to within experimental error; after this, the experimentalists aborted the measurement out of boredom [15, p. 259]. From a simple calculation [15, p. 282] the rate of decay of a supercurrent is about $10^{4.3 \cdot 10^7}$ [s], while the age of the Universe is on the order of 10^{18} [s].

was how the effect was first seen. However, another property is of more fundamental importance than the conductivity itself; the Meissner–Ochsenfeld effect. This effect is seen as a superconductor expels an externally applied magnetic field by induced supercurrents on the surface of the material.

In addition to treating the Meissner–Ochsenfeld effect, it is necessary to discuss the critical surface of a superconducting material, the engineering challenges regarding using a material in an actual magnet, and finally the stability of a superconducting magnet.

Table 1.1 lists some key discoveries related to superconductivity and the theories explaining the phenomena. The study of superconductivity as a field of science arose quickly after Kammerling Onnes managed to liquefy Helium in 1908. The importance of this technological development lies in the fact that most simple superconducting materials only show Low Temperature Superconductivity (LTS)[3].

Table 1.1: Important discoveries in the history of superconductivity [16, p. 1].

1908	Liquefaction of Helium, at 4.2 [K]
1911	Superconductivity discovered in Mercury, at 4.1 [K]
1933	Meissner–Ochsenfeld effect observed
1950	Ginzburg–Landau theory of superconductivity is formulated
1957	Bardeen–Cooper–Schrieffer (BCS) theory formulated
1962	Josephson effect discovered
1986	High Temperature Superconductivity (HTS) discovered, at 30–165 [K]

Several materials are now known to be superconducting[4], and table 1.2 gives a list of some important ones. NbTi is used in the superconducting magnets currently installed in the LHC; Nb_3Sn is currently experiencing heavy technological development (as this work is an example of), in many cases with the intention of replacing the current use of NbTi [17]; YBCO is an example of a material showing High Temperature Superconductivity (HTS), discovered in the late 80's, and ss the first example of such a material [18]; MgB_2 is another example of HTS, although at a far lower temperature than YBCO — the interest in this material lies in the low cost, simple structure and relatively high critical temperature [19].

1.2.1 Meissner–Ochsenfeld Effect and the Vortex State

The modern definition of whether or not a material is superconducting is the demonstration of the Meissner–Ochsenfeld effect [7, p. 3][16, p. 54]. This effect manifests in the expulsion of a weak magnetic field from the bulk of the superconductor [15, p. 262]. Figure 1.5 shows how the field inside a superconducting material behaves as the material is cooled below the critical temperature under application of a small and constant magnetic field. The figure does not show the surface currents that arise on the sphere, however. These surface currents are what actually expel the magnetic field.

The mathematical description of the Meissner–Ochsenfeld effect is found in the London

[3] E.g. elemental materials like Mercury and Lead; the point being that alloys and metallurgically processed materials were only developed and studied later. The development here will completely skip the distinction between type I and type II superconductors — only type II SC have any practical applicability, and so, I will present the theory as if only the type II exists.

[4] In fact, nearly 10000 superconductors have been discovered [7, p. 10]

Table 1.2: Critical temperatures for a selection of important superconducting materials [15, p. 262][7, p. 8].

Material	$\mathbf{T_c}$ **[K]**	**Material**	$\mathbf{T_c}$ **[K]**
NbTi	9.8	Hg	4.15
Nb_3Sn	18.05	V_3Ga	16.5
Nb_3Ge	23.2	V_3Si	17.1
Nb_3Al	17.5	$YBa_2Cu_3O_{6.0}$	90
NbN	16.0	Rb_2CsC_{60}	31.3
C_{60}	19.2	MgB_2	39.0

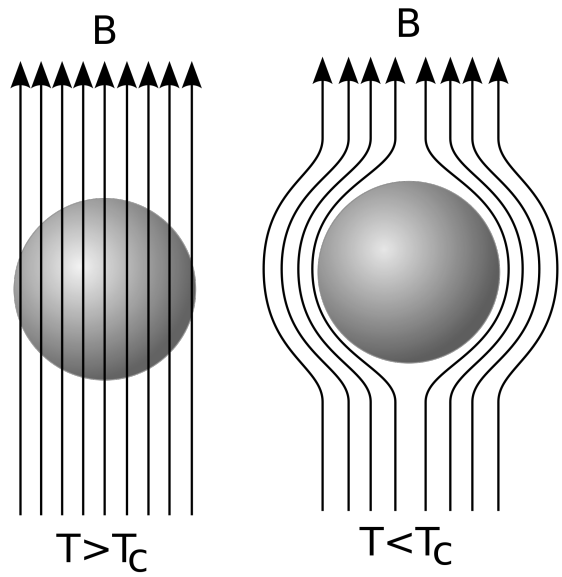

Figure 1.5: Sketch of the field inside a material demonstrating the complete Meissner–Ochsenfeld effect as the material transitions below the critical temperature under a small, constant applied field. Figure recreated from [20].

equation,

$$\nabla \times \mathbf{j} = -\frac{1}{\mu_0 \lambda_L^2}\mathbf{B}, \qquad [\mathrm{A\,m^{-2}\,m^{-1}}] \quad (1.10)$$

which states that under the application of an external field, there will arise a current density such that the external field is opposed [15, p. 274]. The parameter λ_L [m] is called the London penetration depth, and it describes how far into the material bulk the external field is able to penetrate. Figure 1.6 illustrates the exponential screening of the applied field.

There is another fundamental length that characterise a superconductor, apart from λ_L [m]; the *coherence length*, ξ [m], also shown in the figure. This length gives the distance over which the concentration of superconducting electrons cannot change much, despite a

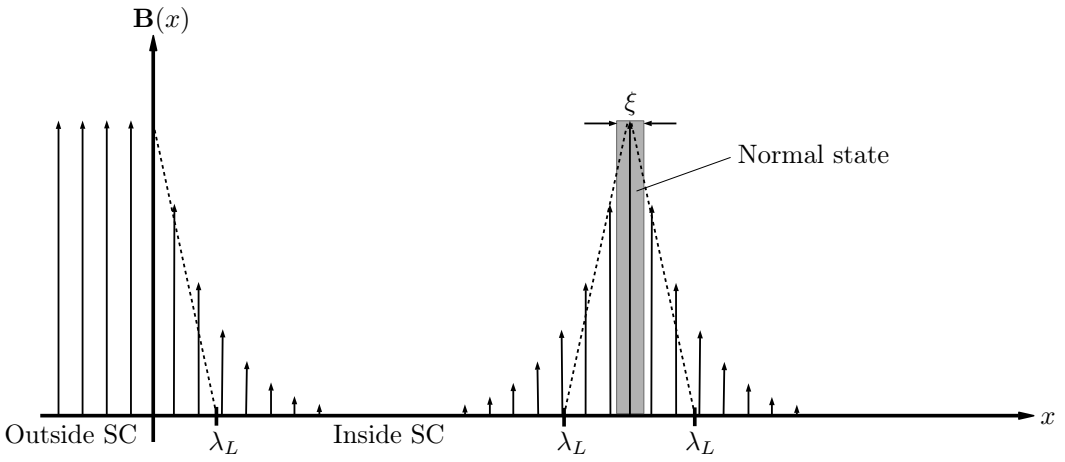

Figure 1.6: Illustration of the London penetration depth and the coherence length. The externally applied field penetrates the SC in the x–direction. In the area indicated *normal state* the SC material is no longer superconducting, and the external field penetrates it completely. Around this volume of normal state material, there flows a supercurrent, a *vortex*, that screens the rest of the SC from the field within the vortex, as given by the London equation.

spatially varying magnetic field [15, p. 276].

The coherence length arises from the Ginzburg–Landau theory of superconductivity, and it will not be shown explicitly here how it comes about, however, the parameter is of importance for two reasons: it gives a measure of the purity of the superconductor and it describes the interface between a normal and a superconducting material in contact with each other (or the interface between the normal and superconducting state within the same material). Figure 1.7 shows how the interface between normal and superconducting phases look as a function of location. The function $\Psi(x)$ is called the order parameter, and is introduced in the Ginzburg–Landau theory, and relates to the concentration of superconducting electrons.

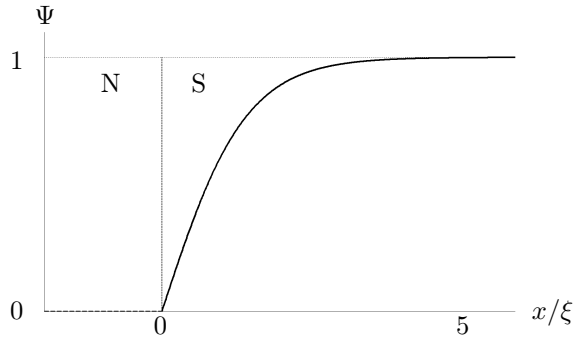

Figure 1.7: $\Psi(x)$ at the interface between the normal (N) and superconducting (S) phase of a material [21, p. 206].

As dictated by the London equation (equation 1.10), since the volume of the normal state in the otherwise superconducting material will be perfectly penetrated by the external field, a supercurrent flowing around the normal state (in the superconducting part of the

material) will arise to screen the rest of the material from the field[5]. The current will flow in a cylindrical shell pattern around the flux line, and this gives rise to the *vortex* name of this state. The size of the vortex is on the order of the coherence length, ξ [21, p. 243 – 244], and the number of vortices, or fluxoids penetrating the material is proportional to the applied field through the flux quantum, Φ_0 [21, p. 282][6].

1.2.2 Short Note on the BCS Theory

The fundamental unit of the superconducting state is the Cooper pair. The existence and properties of both the state in general and the Cooper pairs in particular are of considerable complexity, as the BCS theory that describes them is a quantum mechanical theory. As such the theory will only be discussed briefly and qualitatively.

In certain materials, electrons can experience an attractive interaction, and this will lead to a ground state of lower energy than the one the material would have been in without the interaction [22, p. 172]. This energy gap is explained by the interaction between electrons and phonons [15, p. 278]. Phonons are lattice vibrations, and are in essence mechanical waves that propagate through a crystal structure by way of distorting the locations of the lattice points [15, Chap. 4]. Many effects can cause such a wave, notably temperature, evident in the thermal energy of a material, and as in superconductivity; an electron moving in the electron sea interacts attractively with the positive cores located in a lattice point. This interaction distorts the lattice, causing a propagating wave, this wave then interacts attractively(the cores at the lattice points are all positive) with another electron, and the over–all effect is as if the two electrons had interacted attractively [16, p. 128–129].

In a system governed by attractive forces, a convenient metric is the potential energy of the, in this case, particles involved. The attraction between the electrons will lead to a ground state of lower potential energy than the state the electrons would be in if the electron–phonon–electron interaction was not present [21, p. 113].

Cooper Pairs

The Pauli exclusion principle dictates that an electron, which is a fermionic particle, cannot occupy the same state as another, identical, electron. Here, that means that two (or more) electrons cannot share states; they cannot have the same energy, unless they have opposite spin [21, p. 18]. So, in order for the lower energy state to exist, the two electrons that interacted must have the same energy, but exactly opposite spin. This way the Cooper pair is formed. Two electrons with the same energy (now lower than before) will annihilate each others spin, and effectively produce a boson (particle of integer spin) [21, p. 115].

Since the Pauli exclusion principle does not apply to bosons, there is nothing preventing other electrons to form the same sort of pair at the same, lower, energy. This would indicate that all electrons in the material ought to partake in Cooper pairing to lower the energy of the state as much as possible. However, this does not happen, as the presence of the Fermi surface is essential for this pairing to occur [23][7].

[5]The volume of normal material in the SC is often referred to as a flux line, due to a particular quantisation effect explained by the BCS theory [21, p. 278].

[6]No treatment of the flux quantum is done in this thesis, however, very briefly, the existence of the flux quantum comes from the fact that following a closed path, say a ring, of SC material, the wave function describing the density of superconducting electrons must have a single valued angular phase, and in a ring that will be given in quanta of $2\pi s$, where s is the number of turns around the ring. From this it follows that the magnetic flux enclosed by the ring is quantised the same way; thus the flux quanta is defined [15, p. 279–282].

[7]The Fermi surface is the ground state in a system of non–interacting electrons. Quantitatively this is given

Pair Breaking

In essence, the destruction of superconductivity means that the Cooper pair's bonding energy has been breached by some sort of energy input.

When the temperature in the SC rises, more and more thermal motion takes place in the material. At some point the fundamentally chaotic motion of the thermally excited cores and electrons in the lattice obscure the ordered motion of the electron–phonon–electron interaction, and thus, the Cooper pairs no longer form. In addition to a sufficiently high temperature, a magnetic field and an applied current can destroy the SC state as well. This will be described in the following.

1.2.3 Critical Magnetic Field

From Cooper *pairs* being the key unit in superconductivity it follows that an applied magnetic field will be able to destroy the SC state; for one, the Meissner–Ochsenfeld effect means that the Cooper pairs are the charge carriers making up the supercurrent that screens the interior of the superconductor (or material outside of the vortex cores in the mixed state). For sufficiently high applied fields, the Lorentz force experienced by the moving electrons will be sufficiently high to break the pair apart, and thus destroying the superconductivity.

Secondly, since the Cooper pairs rely on electrons of opposite spin pairing up, it follows that a sufficiently strong applied magnetic field will be able to align the spins of the electrons in the pair, and thus break the pair apart, as they no longer possess the bosonic property of integer spin.

1.2.4 Critical Current

There are two, equivalent, ways to look at the issue of how a current can destroy the SC–state in a material. The first is related to the self–field of the material when a current is passing through it, and the other is related to the kinetic energy of the Cooper pairs when the electrons are moving in the current.

Self–field Destroying the SC–state [22, p. 52]

Given by Ampére's law, a conductor carrying an electric current will produce a magnetic field at its surface (inverse squarely decaying with distance from the conductor)[8]. This field will, of course, penetrate the material a distance given by the penetration depth. As stated in the previous section (1.2.3), a sufficiently high magnetic field will destroy the superconductivity, so it follows that a sufficiently high current, or current density will be able to do the same.

Kinetic Energy of Electrons Destroying the SC–state [21, p. 269–271]

The current density in a superconducting material is given as $j = qn_{SC}v$ [$\mathrm{A\,m^{-2}}$], where q [C] is the charge of the carrier (here 2e since the carrier is a Cooper pair), n_{SC} [$\mathrm{m^{-3}}$] is the density of Cooper pairs and v [$\mathrm{m\,s^{-1}}$] is the velocity of the pairs. By assuming a homogeneous

as the energy of the topmost filled level of the ground state [15, p. 134–135]. The reason this surface must exist for the Cooper pairs to exist is that the electrons in the pair must come from somewhere, and if enough electrons are removed from energies above the Fermi level, then the Fermi level will drop, and the Cooper pairs will break apart and fill the new available states.

[8] The sceptical reader will find this as the 112th equation in J. C. Maxwell's work *On Physical Lines of Force* [24], which is Ampére's original current law with the addition of the Maxwell term.

and very thin wire of SC(radius smaller than both penetration depth and coherence length), Buckel [21] manipulates the Ginzburg–Landau equations, leading to[9],

$$n_{\mathrm{SC}} = n_\infty \left(1 - \frac{mv^2}{2|\alpha|}\right)$$

where $|\alpha|$ is a constant and n_∞ is the density of superconducting electrons when no current is present.

This evidently means that the number of SC charge carriers vanishes once the kinetic energy of the particles surpasses the threshold given by $|\alpha|$. From the BCS theory, this is understood as such: when the kinetic energy of the Cooper pair exceeds the binding energy of the SC–state, the Cooper pairs break apart, and the superconductivity is destroyed.

1.2.5 Flux Pinning in Ideal SC Materials

The most important property of a superconductor, with regards to its technological usefulness in magnets, is the critical current, seeing as the magnet's purpose is to create a field, and the amplitude of that field depends on the amplitude of the current flowing in the current leads. However, the discussion so far has only been of ideal materials, which are of no technological use, even if the upper critical field is high enough to be used in high–field magnets, and the critical temperature is high enough to allow adequate cooling. The following explores the problem and the solution.

Figure 1.8 shows the flux lattice in MgB_2 and $NbSe_2$ under application of external magnetic fields. The samples used were, of course, not perfect, but experiments on very pure materials show that when the flux lattice is very regular and uniform, the supercurrent only flows on the surface of the material, exhibiting the perfect Meissner–Ochsenfeld effect [6, p. 283].

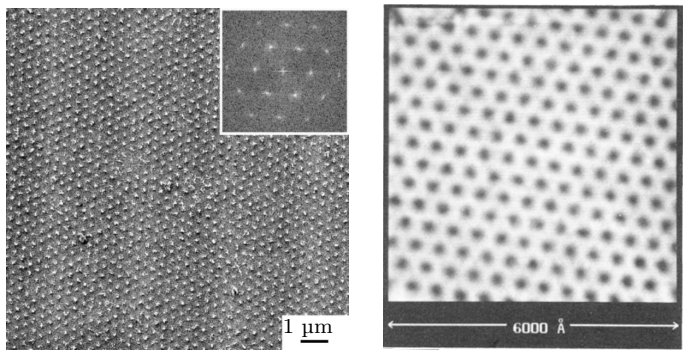

(a) MgB_2 flux lattice in applied field of ~ 0.02 T [25].

(b) $NbSe_2$ flux lattice in applied field of 1 T [26].

Figure 1.8: Flux lattice in two different superconductors.

In an ideal SC the fluxoids, the small current vortices and their normal state cores, can move about freely — there is no location that is more energetically favourable than another for the vortex to occupy since the material's lattice is perfectly symmetric.

Imagining now a single vortex in an ideal SC, as depicted in figure 1.9. Around the fluxoid the field penetrates a length given by the London penetration depth, into the bulk of the material. Since the material itself also carries a current, $\mathbf{J}$ [$\mathrm{A\,m^{-2}}$], the vortex will

[9]The derivations are simple, but not recited here.

experience a Lorentz force, indicated by **F** [N] in the figure[10]. Since the motion of a vortex is freely permitted in the ideal case, the vortex will move according to the Lorentz force at any applied current [21, p. 278]. This motion will cause dissipation of energy due to two different processes.

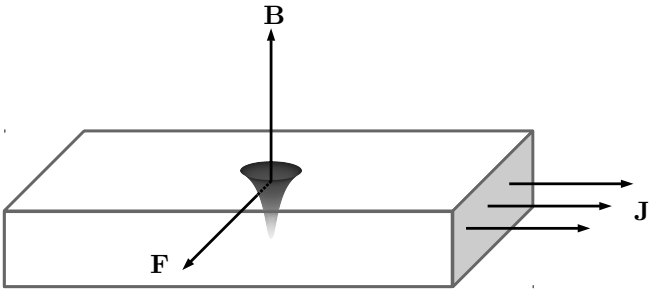

Figure 1.9: A single fluxoid in an ideal superconductor, in applied field **B** [T] and current **J** [A m^{-2}]. The magnetic field around the vortex is indicated by the shading (dark is low, light is high). Based on figure 5.7 [21, p. 278].

dB/dt

When the vortex moves across the material, the electrons in the material, both normal and superconducting ones, will experience a temporally changing magnetic field. Faraday's law then explains the arising of an electric field[11]. All electrons in this electric field will be accelerated, and interact with the lattice of the material. As explained in section 1.2.2, the superconducting electrons, Cooper pairs, will not lose any energy in this interaction. The normal conducting electrons on the other hand will behave just as electrons usually do, and lose energy to friction with the lattice; this is in essence a conversion from electric energy to heat, and constitutes a loss taken from the transport current [21, p. 279].

$\mathbf{dn_{cooper}/dt}$

As the vortex passes a given point in the material, the concentration of Cooper pairs will vary, from its equilibrium value while the vortex is far away, to zero when the centre of the vortex is at the point, and then back up to the equilibrium value once the vortex is far away again[12]. The heat of reaction of breaking up a Cooper pair decreases with magnetic field[13]. When also taking into account the relaxation time for the recreation of the equilibrium value of the Cooper pair density, it becomes apparent that for a sufficiently high velocity of the vortex, the Cooper pairs in front of, and subsequently "hit" by, the vortex, will break up in a high field and thus release only a small amount of energy, while the electrons recombining behind the vortex might take such a long time due to the relaxation process, that they recombine once the field is lower than it was when the pair broke apart[14]. This means that

[10] The SC transport current, **J** [A m^{-2}], will flow where there are superconducting electrons. This will mainly be a distance ξ [m] from the centre of the vortex and outwards. Since the field penetration is λ_{L} [m], and in an SC where $\lambda_L \gg \xi$, the current will flow in a region where there is, indeed, a magnetic field present.

[11] The sceptic is again referred to the original writings by Maxwell for peace of mind. The relevant equation is number 54 [24].

[12] Far away in this context means a distance greater than the coherence length.

[13] The binding energy, which is released upon pair breaking, is lower in higher fields [27].

[14] This is not discussed here, but at least in part, the existence of such a relaxation time, or rather, recombination time, for the process of recombining single electrons into the Cooper pairs from before, can be attributed to phonons(lattice vibrations) escaping from the recombination process, and in turn breaking up

the recombination process requires a larger amount of energy than that which was released, and the difference again constitutes an energy loss from the transport current [21, p. 279].

These two processes mean that as soon as the vortices begin to move, there is heat dissipation, and since the vortices start to move immediately upon application of current(no matter how small), the critical current of an ideal superconductor is exactly zero, which makes them entirely useless for magnet building, even if the critical field is very high [21, p. 279–280].

1.2.6 Flux Pinning in Hard Superconductors

The magnitude of the Lorentz force acting on the vortex in figure 1.9 is given as,

$$F = ILB$$

where I [A] is the current flowing in a wire of length L [m] in a perpendicular magnetic field B [T] [21, p. 278]. This, clearly, means that a larger current will exert a larger force on the vortices. In the ideal case, any current larger than zero is large enough to move the vortex, and in turn cause dissipation and thus loss of superconductivity. If, somehow, the vortices were pinned down, so that they were kept from moving, an equilibrium of forces would be established; the Lorentz force balanced against a *pinning force* [21, p. 296][6, p. 284]. Subsequently, a larger pinning force will be able to withstand a larger Lorentz force, and thus a larger transport current.

How to pin the vortex

The creation of a Cooper pair, as seen in section 1.2.2 and 1.2.5, lowers the energy of the system. This means that a vortex, whose core is in the normal state, must expend energy in order to arise, since it must reduce the concentration of Cooper pairs to zero at its centre. From this it follows that if this energy expenditure can be reduced, the vortex will be located in such a way as to take advantage of this [21, p. 282–283].

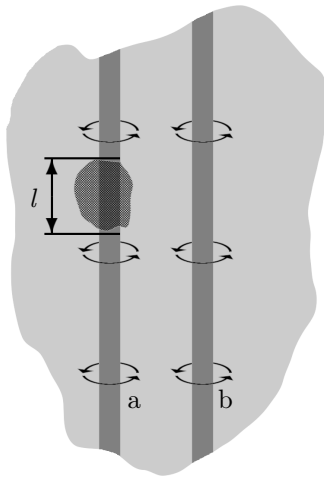

Figure 1.10: Pinning effect of impurity. Recreated from figure 5.9[21, p. 283].

existing Cooper pairs, which will increase the effective recombination time of the process [21, p. 261–262].

Figure 1.10 shows two vortex cores in a superconductor. The hatched area in the left vortex represents some kind of impurity of size l [m]; a normal precipitate[15], a lattice defect, grain boundary or dislocation [22, p. 367]. Such a point is called a *pinning centre* because the vortex will experience a pinning force at this location. This is due to the region being in the normal state, or at the least, closer to the normal state, than the areas surrounding it, and thus it will require less energy for the vortex to cross this part of the material, since less, or no, Cooper pairs will have to be broken up.

The pinning force the vortex experiences is then caused by the energy barrier that needs to be overcome in moving it from location "a" to location "b". With a higher number of pinning centres, more vortices will be pinned, and eventually a transport current of appreciable magnitude can be led through the material.

A superconductor with sufficiently many pinning centres is called a *hard superconductor*, and these materials are the ones of any practical/technological use [21, p. 282].

1.3 Critical Surface

In the previous, three critical parameters within which the superconductive state can persist were established. The critical temperature (section 1.2.2), the critical field (section 1.2.3) and the critical current density (section 1.2.4). Since these parameters are related — a high temperature means lower critical field and current density; running at a higher current density and thus field means the temperature must be lower — a *critical surface* for the magnet can be determined. The critical surface depends only on the superconductor material, since only the superconductor has critical parameters; however, the coil geometry influences *where*, in relation to the critical surface, a given operating point is, as the magnetic field in a given location in the magnet will depend on the geometry[16]. The critical surface will be represented as a function $J_c(B,T)$, that is, the critical current as a function of the local magnetic field and temperature.

1.3.1 $\mathbf{J_c(B,T,\epsilon)}$ [28]

The expressions presented are only valid for Nb_3Sn, and as such cannot be used as a general approach to calculation of the critical surface. That said, for NbTi, the expressions show similar dependencies on the magnetic field, and a somewhat more gradual dependence on the temperature [7, p. 644].

$$J_c(B,T,\epsilon) = \frac{C(\epsilon)}{\sqrt{B}}(1-t^2)^2(1-b)^2, \qquad [\mathrm{kA\,mm^{-2}}] \quad (1.11)$$

[15] A region that is in the normal phase, perhaps due to a contaminant, or a local mixing of materials that result in the area to be normal as opposed to superconducting; in a NbTi conductor, local variations in the mixing ratios might cause the spot to have too high concentration of Titanium, and thus the critical field and temperature might be so that it is no longer SC, while the rest of the sample still is.

[16] For a given power supply/given current the field in the aperture will, of course, depend on how the coil, within which the current flows, is configured.

where,

$$t = \frac{T}{T_{c0}(\epsilon)}, \quad [1] \quad (1.12)$$

$$b = \frac{B}{B_c(T,\epsilon)}, \quad [1] \quad (1.13)$$

$$C(\epsilon) = C_0\sqrt{1 - a|\epsilon|^u}, \quad [\mathrm{kA\,T^{0.5}\,mm^{-2}}] \quad (1.14)$$

where,

$$T_{c0}(\epsilon) = T_{c0m}(1 - a|\epsilon|^u)^{1/w}, \quad [\mathrm{K}] \quad (1.15)$$

$$B_c(T,\epsilon) = B_{c0}(\epsilon)(1 - t^2)[1 - 0.31t^2(1 - 1.77\ln t)], \quad [\mathrm{T}] \quad (1.16)$$

where,

$$B_{c0}(\epsilon) = B_{c0m}(1 - a|\epsilon|^u), \quad [\mathrm{T}] \quad (1.17)$$

T_{c0m} [K] is here the critical temperature of Nb_3Sn at zero applied field and B_{c0m} [T] is the upper critical field at zero temperature. ϵ [%] is the mechanical strain on the material/coil, a, u and w are unit–less model fit parameters[17]. B [T] and T [K] are the local magnetic field and temperature respectively and C_0 [$\mathrm{kA\,T^{0.5}\,mm^{-2}}$] is another model fitting parameter describing the "hardness" of the superconductor (a large C_0 means a large pinning force/large number of pinning centres).

1.3.2 Critical Surface of Nb_3Sn

In a protection setting, as discussed later, in section 1.8, the important goal is to quench as much of the coil as fast as possible. As seen in the strain dependence of equation 1.11, the effect of mechanical strain will make it easier to quench the magnet, as the critical temperature and critical field both deteriorate with applied strain; the protection system will be less taxed when quenching the magnet, as it will reach the necessary temperature sooner when taking strain into account. For this reason, the critical surface of Nb_3Sn is calculated without including strain effects, so as to give a conservative estimate of the performance.

Figure 1.11 shows the critical surface of Nb_3Sn as calculated from equation 1.11. It is abundantly clear that the current carrying capacity of this material far outshines that of a regular conductor — even at the desired 16 [T] magnetic field, the critical current density of the material is several orders of magnitude above that of copper. The "x" in the figure indicates a point at 16 [T] and 1.9 [K], the desired field of the FCC and the typical cryogenic temperature of a newer particle accelerator (such as the LHC); the critical current density at this point is 2.13 [$\mathrm{kA\,mm^{-2}}$].

1.3.3 Pinning Centres

As the critical current of the material is the most important factor for its usefulness, as discussed in section 1.2.5, processing of the material to increase the number of pinning centres or their pinning force, without otherwise deteriorating the performance of the other two critical parameters, is of considerable importance, and a variety of methods are employed to achieve this.

[17] $a = 900$ for $\epsilon < 0$, and 1250 for $\epsilon > 0$, $u = 1.7$ and $w = 3$.

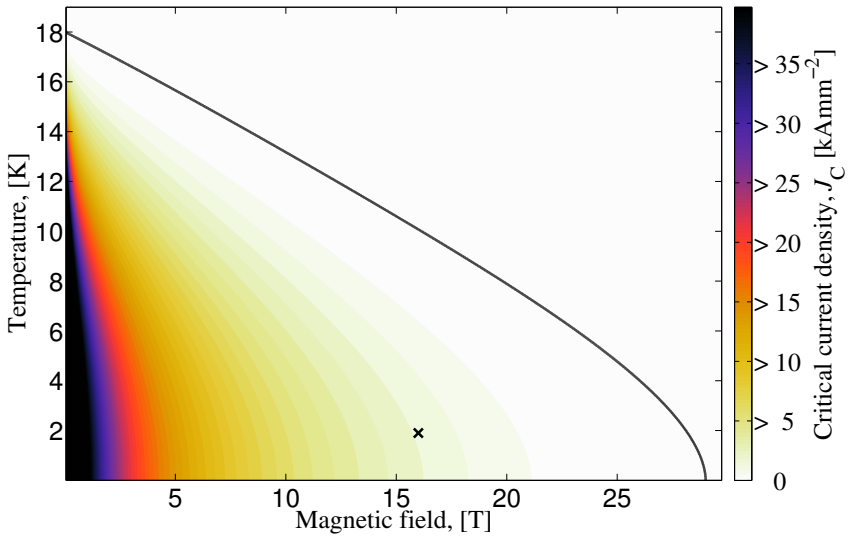

Figure 1.11: Critical surface of Nb_3Sn.

In NbTi the introduction of Titanium precipitates by intermediate heat–treatments at about 400 [°C] improves the critical current density as this is the most effective kind of pinning centres for NbTi [29, p. 701]. For Nb_3Sn the best pinning centres are grain boundaries, and significant improvements in current density have been found when heat treating samples containing nano–meter sized Copper filaments [30]. Doping MgB_2 with nano–sized diamond particles enhances the performance of the material's critical current, at the expense of somewhat lower critical temperature; the diamond particles increases the number of dislocations in the material as well as increasing the pinning strength [31]. In YBCO thin–films, introduction of nano–sized particles of non–superconducting YBCO or Silver provide both direct pinning centres, as Titanium does in NbTi, but also promotes other defects in the YBCO bulk, increasing the critical current [32].

1.4 Superconducting Cables — First Attempt

From the discussion up to now, it may seem like a superconducting magnet can be made by simply choosing a material that has the desired critical parameters and sufficient amount of pinning centres to accommodate the transport current, and then shaping into whatever geometry one desires, discussed in section 1.1.1. The truth, however, is very different; *flux jumps* are one of the large problems that needed solving before SC magnets became useful.

1.4.1 Critical–State Model

Any conductor subject to a changing magnetic field will have shielding currents induced in it, in a direction so such as to oppose the applied field change. If the conductor in question is of a resistive metal, such as copper, the shielding (or eddy) currents will decay due to this resistance. If the conductor material is a SC in which no flux pinning is present, the fluxoids will move, and, as explained in section 1.2.5, this will in practice equate to a resistance and thus decay of the shielding currents. If, finally, the material is a SC with strong pinning, the fluxoids will not move, and thus no resistance arises to attenuate the shielding currents.

Also, in any part of the material where the magnetic field is changing while also an electric field (due to the magnetic field change) is present, the current induced will always have a magnitude equal to the critical current density, as that is the only bounding value imposed. Only in parts of the material that are completely shielded from the magnetic field change will the current have a value non–equal to the critical value; it will here be zero [33, p. 38][6, p. 131].

Figure 1.12 shows a slab of superconductor, with thickness $2d$ [m] in the y–direction and infinite length in the x– and z–directions. A current ramp is applied to the slab in the z–direction[18]. The magnetic field caused by the current applied will be in the positive x–direction to the left of the slab's centre and in the negative x–direction to the right. Since the current is changing, the magnetic field is changing. This in turn means that a shielding current will be induced as indicated in the figure. This shielding current will then oppose the flow of the current towards the centre of the slab and promote it towards the surface. This is the same effect that results in the skin–effect in normal conductors. In a superconductor the effect is similar, but the current density near the surface is bounded by the critical current density of the material. The total applied current, I [A], will have to flow in the conductor, and thus, two layers of thickness $a = I/2J_c$ [m], carrying exactly the critical current, will form inwards from the surface of the slab on either side. The thickness of this layer is called the *penetration depth* (not to be confused with the London penetration depth!), and will increase with I [A] until the ramp is topped out, or the layer of critical current penetrates the whole slab ($a = d$ [m]). Figure 1.13a illustrates the full situation.

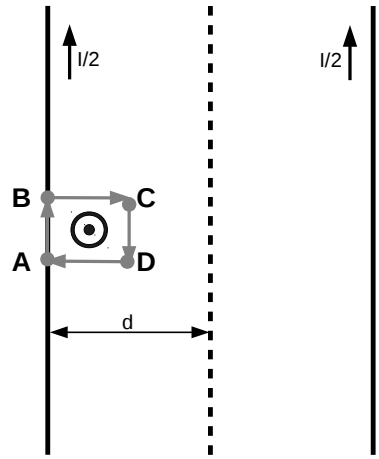

Figure 1.12: Sketch of how layers of critical current density develop [33, Fig. 3.4].

1.4.2 Unstable Equilibrium

After the current ramp stops, the superconductor will be in the state shown in figure 1.13a. The SC is in equilibrium, but it is not stable; by adding some small heat pulse, the temperature of the slab will increase somewhat. Since the critical current of the material will fall with increasing temperature, this means that the penetration of the current layer, and thus also the magnetic field, will have to increase to accommodate the applied current. By this, parts of the slab will experience both a current flow as well as a magnetic field change, as seen in figure 1.13b. The induced electric field (by the magnetic field change) will be parallel to the current in the slab, so heat is dissipated by the movement of the charge carriers. This heats causes a temperature increase, which again lowers the critical current. This will obviously mean that the equilibrium from before is lost, and this thermal runaway process is called a *flux jump* [6, p. 133][33, p. 43].

The secondary temperature rise can be controlled, however, and the following is a stability criterion to avoid flux jumping. Supposing the initial temperature increase is dT [K], the

[18] Such a ramp–up happens when the magnet is to be charged up for use. Since the magnet is a large inductance, the current cannot instantaneously be turned on, and needs to be applied at a certain rate to build up the field.

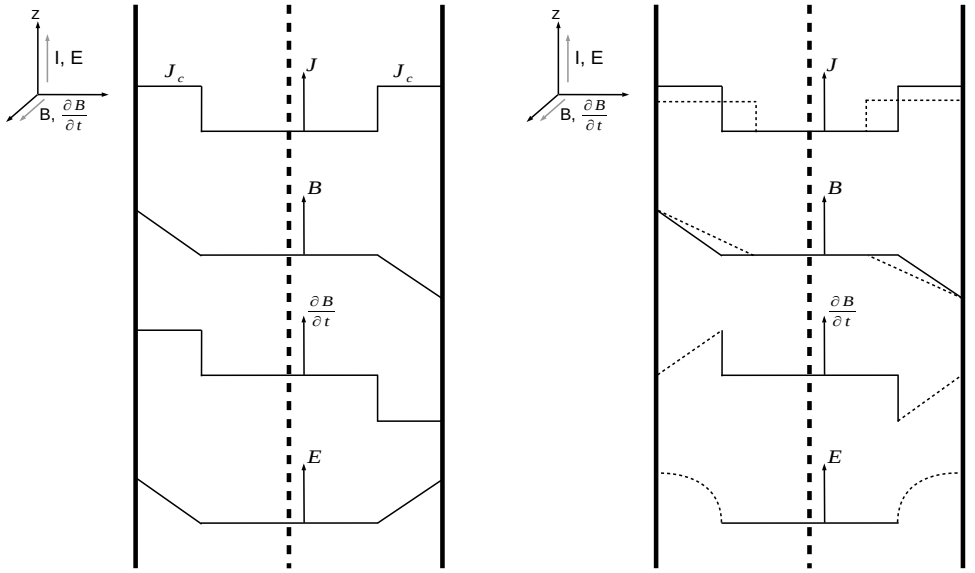

(a) At equilibrium [33, Fig. 3.5].

(b) During heat change of layer thickness [33, Fig. 3.6].

Figure 1.13: Qualitative shapes of critical current, J [kA mm^{-2}], magnetic penetration field, B [T], time derivative of the magnetic field, $\partial B/\partial t$ [T s^{-1}] and electric field, E [V m^{-1}].

secondary increase dT' [K] can be determined thusly [33, p. 44]:

By setting the origin in the y–direction at the left–most surface of the slab, the magnetic field in the penetrated region will be given as,

$$B = \mu_0 J_c(a - y) = \frac{\mu I}{2} - \mu_0 J_c y, \qquad [\mathrm{T}] \quad (1.18)$$

where a is, as before, $I/2J_c$ [m]. So[19],

$$\frac{\partial B}{\partial t} = -\mu_0 \frac{\mathrm{d}J_c}{\mathrm{d}t} y, \qquad [\mathrm{T\,s^{-1}}] \quad (1.19)$$

$$\Rightarrow E = \mu_0 \frac{\mathrm{d}J_c}{\mathrm{d}t} \frac{y^2 - a^2}{2}, \qquad [\mathrm{V\,m^{-1}}] \quad (1.20)$$

The power, P [W m^{-2}], dissipated per unit face area of the slab, between $y = 0$ [m] and $y = a$ [m],

$$P = \int_0^a J_c E \mathrm{d}y = -\mu_0 J_c \frac{\mathrm{d}J_c}{\mathrm{d}t} \frac{a^3}{3}, \qquad [\mathrm{W\,m^{-2}}] \quad (1.21)$$

The time this power has to dissipate, dt [s], gives the heat, $P\mathrm{d}t = \mathrm{d}Q$ [J m^{-2}], produced per unit face area of the slab, caused by the temperature increase dT [K]. Assuming adiabatic conditions, the heat generated can only be spent on increasing the temperature of the slab by $\mathrm{d}T' = \mathrm{d}Q/C_v a$ [K], where C_v [J m^{-3}] is the volumetric heat capacity of the material. So,

$$\frac{\mathrm{d}T'}{\mathrm{d}T} = -\mu_0 J_c \frac{\mathrm{d}J_c}{\mathrm{d}T} \frac{a^2}{3C_v}, \qquad [\mathrm{K\,K^{-1}}] \quad (1.22)$$

If, now, $\mathrm{d}T'/\mathrm{d}T$ [$\mathrm{K\,K^{-1}}$] is less than 1, it means that the further increase in temperature is smaller than the initial, and thus the process will slow down, and eventually come to a stop. If the ratio is larger than 1, the process speeds up, and a flux jump occurs. Note however, that the original equilibrium state from right after the current ramp is not reestablished; the slab simply avoids a flux jump when the ratio is less than 1.

Assuming a simple linear $J_\mathrm{c}(T)$ [$\mathrm{A\,m^{-2}}$] dependence,

$$\frac{\mathrm{d}J_\mathrm{c}}{\mathrm{d}T} = -\frac{J_\mathrm{c}}{T_\mathrm{c}-T}, \qquad [\mathrm{A\,m^{-2}\,K^{-1}}] \quad (1.23)$$

$$\Rightarrow \frac{\mathrm{d}T'}{\mathrm{d}T} = \frac{\mu_0 J_\mathrm{c}^2 a^2}{3C_\mathrm{v}(T_\mathrm{c}-T)}, \qquad [\mathrm{K\,K^{-1}}] \quad (1.24)$$

Since the penetration cannot exceed the actual dimensions of the slab ($a \leq d$) [m], there exists a d sufficiently small to give a maximum a such that $\mathrm{d}T'/\mathrm{d}T$ is always smaller than 1, and the slab is protected from flux jumps [33, p. 44].

For NbTi at 4.2 [K] and 6 [T], and the following properties [6, p. 134–135],

Critical current density	J_c	$= 1.5 \cdot 10^9$ [$\mathrm{A\,m^{-2}}$]
Density	ρ	$= 6.2 \cdot 10^3$ [$\mathrm{kg\,m^{-3}}$]
Specific heat capacity	C	$= 0.89$ [$\mathrm{J\,kg^{-1}}$]
Critical temperature	T_c	$= 6.5$ [K]

the stability criterion is fulfilled only for a half–width, d, of less than 115 [µm]. In reality, the dimension is set much lower, in order to protect from flux jumps at a wider range of conditions. Since the slab in a real magnet might very well be exposed to fields that are not perfectly perpendicular to its broad face, such as the discussion here has assumed, the dimensional restriction must be imposed on all directions normal to the applied field, and thus the slab will be reduced to a thin cylindrical filament of radius smaller than or equal to d, necessary to protect it from flux jumps.

A cable of radius on the order of 100 [µm] is very difficult to both produce and utilise, and so, the practical construction of a magnet coil is done by way of filamentary composites; the cables shown in the cross sectional figures in section 1.1.1 are thus made up of several very thin filaments of superconducting material.

1.4.3 Superconducting Cables — Second Attempt

So, the smallest piece in a magnet coil is the filament of superconducting wire. Figure 1.14b shows the filaments in the LHC dipoles, as they are installed today. Around each filament, which has a diameter of about 6 [µm], there is a 0.5 [µm] thick layer of high purity copper [34].

[19] From Farady's law, $\nabla \times E = -\partial B/\partial t$ with boundary condition that $E = 0$ for $y \geq a$ as $\partial B/\partial t = 0$, where a takes the value given by the new critical current,

$$\begin{aligned} \partial E/\partial y &= -\,\partial B/\partial t \\ \Rightarrow E &= -\int \partial B/\partial t dy \\ &= -\int -\mu_0 \frac{dJ_c}{dt} y dy = \frac{\mu_0}{2}\frac{dJ_c}{dt} y^2 + C \\ \Rightarrow E &= \mu_0 \frac{dJ_c}{dt}\frac{y^2 - a^2}{2} \end{aligned}$$

In the LHC dipoles these filaments are made of NbTi, while the magnet investigated in this thesis will use Nb_3Sn, with filaments around 50 [µm] in diameter [35].

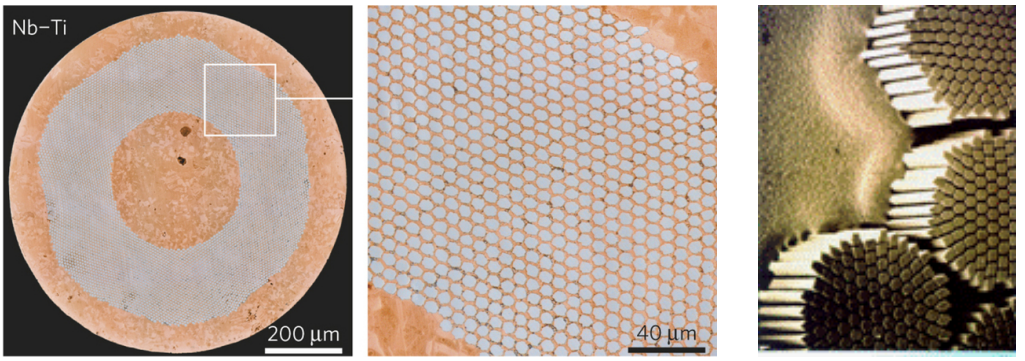

(a) Cross section of a strand in the current LHC dipoles [36].

(b) View of individual filaments [34].

Figure 1.14: Cross section of strand, magnification of the copper matrix and view of individual filaments, all from the currently installed dipoles in the LHC.

The filaments (ordered in bundles, four of which are visible in figure 1.14b) are inserted into the honey–comb structure of a copper matrix as seen in figure 1.14a[20]. The reason for using such a copper matrix is that this improves the stability of the magnet, as discussed more in–depth in section 1.7.2, as well as providing mechanical strength, as SC materials often are quite weak and brittle [7, p. 646]. The diameter of the strands in the LHC dipoles is 825 [µm], while the strands in the Nb_3Sn magnet of this thesis are 700 [µm] in diameter.

In the strand, the filaments are twisted with a given pitch. This is, just as for the size of the filaments, in order to avoid flux jumps, as a strand with non–twisted filaments would behave as if it was a large filament of radius equal to the strand rather than the individual filaments (with respect to flux jumps) [6, p. 137–139][33, p. 49].

1.5 Time–Varying Fields and AC Losses in Superconductors

When a superconducting strand composed of multiple twisted filaments is exposed to a varying magnetic field, four distinguishable kinds of coupling currents are induced. The difference between the four currents lie in which part of the conductor the current flows, the loop length of the path the current follows and the time constant with which the current decays.

For this thesis only one of these currents have significance, and the others are only mentioned briefly in table 1.3 [10, p. 13–14].

There will also be eddy–currents induced in the copper of the strand when an external field changes, and these currents will give rise to ohmic heating in the copper. Just as the coupling currents mentioned in table 1.3, the eddy–loss in the copper matrix is not treated further.

The most significant sort of coupling currents for this report are the Inter Filament Coupling Currents (IFCC). These currents are caused by the variation in the applied magnetic field, and their magnitude increases for increasing filament twist pitch and reduced resistivity of the matrix material. The characteristic time for these currents range from on the order of

[20] Normally, the metal used is Copper, but for some applications; silver or aluminium [6, p. 77][7, p. 10].

Table 1.3: Short description of the three kinds of induced coupling currents that are not treated in this report.

Currents	Cause	Characteristic time
Persistent Currents	Induced by the existence of an applied magnetic field, these are currents that partially screen the interior of a filament from the external field. The loss itself can be thought of as a hysteresis loss as it will follow the cycling of the externally applied field [6, p. 159][1, p. 591]	$\to \infty$
Inter Strand Coupling Currents	Induced by the variations in an applied magnetic field, these currents flow in and between strands in the Rutherford cable. Their magnitude increases with increasing twist pitch of the strands and decreasing contact resistance between strands [1, p. 592–593].	0.01 – 10 s
Boundary Induced Coupling Currents	Induced mainly by variations in the applied field's sweep rate, these currents flow in and between strands and between filaments within a strand. The BICC's are also caused by variations in the contact resistance between strands along the length of the cable [10, Chap. 5].	$> 10 - 10^5$ s

a few milliseconds to about 100 milliseconds. These currents generate IFCL, causing heating of the conductor.

1.5.1 Inter Filament Coupling Currents (IFCC)

The thin filaments of SC material are embedded in a conductive copper matrix, and since, to avoid flux jumping, the filaments in a strand are twisted around each other, a situation qualitatively like the one shown in figure 1.15 will arise when the strand is subject to a transverse magnetic field.

Figure 1.15a shows a simple 3D representation of two filaments twisted around each other within a strand, with a given twist pitch l_f. For a transverse applied magnetic field, a current loop can be closed by flowing partially through the SC filaments and partially straight through the normal conducting copper matrix. In figure 1.15b a strand of diameter d_s is shown. The outermost layer of filaments in the strand are at a diameter d_s^*, and the closed current loop will be formed by the path RQPUTS.

Applying an external magnetic field change, $\dot{\mathbf{B}}$ [T s^{-1}] will induce coupling currents (IFCC), producing their own magnetic field, such that the total field in the strand will be,

$$\dot{\mathbf{B}}_{\text{strand}} = \dot{\mathbf{B}}_{\text{applied}} + \dot{\mathbf{B}}_{\text{induced}}, \qquad [\text{T s}^{-1}] \quad (1.25)$$

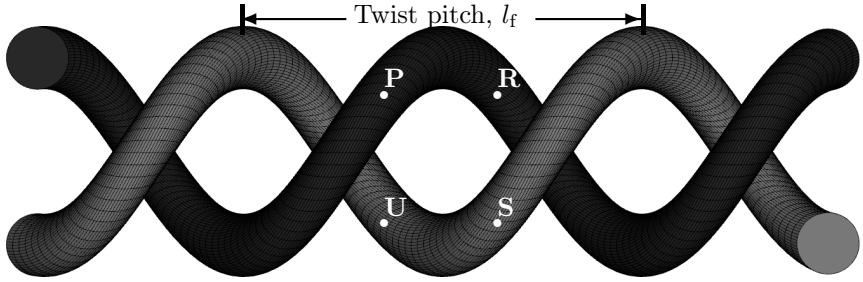

(a) Simple 3D view two filaments in a strand, twisted around each other.

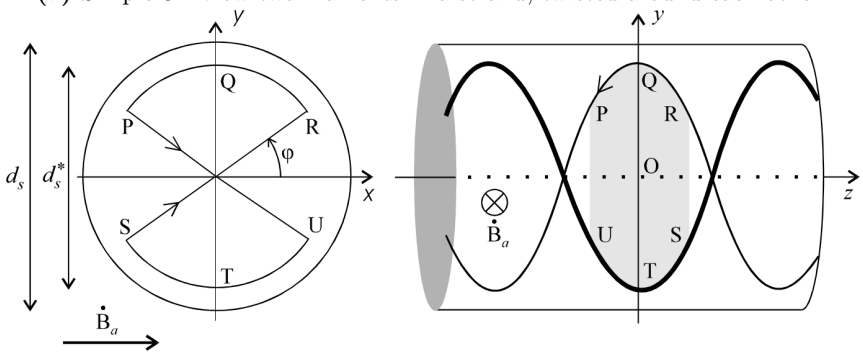

(b) Qualitative representation of the current loop created by the twisted filaments and the copper matrix in a strand. Courtesy of Arjan Verweij [10, Fig. 3.5].

Figure 1.15: Twisted filaments in a strand, subject to an applied transverse magnetic field change $\dot{\mathbf{B}}$ [T s^{-1}], with indication of how the IFCC's will find a closed loop through the matrix.

Assuming the applied field to be homogeneous in space, the induced field will also be homogeneous, and thus, the total field in the interior of the strand will be homogeneous. The voltage induced by the magnetic flux change through the RQPUTS surface, U_{induced}, with $\phi = \pi/2 - 2\pi z/l_{\text{f}}$, can only lie on the resistive part of the path, that is, SR and PU, since the voltage across a superconductor is zero. So[21],

$$\begin{aligned} U_{\text{induced}}(z) &= -\int_{\text{RQPUTS}} \dot{\mathbf{B}}_{\text{strand}} \mathrm{d}A \\ &= -4\frac{d_s^*}{2}\dot{\mathbf{B}}_{\text{strand}} \int_0^z \cos\left(\frac{2\pi z}{l_{\text{f}}}\right) \mathrm{d}z \qquad \text{[V]} \quad (1.26) \\ &= -2d_{\text{s}}^* \left(\frac{l_{\text{f}}}{2\pi}\right) \dot{\mathbf{B}}_{\text{strand}} \cos(\phi), \end{aligned}$$

Separating the voltage across the two resistive parts of the paths into four by including the origin (paths are now OR, PO, OU and SO), the voltage at the surface of any filament at position ϕ [rad] will be given as,

$$U(\phi) = \frac{1}{4}U_{\text{induced}}(z) = -\left(\frac{l_{\text{f}}}{2\pi}\right)\frac{d_{\text{s}}^*\dot{\mathbf{B}}_{\text{strand}}}{2}\cos(\phi), \qquad \text{[V]} \quad (1.27)$$

[21] Using $\sin(\pi/2 - \alpha) = \cos(\alpha)$

using that $x = d_s^* \cos(\phi)/2$ [m], this voltage gives rise to an electric field, parallel to $\dot{\mathbf{B}}_{\text{applied}}$ [$\mathrm{T\,s^{-1}}$][22],

$$\mathbf{E} = -\left(\frac{l_\mathrm{f}}{2\pi}\right)\dot{\mathbf{B}}_{\text{strand}}, \qquad [\mathrm{V\,m^{-1}}] \quad (1.28)$$

This electric field will give rise to a current density, $\mathbf{J}$ [$\mathrm{A\,m^{-2}}$], flowing across the strand, in anti–parallel to $\dot{\mathbf{B}}_{\text{strand}}$ [37],

$$\mathbf{J} = -\left(\frac{l_\mathrm{f}}{2\pi}\right)\frac{\dot{\mathbf{B}}_{\text{strand}}}{\rho_{\text{eff}}}, \qquad [\mathrm{A\,m^{-2}}] \quad (1.29)$$

where ρ_{eff} is the effective transverse resistivity of the matrix material, as defined in section 1.6, in most cases, such as this one, Copper.

1.5.2 Inter Filament Coupling Loss (IFCL)

The IFCC flowing in the outer filaments of the strand will serve to screen the interior of the strand from the external field, and Wilson gives this screening effect as [6, p. 179],

$$\mathbf{B}_{\text{strand}} = \mathbf{B}_{\text{applied}} - \tau\dot{\mathbf{B}}_{\text{induced}}, \qquad [\mathrm{T\,s^{-1}}] \quad (1.30)$$

where,

$$\tau = \frac{\mu_0}{2\rho_{\text{eff}}}\left(\frac{l_\mathrm{f}}{2\pi}\right)^2, \qquad [\mathrm{s}] \quad (1.31)$$

is the time constant of the decay of the IFCC once the field change stops (and also its rise rate when the field starts changing).

The current flowing in the matrix material will dissipate power, with a power density given by equations 1.28 and 1.29, with τ as defined in equation 1.31 [6, p. 180][10, p. 52],

$$P_{\text{IFCL}} = \frac{|\dot{\mathbf{B}}_{\text{induced}}|^2}{\rho_{\text{eff}}}\left(\frac{l_\mathrm{f}}{2\pi}\right)^2 = \frac{2|\dot{\mathbf{B}}_{\text{induced}}|^2}{\mu_0}\tau, \qquad [\mathrm{W\,m^{-3}}] \quad (1.32)$$

This indicates that a higher twist pitch will cause larger IFCL; this is true in therms of maximum possible amplitude of the loss, but since a larger twist pitch means that the time constant grows, the IFCC's may not have time to develop fully if the applied field oscillates too fast. So, for a growing applied field frequency, the total loss will fall given the same time constant. In fact, the dependence on frequency is quite sharp as seen in figure 1.16.

1.6 Material Properties

The superconducting cable used in an accelerator magnet, now, consists of more than the superconductor itself. This means that new material properties must be taken into account, and that differences in properties between the SC material and the copper matrix may influence the overall behaviour of the composite.

1.6.1 Residual Resistivity Ratio (RRR)

The Residual Resistivity Ratio is defined as the ratio between a materials resistivity at ice temperature and at cryogenic temperature, in the normal state (if relevant) [1, p. 466],

$$RRR = \frac{\rho(T = 273[\mathrm{K}])}{\rho(T = 4[\mathrm{K}])} \quad (1.33)$$

[22] Note that the small component of the electric field that lies in the z–direction due to the twist angle is neglected.

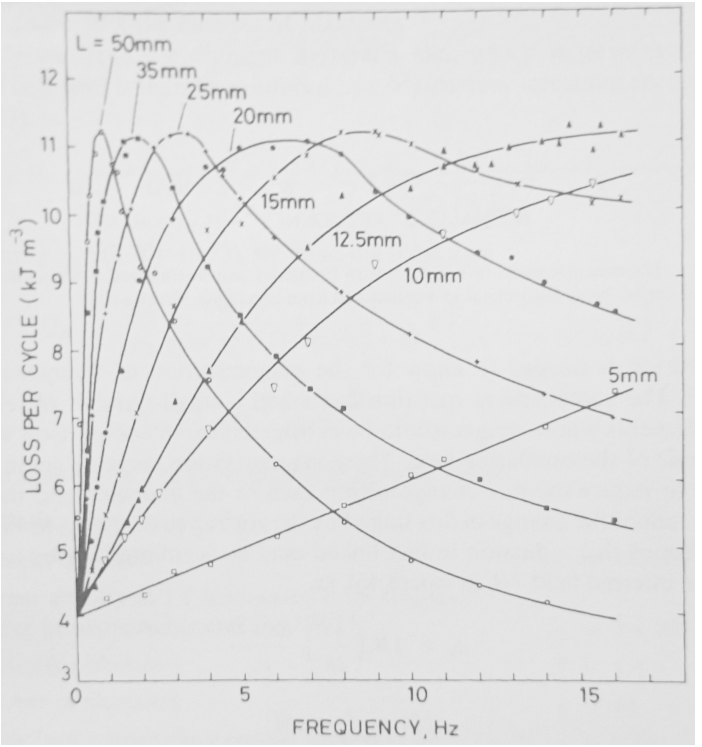

Figure 1.16: Experimental measurements of AC loss in a twisted multifilamentary composite, as a function of applied frequency and filament twist pitch ("L" in the figure). Figure itself is taken from [6, p. 185], based on data from [38].

This value will be indicative of the materials purity, as at room temperature, the resistivity is completely dominated by the electron–phonon scattering, while at cryogenic temperature, where the density of phonons is far lower, the resistivity is dominated by the electron's interactions with lattice imperfections and impurities [15, p. 148–150]. So a high RRR means that the resistivity at low temperature is low, because the purity of the material is high.

Table 1.4 gives approximate values for the electrical resistivity of copper and Nb_3Sn(in the normal state) at low temperatures. From this it is clear that if the superconductor should lose its superconductivity, the current that previously flowed in it will now mostly flow in the copper matrix, as the resistivity of the copper is between 3 and 1 orders of magnitude lower than that of Nb_3Sn in the normal state. This is the reason why the temperature at which superconductivity is destroyed mostly commonly is called the *current sharing temperature*.

Table 1.4: Approximate values of electrical resistivity for low temperatures for copper at RRR around 100, and Nb_3Sn in the normal state [39, 40].

Material	ρ **(4 [K]) [n**Ω **m]**	ρ **(100 [K]) [n**Ω **m]**	ρ **(200 [K]) [n**Ω **m]**
Copper	0.2	2	10
Nb_3Sn	240[23]	300	370

1.6.2 Cross Contact Resistance and Effective Transverse Resistivity

Section 1.5 discusses currents flowing between the filaments within a strand, through the matrix material. The path this current takes will influence the equivalent resistance the matrix material poses for these currents. Figure 1.17 gives a qualitative description of how the currents can flow. In the left hand case, the contact resistance between the SC filament and the matrix metal is zero, and so transverse currents in the strand will partially flow through superconducting regions, effectively decreasing the transverse matrix resistivity. For the right hand case, the cross contact resistance between the filament and matrix is infinite, which causes the transverse currents to flow around the filaments, thus lengthening the resistive path, and increasing the effective transverse matrix resistance.

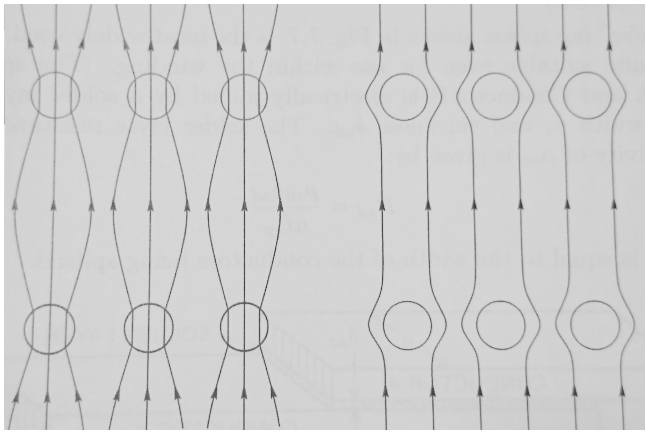

Figure 1.17: Current paths in the perpendicular direction in a multifilamentary strand. Left hand side is the limit for zero contact resistance between matrix and filament, while the right hand side is the limit for infinite contact resistance between the matrix material and the filament [7, Fig. 7.6].

Two models have been proposed for the limiting cases [7, p. 407],

$$\rho_{\mathrm{eff},0} = \frac{1 - f_{\mathrm{SC}}}{1 + f_{\mathrm{SC}}}\rho_{\mathrm{m}}, \qquad [\Omega\,\mathrm{m}] \quad (1.34)$$

$$\rho_{\mathrm{eff},\infty} = \frac{1 + f_{\mathrm{SC}}}{1 - f_{\mathrm{SC}}}\rho_{\mathrm{m}}, \qquad [\Omega\,\mathrm{m}] \quad (1.35)$$

where f_{SC} is the volumetric fraction of superconductor in the strand, and ρ_{m} is the matrix materials electrical resistivity.

Equation 1.34 is normally used to describe Nb_3Sn conductor matrices, while equation 1.35 is used for NbTi conductors.

1.6.3 Magnetoresistivity

When a normal conductor carrying a current is exposed to a transverse magnetic field, the moving charges experience a Lorentz force that changes their trajectories somewhat. This results in an increase in the electrical resistance, and the effect is called *magnetoresistivity* [33, p. 31–32].

[23] The material was brought to the normal state by applying a magnetic field or a current above the critical value; in the superconducting state is, of course, zero.

For many metals, among them, copper, the magnetoresistivity is simply proportional to the applied field [1, p. 466],

$$\rho_{mag} = \alpha B, \qquad [\Omega\,\mathrm{m}] \quad (1.36)$$

where α $[\Omega\,\mathrm{m\,T^{-1}}]$ is the proportionality constant, which for copper is about $4.5 \cdot 10^{-11}$ $[\Omega\,\mathrm{m\,T^{-1}}]$.

Comparing the residual resistivity of copper at cryogenic temperature to its magnetoresistance at 16 [T](the proposed operating field of the magnet investigated in this thesis), the contributions to the resistivity is about 0.7 [nΩ m] from magnetoresistance and 0.2 [nΩ m] from electrical resistance, which means that for as long as the field is high and temperature is low, magnetoresistance is a very important factor in the total resistance of the matrix.

1.6.4 Note on NbTi and Nb_3Sn Manufacture

NbTi is by far the most widely used material in SC magnets, even if Nb_3Sn is practically as old (and, thus, researched) and has better critical parameters. A main reason for this is the brittleness of the material [41]. While NbTi can be made into filamentary composites by simple extrusion, cold drawing and twisting [6, p. 290], Nb_3Sn would break, or at the least suffer severe J_c deterioration [42]. For this reason the coil of a magnet made with Nb_3Sn must be made using the *wind–and–react* method [41, 43]. This method consists of making the cable with pure Niobium and Bronze and then winding the coil with this cable *before* the actual superconductor is created. To create the actual Nb_3Sn, the coil undergoes heat treatment of up to 650 [°C] for up to 10 days [6, p. 298], which causes the Tin from the Bronze to diffuse into the Niobium, leaving Copper behind.

1.7 Quench and Stability of a Magnet

What happens, then, if the critical surface of the magnet, somehow, is breached; the current becoming too large, or the field superseding the upper critical value, or perhaps the temperature rises above the transition value? The location at which this occurs will experience a *quench*.

> **Quench**: The superconducting–to–normal transition; specifically, the rapid, irreversible process in which the magnet, or a part of the magnet, is driven fully normal [7, p. 656].

During a quench, the magnetic energy stored in the coil will be released into the normal conducting parts of the magnet. Even for very high current densities, the total stored energy is not so large as to be a problem; if it was distributed completely uniformly across the volume of the coil, it will cause a temperature rise, but not so large as to be dangerous [7, p. 467][6, p. 200].

However, in practice, the quench starts in only a very small point, and from there propagates outwards due to ohmic heating and thermal conduction. As this normal zone grows (the quench spreads to other parts of the coil) the electrical resistance it constitutes will eventually be sufficient to make the magnet current decay. This, however, will take far too long to avoid damage to the coil; either the insulation between turns is destroyed by heat, the coil itself can melt[24], or the voltage across the normal zone can become so large as to cause arcing between turns [6, p. 200–201]. The point in the coil that reaches the highest

[24] Although quite unlikely.

temperature during a quench is called the *hot–spot* and often, though not always, this point is also where the quench initially started[25].

An additional problem to consider is that the pressure in the cryostat may reach very high levels due to the cryogen boiling as it comes in contact with the rapidly heating normal zone[26].

What hot–spot temperature is considered safe is a matter of some controversy; Fazilleau et al. aims for 150 [K] in a Nb_3Sn magnet [45], Iwasa considers 300 [K] "very risky" for magnets in general [7, p. 470], while Ambrosio suggests that a hot–spot temperature as high as 400 [K] will not cause permanent damage to a Nb_3Sn magnet [46].

In this thesis it has been decided to take 350 [K] as the hard limit under which the hot–spot *has* to be kept [47, 48].

What Causes a Quench

Several sources that lead to a quench can be identified; the most important ones are Lorentz forces in the coil causing movement and thus friction between components in the magnet, and heating due to beam losses [1, p. 593]. Other sources include flux jumps, AC losses and heat leaks [49]. For this thesis the kind of AC losses called IFCL are of particular importance, and this was treated separately in section 1.5.

It is usual to distinguish between two different kinds of quenches; the *natural* quench is one that occurs when the field, current or temperature is raised, on purpose, say during a test, beyond their respective critical values. A *disturbance* quench is one caused unintentionally during operation, due to one of the above mentioned causes. As will be described in more detail in section 1.7.2, only a few $\mathrm{mJ\,cm^{-3}}$ is needed to raise the temperature of a small volume of the coil above the local current sharing temperature [1, p. 593].

1.7.1 Quench Load

During a quench, the electrical resistance of the coil increases, and the resultant circuit will be an RL–circuit, in which the current decays exponentially. By assuming adiabatic conditions, a conservative estimate of the hot–spot temperature can be found by a local heat balance approach [7, p. 471–473][50][27],

$$f_{\mathrm{stab}}\bar{c}(T)\frac{\mathrm{d}T}{\mathrm{d}t} = \rho_{\mathrm{stab}}(T)J^2(t), \qquad [\Omega\,\mathrm{A^2\,m^{-3}}] \quad (1.37)$$

where $\bar{c}(T)$ $[\mathrm{J\,K^{-1}\,m^{-3}}]$ is the volumetric heat capacity of the of the conductor[28], ρ_{stab} $[\Omega\,\mathrm{m}]$ is the resistivity of the stabiliser, f_{stab} is the fraction of stabiliser in the conductor and J $[\mathrm{A\,m^{-2}}]$ is the current density.

Integrating from initial to end conditions, and sorting magnet and material properties on the left hand side,

$$f_{\mathrm{stab}}\int_{T_0}^{T_{\max}}\frac{\bar{c}(T)}{\rho_{\mathrm{stab}}(T)}\mathrm{d}T = \int_0^{\infty}J^2\mathrm{d}t, \qquad [\mathrm{A^2\,s\,m^{-4}}] \quad (1.38)$$

[25] Given that it is here, after all, the magnetic energy and current in the coil have the longest time to deposit energy.

[26] While not entirely the same situation, the famous incident in 2008 at the LHC was indeed caused by excessive pressure built up by the breaching of the helium cooling system when a faulty electrical lead, causing arcing, vaporised the helium line [44].

[27] Valid for any adiabatic heating of a magnet.

[28] Weighted over the fractions of all materials composing it; copper matrix, SC, insulation, epoxy, etc.

where T_0 [K] is the initial temperature, normally the operating temperature of the magnet, and $T_{\max}$ [K] is the temperature at the end of the discharge, normally the hot–spot temperature.

The protection function $\Gamma(T_{\max})$ [$\mathrm{A^2\,s\,m^{-4}}$] is defined from the left hand side of equation 1.38, while the right hand side is called the *quench load*[29];

$$\Gamma(T_{\max}) = \int_0^\infty J^2 \mathrm{d}t, \qquad [\mathrm{A^2\,s\,m^{-4}}] \quad (1.39)$$

This means that when using a matrix material with large heat capacity and small resistivity, the hot–spot temperature will fall given the same quench load. Also, if the quench load is reduced by a faster decay of the current, the same effect on hot–spot temperature will be seen.

1.7.2 Stability

In a magnet carrying its operating current, I_{op}, the temperature, T [K], of a unit volume of the coil is governed by the following equation [7, p. 352]:

$$\begin{aligned} C_{\mathrm{hc}}(T)\frac{\partial T}{\partial t} &= \nabla \cdot [k_{\mathrm{tc}}(T)\nabla T] + \rho_{\mathrm{c}}(T)J_{\mathrm{c}}^2(t) \\ &\quad + g_{\mathrm{d}}(t) - \frac{f_{\mathrm{c}}\mathcal{P}}{A_{\mathrm{c}}} g_{\mathrm{q}}(t), \end{aligned} \qquad [\mathrm{J\,m^{-3}\,s^{-1}}] \quad (1.40)$$

The left hand side of equation 1.40 gives the time rate of change of the thermal energy in the unit volume, where C_{hc} [$\mathrm{J\,K^{-1}\,m^{-3}}$] is the materials heat capacity. In order to have complete steady–state stability, this term must remain zero; however, in real magnets, a small deviation, ΔT_{op} [K], from the operating temperature, T_{op} [K] is allowed.

On the right hand side of the equation, the terms are as follows; the first term gives the thermal conduction into the volume from outside the volume, where k_{tc} [$\mathrm{W\,K^{-1}\,m^{-1}}$] is the materials thermal conductivity. $\rho_{\mathrm{c}}(T)J_{\mathrm{c}}^2(t)$ [$\Omega\,\mathrm{A^2\,m^{-3}}$] gives the ohmic heating of the volume, where ρ_{c} [$\Omega\,\mathrm{m}$] is zero before quench and non–zero after, and J_{c} [$\mathrm{A\,m^{-2}}$] is the current density, which can vary with time[30]. g_{d} [$\mathrm{W\,m^{-3}}$] is heat caused primarily by magnetic and mechanical effects (and other disturbances), while the last term gives the cooling, where $\mathcal{P}$ [m] is the total conductor perimeter, f_{c} is the fraction of this perimeter exposed to cryogen, A_{c} [$\mathrm{m^2}$] is the conductor cross section and g_{q} [$\mathrm{W\,m^{-2}}$] is the convective heat transfer flux from the conductor to the cryogen.

In the case of interest in this report, *protection* of a quenching magnet, only the ohmic loss contributes significantly to the energy density in the normal zone, and as such, the case in question is considered adiabatic, and all other terms are neglected [7, p. 471].

Note on the Disturbance Spectrum

Figure 1.18 gives an estimated spectrum of the different kinds of disturbances a LTS magnet can be subject to under normal operation. For most magnets, AC losses and wire motion, i.e. magnetic and mechanical disturbances, pose the largest risks, as most magnets are used outside of heavily radiated environments. However, magnets used in particle accelerators, such as the 11T High Luminosity LHC (HL–LHC) dipole, will experience a large contribution from particle showers due to several kinds of beam losses [1, Chap. 8].

[29] In literature, the protection function is often called $U(\theta)$ [6] or $Z(T_{\mathrm{f}}, T_{\mathrm{i}})$ [7]. The choice of $\Gamma(T_{\max})$ was made for consistency with my supervisor's PhD in the subject [51].

[30] During a quench, the current decays, and thus changes with time.

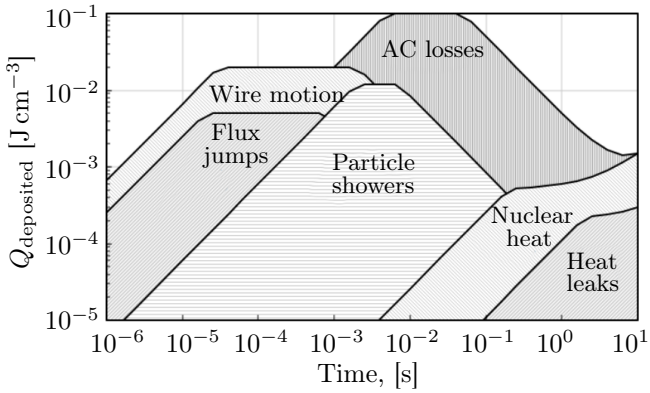

Figure 1.18: Disturbance spectrum; energy density of heat deposition plotted against the processes characteristic deposition time [49].

Heat Capacity

For long–term stability of a magnet during operation, one requires that $\partial T/\partial t \simeq 0$ [K s^{-1}] [7, p. 354]. As seen from equation 1.40, this is inversely proportional to the heat capacity of the conductor material. The fundamental challenge with stability in a LTS SC magnet is what is known as the *Debye T^3 law*; at low temperatures the heat capacity of a material follows a cubic proportionality to the temperature [15, p. 114][31]. This means that at low temperatures, certainly the ones relevant for LTS magnets, the heat capacities are *very* low. Table 1.5 gives the heat capacities of some important materials over interesting temperature spans.

Margin to Quench

From this is useful to define a *margin to quench*, or *energy margin*, that gives the maximum energy density, Δe_{q} [mJ cm^{-3}] a superconductor can absorb safely; that is, without quenching. Under adiabatic conditions the quench margin is given as [7, p. 357],

$$\Delta e_{\text{q}} = \int_{T_{\text{op}}}^{T_{\text{cs}}} C_{\text{hc}}(T)\mathrm{d}T, \qquad [\text{mJ cm}^{-3}] \quad (1.41)$$

where T_{op} [K] is the operating temperature, T_{cs} [K] is the current sharing temperature and C_{hc} [J K^{-1} m^{-3}] is the heat capacity of the whole cable, including copper matrix and insulation.

As seen from figure 1.18, the magnet can easily be subject to disturbances on the order of a few tens of mJ cm^{-3}, which from table 1.5 will translate, for Nb_3Sn at an operating temperature of 1.9 K, to a temperature increase of about 4 to 5 K (assuming a 20 mJ cm^{-3} energy deposition), which in the high field regions of the magnet during regular operation is very close to the current sharing temperature[32].

[31] Low temperatures here mean temperatures at which only long wavelength acoustic phonons are excited. These phonons (recall: lattice vibrations) are called so due to their resemblance to acoustic waves in air; elastic longitudinal waves (note that also transverse phonons can exist in the acoustic mode). The higher energy optical phonons are not excited (or very sparsely excited) at temperatures close to absolute zero [15, Chap. 4 & 5].

[32] As seen in figure 3.7 of chapter 3, the current sharing temperature of the magnet at nominal current is about 4 [K].

Table 1.5: Specific heat for several materials and temperatures. Note that value for Nb_3Sn at 20 [K] in the table is really for 18.2 [K]. Numbers for Nb_3Sn from Kim [40], the rest from Iwasa [7, p. 354].

Superconductor operating temperature range	⇐ NbTi (T_c = 9.8 [K]) ⇒						
	⇐ Nb_3Sn (T_c = 18.2 [K]) ⇒						
	⇐ MgB_2 (T_c = 39 [K]) ⇒						
	⇐ YBCO (T_c = 93 [K]) ⇒						
	$C_p(T)$ [J cm^{-3} K^{-1}]						
Material	2 [K]	4 [K]	10 [K]	20 [K]	30 [K]	50 [K]	90 [K]
Copper	0.00025	0.00089	0.0076	0.067	0.236	0.857	2.07
NbTi	0.00018	0.0014	0.022	—	—	—	—
Nb_3Sn	0.0031	0.0066	0.0225	0.0696	—	—	
MgB_2	0.00004	0.00032	0.00181	0.0081	0.0242	—	—
YBCO	0.000086	0.0007	—	—	0.120	0.454	1.12

It is important to note that this is a worst case scenario approach to the stability of the magnet. While the quench margin at nominal conditions is very small, the number of quenches in the LHC is far lower than what has been hinted at here. Reliability studies of the quench protection system assumes a total of 24 magnet quenches per week of operation; of a total of approximately 1200 dipole magnets, 24 will experience a quench in a given week. This number is further reduced by looking at the actual cause of the quench, as most will be due to propagation of the quench from one magnet to its neighbour, and some quenches are caused by false triggers of the quench protection system [52–54].

1.8 Quench Protection

If, then, a quench occurs, the magnet is at risk of serious damage, and given the cost of the magnet as well as the time it takes to replace one, the need for good protection systems cannot be overstated — an unprotected magnet simply will not be used.

Four different approaches to quench protection are identified and summarised in figure 1.19 [47, 50].

Active vs Passive Quench Detection An active protection system relies on external circuitry to detect the quench, and subsequent switching on of some kind of energy discharge system. A passive protection system is activated by the quench itself.

Internal vs External Discharge System An external discharge protection system will rely on leading the current away from (by–passing) the magnet coil, and into an external dump resistor, while an internal discharge system will spread the energy of the quench uniformly across the coil volume.

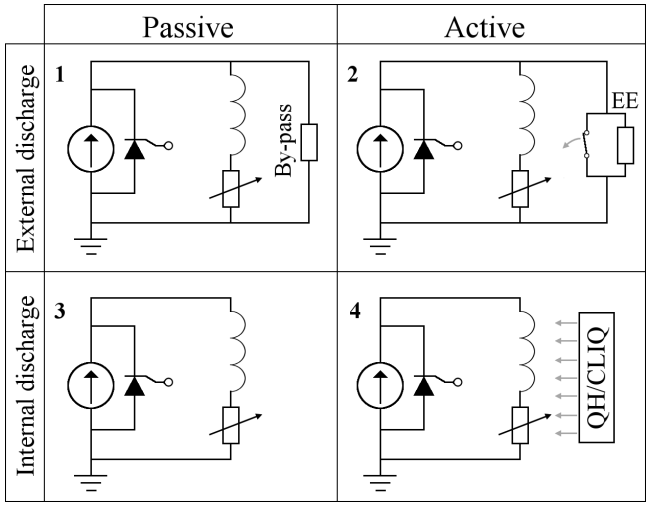

Figure 1.19: Quench protection strategies. Courtesy of Emmanuele Ravaioli.

For the large high–field magnets of modern particle accelerators only active internal discharge protection systems have the necessary performance, and as such, the other strategies are very little interest for this thesis.

1.8.1 Active, Internal Discharge Protection System

The constant push for magnets with higher fields and/or higher current densities, such as the plans for the long term upgrades to the LHC [55–57], require tremendous effort in developing quench protection systems capable of efficiently and reliably discharging the magnetic energy when a quench occurs.

By actively forcing the coil to quench uniformly, very quickly after an initial normal transition is detected, the discharge of the magnet can be done without excessive heating of any single volume of the coil. Such active internal energy discharge systems are the ones normally used in modern high–performance SC magnets. For chains of several magnets, the complete protection system will comprise active internal discharge quench protection, as well as an external by–pass system, for each individual coil, and an energy extraction system arching several magnets in order to extract the energy of any still–superconducting coils during quench in one of the magnets in the chain[58–60].

If the energy stored in the magnetic field was released as heat in the SC conductor perfectly uniformly, the total temperature rise for an operating field of 25 [T] would only be about 200 [K], which is certainly acceptable [7, p. 467]. However, during a quench without interference of any protection system, the resistive volume into which the energy is deposited is far from uniform, as it starts in a point and grows from there. If the entire coil could be turned resistive very fast, then the energy deposition would also be more uniform, reducing the risk of serious damage.

To transition a volume of 0.1 m^3 of NbTi (roughly equal to the volume of conductor in the LHC dipoles) within 10 [ms], the power delivered needs to be around 250 kW. Delivering this kind of power safely, reliably and uniformly to an object of several meters length is a considerable challenge. Taking also into account the non–uniform initial magnetic field in the coil, the magnetoresistivity will cause non–uniform ohmic heating even if the entire coil was taken to the normal state simultaneously.

1.8.2 Quench Heaters

The most widely used protection system for high–performance magnets is the active internal discharge Quench Heaters (QH) system, consisting of very thin (few tens of micrometers) stainless steel strips covered in polyamide electrical insulation foil, and attached to the insulation of the coil one wants to protect. Figure 1.20 shows how the QH strips are attached to the double aperture main dipoles of the LHC [58, 60–63][11, Chap. 7 and 9].

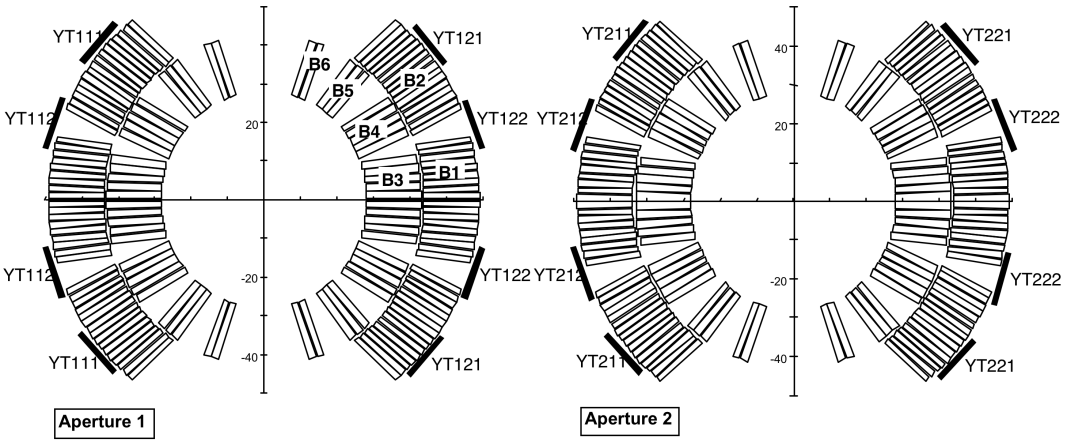

Figure 1.20: Cross section of the twin aperture dipole magnets currently installed in the LHC. The heater strips are located as indicated by the labels "YT" [64].

The terminals of each QH strip are connected to a capacitor, C_{QH}, charged to a voltage, U_0. When a quench is detected, the capacitor discharges, and the strips heat up, causing a transfer of energy from the strips to the magnet coil. Assuming a negligible dependence of the strip resistance, R_{QH}, on temperature, the voltage across the strip, $U_{\mathrm{QH}}(t)$, will decay exponentially, with time constant $\tau_{\mathrm{QH}} = R_{\mathrm{QH}}C_{\mathrm{QH}}$. The instantaneous ohmic loss developed in the QH strips will be $P_{\mathrm{QH}}(t) = U^2_{\mathrm{QH}}(t)/R_{\mathrm{QH}}$. This power is to be delivered to the windings by thermal diffusion through the insulation foil around the heater strips, and as such, the thickness of this insulation is a very important parameter influencing the performance of the QH system; the choice is a compromise between large thermal diffusion, demanding thin insulation, and reduction of risk of electrical breakdown, demanding thicker insulation [65].

Modern NbTi magnets typically have time margins in the range of 100–200 [ms][33], while next generation Nb_3Sn magnets, such as the 11 [T] dipole proposed for the HL–LHC, will have margins in the range 10–50 [ms] [66]. This means that protection systems for new magnets must be much more effective than the current QH systems. In fact, looking at the quench–heater delay, the time between QH triggering and the initiation of quench in the high–field areas of the coil, in Nb_3Sn model magnets for the HL–LHC, this time is in the range of 10–30 [ms] for both the 12 [T] quadrupole and 11 [T] dipole[67, 68]. This time, then, refers to the start of the protection–system–induced quench, while the time margin refers to the entire time needed to bring all of the coil to the normal state. As seen in figure 1.20, the heater strips do not touch all the cables of the coil; none of the inner layer cables are in contact with the strips, and many of the outer layer cables are not in contact with the strips. This means that the quench must propagate from the heat–quenched turns across the

[33]The time within which the coil has to be transferred to the normal state in order to stay protected (having the final hot–spot temperature below its threshold.

insulation to cables not touched directly by the heat source. Propagation from one turn to another in the same layer typically takes 10 [ms], while propagation from one layer to the other takes 30–50 [ms] [66, 69].

Given also the complicated design, with fastening glues and insulation materials, mechanical strain during thermal cycles and possible damage from overheating, it is seen that the QH approach to protection of magnets may not be the best way to move forward [70, 71].

1.8.3 CLIQ

Section 1.5 describes the Inter Filament Coupling Loss as a disturbance, that, according to the stability discussion in section 1.7.2 may cause a quench in the magnet. However, a novel protection system called the Coupling–Loss Induced Quench protection system is based on this exact loss in order to quench the magnet.

By introducing IFCC on purpose to the composite cables, ohmic loss is generated very uniformly in the coil, heating it up very quickly. With suitable system components, the power and energy developed and deposited will quench the magnet much faster than the currently applied QH technology, while both being electrically simpler, and completely external to the magnet. With faster quenching of the magnet comes lower hot–spot temperature and reduced risk of both thermal and electrical damage to the coil and surrounding equipment.

Chapter 2

Coupling–Loss Induced Quench Protection System

How does the CLIQ system work?

In this chapter I lay the foundation for just that — the electrical circuit, the governing equations and most importantly, the magnetic field transient the CLIQ creates in the magnet upon triggering.

The system also allows for several different configurations with varying properties in terms of a parameter called the CLIQ effectiveness, Ψ.

Finally, the modelling approach I use in the thesis is described briefly, as the transient introduced by CLIQ is very complex, and several physical domains influence each other.

2.1 CLIQ Discharge Circuit

After the LHC proved that the 2–in–1 cryostat design, with both beam pipes and magnet coils in the same cryostat, achieved both large spatial and monetary savings, new magnet designs for high–energy particle accelerators are usually intended with the same 2–in–1 design [11, Chap. 7] [72, p. 75]. These two coils must be protected individually, regardless of the protection scheme used. So, treating the CLIQ system as a black box for now, a very simple electrical circuit of the CLIQ connection to such a dipole will look as in figure 2.1. The circuit indicates with dashed lines that the magnet chain continues on both sides, as several dipoles are connected together[1]. Qualitatively, the figure serves to illustrate one of the main advantages of the CLIQ system: it is external to the magnet, in that it does not interfere with the coil winding itself the way QH do[2]; so long as there are connection points for the CLIQ leads, the coil geometry is not influenced by any requirements of the CLIQ unit.

[1] In the LHC, 154 dipoles are connected in series to form a section of the accelerator arc.
[2] Recall section 1.8.2

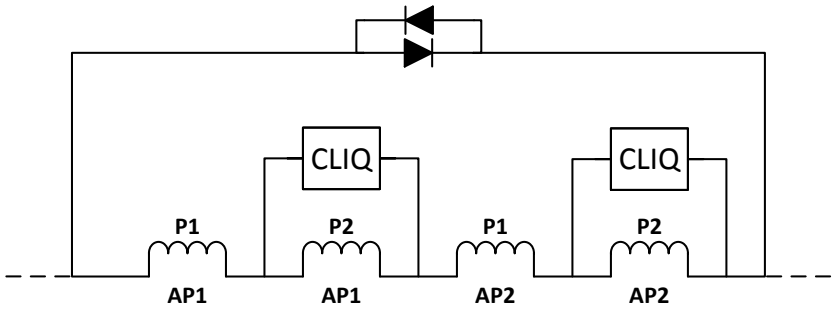

Figure 2.1: Simple representation of how two CLIQ black boxes will be connected to a double aperture dipole magnet.

For this thesis only a one aperture version of a 16 [T] block–coil dipole magnet has been studied. This is done for two reasons; firstly, while design propositions exist for a double aperture magnet of this kind [3], the only model magnets that have been built so far are of the single aperture version. Secondly, assuming that the two CLIQ units one would use for a double aperture design are identical, that the coils in the two apertures are identical and that there are no equipment malfunctions, the discharges through the two sub–circuits will be entirely symmetrical, and as such, only one discharge needs to be modelled. In addition to this, the mutual inductance between the two apertures of a 2–in–1 coil is very small, so any current changes in one of the apertures will have negligible effect on the other[3], as the iron yoke very effectively screens the two apertures from each other.

The proposed solution for the double aperture 16 [T] block–coil dipole does, in fact, include a left–right asymmetry in the two apertures, but this is done in order to better decouple the two coils, and as such should support rather than weaken the assumption of symmetry in the individual discharges.

CLIQ in Essence

The Coupling–Loss Induced Quench protection system relies on creating a few short current oscillations in the circuit by using a capacitance of suitable value in series with the inductive magnets [74]. As described in section 1.5, these oscillations will generate IFCL as they constitute a time–varying current, which in turn gives rise to a time–varying magnetic field. If this loss is sufficiently high, it will initiate a quench in the magnet.

Figure 2.2 shows the transient response of a Nb_3Sn quadrupole developed by the US LHC Accelerator Research Program (LARP) collaboration for the HL–LHC [75] during a CLIQ discharge. The employed CLIQ unit, connected to the midpoint of the coil, has a capacitance of 28.2 [mF] and a charging voltage of 500 [V]. At a time t = 0, the magnet is operating at its nominal current (14.6 [kA]) and the CLIQ unit is triggered. This introduces an oscillating current, I_C, of about 2 [kA] and 26 [Hz] on top of the transport current. These oscillations are sufficient to quench the entire coil within 10 [ms]. This gives rise to a large electrical resistance that then discharges the current in the magnet. The simulated curves are obtained with the same model as the other simulation results presented in the thesis, and the model

[3]In the LHC main dipoles, it is indeed true that for perfectly symmetric apertures, the influence of one aperture on the other is very small [73].

itself is described briefly in section 2.5. As can be seen, there is very good agreement between the measured curves and the simulated ones [47].

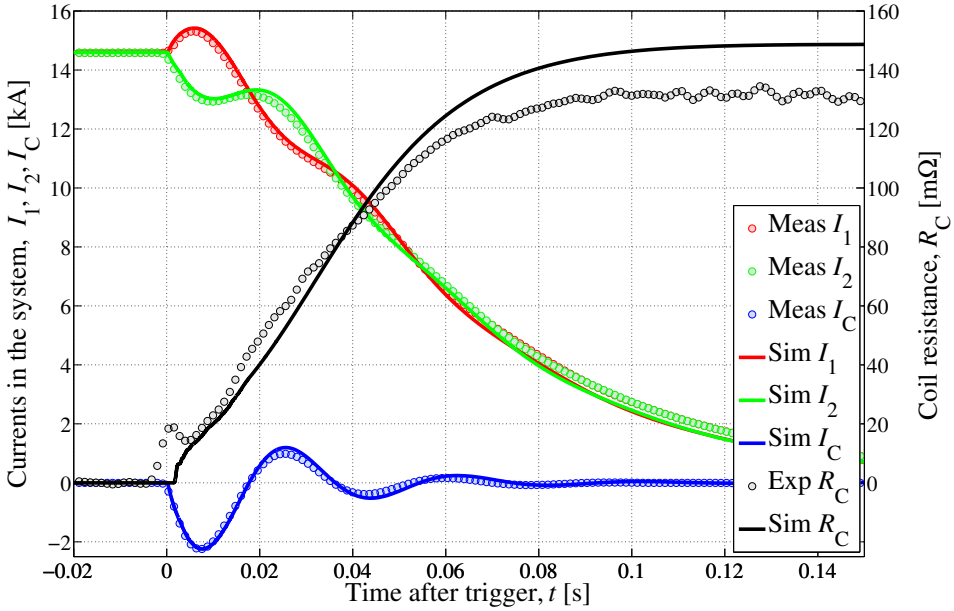

Figure 2.2: Characteristic transient response of a coil during a CLIQ discharge. The CLIQ unit was triggered at time t = 0, and the figure then shows both the measured values and the simulated ones. Courtesy of E. Ravaioli [76].

2.1.1 Full CLIQ Circuit

Looking more closely at the complete CLIQ circuit, figure 2.3 shows how the black box from before is actually connected to the dipole. A capacitor[4], C, of value C_{CLIQ} [F], charged by the floating voltage source, S, to a voltage U_0 [V], is connected to the magnet through the two resistive leads CL1 and CL2. This divides the magnet coil into two separate discharge paths, L_1 and L_2. Along the CLIQ lead there is a thyristor, Th, with a reverse diode D, to allow for oscillating currents[5]. The rest of the circuit consists of the power converter, PC, with its own reverse diodes D_{PC}. This is to protect the PC against reverse currents in the case of a CLIQ discharge at low transport currents, as in this case, the total current in the I_2 branch can become negative.

As will be shown in this thesis, the choice of discharge path significantly influences the level of protection a given CLIQ unit is able to achieve for the magnet in question.

[4]In reality, of course, a capacitor bank.

[5]Earlier proposals for quench protection systems based on capacitive discharge into the magnet coil were without this reverse diode [77, 78], while the substantially improved CLIQ system under investigation in this thesis is only possible due to the recently patented addition of the reverse diode [51, 79].

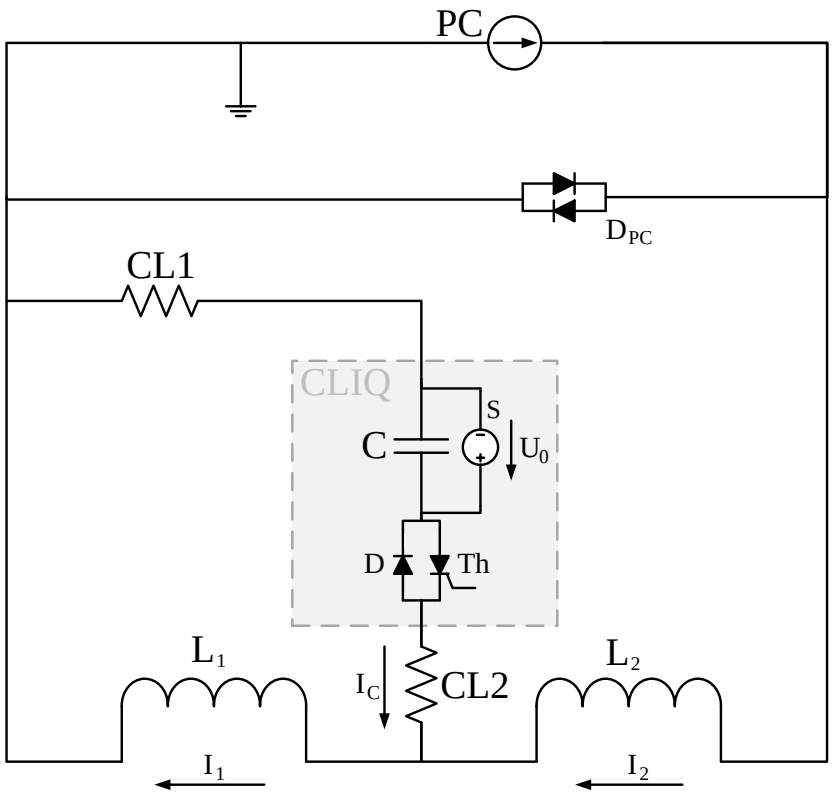

Figure 2.3: Complete CLIQ circuit [74, Fig. 1].

Upon detection of a quench in the magnet, the thyristor is activated, and a discharge current, I_{C}, will flow through CL2. A part of it, I_{C1}, flows into L_1 and part of it, I_{C2}, flows into L_2. The circuit is now an RLC circuit, and the time development of I_{C} is found by solving the regular expressions for such circuits with equivalent resistance R_{eq}, equivalent inductance, L_{eq} and the capacitance, C_{CLIQ}.

It is assumed that the resistances in the circuit are the CLIQ leads, R_{CL1} and R_{CL2}, the equivalent series resistance of the capacitor bank, $\mathrm{R_{cb}}$, as well as the effective resistance of the thyristor, $\mathrm{U_{Th}/I_C}$. The equivalent inductance is given as the parallel connection of the two branches L_1 and L_2 [74].

2.1.2 Governing Equations

Through Kirchoff's voltage and current laws the electrical transient during a CLIQ discharge can be determined by applying said laws to the circuit in figure 2.3,

$$\begin{aligned} 0 &= (L_1 + M_{12})\dot{I}_1 + (L_2 + M_{12})\dot{I}_2 + R_1 I_1 + R_2 I_2 + U_{\mathrm{D}} && [\mathrm{V}] \\ U_{\mathrm{C}} &= L_1\dot{I}_1 + M_{12}\dot{I}_2 + R_1 I_1 + (R_{\mathrm{cb}} + R_{\mathrm{CL1}} + R_{\mathrm{CL2}})I_{\mathrm{C}} + U_{\mathrm{Th}} && [\mathrm{V}] \\ I_1 &= I_2 + I_{\mathrm{C}} && [\mathrm{A}] \\ I_{\mathrm{C}} &= -C_{\mathrm{CLIQ}}\dot{U}_{\mathrm{C}} && [\mathrm{A}] \end{aligned} \tag{2.1}$$

with initial conditions,

$$\begin{aligned} I_1(0) &= I_2(0) &&= I_0 && \text{[A]} \\ I_{\mathrm{C}}(0) &= \dot{U}_{\mathrm{C}}(0) &&= 0 && \text{[A]} \\ U_{\mathrm{C}}(0) &= U_0 && && \text{[V]} \end{aligned} \tag{2.2}$$

Now, I_1 and I_2 [A] are the currents flowing in L_1 and L_2, with L_1 and L_2 [H] their self–inductances, while M_{12} [H] is the mutual inductance between the two paths. R_1 and R_2 [Ω] denote the electrical resistances of the normal zones as they develop in the paths[6]. U_{D} [V] is the voltage across the PC diode, $\mathrm{D_{PC}}$, U_{C} [V] is the voltage across the CLIQ capacitor, R_{cb} [Ω] is the equivalent resistance of the capacitor bank that makes up the CLIQ capacitor, C. R_{CL1} and R_{CL2} [Ω] are the resistances of the two CLIQ leads, U_{Th} [V] is the voltage drop over the thyristor, Th, and, finally, I_0 [A] is the initial transport current in the magnet coil.

When the CLIQ unit is initially discharged, the resistance in the magnet is practically zero, so $R_1 \simeq R_2 \simeq 0$. Further assuming that the voltage U_{D} across the diode is much smaller than the charging voltage of the CLIQ unit, the system described by equation 2.1 can be reduced to the following series RLC circuit equation,

$$\ddot{I}_{\mathrm{C}} + \frac{R_{\mathrm{eq}}}{L_{\mathrm{eq}}}\dot{I}_{\mathrm{C}} + \frac{1}{L_{\mathrm{eq}}C_{\mathrm{CLIQ}}}I_{\mathrm{C}} = 0, \qquad [\mathrm{A\,s^{-2}}] \tag{2.3}$$

with $R_{\mathrm{eq}} = R_{\mathrm{cb}} + R_{\mathrm{CL1}} + R_{\mathrm{CL2}} + U_{\mathrm{Th}}/I_{\mathrm{C}}$ [Ω], and L_{eq} given as the parallel connection of the two discharge paths,

$$L_{eq} = \frac{L_1 L_2 - {M_{12}}^2}{L_1 + L_2 + 2M_{12}}, \qquad [\mathrm{H}] \tag{2.4}$$

It is important to note that the inductances in equation 2.4 are not entirely static — they show a certain current dependence due to the dynamic effects of coupling currents that change the magnetic flux linking in the coil [80, 81], also explained somewhat more in–depth later, in section 2.5.

By defining an attenuation, $\alpha = R_{\mathrm{eq}}/2L_{\mathrm{eq}}$ [rad s^{-1}], and an angular frequency, $\omega_0 = 1/\sqrt{L_{\mathrm{eq}}C_{\mathrm{CLIQ}}}$ [rad s^{-1}], equation 2.3 can be rewritten as,

$$\ddot{I}_{\mathrm{C}} + 2\alpha\dot{I}_{\mathrm{C}} + \omega_0^2 I_{\mathrm{C}} = 0, \qquad [\mathrm{A\,s^{-2}}] \tag{2.5}$$

Defining the damping factor $\zeta = \alpha/\omega_0$, the solution of equation 2.5 will be either over–damped, for $\zeta > 1$, and the current in the magnet decays without oscillating, or the circuit is under–damped, for $\zeta < 1$, and the current oscillates during its decay as a damped sinusoidal oscillation with angular frequency $\omega = \sqrt{\omega_0^2 - \alpha^2}$ [rad s^{-1}].

For the CLIQ circuit given in figure 2.3, the resistance R_{eq}, denoting the total resistance of the warm parts of the circuit, is very small, and thus, the under–damped condition is expected. This means that the assumption of $R_{\mathrm{eq}} < \sqrt{L_{\mathrm{eq}}C_{\mathrm{CLIQ}}}$ is usually true. By the same logic, $\alpha \ll \omega_0$, giving $\omega \simeq \omega_0$. Solving, then, equation 2.5 by means of well known techniques[7] yields,

$$U_{\mathrm{C}}(t) = U_0 \exp(-\alpha t)\left[\cos(\omega t) + \frac{\alpha}{\omega}\sin(\omega t)\right], \qquad [\mathrm{V}] \tag{2.6}$$

and,

$$I_{\mathrm{C}}(t) = -C\frac{\mathrm{d}U_C(t)}{\mathrm{d}t} = CU_0\frac{\omega^2 + \alpha^2}{\omega}\exp(-\alpha t)\sin(\omega t), \qquad [\mathrm{A}] \tag{2.7}$$

[6] The material is initially fully superconducting, and only after a time will these numbers take on non–zero values.

[7] The literature is abound with examples of such solutions. I recall with somewhat less than glee the *Electric Circuits* [82] used in my education.

With the initial transport current as I_0 [A], the current in the two branches are,

$$I_1(t) = I_0 + \frac{L_2 + M_{12}}{L_1 + L_2 + 2M_{12}} I_C(t) = I_0 + f_{g,1} I_C(t), \quad [\text{A}] \quad (2.8)$$

$$I_2(t) = I_0 - \frac{L_1 + M_{12}}{L_1 + L_2 + 2M_{12}} I_C(t) = I_0 + f_{g,2} I_C(t), \quad [\text{A}] \quad (2.9)$$

where the two parameters $f_{g,1}$ and $f_{g,2}$ are purely geometric and non–dimensional, assuming constant inductances[8]. The two parameters will always have opposite signs, and in the case of completely symmetric discharge paths, they will have the same magnitude; $f_{g,1} = -f_{g,2}$.

By assuming an over–all warm resistance, R_{eq}, of 50 [mΩ], and calculating the equivalent inductance for a symmetric discharge circuit into the upper and lower pole of a block–coil dipole, L_{eq}, as 8.33 [mH], gives CLIQ currents as in figure 2.4 for three sets of CLIQ parameters[9]. It is clear how the oscillations are affected by the parameters: higher voltage gives a larger amplitude without changing the frequency of oscillation, while a larger capacitance slightly increases the amplitude and also lengthens the period of oscillation.

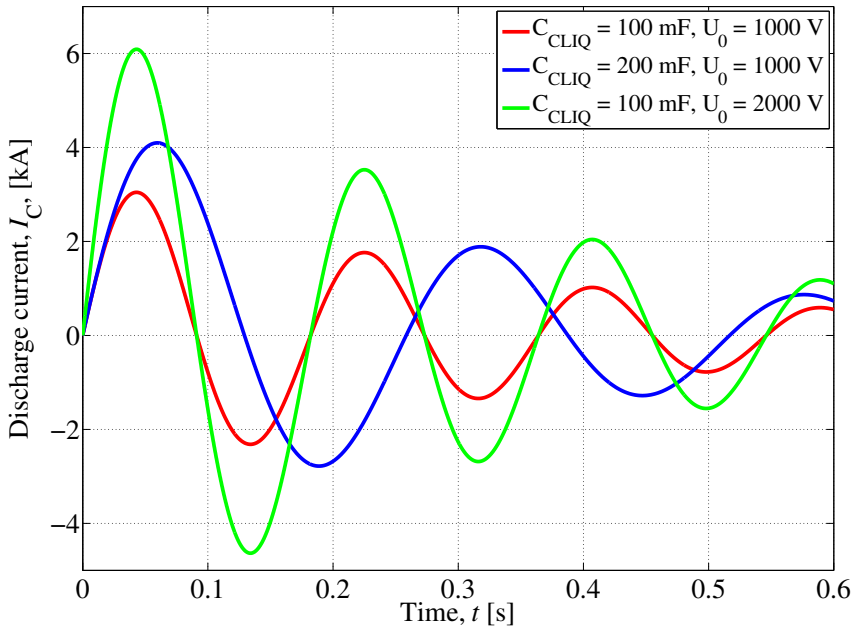

Figure 2.4: CLIQ current oscillations for various capacitances and voltages.

2.1.3 After CLIQ Oscillations Are Completely Damped

Once the oscillations introduced by the CLIQ discharge are completely damped, that is, $I_C \simeq 0$, the system described by equation 2.1 reduces to,

$$\begin{aligned} 0 &= (L_1 + L_2 + 2M_{12})\dot{I}_1 + (R_1 + R_2) I_1 + U_D \quad [\text{V}] \\ I_1 &\simeq I_2 \simeq I_M \quad [\text{A}] \end{aligned} \quad (2.10)$$

[8] As already mentioned, this is not entirely true.

[9] The block–coil in question is the HD2 coil about which this thesis discusses protection and design options. The magnet itself is only presented proper later on, in chapter 3, although it is convenient to use it for exemplifying some theoretical concepts here, earlier on.

Assuming that the voltage over the diode, U_{D}, is small, the magnet current will discharge following this relation,

$$\frac{\mathrm{d}I_{\mathrm{M}}}{\mathrm{d}t} = -\frac{L_1 + L_2 + M_{12}}{R_1 + R_2} I_{\mathrm{M}} = -\frac{L_{\mathrm{M}}}{R} I_{\mathrm{M}} = -\frac{I_{\mathrm{M}}}{\tau_{\mathrm{d}}}, \qquad [\mathrm{A\,s^{-1}}] \quad (2.11)$$

where τ_{d} [s] denotes the over–all time constant of the current decay in the magnet. This time constant will tend to increase as the resistance in the coil increases due to quench propagation and temperature increase[10].

2.2 Magnetic Field Transient

The local magnetic field within the coil[11] is determined by the two currents I_1 and I_2 [A]. By having x and y [m] denote the horizontal and vertical directions with respect to the coil cross section, both being normal to the direction of the transport current in the coil[12], the total applied magnetic field in the x and y [m] directions, $B_{\mathrm{a,x}}$ and $B_{\mathrm{a,y}}$ [T], at the location of each individual strand of the coil, can be expressed as such,

$$\begin{aligned} B_{\mathrm{a,x}} &= (f_{\mathrm{x},1} + f_{\mathrm{x},2}) I_0 + (f_{\mathrm{g},1} f_{\mathrm{x},1} + f_{\mathrm{g},2} f_{\mathrm{x},2}) I_{\mathrm{C}} \\ &= B_{\mathrm{a,x},0} + f_{\mathrm{CLIQ,x}} I_{\mathrm{C}}, \end{aligned} \qquad [\mathrm{T}] \quad (2.12)$$

and,

$$\begin{aligned} B_{\mathrm{a,y}} &= (f_{\mathrm{y},1} + f_{\mathrm{y},2}) I_0 + (f_{\mathrm{g},1} f_{\mathrm{y},1} + f_{\mathrm{g},2} f_{\mathrm{y},2}) I_{\mathrm{C}} \\ &= B_{\mathrm{a,y},0} + f_{\mathrm{CLIQ,y}} I_{\mathrm{C}}, \end{aligned} \qquad [\mathrm{T}] \quad (2.13)$$

where $B_{\mathrm{a,x},0}$ and $B_{\mathrm{a,y},0}$ [T] denote the x and y components of the initial magnetic field (caused by I_0 [A]). The magnetic field parameters $f_{\mathrm{x},1}$, $f_{\mathrm{x},2}$, $f_{\mathrm{y},1}$ and $f_{\mathrm{y},2}$ [$\mathrm{T\,A^{-1}}$] can be found through dedicated software; the one used in this work is ROXIE [83]. Other than second–order effects such as iron saturation and coupling currents, these parameters are completely geometric, and the magnetic field is assumed linear with applied current. Figure 2.5 shows the magnetic field parameter, f [$\mathrm{T\,A^{-1}}$], for a block–coil and $\cos(\theta)$ coil dipole magnet, where f [$\mathrm{T\,A^{-1}}$] is given as,

$$f = \sqrt{(f_{\mathrm{x},1} + f_{\mathrm{x},2})^2 + (f_{\mathrm{y},1} + f_{\mathrm{y},2})^2}, \qquad [\mathrm{T\,A^{-1}}] \quad (2.14)$$

[10] At higher temperatures, the relative contribution to electrical resistance from the magnetoresistivity is much lower than at cryogenic temperatures.
[11] Also, of course, outside the coil and in the aperture, but of no interest for this discussion.
[12] The magnet current, then, flows in the z–direction [m].

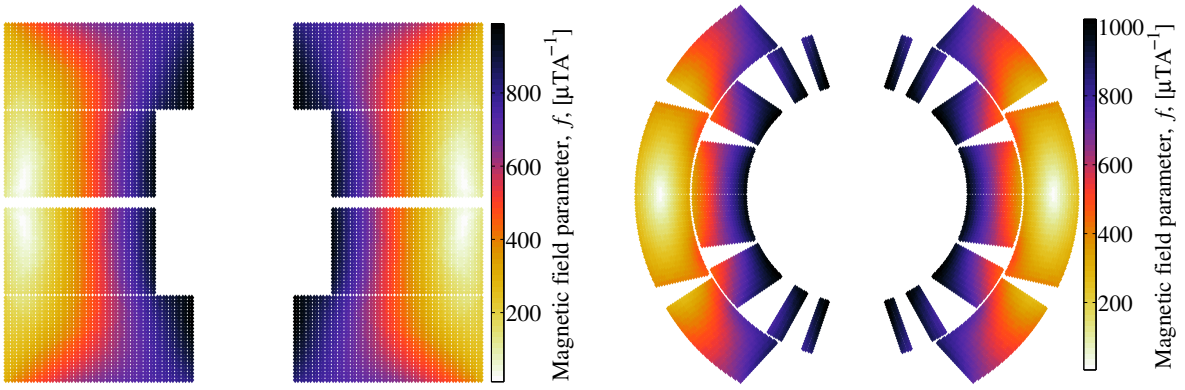

(a) Block–coil **(b)** cos(θ) coil

Figure 2.5: Magnetic field parameter, f [T A^{-1}], for the block–coil dipole magnet.

$f_{\mathrm{CLIQ,x}}$ and $f_{\mathrm{CLIQ,y}}$ [T A^{-1}] in equations 2.12 and 2.13 describe the behaviour of the CLIQ system. Through time–derivation of the two equations it is seen that these parameters are proportionality constants describing the magnetic field change in the coil,

$$\frac{\mathrm{d}B_{\mathrm{a,x}}}{\mathrm{d}t} = f_{\mathrm{CLIQ,x}}\frac{\mathrm{d}I_{\mathrm{C}}}{\mathrm{d}t}, \qquad [\mathrm{T\,s^{-1}}] \quad (2.15)$$

and,

$$\frac{\mathrm{d}B_{\mathrm{a,y}}}{\mathrm{d}t} = f_{\mathrm{CLIQ,y}}\frac{\mathrm{d}I_{\mathrm{C}}}{\mathrm{d}t}, \qquad [\mathrm{T\,s^{-1}}] \quad (2.16)$$

The total applied magnetic field–change is then,

$$\frac{\mathrm{d}B_{\mathrm{a}}}{\mathrm{d}t} = \sqrt{\left(\frac{\mathrm{d}B_{\mathrm{a,x}}}{\mathrm{d}t}\right)^2 + \left(\frac{\mathrm{d}B_{\mathrm{a,y}}}{\mathrm{d}t}\right)^2} = f_{\mathrm{CLIQ}}\frac{\mathrm{d}I_{\mathrm{C}}}{\mathrm{d}t}, \qquad [\mathrm{T\,s^{-1}}] \quad (2.17)$$

where,

$$f_{\mathrm{CLIQ}} = \sqrt{f_{\mathrm{CLIQ,x}}^2 + f_{\mathrm{CLIQ,y}}^2}, \qquad [\mathrm{T\,A^{-1}}] \quad (2.18)$$

When the CLIQ unit is connected to either a block–coil or a cos(θ) coil dipole so that the first discharge path, namely L_1, in figure 2.3 is the upper pole, while L_2 is the lower pole, an example of how f_{CLIQ} [T A^{-1}] will look is given in figure 2.6[13].

[13] How the CLIQ magnetic field parameter produces this particular field distribution is explained more in–depth in chapter 3 for the block–coil.

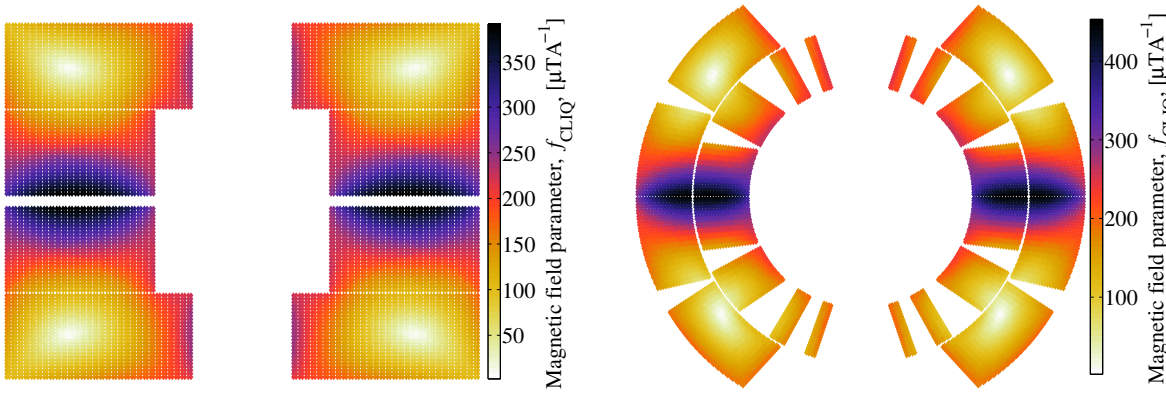

(a) Block–coil **(b)** cos(θ) coil

Figure 2.6: CLIQ field parameter, f_{CLIQ} [T A^{-1}], for the block–coil dipole magnet.

As discussed in section 1.5, a change in the magnetic field applied to a superconductor will give rise to several different transient losses. For the application of CLIQ, the most important is the Inter Filament Coupling Loss. By inserting equation 2.7 into equations 2.15 and 2.16, the magnetic field–change in the two directions are given as follows,

$$\frac{\mathrm{d}B_{\mathrm{a,x}}}{\mathrm{d}t} = f_{\mathrm{CLIQ,x}} C U_0 \frac{\omega^2 + \alpha^2}{\omega} \exp(-\alpha t) \left[\omega \cos(\omega t) - \alpha \sin(\omega t)\right], [\mathrm{T\,s^{-1}}] \quad (2.19)$$

and,

$$\frac{\mathrm{d}B_{\mathrm{a,y}}}{\mathrm{d}t} = f_{\mathrm{CLIQ,y}} C U_0 \frac{\omega^2 + \alpha^2}{\omega} \exp(-\alpha t) \left[\omega \cos(\omega t) - \alpha \sin(\omega t)\right], [\mathrm{T\,s^{-1}}] \quad (2.20)$$

Looking, then, only at the x–component, for convenience, this magnetic field–change can be described as being made up of a *total* local magnetic field–change and an *induced* magnetic field–change. The induced magnetic field–change arises in the opposite direction to the applied magnetic field–change, and it is caused by the IFCCs,

$$\frac{\mathrm{d}B_{\mathrm{t,x}}}{\mathrm{d}t} = \frac{\mathrm{d}B_{\mathrm{a,x}}}{\mathrm{d}t} + \frac{\mathrm{d}B_{\mathrm{IF,x}}}{\mathrm{d}t}, \quad [\mathrm{T\,s^{-1}}] \quad (2.21)$$

The relation between the magnetic field induced by the IFCC and the total magnetic field–change is given as such [51, p. 26][84],

$$B_{\mathrm{IF,x}} = -\tau_{\mathrm{IF,x}} \frac{\mathrm{d}B_{\mathrm{t,x}}}{\mathrm{d}t}, \quad [\mathrm{T}] \quad (2.22)$$

where $\tau_{\mathrm{IF,x}}$ [s] is the characteristic time–constant of decay and growth of the IFCC, as also given in equation 1.31,

$$\tau_{\mathrm{IF,x}} = \frac{\mu_0}{2} \left(\frac{l_{\mathrm{f}}}{2\pi}\right)^2 \frac{1}{\rho_{\mathrm{eff,x}}} = \frac{\mu_0}{2} \beta_{\mathrm{IF,x}}, \quad [\mathrm{s}] \quad (2.23)$$

with l_{f} [m] denoting the filament twist pitch, $\rho_{\mathrm{eff,x}}$ [Ω m] the effective transverse resistivity of the copper matrix in the x–direction [m] (as discussed in section 1.6.2), and μ_0 [T m A^{-1}] being the magnetic permeability of vacuum.

Using the expression in equations 2.19 and 2.22 in equation 2.21 with initial conditions,

$$\begin{aligned} B_{\mathrm{a,x}}(0) &= B_{\mathrm{a,x,0}}, \\ B_{\mathrm{IF,x}}(0) &= 0, \end{aligned} \quad [\mathrm{T}] \quad (2.24)$$

the total magnetic field–change (still in the x–direction [m]) caused by the CLIQ discharge will be given as,

$$\begin{aligned}\frac{\mathrm{d}B_{\mathrm{t,x}}}{\mathrm{d}t} &= f_{\mathrm{CLIQ,x}} C U_0 \frac{\omega^2+\alpha^2}{\omega_{\mathrm{n}}\left(\omega_{\mathrm{n}}^2+(1-\alpha_{\mathrm{n}})^2\right)}\cdot \\ &\{\exp(-\alpha t)\left[\omega_{\mathrm{n}}\cos(\omega t)+(\omega_{\mathrm{n}}^2+\alpha_{\mathrm{n}}^2-\alpha_{\mathrm{n}})\right]- \\ &\omega_{\mathrm{n}}\exp(-t/\tau_{\mathrm{IF,x}})\},\end{aligned} \qquad [\mathrm{T\,s^{-1}}] \quad (2.25)$$

where $\omega_{\mathrm{n}} = \omega\tau_{\mathrm{IF,x}}$ and $\alpha_{\mathrm{n}} = \alpha\tau_{\mathrm{IF,x}}$ are the angular frequency and attenuation normalised to $1/\tau_{\mathrm{IF,x}}$.

Now, for large values of ω_{n} and α_{n}, the variation of the *applied* magnetic field is much larger than the time it takes for IFCCs to grow substantial, this means that the *total* magnetic field change (as given by equation 2.25) is very small. If, however, $\omega_{\mathrm{n}} \simeq \alpha_{\mathrm{n}} \simeq 0$, then the IFCCs develop much faster than the magnetic field–changes, and $\mathrm{d}B_{\mathrm{t,x}}/\mathrm{d}t \simeq \mathrm{d}B_{\mathrm{a,x}}/\mathrm{d}t$.

Figure 2.7 shows how the magnetic field changes in a dipole block–coil when a CLIQ unit, with parameters $C_{\mathrm{CLIQ}} = 100$ [mF], $U_0 = 1000$ [V], is discharged into the symmetric path of the upper and lower pole of the magnet. As evident, the previous prediction holds; for a small filament twist pitch, and thus a small time–constant τ_{IF}, the total magnetic field–change follows the applied field–change very closely, while a larger twist pitch results in a progressively slower response to the change.

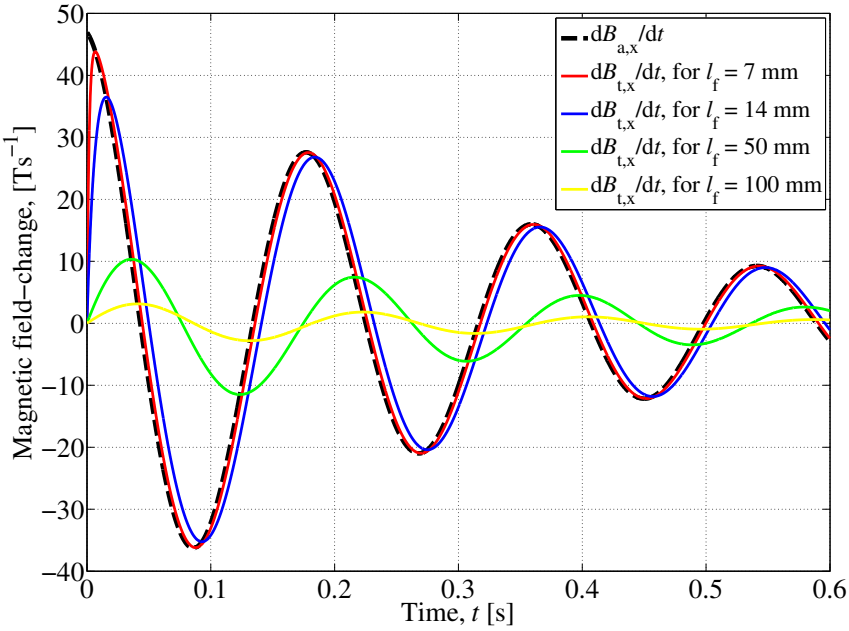

Figure 2.7: Magnetic field–change in the x direction of a dipole block coil during symmetric CLIQ discharge into the upper and lower pole of the magnet, for various filament twist pitches, l_{f} [m].

As shown in section 1.5, the IFCCs flowing in the resistive copper matrix will generate

local ohmic losses, called IFCL, with a magnitude,

$$\begin{aligned} P_{\mathrm{IF,x}} &= \left(\frac{l_\mathrm{f}}{2\pi}\right)^2 \frac{1}{\rho_{\mathrm{eff,x}}} \left(\frac{\mathrm{d}B_{\mathrm{t,x}}}{\mathrm{d}t}\right)^2 \\ &= \beta_{\mathrm{IF,x}} \left(\frac{\mathrm{d}B_{\mathrm{t,x}}}{\mathrm{d}t}\right)^2, \end{aligned} \qquad [\mathrm{W\,m^{-3}}] \quad (2.26)$$

A similar expression will describe the IFCL in the y direction, and the total IFCL will then be,

$$\begin{aligned} P_{\mathrm{IF}} &= P_{\mathrm{IF,x}} + P_{\mathrm{IF,y}} \\ &= \left(\frac{l_\mathrm{f}}{2\pi}\right)^2 \frac{1}{\rho_{\mathrm{eff,x}}} \left(\frac{\mathrm{d}B_{\mathrm{t,x}}}{\mathrm{d}t}\right)^2 + \left(\frac{l_\mathrm{f}}{2\pi}\right)^2 \frac{1}{\rho_{\mathrm{eff,y}}} \left(\frac{\mathrm{d}B_{\mathrm{t,y}}}{\mathrm{d}t}\right)^2 \\ &= \beta_{\mathrm{IF,x}} \left(\frac{\mathrm{d}B_{\mathrm{t,x}}}{\mathrm{d}t}\right)^2 + \beta_{\mathrm{IF,y}} \left(\frac{\mathrm{d}B_{\mathrm{t,y}}}{\mathrm{d}t}\right)^2 \\ &= \frac{2}{\mu_0} \left[\tau_{\mathrm{IF,x}} \left(\frac{\mathrm{d}B_{\mathrm{t,x}}}{\mathrm{d}t}\right)^2 + \tau_{\mathrm{IF,y}} \left(\frac{\mathrm{d}B_{\mathrm{t,y}}}{\mathrm{d}t}\right)^2\right], \end{aligned} \qquad [\mathrm{W\,m^{-3}}] \quad (2.27)$$

In strands where the filaments have uniformly distributed positions over the cross section, and assuming that there is no large dependence on the field direction, one can assume the effective transverse resistivities to be equal (that is, $\beta_{\mathrm{IF,x}} = \beta_{\mathrm{IF,x}} = \beta_{\mathrm{IF}}$), and by that, equation 2.27 reduces to,

$$\begin{aligned} P_{\mathrm{IF}} &= \beta_{\mathrm{IF}} \left[\left(\frac{\mathrm{d}B_{\mathrm{t,x}}}{\mathrm{d}t}\right)^2 + \left(\frac{\mathrm{d}B_{\mathrm{t,y}}}{\mathrm{d}t}\right)^2\right] \\ &= \beta_{\mathrm{IF}} \left(\frac{\mathrm{d}B_{\mathrm{t}}}{\mathrm{d}t}\right)^2 \\ &= \left(\frac{l_\mathrm{f}}{2\pi}\right)^2 \frac{1}{\rho_{\mathrm{eff,x}}} \left(\frac{\mathrm{d}B_{\mathrm{t}}}{\mathrm{d}t}\right)^2, \end{aligned} \qquad [\mathrm{W\,m^{-3}}] \quad (2.28)$$

Figure 2.8 shows how the IFCL will develop in the x direction for the strand with the highest $f_{\mathrm{CLIQ,x}}$ in a block–coil dipole magnet during a CLIQ discharge into the upper/lower pole paths. Recalling figure 2.6, the largest over–all f_{CLIQ} in the block–coil is in the midplane of the coil, and at this location the x component is by far the largest.

From figure 2.7 it seemed as if any small filament twist pitch would be the best choice, as that allowed for the largest total magnetic field–change; the actual power deposited, however, depends inversely on the filament twist pitch as compared to the field–change. As described briefly in section 1.5, the peak power depends differently on the frequency of the oscillations for different filament twist pitches, because the time–constant of the IFCC's grows with twist pitch, and so takes longer and longer to develop.

Due to this, there will be an optimal choice of filament twist pitch, when thinking of protection with CLIQ. At fist glance, a twist pitch of 50 [mm] seems the best, but the initial time development must also be taken into account, as with the first few milliseconds are the most important for the performance of CLIQ, given its speed (frequency of oscillation). With this in mind, the 14 [mm] twist pitch seems a better choice.

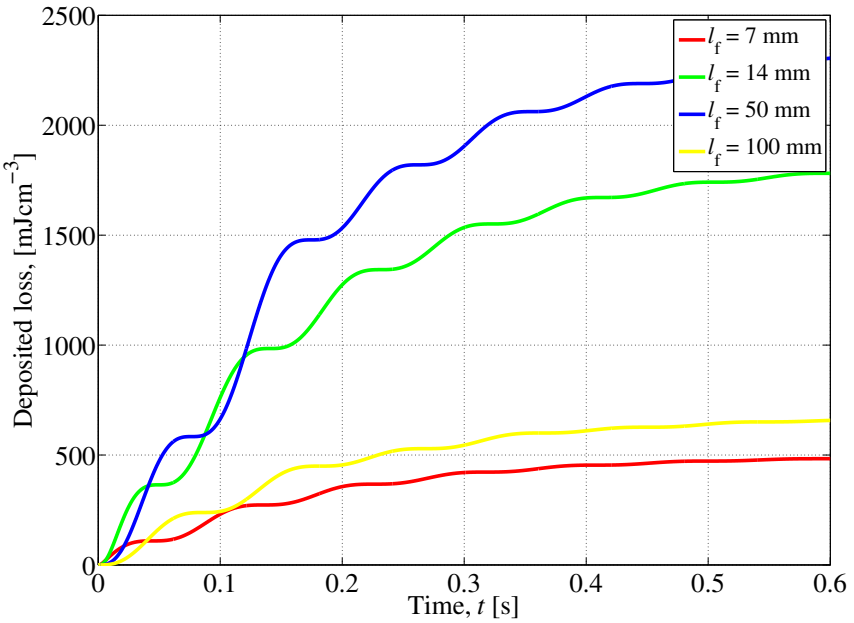

Figure 2.8: Magnetic field–change in the x direction of a dipole block coil during symmetric CLIQ discharge into the upper and lower pole of the magnet, for various filament twist pitches, l_f [m].

2.3 CLIQ Configuration Circuits

Recalling the complete CLIQ circuit from figure 2.3, it is convenient to establish exactly how to refer to the discharge path in a coil.

Figure 2.9 shows how the "electrical parts" of the coil are labelled — the outer layer of the upper pole is electrical part number 1, the inner layer of the upper pole is electrical part 2, and so on — for both a block–coil dipole and a $\cos(\theta)$ dipole magnet. "Inner" and "outer", for the block–coil, refer to the location relative to the midplane, while for the $\cos(\theta)$ coil to the location relative to the centre of the bore.

When talking of the chosen discharge path for the CLIQ connection, in section 2.1.1, it was meant what electrical parts are in series and what parts are in parallel. While, in principle, one can connect the CLIQ unit however one likes, only four different configurations are, 1) meaningful, 2) physically realisable due to magnet design restrictions and 3) unique due to the symmetry of the coil. These four CLIQ configurations are the Pole–Pole CLIQ configuration (PP), Crossed–Layer CLIQ configuration (CL), Layer–Layer CLIQ configuration (LL) and Layer–Layer Reverse CLIQ configuration (LLrev).

The naming of these four configurations refer to the interfaces between parts of the coil receiving opposite polarity in the initial stage of the CLIQ discharge.

Figure 2.10 shows the electrical connection diagrams for the four CLIQ configurations. The green arrows in the figures indicate the direction of the initial transport current in the magnet, while the red signs indicate the initial polarity of the CLIQ current in each electrical part. As is seen, the LL and LLrev connections require that the inner layer of the lower pole is connected to the inner layer of the upper pole, in order to be able to connect the CLIQ unit across these electrical parts.

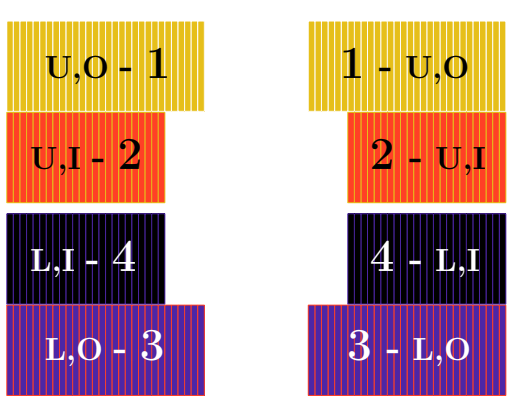

(a) Electrical parts of a block–coil dipole magnet, specifically, the 16 [T] Nb_3Sn block–coil developed by the US LARP collaboration [3].

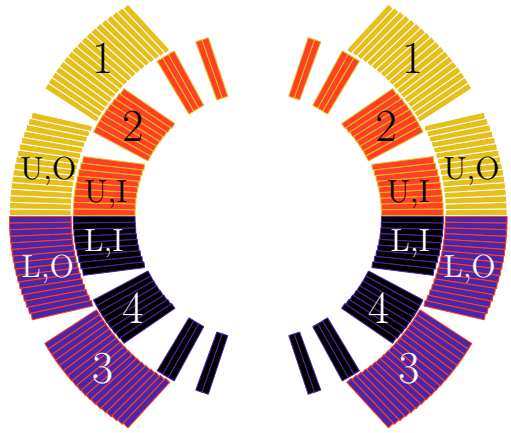

(b) Electrical parts of a $\cos(\theta)$ dipole coil, specifically, the 11 [T] dipole for the HL–LHC upgrade [35, 85].

Figure 2.9: Examples of how the electrical parts of a block–coil and a $\cos(\theta)$ coil are defined.

On existing magnets, typically, only the PP configuration will be possible, simply because the necessary CLIQ leads do not exist. On non–existing magnets, such as the 16 [T] block–coil dipole, which are still in development, it is assumed possible to design the coil in such a fashion as to provide the needed connections [47, 48].

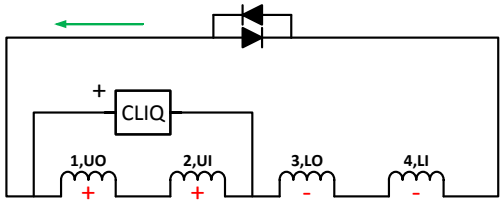

(a) Pole–Pole CLIQ configuration

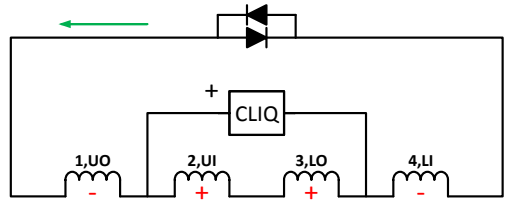

(b) Crossed–Layer CLIQ configuration

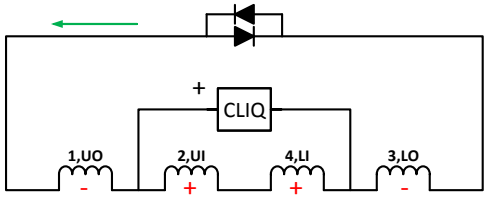

(c) Layer–Layer CLIQ configuration

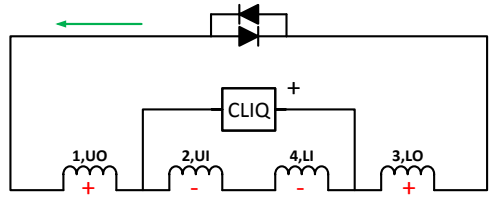

(d) Layer–Layer Reverse CLIQ configuration

Figure 2.10: All four CLIQ configurations possible for the block–coil dipole magnet. Note that LL and LLrev only differ in the polarity of the CLIQ unit. The green arrow indicates the initial transport current, while the red signs indicate the initial polarity of the CLIQ current.

2.4 CLIQ Effectiveness [51, Sec. 3.1]

Equation 2.28 gives the power of the IFCL; proportional to the square of the filament twist pitch, l_f [m], inversely proportional to the effective resistivity of the copper matrix, ρ_eff [$\Omega\,$m], and finally to the square of the total magnetic field–change, $\mathrm{d}B_\mathrm{t}/\mathrm{d}t$ [$\mathrm{T\,s^{-1}}$]. If the strand used in the coil's cables is given, only the magnetic field–change can be influenced by changing the parameters and configuration of the CLIQ unit in use. If it is possible to change the strand parameters, it is possible to further tailor the system as a whole (magnet plus CLIQ) for improved protection[14].

From the loss being proportional to the applied magnetic field change, one very important conclusion can be drawn: looking again at figure 2.10, one wants to choose a discharge path so that the polarities of the current in each individual electrical part is the opposite of what it is in any adjacent part. This will mean that the applied magnetic field change will superpose in the interface region of the two parts, and thus, the generated loss will be much higher than if the polarities were the same.

Now, the peak power developed by the IFCCs will occur immediately after the initiation of the CLIQ discharge, given that this is when the $\mathrm{d}I_\mathrm{C}/\mathrm{d}t$ is the largest. It then follows from the equation describing the IFCL power, equation 2.28, and the equation describing the total magnetic field–change, equation 2.25, that there is a proportionality between the power and the *applied* field–change,

$$\begin{aligned} P_\mathrm{IF,peak} &= \left(\frac{l_\mathrm{f}}{2\pi}\right)^2 \frac{1}{\rho_\mathrm{eff}} \left(\frac{\mathrm{d}B_\mathrm{t,peak}}{\mathrm{d}t}\right)^2 \\ &\propto \left(\frac{\mathrm{d}B_\mathrm{a,peak}}{\mathrm{d}t}\right)^2 \qquad [\mathrm{W\,m^{-3}}] \quad (2.29) \\ &= \left(f_\mathrm{CLIQ}\frac{\mathrm{d}I_\mathrm{C,peak}}{\mathrm{d}t}\right)^2 = \left(f_\mathrm{CLIQ}\frac{U_0}{L_\mathrm{eq}}\right)^2, \end{aligned}$$

By giving the equivalent inductance per meter, the proportionality relation can be rewritten as,

$$P_\mathrm{IF,peak} \propto \left(\frac{f_\mathrm{CLIQ}}{L'_\mathrm{eq}}\frac{U_0}{l_\mathrm{m}}\right)^2, \qquad [\mathrm{W\,m^{-3}}] \quad (2.30)$$

where L'_eq [$\mathrm{H\,m^{-1}}$] is the equivalent inductance per meter, given as,

$$L'_\mathrm{eq} = \frac{L'_1 L'_2 - {M'_{12}}^2}{L'_1 + L'_2 + 2M'_{12}}, \qquad [\mathrm{H\,m^{-1}}] \quad (2.31)$$

From equaiton 2.30 it is then possible to define the CLIQ effectiveness,

$$\Psi = \frac{f_\mathrm{CLIQ}}{L'_\mathrm{eq}}, \qquad [\mathrm{m^{-1}}] \quad (2.32)$$

Recalling from equations 2.12 and 2.13 that the parameter f_CLIQ [$\mathrm{T\,A^{-1}}$] depends on a given strand's location in the coil, the Ψ [$\mathrm{m^{-1}}$] then describes the distribution of the peak applied field–change obtainable for each individual strand, per volt of CLIQ charging

[14] Several issues must be taken into account, not only the protection, of course! This thesis, however, only briefly touches upon considerations other than protection.

voltage and meter of magnetic length[15]. It is independent of the cable and strand parameters themselves, and also the parameters of the CLIQ unit. Apart from the second–order effects of iron–yoke saturation and the dynamic coupling–current time–constants, this parameter is purely geometric, and thus serves as a way to assess the "protectability" of a given coil with CLIQ in mind.

Note that Ψ only describes the peak power development in a region of the coil, and it has no influence over how *much* energy is deposited in total across the coil, as this last feature largely depends on the available energy in the CLIQ capacitor as well as the way the currents decay in the magnet.

Then, while Ψ does not give the actual magnitude of peak power developed, its distribution will give valuable information, through its peak and average value over the coil, about how the magnet will behave during a CLIQ discharge. In coils with high magnetic field and large energy densities, the optimal protection strategy is to introduce a quench as homogeneously and quickly as possible across the cables of the coil, and the degree of success for a given CLIQ unit and configuration hinges on having a uniformly distributed Ψ of high average value across the coil[16]. In magnets operating at lower field and energy densities (such as a high–field magnet during current ramp) it is not as important to quickly quench the whole magnet, as the margin to quench is large, and a slow transition to the normal state will not risk damaging the hot–spot[17]. It is now much more beneficial if the Ψ is concentrated in a smaller region, indicating that a larger fraction of the total energy in the CLIQ capacitor is deposited in a small volume, and as such is able to initiate the quench at all — with a large margin to quench it is also harder to start the *desired* SC–to–normal–state transition!

2.4.1 CLIQ Effectiveness for the Three Configurations

The three CLIQ configurations possible for a dipole magnet have very different Ψ[18]; the PP, where the upper and lower poles of the coil receive opposite initial CLIQ currents (see figure 3.8a), shows a fairly small effectiveness, while also concentrating the loss in the midplane region of the coil. This is shown in figure 2.11.

This indicates that the PP will be a good choice for protecting magnets at low currents (or at high margin to quench), since most of the IFCL will be concentrated in a small region. Comparing the CLIQ effectiveness of the block–coil and the $\cos(\theta)$ coil, it is clear that the design of the block–coil suits the CLIQ protection system very well — in the $\cos(\theta)$ coil, the PP deposits loss only in a very limited number of cables, and thus the quench needs to propagate through heat diffusion from there, while for the block–coil, the deposited IFCL will quench many cables initially, and not rely as heavily on the slower process of heat propagation in the coil.

[15] Note that the strand is the smallest meaningful unit of a superconducting cable for the sake of numerical treatment, and as such, even if the field varies continuously it is convenient to treat it only at the location of the strands.

[16] By "large energy density", it is meant, large energy stored in the magnetic field, combined with an over–all small magnet volume.

[17] The term "margin to quench" is explained qualitatively and developed quantitatively in chapter 3 for the 16 [T] block–coil dipole magnet.

[18] From before, there are, indeed, four configurations; however, the LL and LLrev have the same CLIQ effectiveness, and thus there is no need to treat it uniquely — the case for why it makes sense to consider a LLrev configuration after all is made later in this section.

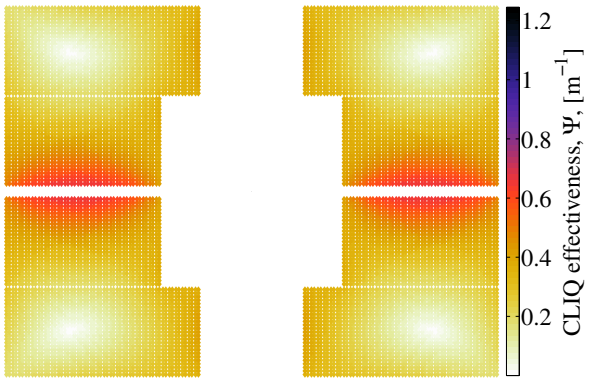

(a) PP on block–coil.

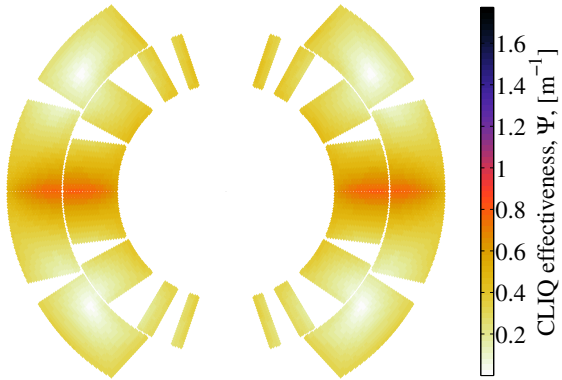

(b) PP on cos(θ) coil.

Figure 2.11: CLIQ effectiveness, Ψ, for the PP CLIQ configuration.

LL CLIQ configuration

For the LL, the case is very different; the equivalent inductance of this circuit is very small as compared to the PP, because the mutual inductance between the inner and outer layers is higher while the self–inductance is lower, the Ψ (as given in equation 2.32) is much higher and more evenly distributed along the interface in question (the layer–layer interface). The effectiveness of the LL is shown in figure 2.12.

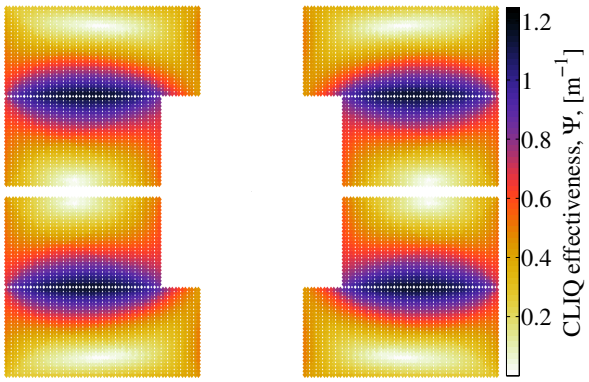

(a) LL on block–coil.

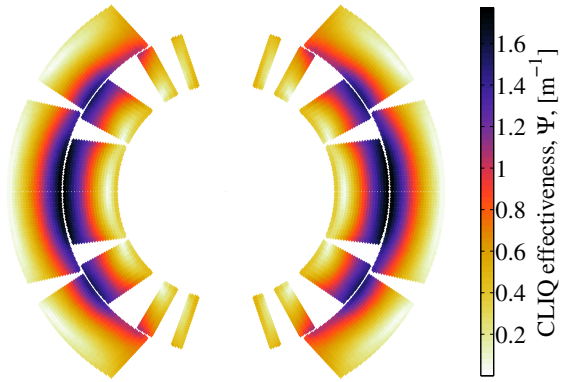

(b) LL on cos(θ) coil

Figure 2.12: CLIQ effectiveness, Ψ, for the LL CLIQ configuration.

The losses generated with the LL are higher than for PP, and do, in fact, touch strands in the coil belonging to cables that experience close to the highest fields (see figure 2.5). Now, oppositely to the conclusion for PP, the LL risks struggling at lower currents in the magnet, because the energy in the CLIQ unit (being given only by the capacitance and charging voltage) will be distributed over a far larger volume.

Before describing the CL it is convenient to justify the LLrev; both LL and LLrev will have the same Ψ, seeing as the magnetic field change, generating IFCL, does not depend on what side of the interface carries what current. It is, however, not irrelevant what electrical part receives the initial *positive* CLIQ current. For the LL the positive current goes into the inner layers while the negative goes in the outer layers. Referring back to the critical surface

plot of Nb_3Sn in figure 1.11, it is clear that when the CLIQ unit discharges a positive current, the electrical part that receives this current will be pushed closer to its critical current (keep also in mind that a higher current means a higher magnetic field), while the part that gets the negative current is brought further away from the surface. This will translate into a slight difference in the time it takes to initiate a quench in the magnet when talking of the LL and LLrev; since the field distribution in a dipole is not uniform between the layers in the coil, some parts of the coil will already be close to the critical surface than other parts. In dipoles, it is always the inner layer that sees the largest magnetic fields, while in a block–coil it will depend on the design, but typically, the outer layers will see the largest fields. If this difference between inner and outer layers can be enhanced by the right choice of discharge path, the protection of the magnet will be even more successful.

The other two (PP and CL) CLIQ configurations also see a difference when reversing what branch receives the initial positive current; however, this difference does not translate into a better protection performance, since the time to initiate the quench is the same, it just changes whether it occurs in the upper or lower pole, due to the symmetry of the other two configurations.

CL CLIQ configuration

The CL is, in a sense, a combination of the PP and LL. Since there will be current changes of opposite polarity across the midplane as well, some IFCL will be generated there in addition to the loss in the layer–layer interfaces. The effectiveness of the CL is shown in figure 2.13.

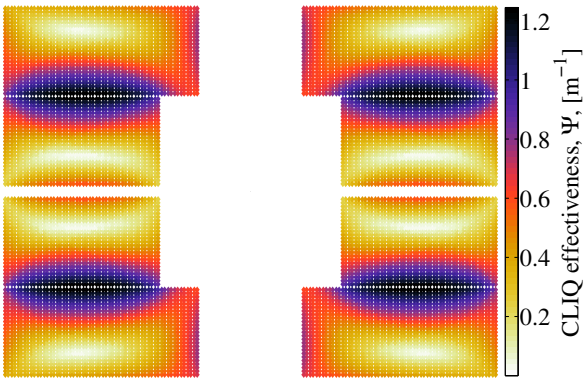

(a) CL on block–coil.

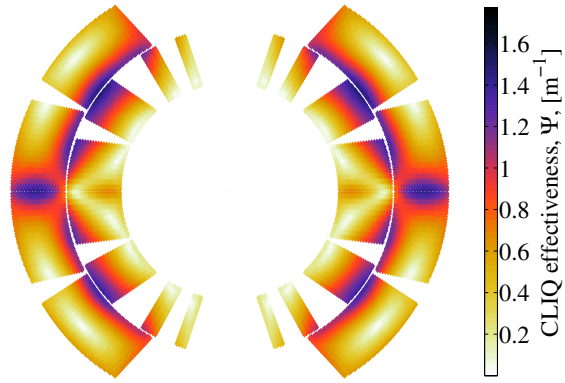

(b) CL on $\cos(\theta)$ coil.

Figure 2.13: CLIQ effectiveness, Ψ, for the CL CLIQ configuration.

The same possible limitations to the LL also apply to the CL; since the energy of the CLIQ unit is distributed as homogeneously as it is, it might prove difficult to protect a magnet at lower currents, while on the other hand, it should perform similarly to the LL when discharged at the magnet's nominal initial transport current.

2.5 Lumped–Element Dynamic Electro–Thermal (LEDET) Model

In order to account for all the transient effects occurring in a SC magnet during a CLIQ discharge, a comprehensive new modelling approach has been necessary as compared to existing models [51, Chap. 4][81]. This section only gives a brief overview of the modelling

approach adopted[19].

2.5.1 Lumped–Element Modelling of Dynamic Electro–Thermal Effects

The model used is based on three separate parts; purely electrical, lumped, components; 2D heat transfer model of the full magnet coil cross section; and a model accounting for the coupling currents present in the coil during a magnetic transient (including their effect on the electrical and thermal components).

With finite–element modelling it is possible to simulate the non–linear behaviour of SC cables [86, 87], it, however, requires very long computational times, and if a faster approach is possible, that is to be preferred for the sort of modelling one would want to do when designing a protection system for a magnet — parametric studies with hundreds of simulations for slightly varying input parameters.

Reducing the problem to a set of differential–algebraic equations by lumping together the components of the problem, one can, with sufficient accuracy, simulate the electro–thermal transient in a SC magnet. This approach provides a large improvement in computational load, while still maintaining flexibility to model both large scale electrical transients in the magnet as a whole as well as the coupling currents at strand level.

2.5.2 The Model

A purely electrical model, with components sorted as *sources*, *storage* and *sinks* is shown schematically in figure 2.14. The power source, PS, provides energy that is stored in the inductive and capacitive elements, L and C, and dissipated in the resistive element, R. As the model is a closed system, energy exchanged with the exterior is to either the main electrical network, EN, as a source, or the room–temperature infinite sink, RT.

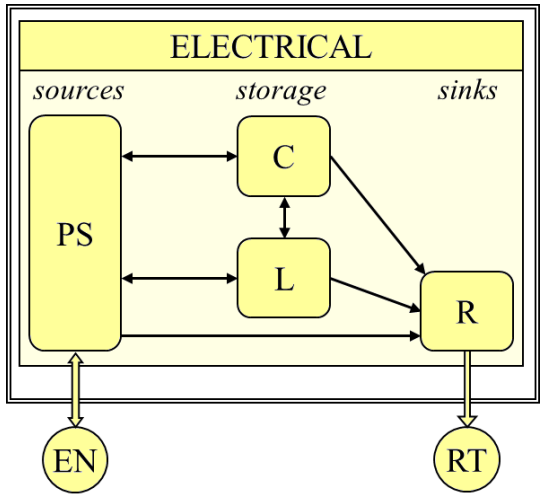

Figure 2.14: Schematic representation of energy exchanges in an electrical model. Courtesy of Emmanuele Ravaioli [51, Fig. 4.1].

Expanding this model to include thermal effects gives the schematic representation in figure 2.15. Such electro–thermal models are important tools for the design of electrical

[19]It is important to make entirely clear that I did not myself contribute to the development of the Lumped–Element Dynamic Electro–Thermal model (LEDET) model.

systems where thermal behaviour also plays an important role [88, 89].

Since the transient occurring in the two domains influence each other, the software must solve them simultaneously — when ohmic loss arises on the electrical side, this provides a heat input to the thermal side, which in turn means a rise in temperature for the resistance in question; this, of course, changes the voltage across the resistance, and in turn the power developed in the element.

The schematic then consists of the same electrical elements as for a purely electrical model, but introduces the thermal and electro–thermal coupling elements as well. Thermal energy is stored in heat–capacitive elements, C_{th}, which will exchange energy with each other through P_{ex}. In an accelerator magnet for applications such as the LHC, it is usual to have the magnet in a liquid helium bath — this constitutes an infinite sink for the thermal energy escaping the system; transfer to the helium, HE, goes through P_{He}. The electro–thermal coupling happens as ohmic loss develops in the conductor, R_C, and transfers heat through P_{ohm} to the thermal domain. Other external heat sources can be accounted for, such as beam loss or radiation, but if the heat source depends on the generation of loss through a mechanism that relies on the very system itself, then this modelling approach is not satisfactory — the coupling losses generated from the magnetic transient is dependent on the electromagnetic interaction between the magnet's field and the magnet's conductor.

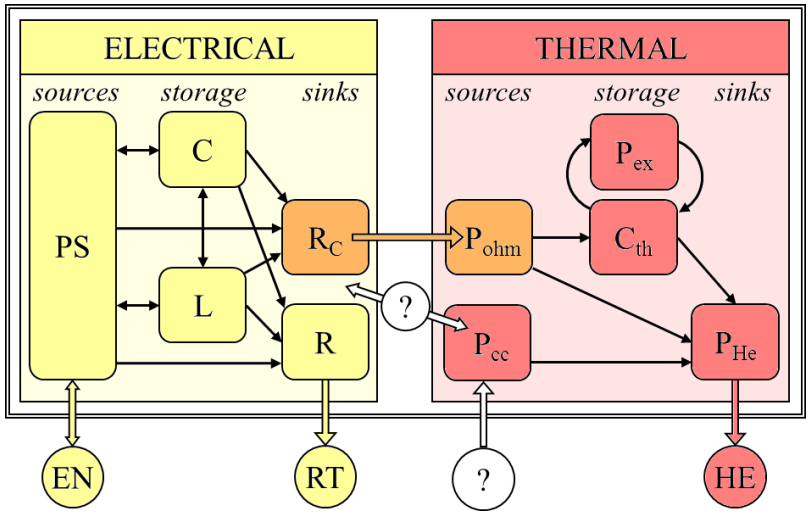

Figure 2.15: Schematic representation of energy exchanges in an electro–thermal model. Courtesy of Emmanuele Ravaioli [51, Fig. 4.2].

The reality is that when the current in the magnet changes, this creates a change in the magnetic field applied to the conductor, $\mathrm{d}B_a/\mathrm{d}t$ [$\mathrm{T\,s^{-1}}$], which in turn gives rise to an induced, opposing, magnetic field, $B_{induced}$ [T] [6, sec. 8.3.2][20]. This means that during an electromagnetic transient, part of the energy stored in the magnetic field will go towards inducing local magnetic fields rather than contributing to the main field of the magnet. These local fields cause currents to flow between the filaments of the SC strands, and between strands (where that is relevant for the design). Seeing as these currents, developing with a characteristic time–constant, flow through the copper matrix, they generate ohmic losses called IFCL and ISCL.

The failure to account for these effects are indicated in the electro–thermal schematic

[20] Also discussed in section 1.5 and 2.2.

(figure 2.15) as question marks, and the problem is two–fold: 1) Such a model does not correctly take into account where the coupling loss comes from; as it stands in the model, the loss is taken from an external source, but in reality, the source is internal to the system. The energy is taken from energy stored in the magnetic field, which, ultimately, comes from the power supply of the magnet. 2) The magnet's varying differential self–inductance, which depends on the coupling currents developed in the conductor and the saturation of the iron yoke, is completely disregarded; as local coupling currents will alter the local magnetic field, and thus, flux, in the conductor, Φ [Wb], they will also have an effect on the differential self–inductance of the magnet, $L_{\mathrm{d}} = \mathrm{d}\Phi/\mathrm{d}I_{\mathrm{M}}$ [H], while the yoke will influence the inductance by screening parts of the coil from one another.

Figure 2.16 shows, schematically, how the LEDET model used for simulations in this thesis solves the problem. By introducing a third domain, for coupling currents, it is possible to accurately model the energy exchange between the electrical and thermal domains through the locally arising coupling currents; the energy subtracted from the magnet, giving a change in its differential self–inductance, is the input to the coupling current domain, $\mathrm{M_{cc}}$ from the electrical to $\mathrm{M_{cc}}$ in the coupling domain. This energy is stored in the currents flowing between the filaments and strands, $\mathrm{L_{cc}}$, while a part of the energy is returned to the electrical domain and another is turned to heat as input to the thermal domain going from $\mathrm{R_{cc}}$ through $\mathrm{P_{cc}}$. In addition to this, the self–mutual inductance of the magnet coil is scaled down by a factor that depends non–linearly on the current in the magnet.

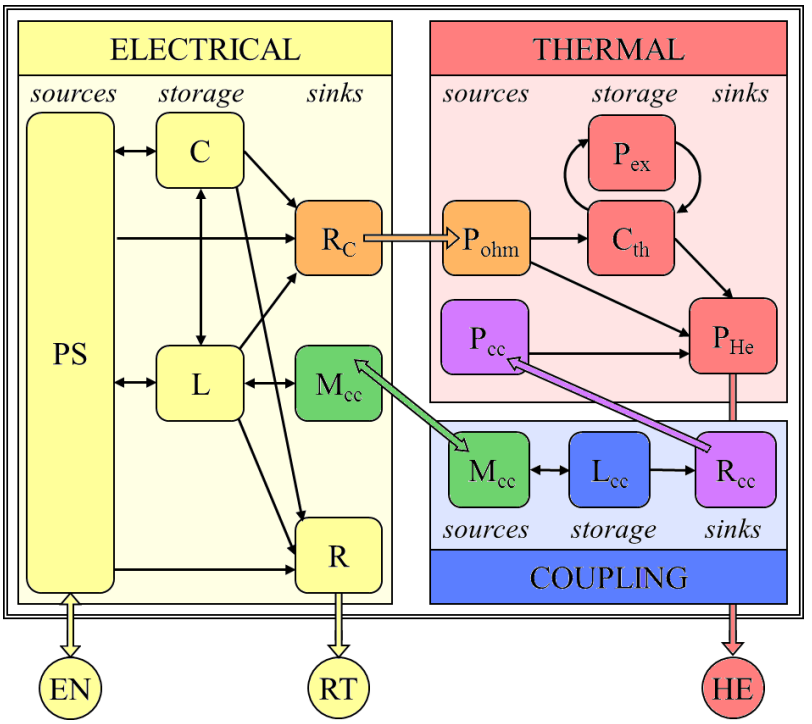

Figure 2.16: Schematic representation of energy exchanges in the LEDET model used for simulation in this thesis. Courtesy of Emmanuele Ravaioli [51, Fig. 4.3].

The LEDET model on which all transient simulation results presented in this thesis relies, then, consists of three lumped–element sub–domains, able to accurately reproduce the electrical transient in the main magnet circuit, the thermal transient in the coil's cross section, and the inter–filament and inter–strand coupling currents in the coil's superconductor,

including the complex interdependence between the three domains. The software solves the three sub–networks simultaneously, treating them as coupled networks.

Chapter 3

Modelling of a 16 [T] Block Coil Dipole Magnet

*My thesis is, in essence, a description of how well it is possible to protect one particular magnet — the block–coil dipole magnet intended for use in the 100 [*TeV*] FCC. This chapter describes the magnet.*

It also shows the energy margin of the magnet, how the CLIQ system relates to it, with its several configurations, and I also describe how this particular magnet is modelled.

Finally, I give a brief description of the investigated parameter space.

3.1 Magnet Parameters

The block–coil dipole magnet shown in figure 3.1 is a magnet designed at Lawrence Berkeley National Laboratory (LBNL) over the last decade, as a response to the desire of creating a 100 [TeV] hadron collider named the Future Circular Collider. The design is a first–of–its–kind aproach to a high–field dipole magnet, and has been chosen as such for two main reasons: 1) with this design, the width of the coil is controlled by the number of cables rather than the number of layers (as for a $\cos(\theta)$ coil), this makes it much easier to create a high magnetic field as one can simply add cables according to the desired field[1]. 2) The design allows a separation between the coil's high–field and high–stress regions in order to better deal with the strain dependence of Nb_3Sn [3, 90–97].

[1] In a $\cos(\theta)$ coil, the field is much more strictly given by the critical properties of the conductor — adding a new layer takes a lot of space, and so an increase in the field will likely come from an increased current — if the conductor is already operating at its peak, then this is not possible. For a block–coil, so long as the critical field value is not exceeded, one can just add another cable/turn on the coil, and by that increase the Ampére–turns very cheaply.

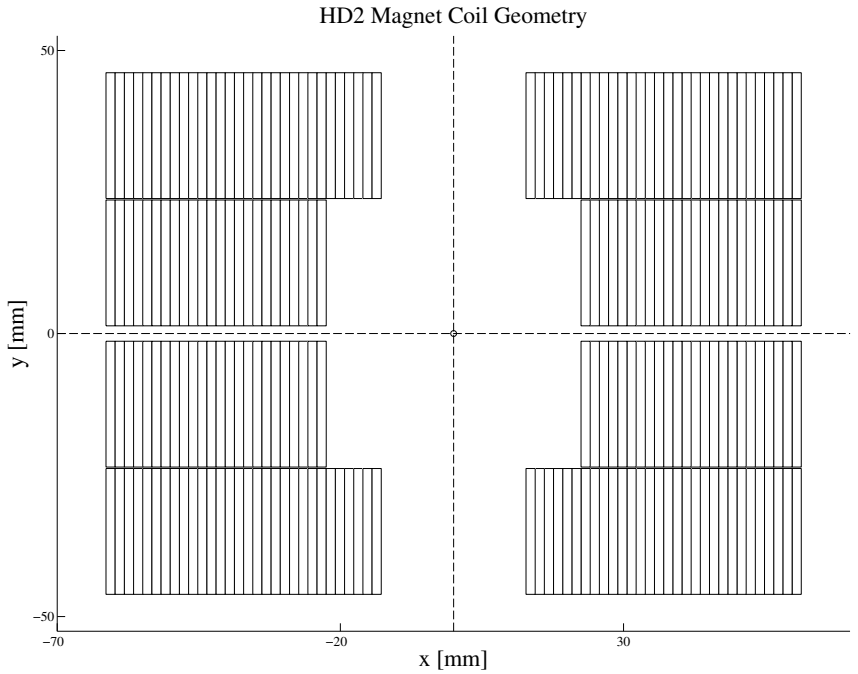

Figure 3.1: Coil cross section of the block–coil dipole magnet investigated in this thesis.

Table 3.1 gives a non–exhaustive list of the parameters of the block–coil dipole magnet. The parameters of the cable, from which the coil is wound, are given in table 3.2, and parameters of the individual strands of the cable are given in table 3.3. Values marked with "*" are those used directly in the simulation definitions[2].

Table 3.1: Some important parameters of the magnet [3, 48].

Parameter	**Unit**	**Value**
Aperture	[mm]	40–50
*Magnetic length	[m]	14
*Nominal operating current	[kA]	18.6
Bore field @ nominal current	[T]	16.0
*Operating temperature	[K]	1.9
Load line margin	[%]	6

[2]Note that the physical dimensions given for the cable, namely height, width and insulation thickness, are all values *after* the reaction process used to form Nb_3Sn(see section 1.6.4).

Table 3.2: Some important parameters of the cable used in the magnet [3, 48].

Parameter	Unit	Value
*Number of strands		51
Strand twist pitch[3]	[mm]	127
*Cable width	[mm]	22
*Cable height, inner edge	[mm]	1.4
*Cable height, outer edge	[mm]	1.4
*Insulation thickness	[mm]	0.1

Table 3.3: Some important parameters of the strands used to wind the cables in the magnet [3, 48].

Parameter	Unit	Value
*Strand diameter	[mm]	0.8
Nominal filament diameter	[µm]	77
*Filament twist pitch	[mm]	14
*Cu to non–Cu volume ratio		0.82
*RRR		287

3.2 Magnetic Field Distribution

With the magnet's parameters defined, a computer program called ROXIE, developed at CERN to aid in the design of the magnets for the LHC, simulates the steady state field in the magnet, and will also be used to simulate the field in the coil when powering only one electrical part at a time [83].

The magnetic field distribution, calculated for each individual strand, including both the contribution from the iron yoke and the strand self–field effect[4], from ROXIE, is given in figure 3.2. It is of note that the strands closest to the bore are at, or very close to, the peak magnetic field; this means that these strands will be very close to the critical surface of the material (recall the critical surface of Nb_3Sn given in figure 1.11), and consequently, the enthalpy margin to quench is both quite similar and very low for this inner region, as discussed in–depth in section 3.3. For the strands further away from the aperture the case is the opposite; most strands experience a fairly low field, and will have larger margins to quench.

Since CLIQ is able to deposit energy very uniformly in the coil, as postulated in section 1.8.3 and shown in chapter 2, the given field and strand distribution of the block coil indicates that protection with CLIQ should be very feasible [98], seeing as the loss deposited by CLIQ

[3]Strand twist pitch is not deemed important for this thesis — an explanation for this is given in section 3.6.
[4]Including the self–field in ROXIE means that the simulation takes into account the magnetic field in the outer regions of a strand caused by itself as well as the default calculation taking account only of all the other strands in the coil.

will touch a large number of individual cables of the coil, no matter what CLIQ configuration is used[5].

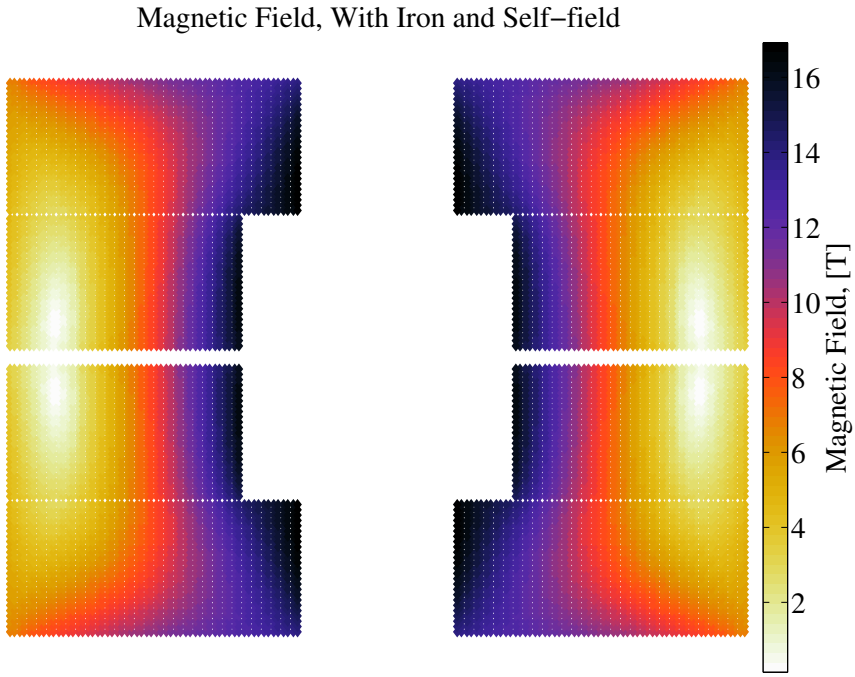

Figure 3.2: Field distribution in the block–coil dipole magnet, for the nominal transport current of 18.6 [kA], including the effect of the iron yoke and the self–field effect.

3.2.1 Separately Powered Electrical Parts

Since a CLIQ discharge introduces a different current in the two discharge paths of the magnet (as discussed in section 2.1.1), it will be necessary to decompose the magnetic field in the coil to the individual contributions from the four electrical parts. Assuming that the magnetic field is a purely linear function of the applied current, one can obtain this decomposed field, at the nominal transport current, using ROXIE once again. The resulting field components are shown in figure 3.3

When superposing these four fields, in order to obtain the complete field in the magnet, it becomes apparent that the non–linear effect of the iron saturation introduces some error. Figure 3.4 shows the error in absolutes terms. As seen, the error is fairly uniform in the central section of the coil, while quite a large error is also incurred in the outer regions. Here, the magnetic field (as seen in figure 3.2) is very close to zero, so any difference will mean a large relative error but not a critical one, as a quench is expected to begin in the cables close to the coil rather than in the outer regions, which means that the magnetic field's influence on various material properties and the quench itself is not very large.

This, of course, means that the larger error incurred close to the bore is of concern. To counter this, the magnetic field used for the calculation of the enthalpy margin to quench (see section 3.3) is scaled down to make sure that it suppresses the superposition error. Given

[5] As opposed to a $\cos(\theta)$ coil where the deposited loss, particularly for the PP CLIQ configuration, is localised to only a few cables, as discussed in section 2.4.

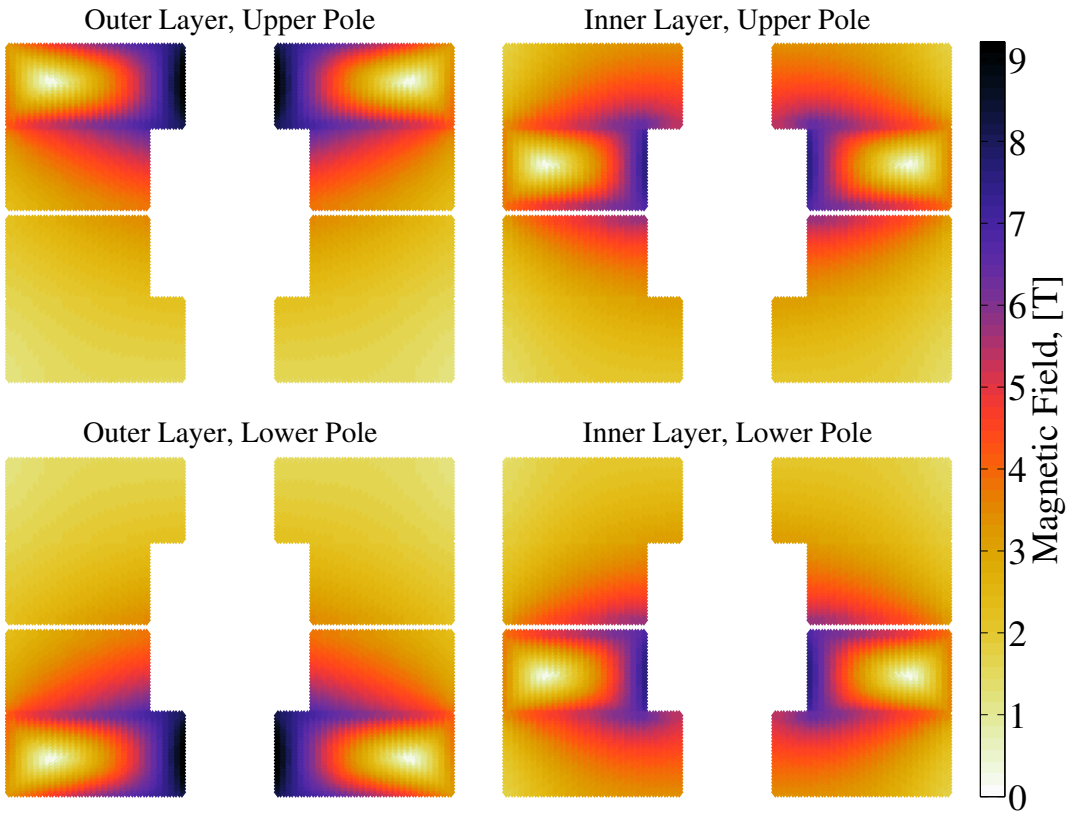

Figure 3.3: Contributions to the total magnetic field from the individual powering of all four electrical parts, at the nominal transport current, 18.6 [kA].

the uniformity of the error, this is a good compromise between ease of implementation and simulation versus the gain in accuracy.

3.2.2 Differential Inductance

As mentioned in section 2.5, the model must take into account the saturation effect of the iron yoke. The approach adopted here is by using ROXIE to calculate the self and mutual inductance of the various electrical parts of the coil at several different transport currents, and with this, create a curve of coefficients used to scale the self–mutual inductance matrix of the magnet during run–time. Figure 3.5 shows the differential inductance coefficient used when running the model.

3.3 Enthalpy Margin to Quench

It is possible to define the coil's enthalpy margin to quench, as discussed in section 1.7.2. For this, the critical surface of Nb_3Sn is needed, as shown in figure 1.11, in addition to the heat capacities of the main materials constituting the coil's cables in order to generate the equivalent properties of each whole, individual, cable[6].

[6]That is, the over–all heat capacity and thus, heat content, of the cable.

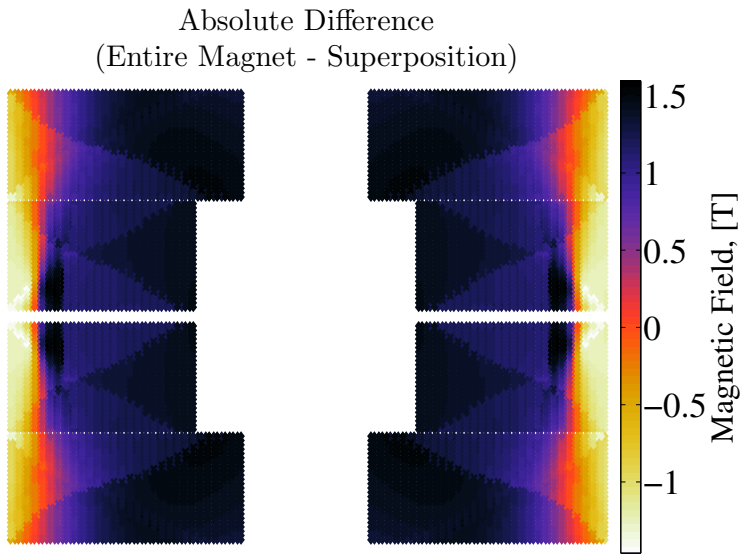

Figure 3.4: Absolute difference between the fully powered field and the superposition of the four partially powered fields.

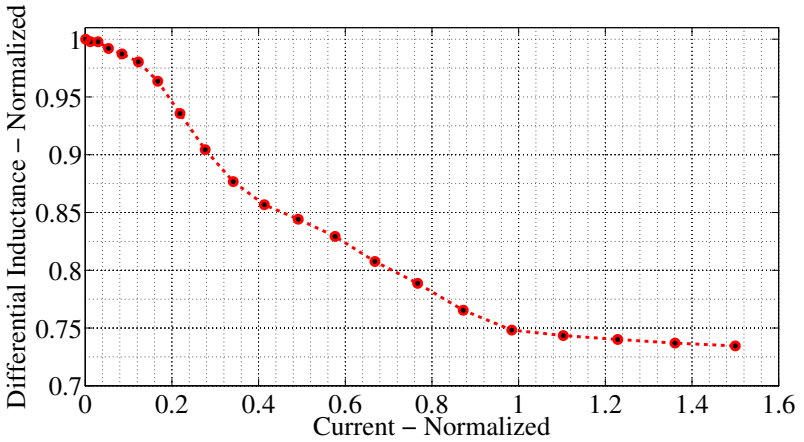

Figure 3.5: Normalised differential inductance as it varies with magnet current (current normalised to nominal transport current of 18.6 [kA]).

Finding the heat content of the cable at any given temperature and magnetic field requires taking volumetric averages over the different components/materials, and with that, weight their contribution to the over–all enthalpy of the cable[7].

Once all temperatures and magnetic field values have an associated enthalpy, one needs the current sharing temperatures of each individual cable for all applied currents. This

[7]The heat capacities and their fit functions used for the calculation of the enthalpy are amassed from several sources, some of which are private communications with supervisors [47]. The heat capacity fit function for Nb_3Sn is found in [99], while the one for copper is from [100].

process is done in several steps, but the idea is to locate where on the critical surface of the material the given operating point is[8]. At any applied current, that will be equal in all cables, the field across the different strands will vary, as seen in figure 3.2, which means that the cables will be at different distances from the critical current it can carry; remember also that the entire magnet is at a temperature of 1.9 [K].

Since the strands are fully transposed several times within the length of a given cable, all strands will at some point be located at the point in the cable that experiences the largest magnetic field within that cable. This peak field is what is used to determine the enthalpy margin in the individual cables[9].

The task now is to go through each cable, and see how high the temperature needs to be in order for the applied current density to be equal to the critical current density; this is the current sharing temperature. From this and the temperature dependent enthalpy, the margin to quench is found.

Figures 3.6 and 3.7 show the margin to quench and the temperature margin for each cable in the coil, for the nominal transport current. As seen, the margin to quench in regions of low magnetic field is far higher, about two orders of magnitude, than the margins at very high fields. This is because at lower fields the distance between the given operating point and the critical surface is enormous. This also means that it might be harder to protect a magnet at lower current than higher, in the sense that more energy must be delivered, since the magnetic field in the coil is lower for lower currents. On the other hand, the protection system does not need to be as fast, since the energy density in the coil is low, and thus heating of the hot–spot during a quench is slow. At higher current levels, the challenge will be to deliver energy fast enough to avoid damage to the hot–spot. Appendix B plots the quench and temperature margins for 75%, 50% and 25% of the nominal current as well.

Nominal Transport Current — Enthalpy Margin to Quench

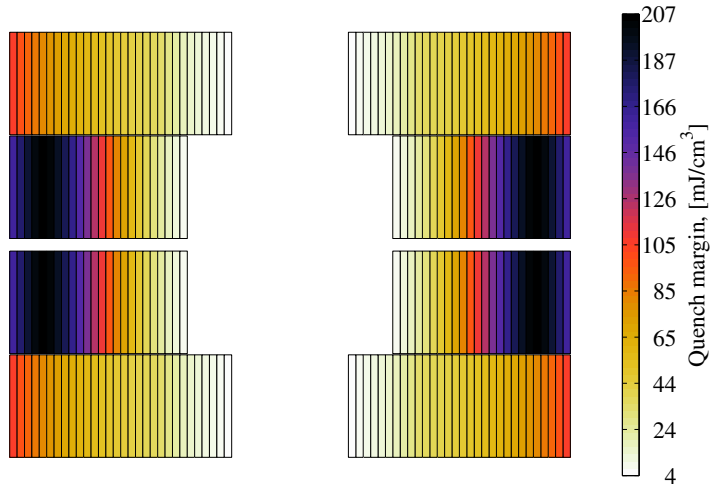

Figure 3.6: Enthalpy margin to quench in the different cables of the coil for an initial transport current of 18600 [A] (the nominal current).

[8]The operating point here refers to what current is applied to the magnet "at the moment".

[9]Note that in section 3.2.1, the scaling done to the main field was to obtain just the field needed for the calculation here.

Nominal Transport Current — Temperature Margin

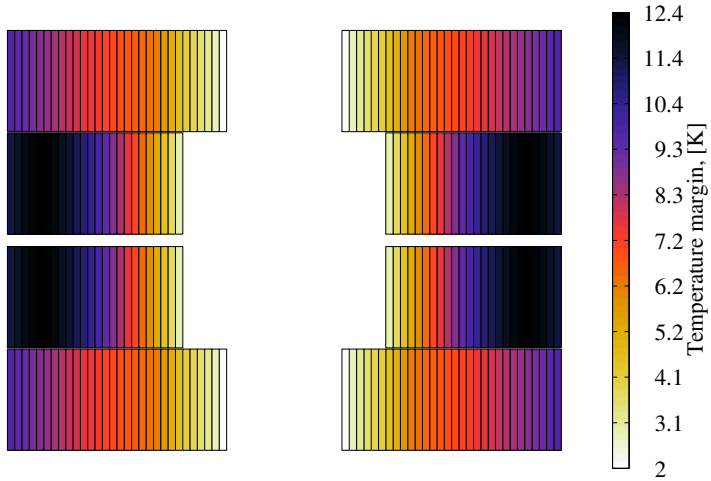

Figure 3.7: Temperature margin in the different cables of the coil for an initial transport current of 18600 [A] (the nominal current). Note that the given temperatures signify the temperature *above* the operating temperature of 1.9 [K] the cable needs to be heated to.

The temperature margin shown in figure 3.7 gives the needed temperature increase *above* the operating temperature that will quench the cable. The temperature increase will come from a combination of heat propagation from adjacent cables, particularly the ones that have already quenched, and thus experience large ohmic losses, and the heat generated by the protection system; in this case, the IFCL from a CLIQ discharge.

3.4 CLIQ on the 16 [T] Block–Coil Dipole Magnet

The initial current polarities indicated in figure 2.10 are recreated in figure 3.8 for the cross–section of the block–coil. As pointed out in section 2.4, the CLIQ protection system relies on having regions of the magnet receive oppositely directed current changes. As seen, there is a large difference in what regions receive what current between the different CLIQ configurations; performance differences are thus expected to be clearly visible in results.

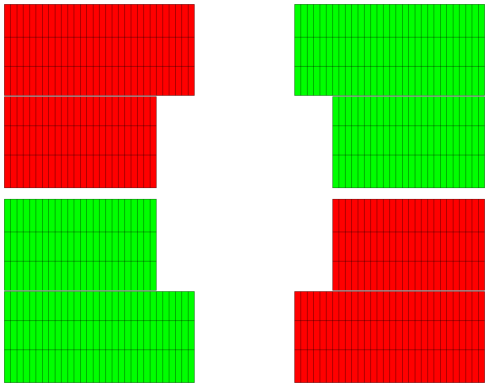

(a) Initial current polarity for a discharge with the Pole–Pole CLIQ configuration.

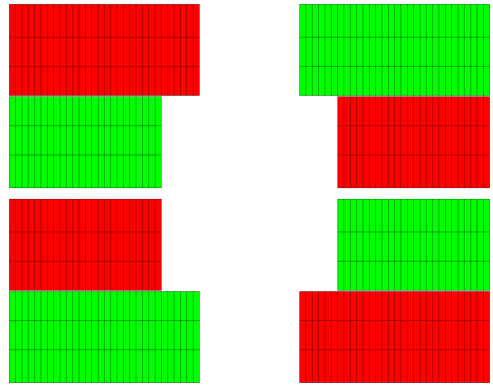

(b) Initial current polarity for a discharge with the Crossed–Layer CLIQ configuration.

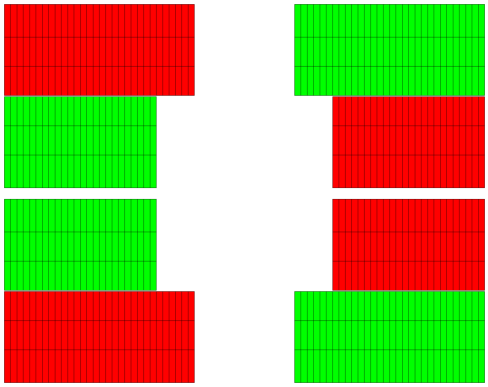

(c) Initial current polarity for a discharge with the Layer–Layer CLIQ configuration.

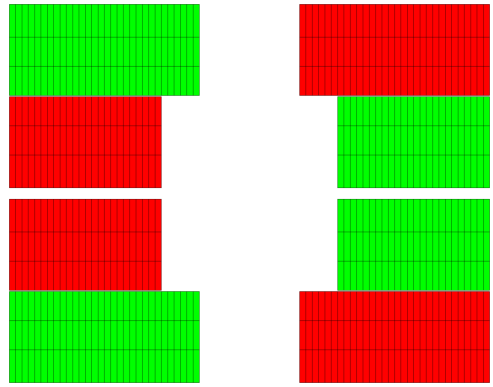

(d) Initial current polarity for a discharge with the Layer–Layer Reverse CLIQ configuration.

Figure 3.8: Initial current polarity in all four CLIQ configurations possible for the block–coil dipole magnet. Green indicates a current flowing *out of* the page, while a red one indicates a current flowing *into* the page.

Table 3.4 gives the inductance values of the different paths for the three unique CLIQ configurations[10]. As seen, the equivalent inductance for both LL and CL are much lower than for the PP. This is one part of the reason for why there is such a large difference in the CLIQ effectiveness between the PP on one side and LL and CL on the other (the other part of the reason being that the layers within a pole are more strongly coupled than the poles are to each other).

It is important to note that L_1 and L_2 are practically the same for the LL configuration. For a $\cos(\theta)$ coil, discharging the CLIQ between layers is expected to give rise to very asymmetric inductances, seeing as the inner layer in such a coil experiences a substantially different magnetic field, and thus couples very differently to the rest of the coil. For the block–coil, however, the inner and outer layers are almost perfectly matched with respect to inductance — whether this is a design feature, an intrinsic property of block–coils or just

[10]Since the LL and LLrev use the same paths, the inductances are the same, with the caveat that L_1 and L_2 are switched — the equivalent and mutual inductance, of course, stay the same.

a coincidence is unknown to the author. As results presented later in the thesis suggest, it might be an intrinsic property of the block–coil design.

The geometric discharge parameters introduced in equations 2.8 and 2.9, repeated below, are listed in table 3.5. Given the balance between the inner and outer layer inductance, these geometric parameters will also be balanced for the LL CLIQ configuration. The symmetry of the PP and CL, means that for those discharge paths, the parameters are exactly balanced.

$$f_{\mathrm{g},1} = \frac{L_2 + M_{12}}{L_1 + L_2 + 2M_{12}}$$
$$f_{\mathrm{g},2} = -\frac{L_1 + M_{12}}{L_1 + L_2 + 2M_{12}}$$

Table 3.4: Inductance values for the discharge paths when employing the various CLIQ configurations. Note that the LL and LLrev will have the same path, and so they are not entered twice in the table.

Configuration	L_1 [mH m^{-1}]	L_2 [mH m^{-1}]	M_{12} [mH m^{-1}]	L_{eq} [mH m^{-1}]
PP	2.20	2.20	1.01	0.59
LL	1.85	1.87	1.35	0.25
CL	1.81	1.81	1.40	0.20

Table 3.5: Geometric parameter values for the discharge paths for the various CLIQ configurations.

Configuration	$f_{\mathrm{g},1}$	$f_{\mathrm{g},2}$
PP	0.500	-0.500
LL	0.501	-0.499
CL	0.500	-0.500

The CLIQ effectiveness of this magnet is already presented in section 2.4, and so the complete plots are not repeated here, however, when discussing the model size reduction later in this chapter, the plots will be revisited.

The mean and maximum values of the CLIQ effectiveness for the different CLIQ configurations are listed in table 3.6.

Table 3.6: Mean and maximum value of the CLIQ effectiveness for the various CLIQ configurations.

Configuration	Ψ_{mean} [m^{-1}]	Ψ_{max} [m^{-1}]
PP	0.29	0.66
LL	0.50	1.15
CL	0.52	1.24

3.5 Simulating the 16 [T] Block–Coil Dipole Magnet

For running the actual simulations of the quenches, an object oriented simulation framework named Transient Analysis with Lumped Elements in Superconductors (TALES) has been used [101]. This simulation framework applies the LEDET model described in section 2.5 by making use of the Simulink package in MATLAB [102], and all simulation results of transients presented in this thesis are produced by this software. An important note about the results generated by the simulation software is that it assumes that the hot–spot temperature rises adiabatically. This means that a very pessimistic approach to the problem is taken, and thusly, the temperature of the hot–spot, which ultimately is the value used to evaluate the performance of a given protection system, is overestimated.

3.5.1 Model Size Reduction

So far, every single strand in the coil has been taken into account when calculating the field or the CLIQ parameters; running hundreds of simulations with complete modelling of thermal and electromagnetic behaviour, including phase transitions and saturation effects, keeping track of the over 10000 strands in the block–coil dipole magnet is unfeasible[11]. It is also unnecessary; as mentioned when discussing the enthalpy margin to quench in section 3.3, each strand in a cable is transposed so as to be in each possible location in the cable cross section within a length given by the strand transposition pitch. This means that the peak field in the cable, the largest field any one of the strands within the cable is subjected to, can be used as the field of the entire cable for the sake of determining the occurrence of a phase transition[12]. This is the first significant reduction in size of the model eventually run with the TALES software.

Further reduction is made by grouping blocks of strands together for which the magnetic fields on the one hand, and the CLIQ effectiveness on the other, are similar. Using the complete geometry of the block–coil, the way strands are grouped together in blocks is indicated in figure 3.9. By grouping together such large amounts of the coil, the computational load is substantially reduced; provided the loss of accuracy is acceptable.

[11] It is worth mentioning that off the books, E. Ravaioli (my CERN supervisor) is working on a new approach to the LEDET model, which allows for very fast simulation of all strands in the magnet — this is only in development, but seems like a promising and very interesting tool for the future.

[12] The true field of the location in question is used when calculating other parameters that depend on the magnetic field, such as the magnetoresistive contribution to the electrical resistance.

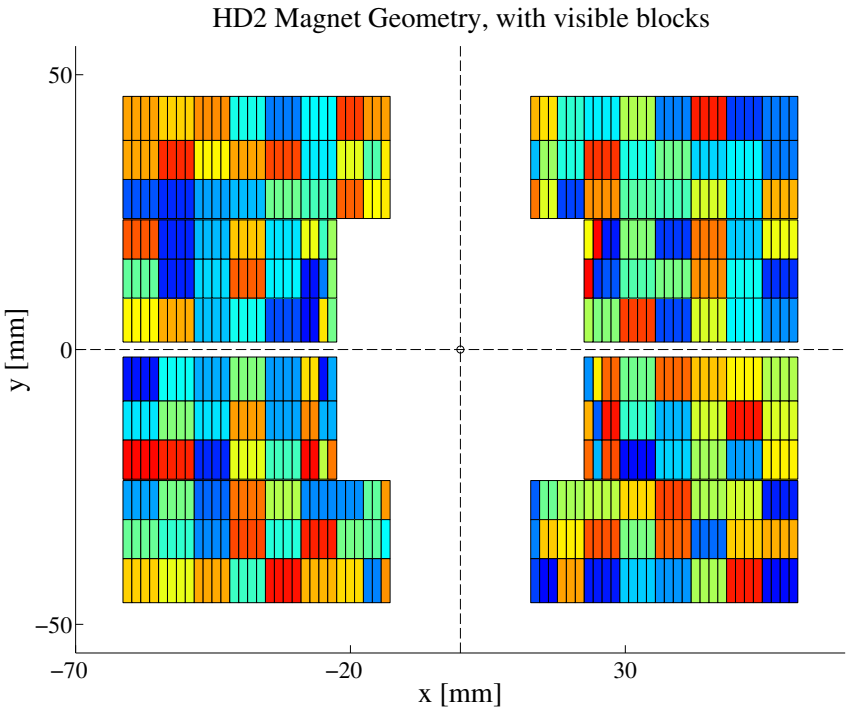

Figure 3.9: All blocks of the block–coil magnet are indicated with a randomly, insignificant, chosen colour.

PP CLIQ configuration

Figure 3.10 shows how well the chosen grouping of strands manages to capture the CLIQ effectiveness for the PP CLIQ configuration. The left hand side of the figure is the strand–by–strand, that is, the complete picture, while the right hand side is the one achieved with the block–by–block grouping. The two sides would, ideally, be perfectly symmetrical. Evidently, this is not entirely the case, but a fair approximation is reached all the same — the losses in the parts closest to the bore are expected to be modelled accurately, and the midplane–region does not see a large loss of accuracy, although there is a small drop in the peak value, due to Ψ being averaged over several strands (typically about 50).

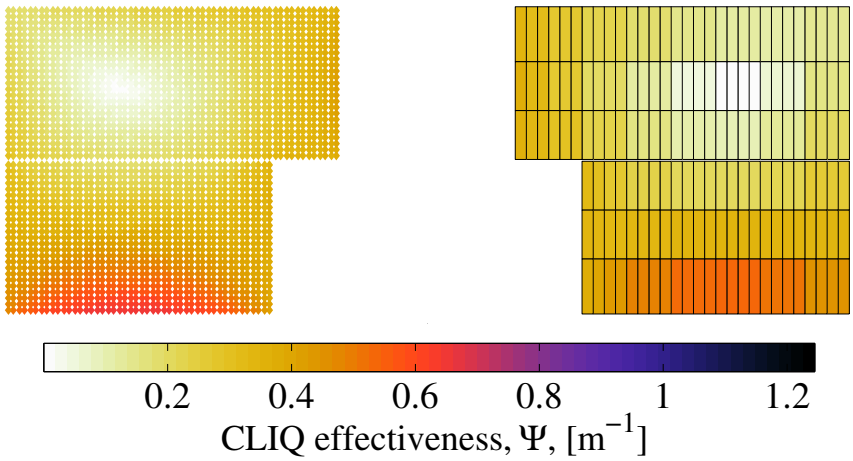

Figure 3.10: Strand–by–strand CLIQ effectiveness in the block–coil on the left, and the block–by–block reproduction achieved with the chosen grouping of strands on the right, for the PP CLIQ configuration.

Table 3.7 shows that while the average value is still the same (as is expected), the peak value as been reduced by about 15%. This means that the loss generated in the peak regions, following the expression in equation 2.30, will fall by about 30% as compared to the full strand–by–strand calculation. This is not extremely large, and as explained when discussing the enthalpy margin to quench in section 3.3, the cables close to the bore are expected to quench much sooner than the ones in the middle of the coil, and thus, an error in the loss generated there will have little influence over the complete transient.

Table 3.7: Mean and maximum value of the CLIQ effectiveness for the strand–by–strand VS block–by–block when adopting the PP CLIQ configuration on the block–coil.

Approach	$\Psi_{\mathbf{mean}}$ **[m^{-1}]**	$\Psi_{\mathbf{max}}$ **[m^{-1}]**
Strand–by–strand	0.29	0.66
Block–by–block	0.29	0.56

LL CLIQ configuration

Figure 3.11 shows how well the chosen strand grouping is able to capture the CLIQ effectiveness in the block–coil for the LL CLIQ configuration, while table 3.8 summarises the mean and peak value of the CLIQ effectiveness.

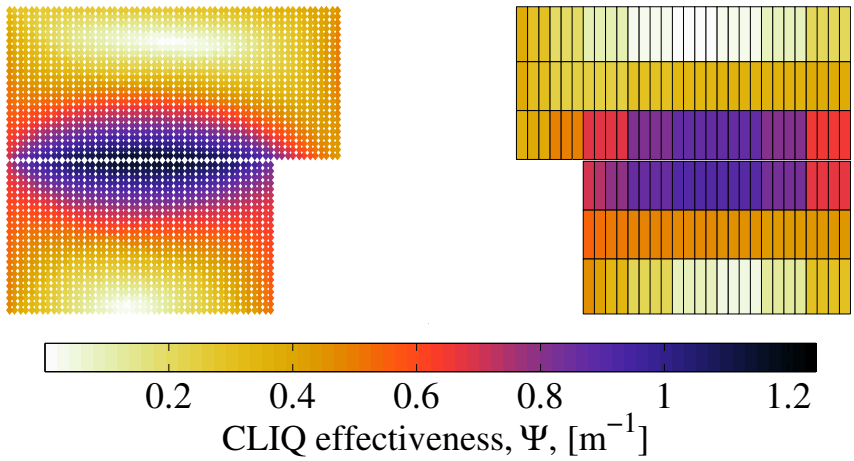

Figure 3.11: Strand–by–strand CLIQ effectiveness in the block–coil on the left, and the block–by–block reproduction achieved with the chosen grouping of strands on the right, for the LL CLIQ configuration.

Table 3.8: Mean and maximum value of the CLIQ effectiveness for the strand–by–strand VS block–by–block when adopting the LL CLIQ configuration on the block–coil.

Approach	$\Psi_{\mathbf{mean}}$ **[m^{-1}]**	$\Psi_{\mathbf{max}}$ **[m^{-1}]**
Strand–by–strand	0.50	1.15
Block–by–block	0.50	0.95

Again, there is a clear drop in the peak value, for this case a little less than 20%, which means about 40% lower peak deposited power. However, as before, the location of the peak deposited power is not where the initial quench is expected to occur, based on the margin to quench, and so, the influence of this error is not expected to be very large. Note also that the loss profile is captured very well, and also, that the region closest to the bore is acceptably reproduced.

CL CLIQ configuration

The final CLIQ configuration, the CL, is shown in figure 3.12, while table 3.9 gives the summary. There is complete loss of accuracy in modelling the Ψ in the midplane region; as for the PP this is not critical, but it is worth noting that this loss of resolution is unfortunate; however, the loss in other parts of the coil is approximated very well, and particularly the loss in the inner–most cables in the upper layer is captured satisfactorily. Since the modelled Ψ for the CL and LL now is quite similar, one would expect them to perform quite similarly, barring the fact that the LL can be reversed to the LLrev. The lowered peak effectiveness follows the same trend as for the LL and thus a drop of about 40% in the peak developed power is expected (as compared to the full strand–by–strand case).

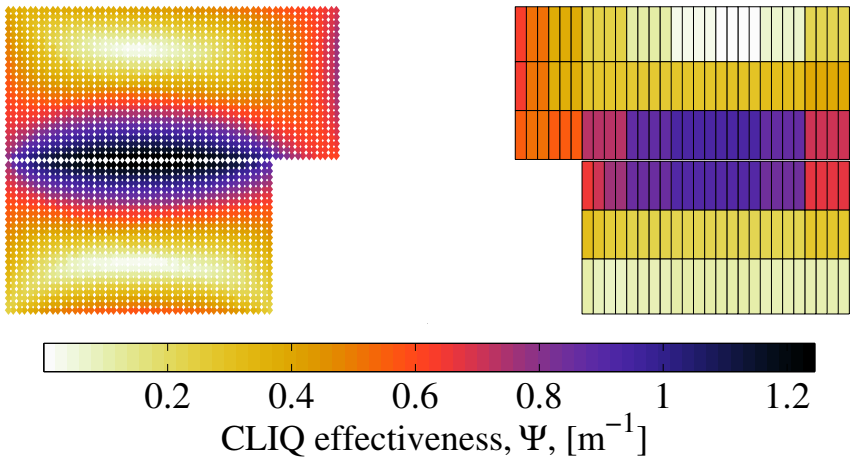

Figure 3.12: Strand–by–strand CLIQ effectiveness in the block–coil on the left, and the block–by–block reproduction achieved with the chosen grouping of strands on the right, for the CL CLIQ configuration.

Table 3.9: Mean and maximum value of the CLIQ effectiveness for the strand–by–strand VS block–by–block when adopting the CL CLIQ configuration on the block–coil.

Approach	$\Psi_{\mathbf{mean}}$ **[m^{-1}]**	$\Psi_{\mathbf{max}}$ **[m^{-1}]**
Strand–by–strand	0.52	1.24
Block–by–block	0.50	0.98

Magnetic field

The magnetic field in the block–coil, at nominal current, is shown in figure 3.13, while table 3.10 gives the summary. The field is captured almost perfectly with the chosen grouping of strands — there is no difference in the peak magnetic field value, and the only loss of features between the full and the reduced representation is in the outermost regions of the midplane region, where the minimum is not out at the edge, but rather a few cables in, while the reduced representation indicates that the zero is at the coil's outside edge.

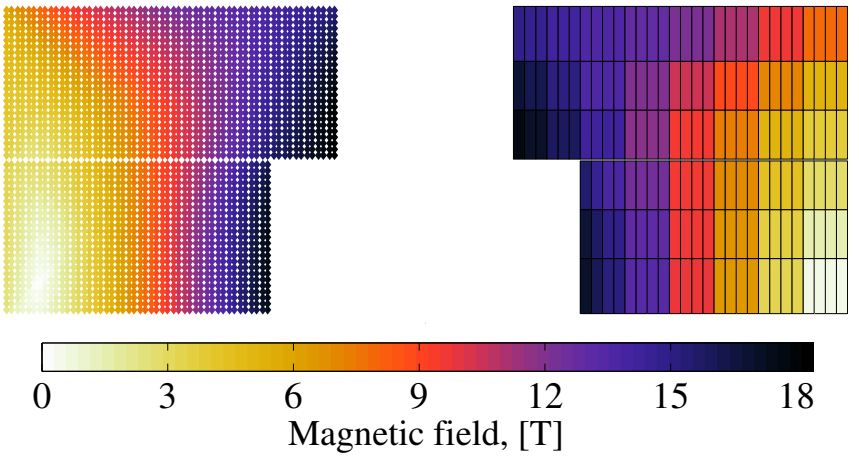

Figure 3.13: Strand–by–strand magnetic field in the block–coil on the left, and the block–by–block reproduction achieved with the chosen grouping of strands on the right.

Table 3.10: Mean and maximum value of the magnetic field for the strand–by–strand VS block–by–block at nominal current in the block–coil.

Approach	$B_{\mathbf{mean}}$ **[T]**	$B_{\mathbf{max}}$ **[T]**
Strand–by–strand	9.24	18.40
Block–by–block	9.25	18.40

3.6 Investigated Parameter Space

With this, everything is set to run simulations, and the remaining chapters of the thesis are dedicated to the presentation and discussion of results from these simulations. This section will briefly outline the parameter space investigated in the simulations.

CLIQ parameters The nominal CLIQ unit is chosen with parameters $C_{\mathrm{CLIQ}} = 100$ [mF], $U_0 = 1000$ [V]. The parameters investigated in addition to these is a CLIQ charging voltage of 1.2, 1.5 and 2.0 [kV], and a CLIQ capacitance of 200 [mF].

CLIQ configurations Initial results will be based on the PP CLIQ configuration, simply because this is the configuration that can usually be employed without large difficulty on an existing magnet. Given that the block–coil investigated here is not actually built, the PP is not chosen as a strictly "nominal" case. In addition to this, the LL, LLrev and the CL is tried.

Initial transport current The nominal initial transport current for the block–coil is chosen as the current needed to achieve 16 [T] in the centre of the magnet aperture. In addition to this current, one larger current, typically 100 [A] below the short–sample current[13]. This is chosen because during initial magnet testing the coil will be run at this current. Also, currents of 75, 50 and 25% of the nominal current are tried, to take into account that the magnet must stay protected also during a ramp of the current.

RRR The nominal design parameter for the strands used in the block–coil is 287. While this is quite high, it has been kept for the sake of consistency with other work done on the block–coil. In addition to the nominal value, RRRs of 200 and 100 have been tried.

Fraction of non–copper The nominal copper fraction is given as 45%, meaning a fraction of non–copper as 55%. In addition to this, the fraction of non–copper has been tried at 45, 50, 60 and 65%. Values of non–copper fraction below the chosen ones will be so low that the critical current of the strand is below the needed nominal current, and as such it is uninteresting to simulate. Values of non–copper above 65% leaves too little copper in the strand, and so the temperature increase is too high to maintain protection at higher currents; thus it is not interesting to simulate.

Filament twist pitch The nominal filament twist pitch is set to 14 [mm]. From the discussion in chapter 2, this seems very close to an optimal value, however, in addition to this, pitches of 10, 12.5, 15, 17.5, 20, 30 and 50 [mm] have been tried.

Critical surface In equation 1.11 there is a parameter called $C(\epsilon)$ where ϵ is the strain, which has been assumed to be zero[14]. Disregarding the strain dependence, the parameter is simply a constant called C_0, that relates to the pinning properties of the superconducting material, and its nominal value is 46.7 [kA $\mathrm{T}^{0.5}$ mm^{-2}]. In addition to this nominal value, 56.1, 70.1, 93.4 and 186.8 [kA $\mathrm{T}^{0.5}$ mm^{-2}] are tried.

Coil geometry So far, only the first design presented in [3] has been discussed. However, the 16 [T] block–coil geometry is not fully decided; changing it will allow for very interesting optimisation possibilities with the CLIQ system. The different geometries will be presented in more detail in chapter 5, but summarised they are as such;

Variant A
: This is the first design presented in [3], and is convenient to use as a base–line design for the sake of having a reference.

Variant B
: Using the same envelope as the base–line design, this coil employs about a 20% reduction in the number of cables by increasing the height of the cables (larger strands). This reduces the inductance of the coil, and CLIQ is expected to perform better for this coil geometry.

Variant C
: Contrary to variant B, this coil lowers the height of the cables, increasing by about 20% the number of them — this increases the inductance of the coil, and CLIQ is expected to perform poorer for this coil. The reason this design is of interest is that a smaller

[13] The short–sample current is the current that causes a quench in the magnet without interference from outside factors; that is, the current that brings a part of the magnet above the critical current.

[14] Argument for this is given in section 3.3.

cable means that all the warm parts of the circuit (power supply, leads, diodes, etc.) can all be dimensioned smaller than in the base–line case.

Variant D

This is the graded coil design presented in [3]. The idea is to have most of the coil made up of many thin cables with low margin to quench, and an insert in the inner regions of the coil, close to the bore, of larger cables that have a larger margin to quench, with the benefit of being able to push the magnet current, and thus, field, higher, since the insert is more stable against quenches. This design is much more complicated than the others, and as such, it is hard to make a prediction; in theory though, the inserts could be used as an electrical part for the sake of CLIQ discharge path, which does open up the possibility to deposit loss right in the middle of the high–field region.

Variant F[15]

In principle very similar to variant A, but the whole coil has been scaled up by a factor so as to increase the aperture of the magnet. This means that the cables are also larger, and therefore have larger margins to quench. This design includes a change in the iron yoke, so as to avoid the coil touching it. The larger coil should prove easier to protect than the base–line design, for the same reason as variant B.

Strand Twist Pitch

In this thesis, the effect of the strand twist pitch has been disregarded completely, and a brief but sufficient explanation for this is given here.

When stacking several cables together, such as is done to create a block–coil dipole magnet, the time–constant for the ISCC is given as such [51, eq. 4.42],

$$\tau_{\mathrm{ISCC,stack}} = \frac{\alpha_{\mathrm{c}} N_{\mathrm{c}}}{\alpha_{\mathrm{c}} + c_{\mathrm{stack}}(N_{\mathrm{c}} - 1)} \tau_{\mathrm{ISCC,cable}}, \quad [\mathrm{s}] \quad (3.1)$$

where c_{strand} is a constant that depends only very slightly on the number of strands in the cable, N_{s}, and it is about 1 for $N_{\mathrm{s}} = 8$ and 1.15 for $N_{\mathrm{s}} = 40$. $\alpha_{\mathrm{c}} = N_{\mathrm{s}}/4$, and $\tau_{\mathrm{ISCC,cable}}$,

$$\tau_{\mathrm{ISCC,cable}} = c_{\mathrm{s}} l_{\mathrm{s}} \frac{N_{\mathrm{s}}^2 - 4N_{\mathrm{s}}}{R_{\mathrm{c}}}, \quad [\mathrm{s}] \quad (3.2)$$

where c_{s} is a constant between 16 and 17 $[\mathrm{n\Omega\,s\,m^{-1}}]$ [10, p. 78], l_{s} is the strand twist pitch and R_{c} is the cross contact resistance.

By assuming a strand twist pitch as the nominal one, 127 [mm], a stack of 25 cables, 40 to 80 strands in each cable, and a cross contact resistance of 100 [μΩ], the expected time–constants of the ISCC will range between 160 and 1300 [ms]. Even the lowest value is far above what is relevant for the oscillations during a CLIQ discharge, as the ISCC will be so slow to develop that the applied magnetic field change will have changed direction before any noticeable ISCL has been deposited in the coil. Thus, the strand twist pitch is not an investigated parameter in this thesis.

[15] There exists a variant E, which is the same as variant A, but with a much wider coil; the aperture is kept the same, but the number of cables wound around this aperture is much larger than the base–line design. The results for this coil are not presented here, as the simulations are very unreliable — the way the differential inductance is taken into account in the model ends up making the simulations unstable due to the heavily reduced self–mutual inductance of the coil. This is caused by the fact that for such a wide coil, the iron yoke comes extremely close to the winding pack, and thus the saturation effect plays a far larger role for this coil than the others.

Effective Transverse Resistivity

Section 1.6.2 mentions the cross contact resistance, and that in the case of Nb_3Sn it is usual to take this parameter as,

$$\rho_{\mathrm{eff},0} = \frac{1 - f_{\mathrm{SC}}}{1 + f_{\mathrm{SC}}} \rho_{\mathrm{m}}, \qquad [\Omega\,\mathrm{m}] \quad (3.3)$$

this is for the limiting case of zero cross contact resistance.

For this thesis, the actual cross contact resistance is not known, and in previous investigations, not recited here, the importance of this parameter is not substantial, particularly not compared to several of the other variables in the parameter space[16]. For this reason, the effective matrix resistivity, ρ_{eff}, is assumed equal to the Copper resistivity without the effect of increased or decreased path–length through superconducting filaments.

[16] I looked at the effect of this parameter in the Specialisation Report earlier in 2015.

Chapter 4

Protection of the 16 [T] Block–Coil Dipole Magnet

The first simulation results are presented in this chapter. They are all for the block–coil dipole presented in chapter 3.

Firstly I show the agreement between CLIQ generated losses and the initial quench in the magnet, then some indicative results about the performance of QH on the magnet.

The effects of varying several parameters are then investigated — initial transport current, the CLIQ parameters, the CLIQ configuration, the RRR and filament twist pitch, the fraction of non–Copper and finally, improvement of the superconductor.

4.1 Initial Results — Nominal Case

As stated in sections 1.7 and 1.8, the hot–spot temperature is the first and foremost measure of a protection system's ability to actually keep a magnet coil from taking damage during a fault. Figure 4.1 shows how the hot–spot temperature develops in the coil during a CLIQ discharge. The initial transport current in the magnet is 18.6 [kA], while the CLIQ unit used has the nominal parameters of $C_{\mathrm{CLIQ}} = 100$ [mF], $U_0 = 1000$ [V].

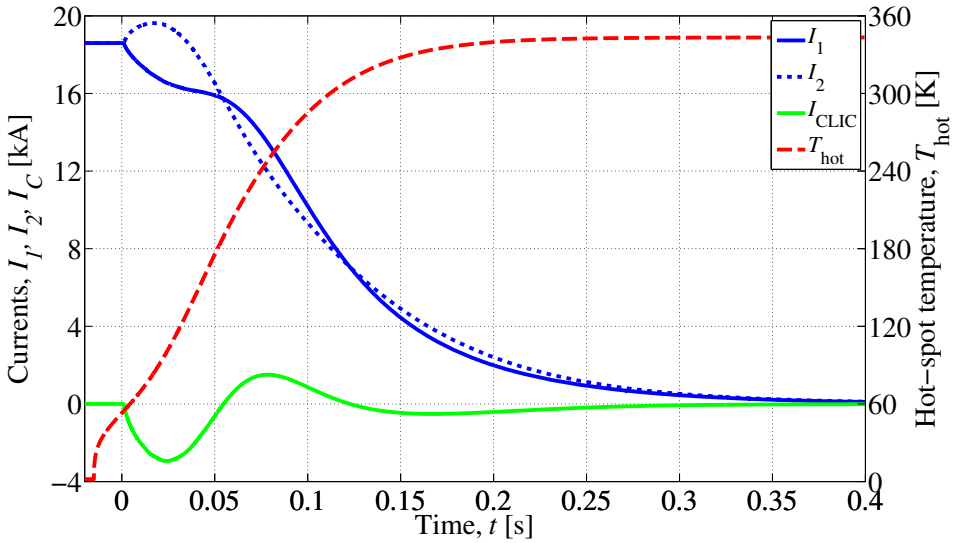

Figure 4.1: Discharge currents, CLIQ current and hot-spot temperature development in the block–coil magnet during discharge of a CLIQ unit of parameters, $C_{\mathrm{CLIQ}} = 100$ [mF], $U_0 = 1000$ [V].

The currents, I_1 and I_2, oscillate and after some time, the coil quenches; the currents in the magnet clearly decay, as they are expected to given the expressions in chapter 2.

As seen, the hot spot temperature is kept right below 350 [K]. While technically protected (as given by the chosen limit of 350 [K]), this also means that there is no real margin during operation, and also, when training the magnet, the current level will be run closer to the short–sample current, and thus an even higher hot–spot temperature will be reached, which in turn means that one risks damaging the coil during the commissioning of the magnet.

The time it takes a block to quench is shown in figure 4.2[1]. It is clear that the initial quench starts very fast after the CLIQ unit is triggered; the unit is triggered at t = 1 [ms], while the quench starts only about 2 [ms] after the triggering. While the quench both arises and propagates extremely fast, it is still insufficient from a protection point of view, given the final hot–spot temperature of 350 [K].

[1] recall section 3.5.1 regarding the definition of a block of the magnet as a volume within which all parameters of the strands are averaged

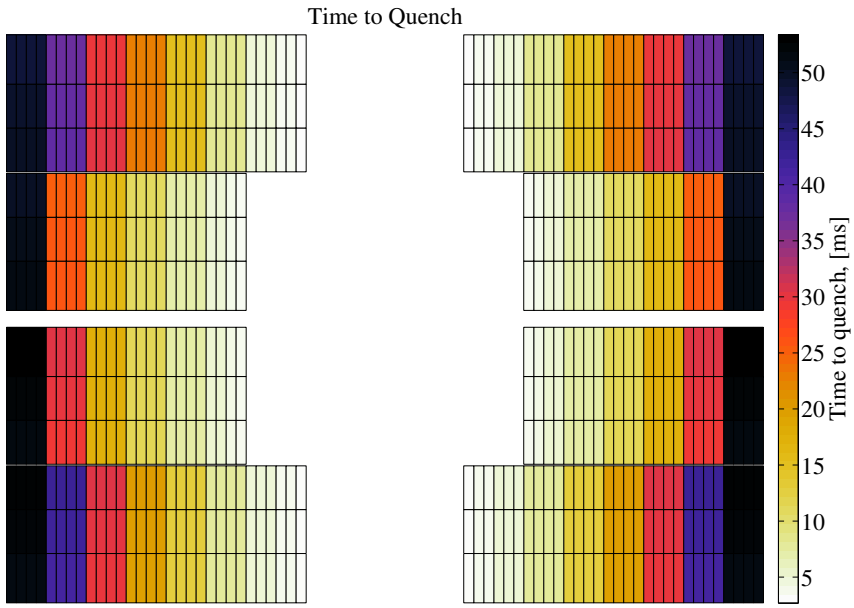

Figure 4.2: Time to quench individual blocks in the magnet coil during discharge of a nominal CLIQ unit of parameters, $C_{\mathrm{CLIQ}} = 100$ [mF], $U_0 = 1000$ [V].

4.1.1 IFCL in the Coil

The IFCL generated in the magnet coil is given in figure 4.3. Only values for electrical part 1 and 2 are shown, as the ones for parts 3 and 4 are symmetric to 1 and 2. By integrating the individual curves in the figure over time, one gets the total energy deposited in a given block, as shown in figure 4.4. Note that a darker colour is assigned to blocks closer to the bore. The loss in electrical part 2 has one subset of curves at the darker colours very similar to the curves in electrical part 1 — these are the blocks closest to the aperture. Then there is a subset of curves with a much lighter colour, indicating that they belong to blocks closer to the middle of the magnet. Looking back to the plot of CLIQ effectiveness in figure 3.10, this is exactly as predicted. Ψ in blocks close to the aperture is very similar when comparing the outer and inner layers of the coil (electrical part 1 and 2 respectively), while in the inner layer, there is a peak in the deposited loss in the middle of the coil (lower part, towards the midplane).

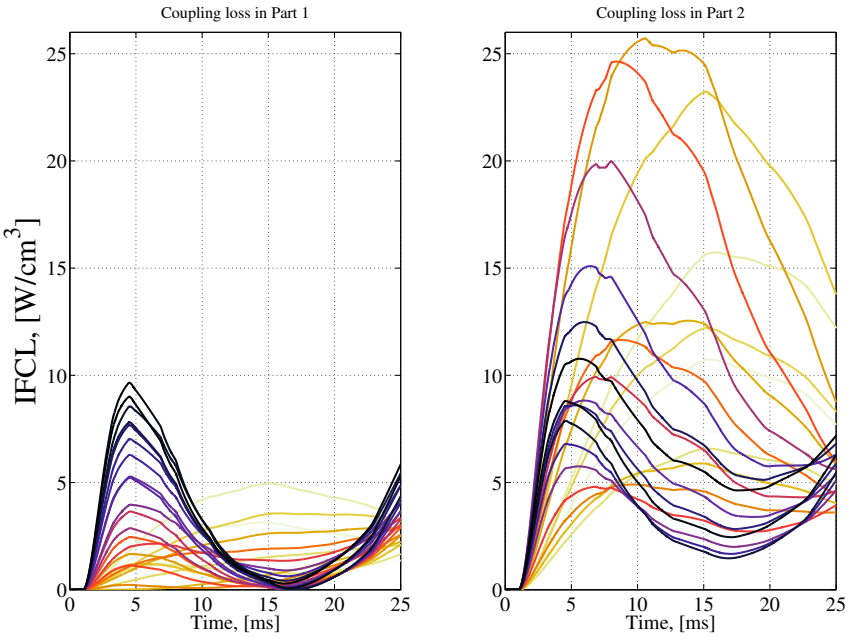

Figure 4.3: IFCL development during CLIQ discharge in the block–coil dipole magnet operating at nominal initial transport current and with nominal CLIQ parameters.

On the scale shown, it is not so easy to discern how the deposited loss causes a quench, as the initial quench occurs after less than 3 [ms]. Figure 4.5 shows only the first 4 [ms] of the discharge, with the CLIQ unit triggered at t = 1 [ms]. The blue curve gives the coil resistance of the relevant electrical part, and as seen, there is excellent agreement with the calculated margin to quench, shown in figure 3.6, and the time of initial quench onset[2]. Note that after the first quench, it becomes increasingly (with time) unreliable to determine when a new block quenches solely from the deposited IFCL because the normal–zone generates large amounts of ohmic heat that propagates to adjacent blocks — this means that the IFCL will only be a part of the over–all energy deposited in the block, and the quench will occur sooner than what a comparison between the enthalpy margin and IFCL deposition would indicate.

[2]Note that the right axis gives the resistance while the left axis gives the deposited loss.

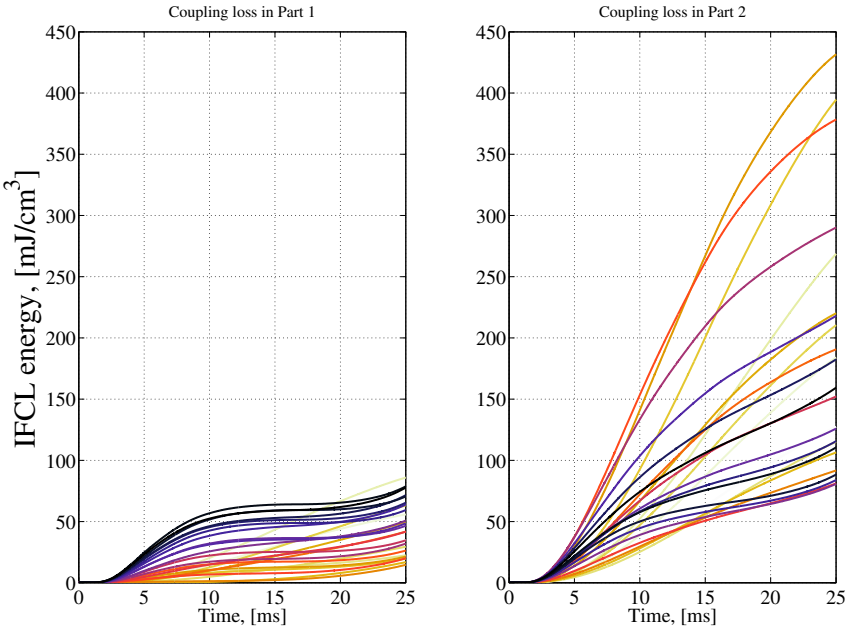

Figure 4.4: Total energy deposited during CLIQ discharge in the block–coil dipole magnet operating at nominal initial transport current and with nominal CLIQ parameters.

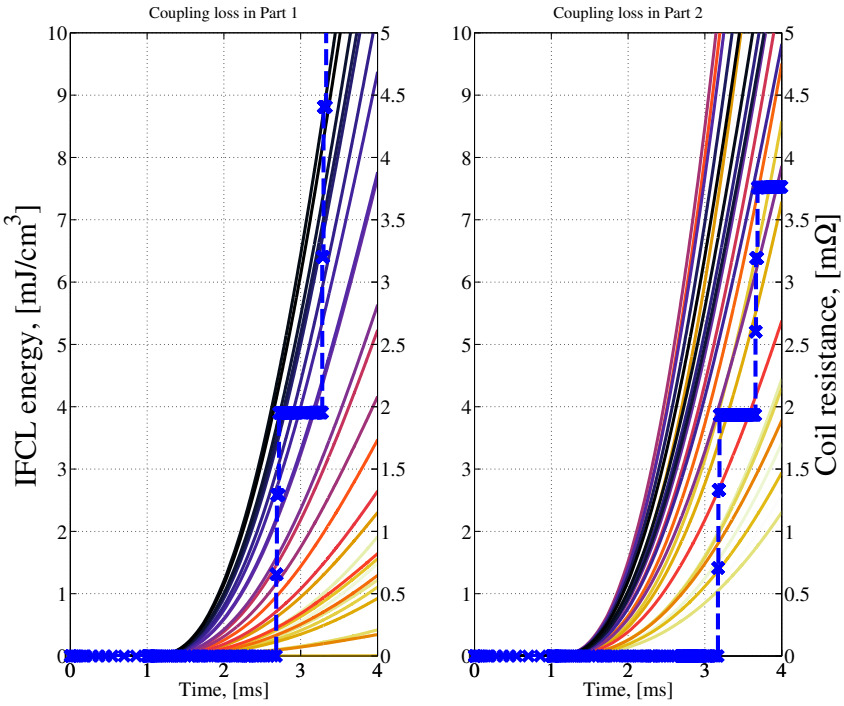

Figure 4.5: Total energy deposited during CLIQ discharge in the block–coil dipole magnet operating at nominal initial transport current and with nominal CLIQ parameters, together with the electrical resistance in the relevant electrical part as it develops in time.

4.1.2 Temperature Margin

The temperatures in the coil develops as shown in figure 4.6. Keeping in mind the temperature margin plot of figure 3.7, also here there is perfect agreement between the critical surface of the magnet and the simulated quench propagation[3]. Initially, the temperature rises only due to the deposition of IFCL[4]. Once a block quenches, the massive ohmic heat generation completely dominates the thermal development of the material. Note that the temperature rise in electrical part 2, in blocks that have yet to quench, is faster than the one in electrical part 1. This, of course, is because the IFCL is a lot higher in part 2 (about 2 to 3 times higher), giving a quicker heating.

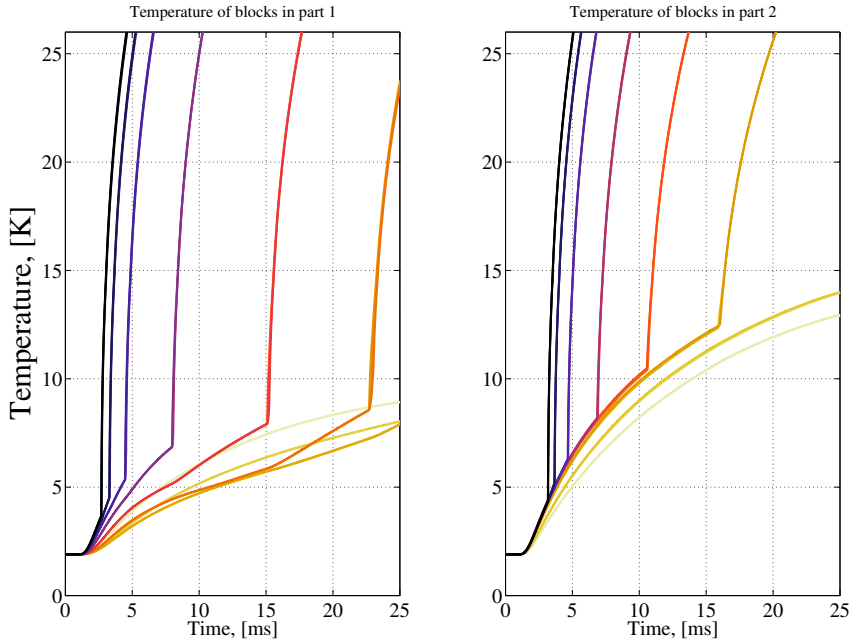

Figure 4.6: Development of the temperature in all blocks during CLIQ discharge in the block–coil dipole magnet operating at nominal initial transport current and with nominal CLIQ parameters.

4.2 Quick Note on Quench Heater Performance

In figure 4.7 the same CLIQ discharge from figure 4.1, but now including results from a simulation with the same magnet parameters, protected with Quench Heaters (QH), is shown. The two main parameters of the QH system are their coverage (how much of their total area actually consist of heat–generating material) and the thickness of the insulation between the QH strip and the coil's cables. It is very important to note that the QH simulations presented briefly in this section are only rough estimates, as there is no reliable way to check the validity of the simulation results for this magnet. They should, however, give an idea of the expected protection performance when applied to the block–coil.

[3]The plots for margins are calculated with different computer codes than the simulations, although the margin plot codes, of course, uses the same material parameters.

[4]And a small contribution from heat propagation, lowering the temperature of hotter blocks while increasing the temperature of colder blocks.

As is clear, the hot–spot temperature rises far too fast and high, and the magnet is not protected at all by QH at nominal initial transport current. The curve showing the discharging current for the QH simulation abruptly stops due to a condition set in the simulation software; when the hot–spot temperature reaches 500 [K] it is assumed that no further simulation is of interest.

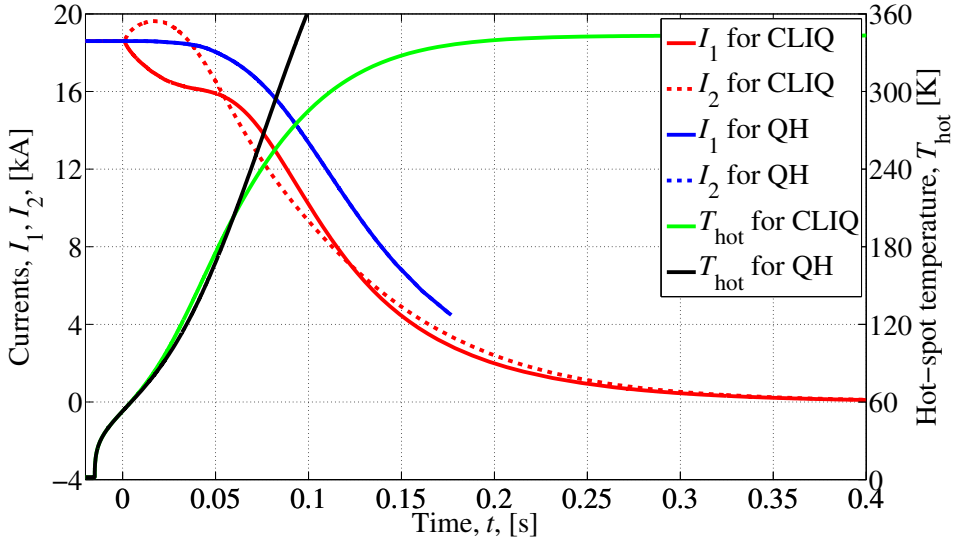

Figure 4.7: Discharge currents and hot-spot temperature development in the block–coil magnet during discharge of a CLIQ unit of parameters, $C_{\mathrm{CLIQ}} = 100$ [mF], $U_0 = 1000$ [V], and a quench heater circuit of 30% coverage and 50 [µm] insulation thickness, at nominal initial transport current.

The resistance development in the two cases are shown in figure 4.8. The QH are only able to start a quench in the coil after about 15 [ms], more than 10 [ms] after CLIQ. The initial resistance rise is also much slower and only picks up once heat propagation from quenched blocks has become substantial.

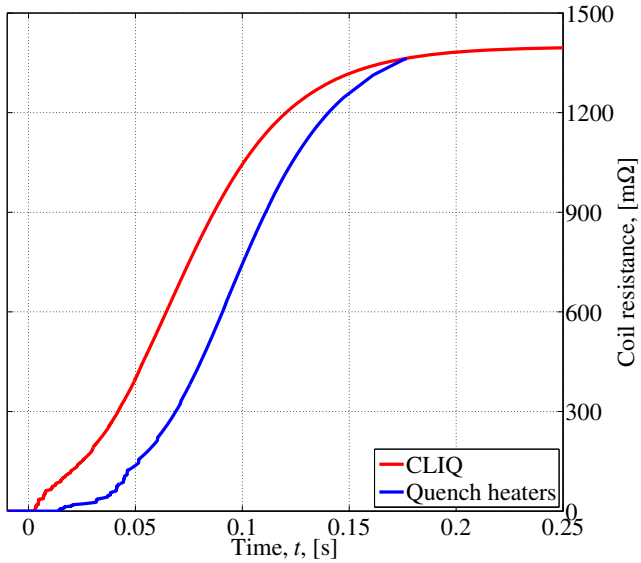

Figure 4.8: Coil resistance development in the block–coil magnet during discharge of a CLIQ unit of parameters, $C_{\mathrm{CLIQ}} = 100$ [mF], $U_0 = 1000$ [V], and a quench heater circuit of 30% coverage and 50 [µm] insulation thickness, at nominal initial transport current.

A simple parametric study of how the QH performance is affected by initial transport current in the magnet, coverage and insulation thickness is shown in figure 4.9 shows a very compact summary of these simulations. In the figure, for the nominal transport current (18.6 [kA]), none of the parameters for the QH provide sufficient protection. For the smallest insulation thickness, both 30 and 50% coverage manage to keep the hot–spot from blowing up only because the enthalpy margin to quench is extremely small at the short–sample current (by definition). From these results, it is clear that QH are nowhere near able to protect the magnet at any current level above about 65% of the nominal, and as such, the need for a better protection system is evident.

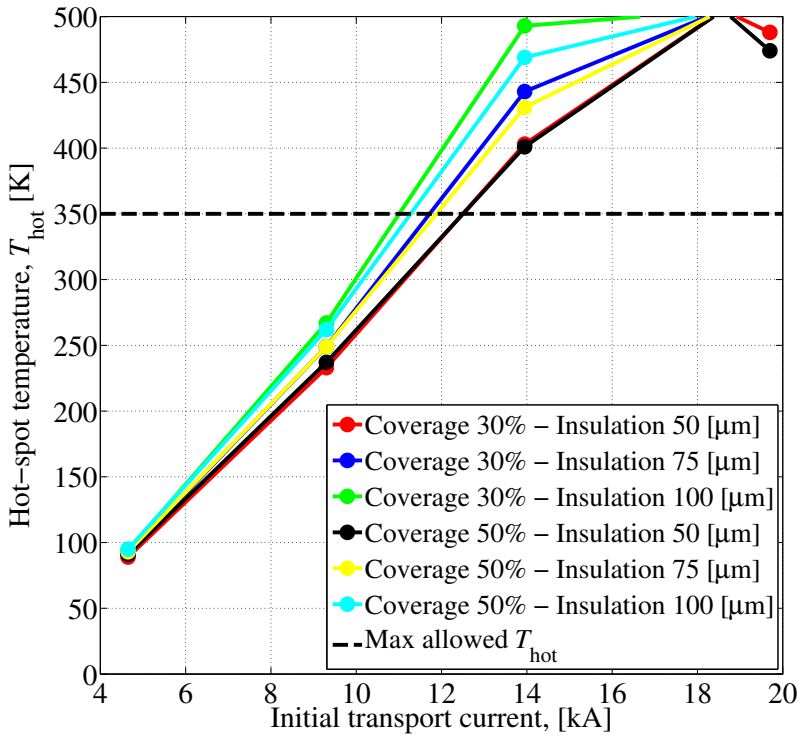

Figure 4.9: Summary of QH performance at all initial transport currents, and varying coverange and insulation thickness.

4.3 Effect of Varying Initial Transport Current

It is important that the protection system is able to keep the magnet from taking damage over a large range of operating conditions; notably, the system must protect the magnet also during current ramp–up and ramp–down in the phases of accelerator operation that require a magnetic field lower than the nominal. It is also necessary to protect the magnet during its commissioning, as training is an essential part of this stage[5].

Figure 4.10 shows how the currents in the magnet decay when the discharge happens at different initial transport current. The two notable features are that the oscillations are far less damped for lower initial transport current, and that the decay itself also decays with a much longer time–constant. The reason for this is found in figure 4.11. The electrical resistance of the coil rises both much later and much slower for a lower initial transport current than for a higher one. From the definition of the attenuation and then equation 2.7 it is clear that a lower resistance will give a much lower damping of the current, and taking also the damping factor into account, the oscillations themselves are also far less damped when the resistance is lower.

[5]Magnet training is a phenomenon where a magnet has better critical parameters after a quench than before — during operation the the coil moves a little bit under the magnetic forces it experiences. These movements release small amounts of frictional heat, enough to quench the magnet, but once one part of the coil has "settled" it no longer moves, and so, the magnet is now more resilient towards a quench during operation [7, p. 411][72, p. 81–82].

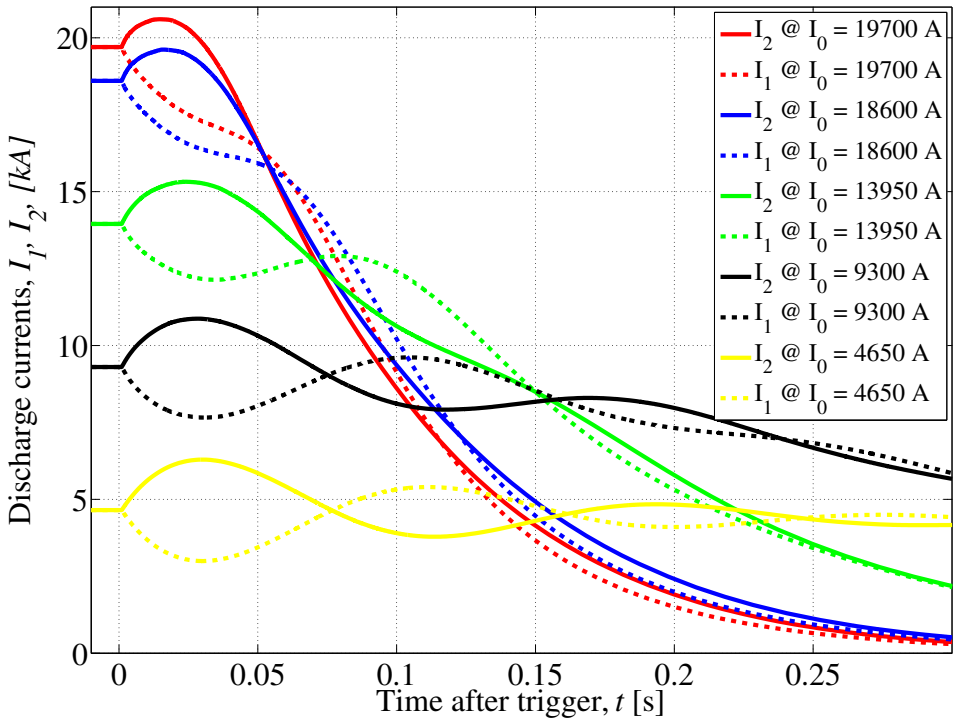

Figure 4.10: Discharge currents in the block–coil during discharge of a nominal CLIQ unit of parameters, $C_{\mathrm{CLIQ}} = 100$ [mF], $U_0 = 1000$ [V]. The initial transport current has been varied as such: 100 [A] below the short sample current, the nominal current, 75% of nominal current, 50% of nominal current and 25% of nominal current

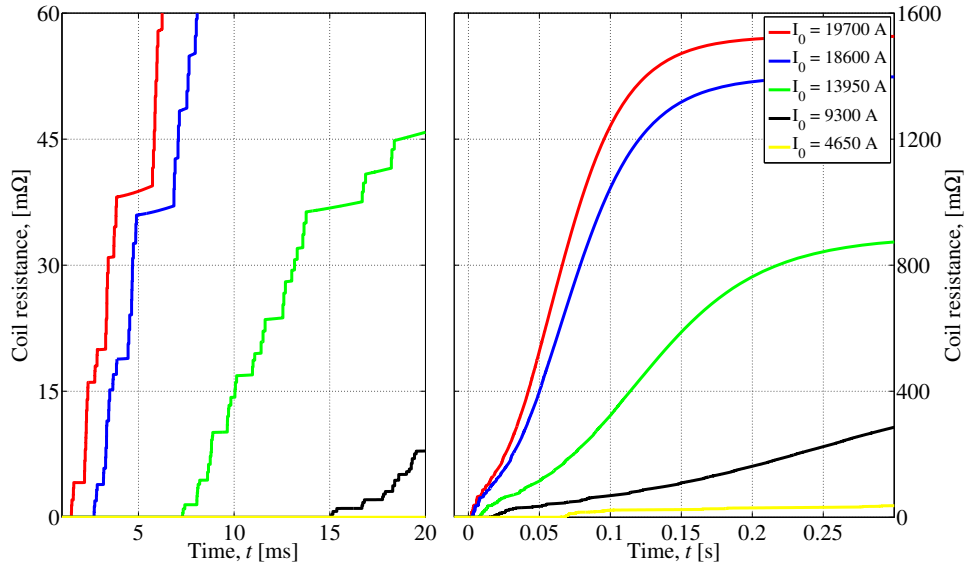

Figure 4.11: Resistance development in the magnet coil during discharge of a nominal CLIQ unit of parameters, $C_{\mathrm{CLIQ}} = 100$ [mF], $U_0 = 1000$ [V]. The initial transport current has been varied as such: 100 [A] below the short sample current, the nominal current, 75% of nominal current, 50% of nominal current and 25% of nominal current

At the higher transport currents two effects contribute to quick and high rise in coil resistance; firstly, the high current means, as discussed before, that a given strand in the coil requires only very little heat input to be driven into the normal state. Secondly, since the energy stored in the magnetic field is proportional to the square of the transport current, much more energy flows into the quenched parts of the coil, resulting in a faster temperature rise, which in turn gives a higher over–all coil resistance.

Despite this large difference in coil resistance development, potentially indicating that the magnet might be insufficiently protected at lower currents, the final hot–spot temperature is monotonically falling with initial transport current, as shown in figure 4.12. This means that the protection challenge for this magnet lies in the current ranges close to and above the nominal operating current.

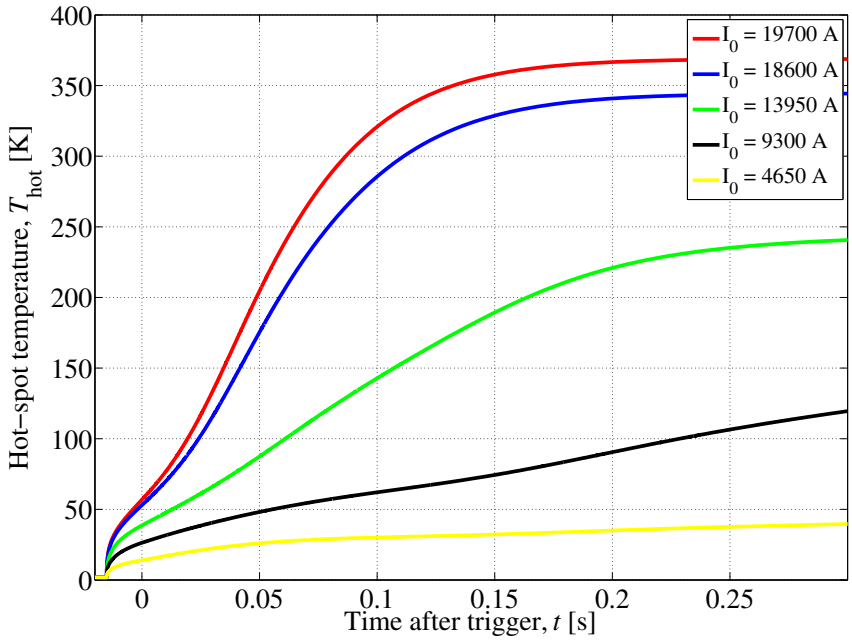

Figure 4.12: Hot–spot temperature development in the block–coil magnet during discharge of a nominal CLIQ unit of parameters, $C_{\mathrm{CLIQ}} = 100$ [mF], $U_0 = 1000$ [V]. The initial transport current has been varied as such: 100 [A] below the short sample current, the nominal current, 75% of nominal current, 50% of nominal current and 25% of nominal current

4.4 Effect of Varying CLIQ Parameters

Equation 2.7 indicates that the choice of CLIQ parameters will have a, potentially, large impact on the way the current oscillates, and figure 4.13 shows how the CLIQ current alone looks when discharging the unit into the block–coil magnet at the nominal initial transport current, for various CLIQ parameters.

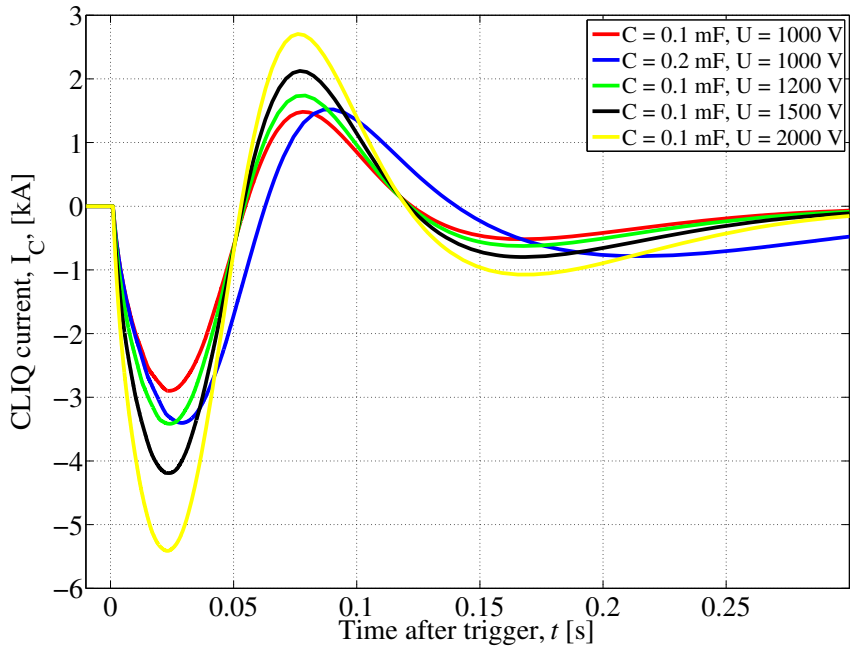

Figure 4.13: CLIQ current during discharge into the magnet coil operating at nominal initial transport current.

As predicted by equation 2.7, only the peak of the current is influenced by the voltage — a higher voltage gives a higher peak current, with the amplitude given by the 2000 [V] unit more or less twice that of the 1000 [V] unit. Theory predicts exactly twice the amplitude, but also the coil resistance development must be taken into account, as the time and speed of quench changes (as seen in figure 4.14). The attenuation is not very sensitive to the CLIQ voltage, as seen by the extrema occurring at the same times among the curves for varying voltage.

The curve for a larger capacitance also follows the predictions of equation 2.7; the larger capacitance somewhat increases the peak amplitude, but when taking into account that the damping factor changes a lot, the amplitude cannot increase as swiftly as for the voltage[6]. However, given the substantially changed damping of the circuit, the "dragging out" of the curve is as expected.

Looking, then, at figure 4.14, showing the coil resistance development for the different CLIQ parameters, as well as figure 4.15, showing the hot–spot temperature in the coil for the same discharges, two conclusions and a few remarks can be made.

Firstly, the difference in hot–spot temperature when changing the voltage or the capacitance by factors of two, is not substantial; only about 25 [K] separates the 1 and 2 [kV] cases, but constructing a system safe at 2 [kV] is a non–trivial problem given space restraints and sensitivity of other equipment in the circuit. Secondly, the quench development, and hence the coil resistance development, for the nominal and double capacitance cases, are very similar. The reason for this is that the initial $\mathrm{d}I/\mathrm{d}t$ stays the same for varying capacitance, which gives the same initial coupling loss.

[6] A larger capacitance gives a smaller oscillating frequency, which in turn means that the damping of the circuit (as compared to the nominal capacitance case) is closer to critically damped.

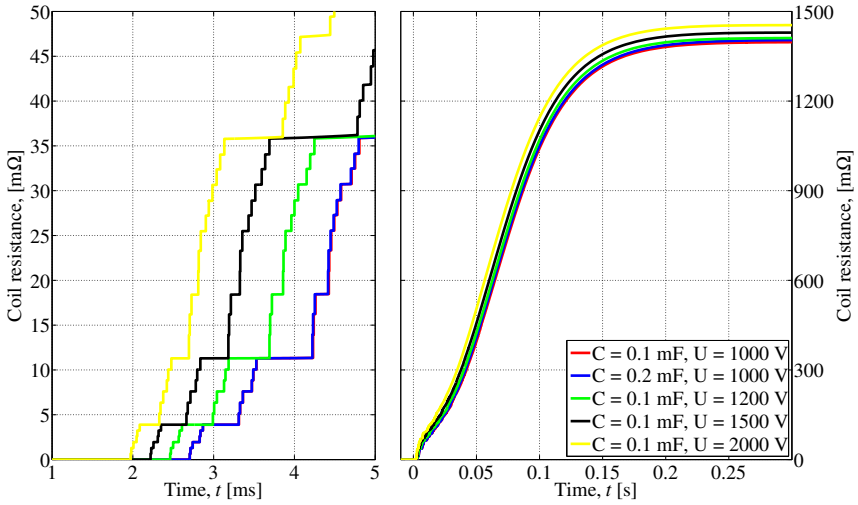

Figure 4.14: Coil resistance development during CLIQ discharge into the magnet coil operating at nominal initial transport current.

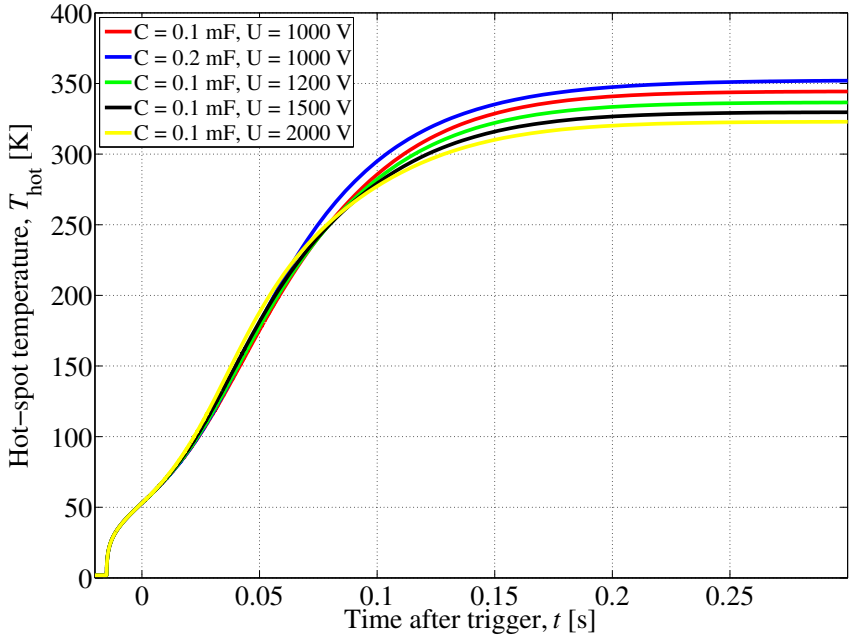

Figure 4.15: Hot–spot temperature development during CLIQ discharge into the magnet coil operating at nominal initial transport current.

Now, as per the theory presented, it would be expected that the hot–spot temperature of the magnet protected by a 200 [mF] CLIQ unit should be lower — it has the same initial $\mathrm{d}I/\mathrm{d}t$, but a slightly higher peak current and thus maintains same $\mathrm{d}I/\mathrm{d}t$ for a somewhat longer time as compared to the nominal CLIQ parameters. However, as seen, the hot–spot temperature actually goes up a little with the larger capacitance. This is explained by looking at figure 4.16.

For a higher capacitance, the oscillations decay slower than for a smaller capacitance;

this means that the hot–spot will experience heat deposition from the CLIQ unit for a longer time and of a larger magnitude. The figure shows the heat deposition from all sources into the hot–spot block of the coil, and it is clear that the time–integrated heat input is larger for the 200 [mF] CLIQ unit than the 100 [mF] unit.

Briefly; the peaks of deposited heat goes up with the CLIQ voltage, but since the quench also initiates sooner, as seen in figure 4.15, the current decays faster (see figure 4.17), and as such, the heat deposition lasts for a shorter time, with the over–all effect that the time–integrated deposition is smaller for higher voltage.

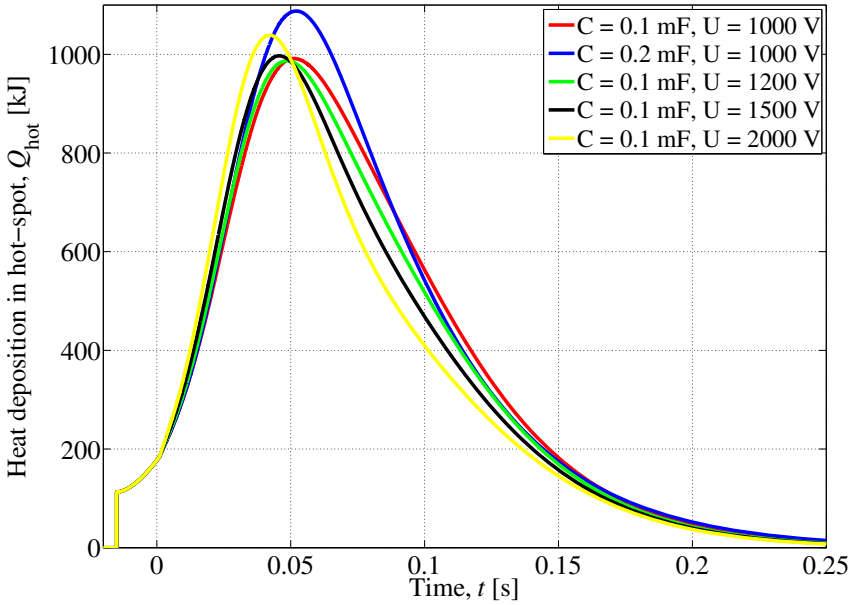

Figure 4.16: Heat deposition from all sources into the hot–spot during CLIQ discharge into the magnet coil operating at nominal initial transport current.

Lastly, the complete current decays for the five different sets of CLIQ parameters are shown in figure 4.17. As predicted by the very similar coil resistance curves and confirmed by very similar hot–spot temperatures, the current decays are not notably different, giving similar quench loads.

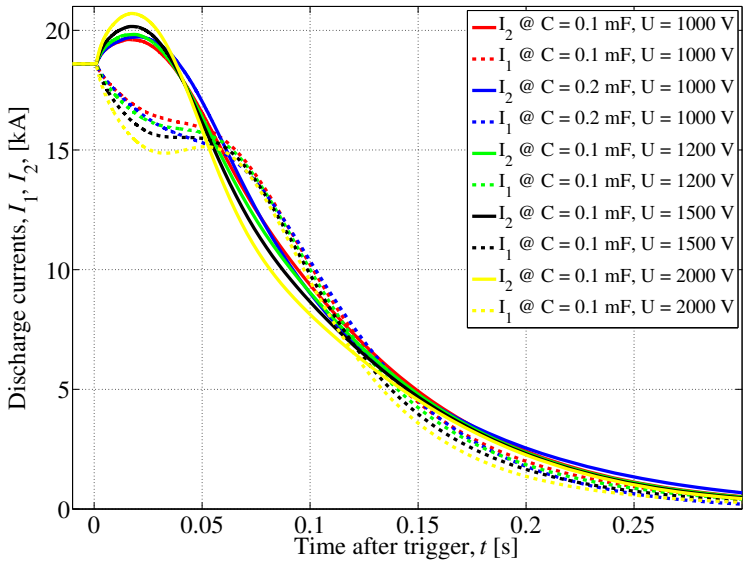

Figure 4.17: Discharge currents for various CLIQ parameters, into the reference coil design. Note that all simulations were run at the same initial transport current, and that the nominal design parameters for the CLIQ unit are $C_{\mathrm{CLIQ}} = 100$ [mF], $U_0 = 1000$ [V].

4.4.1 Summary — CLIQ Parameters

The results for varying CLIQ parameters and initial transport currents are summarised in figure 4.18. It is clear that by increasing the charging voltage of the CLIQ unit, it is possible to gain about 25 [K] in hot–spot; for 2000 [V] the hot–spot ends up at around 325 [K]. However, when taking also other relevant currents into account, the CLIQ system in its chosen configuration is not able to protect the magnet — at the short–sample current the hot–spot temperature is too high, and other measures will be needed to provide sufficient protection of the block–coil dipole magnet.

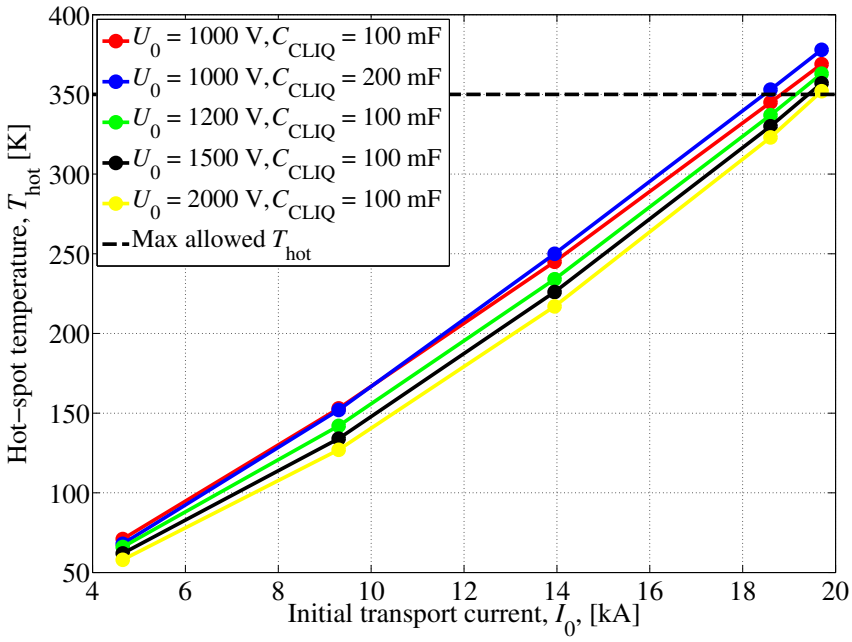

Figure 4.18: Hot–spot temperature for various CLIQ parameters and initial transport currents, into the block–coil dipole magnet. Note that nominal initial transport current is 18.6 [kA], and that the nominal design parameters for the CLIQ unit are $C_{\mathrm{CLIQ}} = 100$ [mF], $U_0 = 1000$ [V].

4.5 Effect of Varying the CLIQ Configuration

As discussed in chapter 2, one can also vary the way the CLIQ unit is connected to the magnet coil. The connection configurations are abbreviated as such,

PP	Pole–Pole
LL	Layer–Layer
LL Rev	Layer–Layer Reverse
CL	Crossed Layer

and the resulting current polarities are shown in figure 3.8.

Figure 4.19 shows the CLIQ currents resulting from discharging a CLIQ unit of nominal parameters ($C_{\mathrm{CLIQ}} = 100$ [mF], $U_0 = 1000$ [V]) into the block–coil for all four CLIQ configurations. The oscillation frequency for LLrev, LL and CL are very similar, as the equivalent inductance of these circuits are almost the same (recall table 3.4). Apart from the difference in frequency between the PP and the others, there is a large difference in the peak current; this is, as seen in equation 2.7, because the peak current has a certain proportionality to the oscillation frequency, and as such, the PP, having the lowest frequency, will have a lower peak current, even if the CLIQ unit itself is the same.

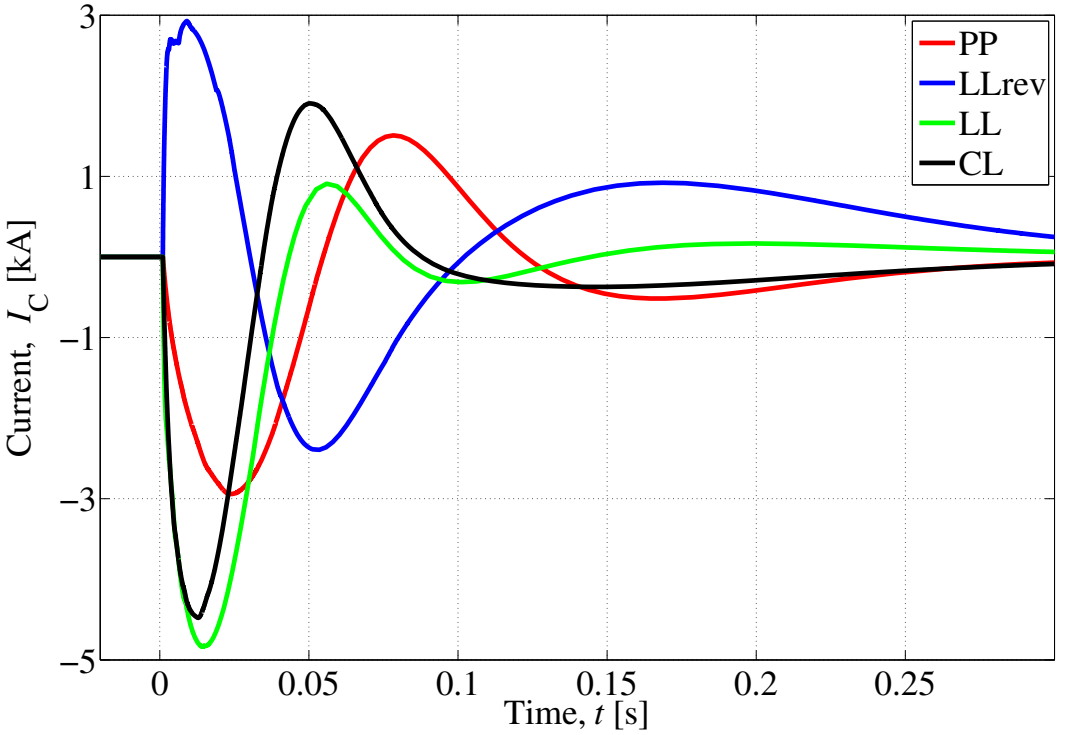

Figure 4.19: CLIQ currents for the four CLIQ configurations, discharged into the 16 [T] block–coil dipole magnet. Note that all simulations were run at the same initial transport current, and that the nominal design parameters for the CLIQ unit are $C_{\mathrm{CLIQ}} = 100$ [mF], $U_0 = 1000$ [V].

Figure 4.20 gives a compact representation of the effect of changing the CLIQ configuration. Both the LL and the CL configurations give approximately 40 [K] gain in the hot–spot temperature with respect to the PP, while the LLrev an additional 10 to 20 [K]. The reason why the LLrev outperforms the LL configuration is that, as discussed in section 2.4, by reversing the charging voltage, the initial positive current will flow into the parts of the magnet coil with the lowest enthalpy margin to quench, giving a faster coil resistance growth and thus a smaller hot–spot temperature.

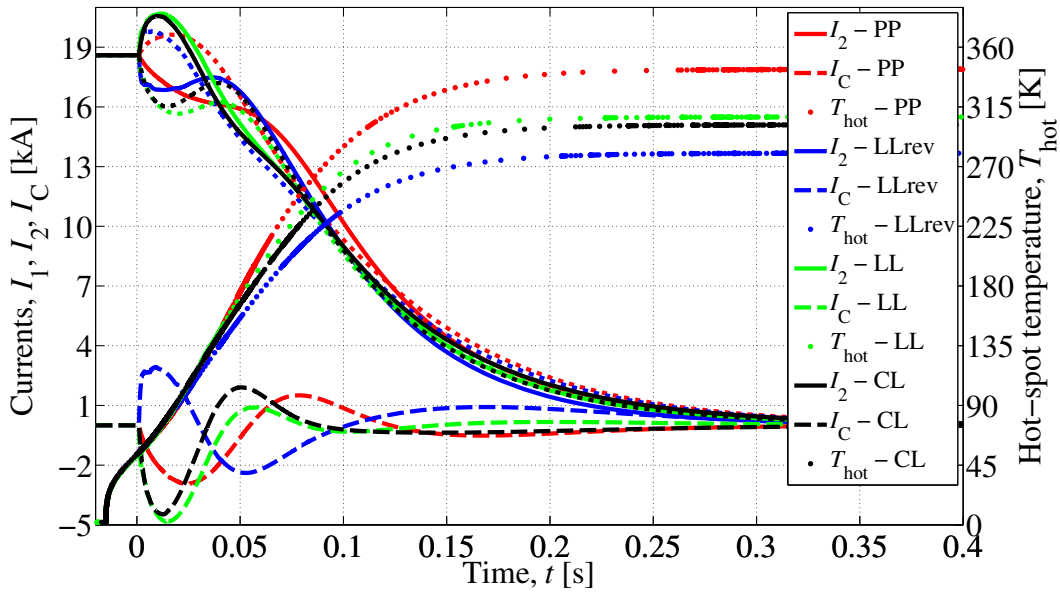

Figure 4.20: Discharge currents and hot–spot temperature development in the block–coil for the four CLIQ configurations. Note that all simulations were run at the same initial transport current, and that the nominal design parameters for the CLIQ unit are $C_{\mathrm{CLIQ}} = 100$ [mF], $U_0 = 1000$ [V]. I_2 indicates the current in the secondary discharge branch, while I_1 is not given its own legend entry for size reasons. I_C denotes the current in the CLIQ lead during the discharge.

In figure 4.21 the coil resistance development is plotted against time for two different time–scales. In the figure showing the CLIQ currents, there are large irregularities visible for the LLrev/ — they are explained by this plot; while the LL does see a quench marginally sooner than the LLrev the rise in resistance for the LLrev is faster[7]. At 2.5 [ms], the LLrev is able to keep the resistance growing, while the LL is stagnating somewhat — this small difference in time, giving a difference of about 50% in the resistance is enough to substantially change the damping of the circuit, as well as altering the coupling currents, and by that the inductance of the circuit as well[8]. The same sort of irregularities arise also for the LL, but they are not as strong and visible on the chosen scale.

[7]The small time–difference can probably not be taken as a reliable result, nor is it significant, so for all practical purposes, the LL and LLrev are seen as initiating the quench at the same time.

[8]In a part of the coil that has quenched, the coupling currents no longer flow, given that they rely on a superconducting phase being present.

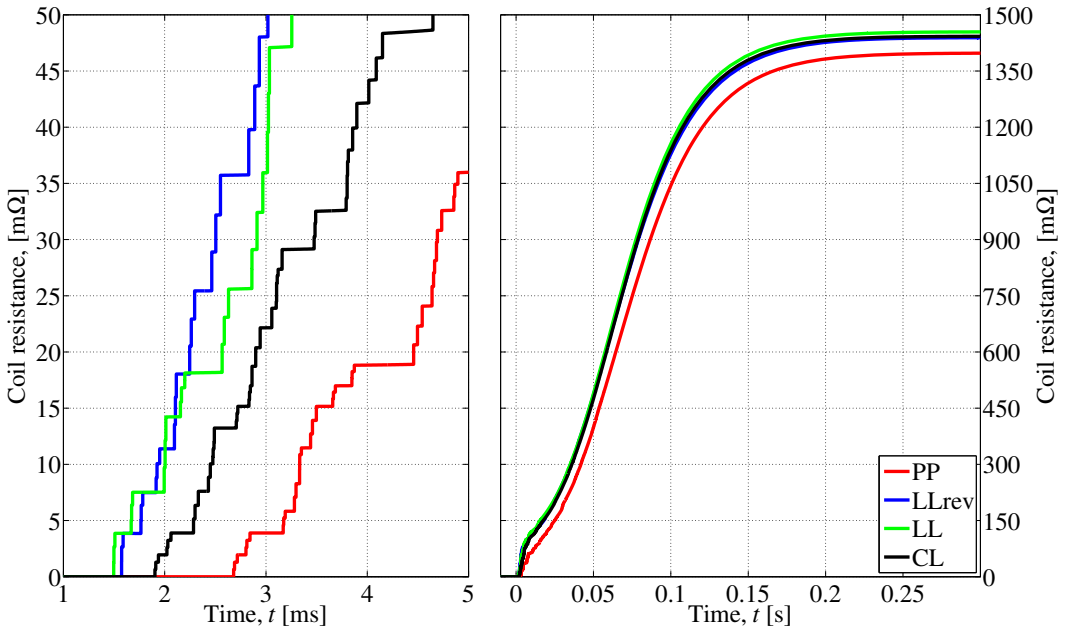

Figure 4.21: Coil resistance development during discharges with the four different CLIQ configurations, into the block–coil. Note that all simulations were run at the same initial transport current, and that the nominal design parameters for the CLIQ unit are $C_{\mathrm{CLIQ}} = 100$ [mF], $U_0 = 1000$ [V].

The time of quench for each individual block of the magnet is shown in figure 4.22[9]. Two particularly interesting things are visible in the plot; 1) although the average time to quench a block of the coil is lower for the LLrev as compared to the LL, there are blocks that are far slower to quench as well. This is because for the LLrev, the inner layers of the coil are brought further away from the critical surface, and as such require more energy input to quench. Combining this with the fact that the over–all temperature of the coil is lower, and thus the heat transfer between blocks is lower, the last few blocks to quench take a long time to build up the necessary energy to overcome the margin. 2) the asymmetry in the PP and CL when looking at upper versus lower pole (more visible for CL); just as for the difference between LL and LLrev, the initial polarity of the discharge plays a role for these two CLIQ configurations as well. For the CL, the outer layer of the upper pole and the inner layer of the lower pole (parts 1 and 4) receive an initial negative current, which takes it away from the critical surface — it takes longer to quench it. In the PP the same is true for the upper versus lower pole, only not as pronounced.

[9]Recall the grouping of individual strands into blocks, presented in section 3.5.1.

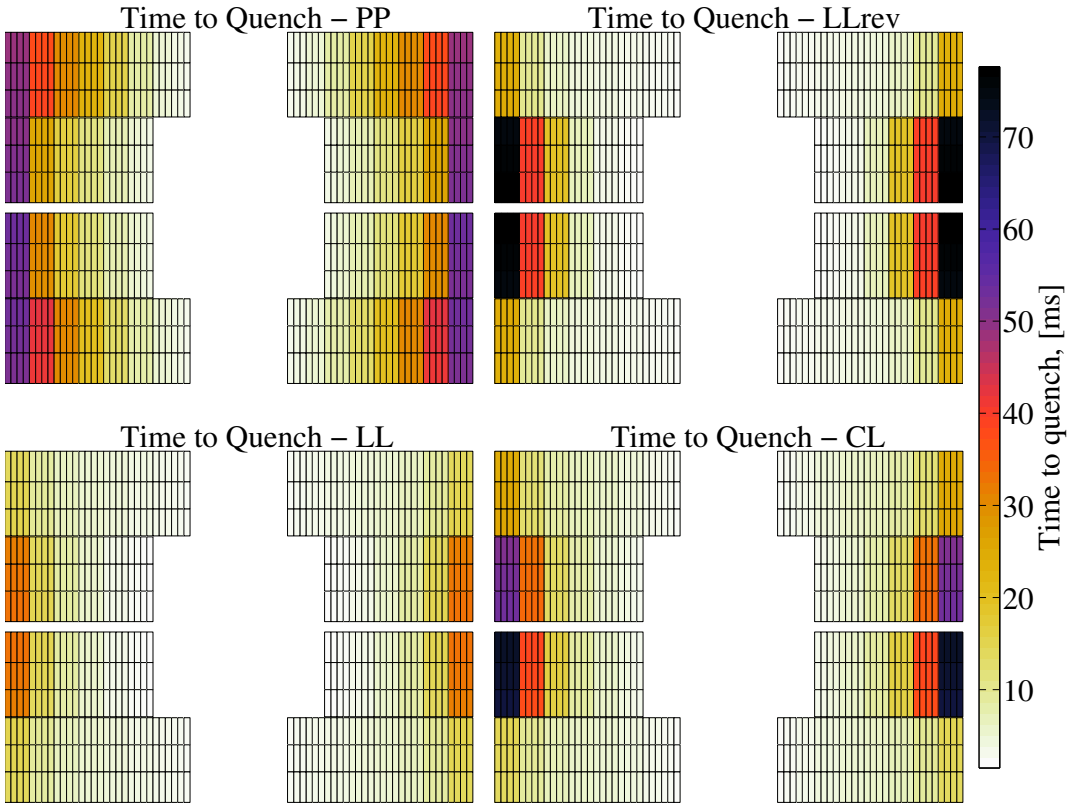

Figure 4.22: The time of quench in each individual block of the coil model during discharges with the four different CLIQ configurations, into the block–coil. Note that all simulations were run at the same initial transport current, and that the nominal design parameters for the CLIQ unit are $C_{\mathrm{CLIQ}} = 100$ [mF], $U_0 = 1000$ [V].

The irregular CLIQ current during the LLrev discharge, as this is what causes the necessary magnetic field–change to generate IFCC, influences the loss deposited in the coil. Figure 4.23 shows the IFCL as it develops during discharges with the four CLIQ configurations. As mentioned before, around the 2.5 [ms] mark, the CLIQ current flattens out for the LLrev, and as such, for a time on the order of about 10 [ms], the $\mathrm{d}I_{\mathrm{C}}/\mathrm{d}t \simeq 0$. This means that, through the time–constant of the IFCC, the loss generated will fall towards zero. For the LL, the same general behaviour occurs, but only later, as the initial current development is smoother, and so it reaches its peak a little later and maintains power generation somewhat longer. The CL and PP have much smoother discharges, and so, have more regular IFCC. Given that the PP CLIQ current oscillates much slower than the others, it also reaches a far lower power.

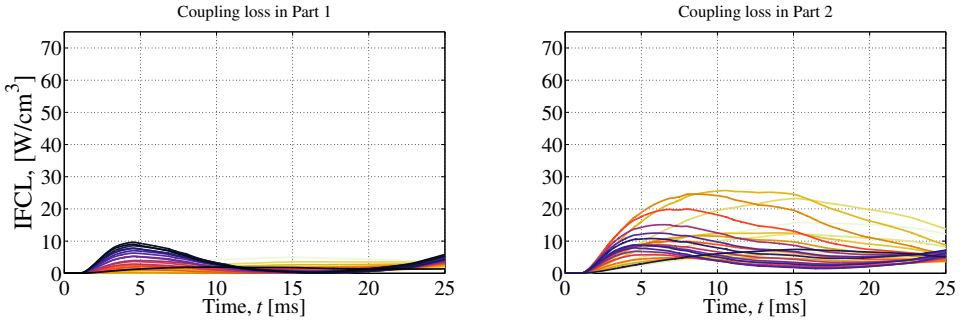

(a) PP CLIQ configuration.

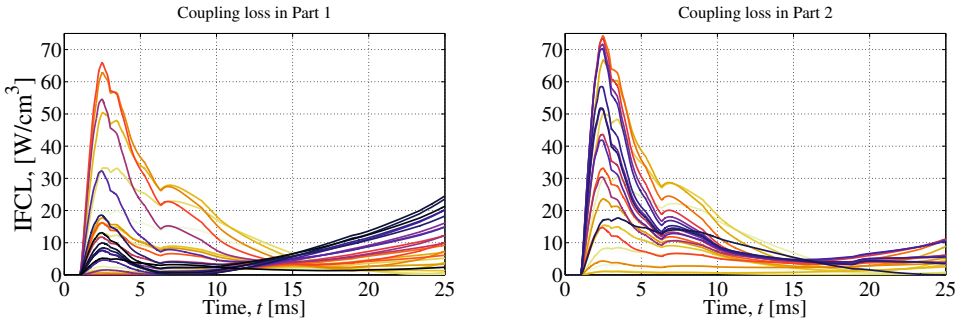

(b) LLrev CLIQ configuration.

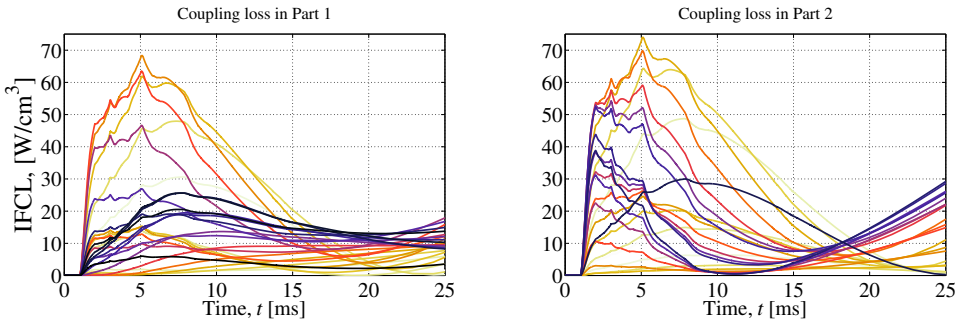

(c) LL CLIQ configuration.

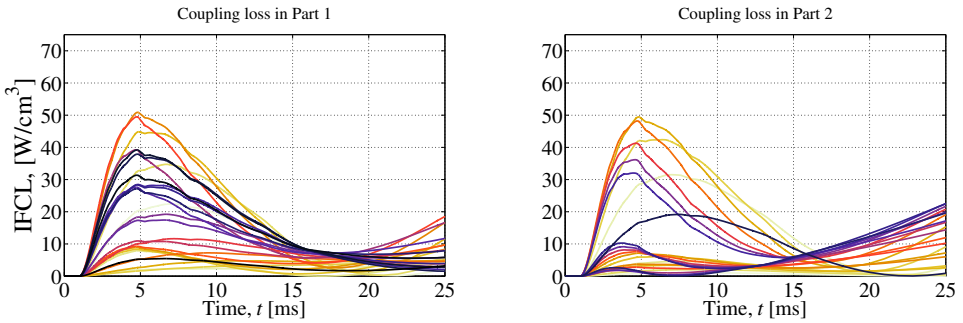

(d) CL CLIQ configuration.

Figure 4.23: IFCL in the outer and inner layers of the block–coil, for varying CLIQ configuration.

4.5.1 Summary — CLIQ Configurations

Figure 4.24 shows a summary of the quench performance of the already presented CLIQ configurations for various initial transport currents. In addition to this, the hot–spot temperature reached when the entire coil has been quenched simultaneously at $t = 1$ [ms]is shown. This ideal protection case, then, assumes that only the quench detection and validation time passes, and after that, all the blocks in the coil are quenched (with resistance development as usual). The Layer–Layer Reverse configuration is impressively close to the ideal case, and it is also seen that the Pole–Pole configuration is unable to protect the magnet coil above the nominal current, such as is required for the magnet training.

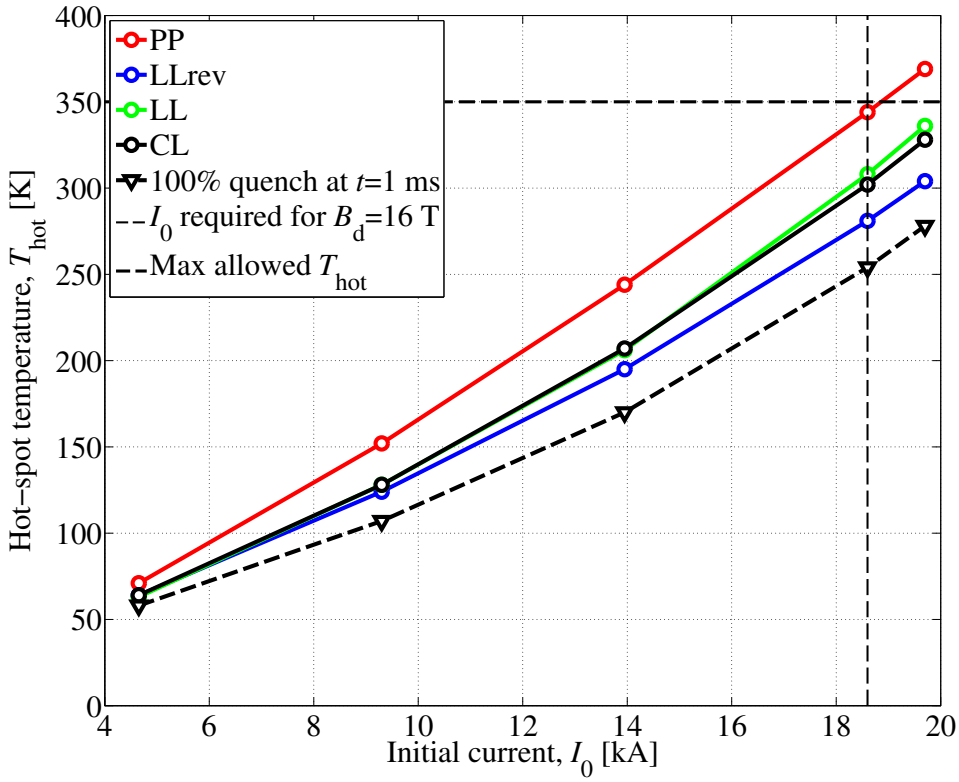

Figure 4.24: Hot–spot temperature for the four CLIQ configurations discharged into the block–coil dipole magnet, including the artificial quenching of the entire coil at $t = 1$ [ms]. Note that the nominal design parameters for the CLIQ unit, $C_{\text{CLIQ}} = 100$ [mF], $U_0 = 1000$ [V], are used.

4.6 Effect of Conductor Properties — Varying RRR and Filament Twist Pitch

Figure 4.25 shows how the hot–spot temperature is influenced by the choice of RRR and filament twist pitch for all four CLIQ configurations. As is evident, for small twist pitches, the dependency of the temperature on the RRR is quite small — the hot–spot temperature is mostly determined by the twist pitch as it determines the IFCL, which in turn determines how fast the coil quenches. The larger twist pitches do seem good design choices purely based on these results, but, as indicated in section 1.4, a larger twist pitch means that the

filaments are more coupled and thus at higher risk of flux jumps. For even larger twist pitches than these, as suggested in section 2.2, the IFCL will start falling, and the CLIQ systems ability to protect the magnet deteriorates. The RRR influences the hot–spot by changing the resistance of the material — large RRR means that the material has a much larger resistivity early on, at low temperatures, and so, the magnet current decays somewhat faster, giving a lower hot–spot temperature.

For the lower twist pitches (10–17.5 [mm]), that are more likely to be used in a magnet, due to stability issues, the temperature ranges from highest to lowest within a CLIQ configuration is practically the same, 30 [K], and there is a larger gain in hot–spot temperature from changing the CLIQ configuration used than to alter the strand parameters.

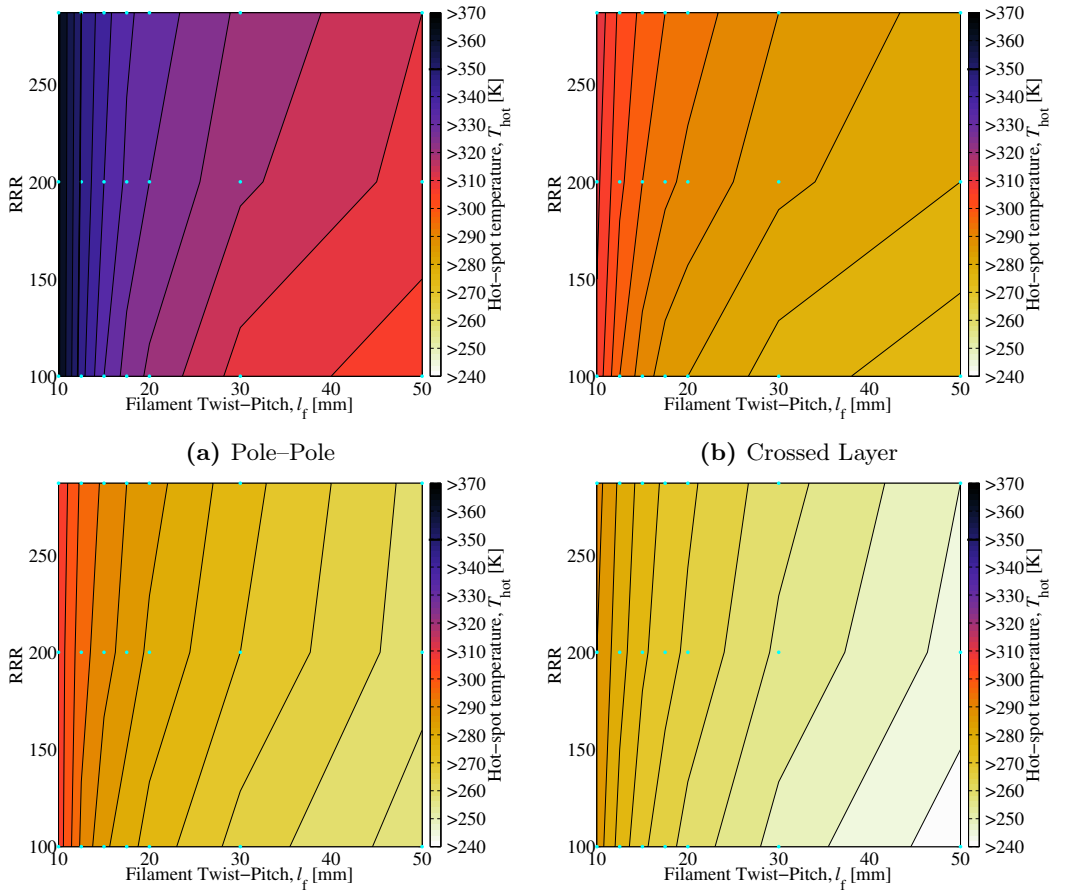

(a) Pole–Pole

(b) Crossed Layer

(c) Layer–Layer

(d) Layer–Layer Reverse

Figure 4.25: Hot–spot temperature at nominal initial transport current for varying RRR and filament twist pitch. Note that the turquoise dots indicate the actual data points while the gradient has been obtained by interpolation in MATLAB.

4.7 Effect of Conductor Properties — Varying Fraction of non–Copper

Each strand of a cable is, as discussed in chapter 1 made up of a combination of superconductor and stabiliser, where the stabiliser material is copper for the strands considered here. Due to the reaction process used to create Nb_3Sn (see section 1.6.4) it is not exactly known how large the true fraction of Nb_3Sn is, as the process will give somewhat different densities along the strand. Therefore, it is customary to refer to the fraction of non–Copper when speaking of the approximate/average fraction of SC in the strands.

By changing the amount of copper in the strands, the thermal behaviour of the coil changes substantially; figure 4.26 shows the coil resistance and hot–spot temperature development in the block–coil during discharges of a nominal CLIQ unit, at the magnet's nominal initial transport current.

A smaller copper content (and, thus, larger non–Copper content) means that the quenched strand has a smaller current carrying cross section, which means a higher electrical resistance[10]. This gives a faster discharge of the magnet current. However, the heat capacity of the composite is also lowered along with the copper content, so that the ohmic losses (as well as the IFCL generated by CLIQ) may cause a very large hot–spot temperature. This is seen in the figure, as the curves for larger than nominal non–Copper fraction (the black and yellow curves) see growing hot–spots[11].

During operation, however, a smaller copper fraction gives the benefit of a larger margin to quench, since less copper means more SC. More SC means that the current density falls, as the total current in the magnet will remain the same. This moves the operating point of the magnet further away from the critical surface, and thus, the magnet is more stable against outside interference, such as beam–loss and heat–leaks.

The opposite is true for larger copper content (and, thus, smaller non–Copper content); the resistance is lowered, given the larger cross section of current carrying material after the quench, and the hot–spot likewise, as the heat–capacity of the composite grows. This is seen with the blue and red curves in the figure.

This, of course, will mean that the magnet has a smaller margin to quench, as the current density in the SC is increased, and eventually the magnet is so susceptible to outside energy input that it will be useless in operation.

[10] Recall that the SC practically leads zero current once it has been driven to the normal state.
[11] The nominal non–Copper fraction is 55%, seeing as the nominal copper fraction is 45%.

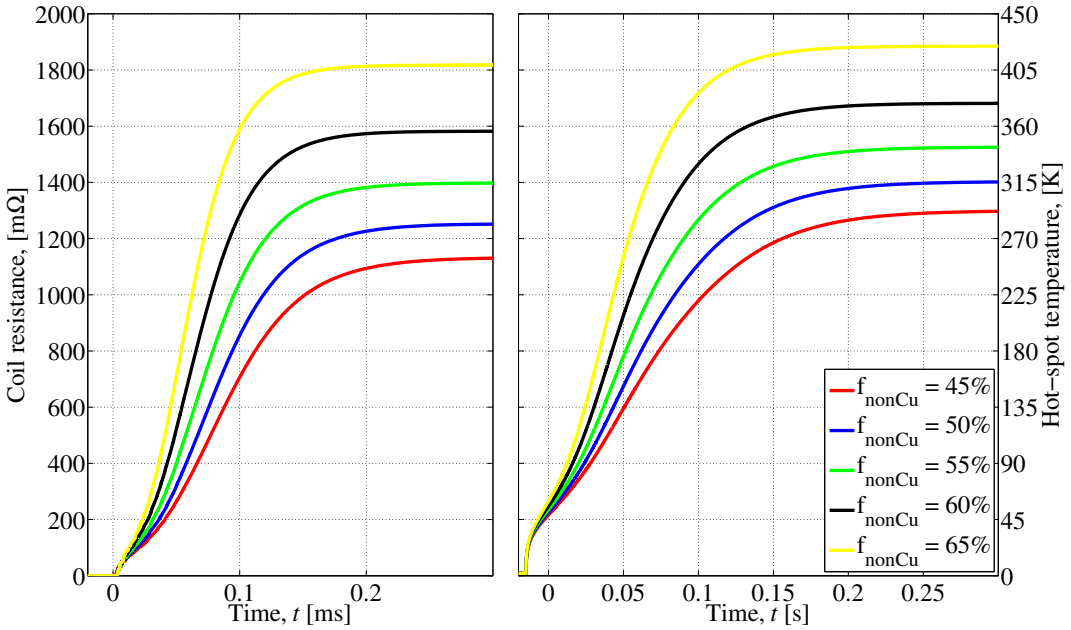

Figure 4.26: Coil resistance and hot–spot temperature development for varying fractions non–Copper in the strands of the block–coil. Note that all simulations were run at the same initial transport current, and that the nominal design parameter is $f_{\mathrm{nonCu}} = 55\%$.

The discharge currents will, of course, be influenced by the difference in resistance, and figure 4.27 shows the currents flowing in the block–coil for varying fraction of non–Copper. Since the resistance is larger for larger non–Copper contents, the current in the magnet will decay faster, and thus, the quench load is lower the lower the amount of Copper. However, the quench load is not a good measure to compare the hot–spots anymore, seeing as the thermal properties of the composite are now very different for the varying Copper contents, meaning that the Γ–function from section 1.8 is different.

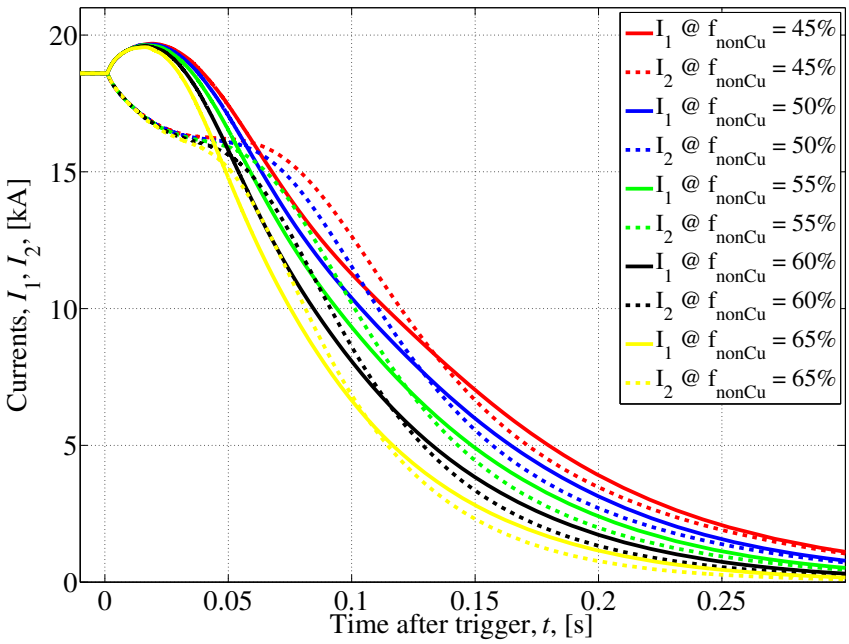

Figure 4.27: Discharge currents for various fractions of non–Copper in the strands of the block–coil. Note that all simulations were run at the same initial transport current, and that the nominal design parameter is $f_{\mathrm{nonCu}} = 55\%$.

4.7.1 All CLIQ configurations

The same simulations have been run for the three other CLIQ configurations, and the results are given in figure 4.28. The LLrev is clearly the best when considering the hot–spot temperature, but all the configurations can be made sufficiently good by increasing the amount of copper in the strands. Barring the limitations mentioned above, regarding the risk of having too little superconductor in the composite, reducing the fraction can be a viable way to improve the protection performace.

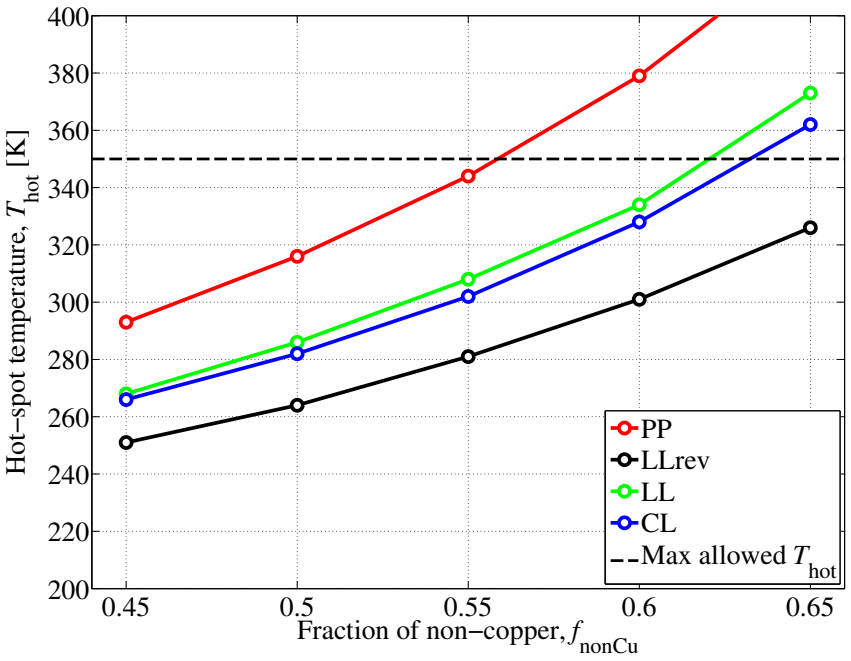

Figure 4.28: Hot–spot temperature in the block–coil for all four CLIQ configurations and varying fraction of non–Copper. Note that all simulations were run at the same initial transport current, and that the nominal design parameter is $f_{\text{nonCu}} = 55\%$.

4.8 Effect of Conductor Properties — Varying the Quality of the Superconductor

As discussed in section 1.2.5 the amount of pinning centres for the vortices in the SC is of large importance to the actual applicability of a given material — a larger number of pinning centres and/or pinning centres with larger pinning force will allow a larger current density in the material, and thus a larger magnetic field.

In equation 1.11 there is a parameter C_0 that scales the critical current density of Nb_3Sn. This parameter relates to the pinning in the material, and increasing this parameter, then, is akin to increasing the number/force of pinning centres.

By increasing the critical current density but keeping the operating current density (keeping the field in the aperture the same), the magnet becomes harder to protect, because it is now further away from the critical surface.

When improving the superconductors pinning properties it is possible to decrease the amount of SC in the strands, as the operating current density can be increased so as to maintain the same magnetic field — the effect of changing both the C_0 parameter as well as the fraction of non–Copper is shown in figure 4.29.

The hot–spot temperature rises with a larger C_0 and larger fraction of non–Copper, as expected. Note the empty corner for low C_0 and non–Copper fraction — here, the amount of superconductor in the strands is not sufficient for stable operation, as the magnet quenches during the current ramp up to its nominal value. This, then, means that the magnet will not be usable in an actual machine.

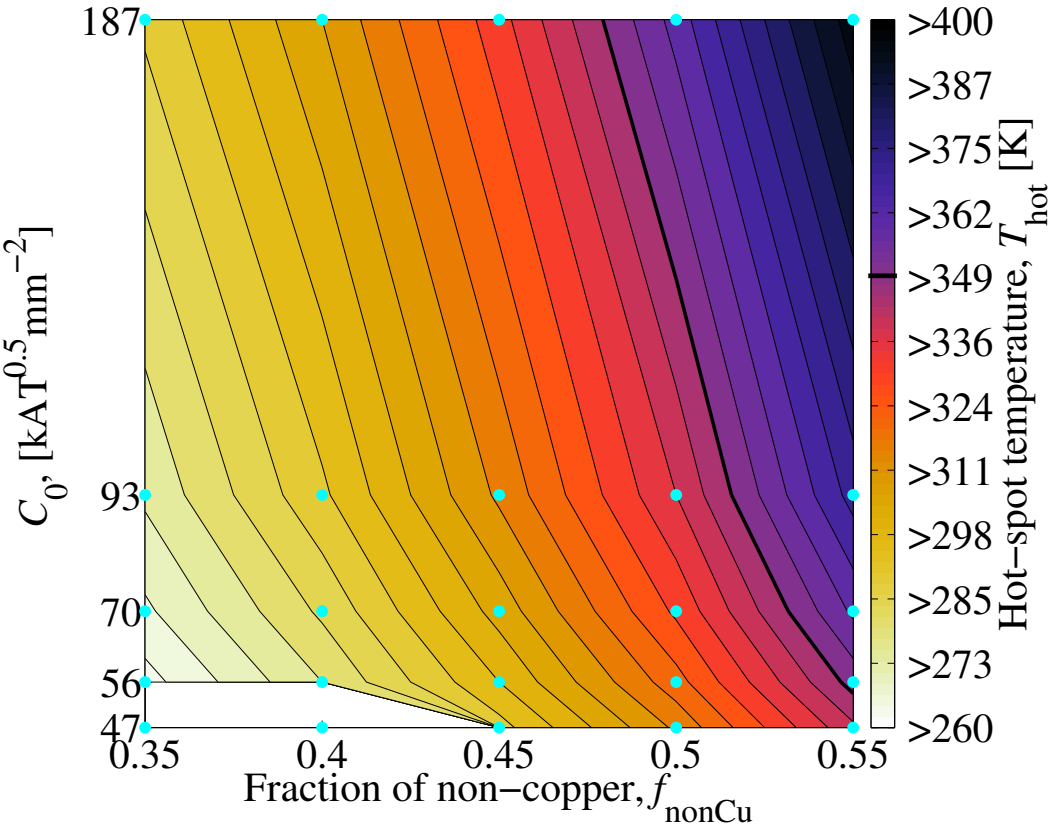

Figure 4.29: Hot–spot temperature in the block–coil for varying fraction of non–Copper and pinning properties of the superconductor. Note that all simulations were run at the same initial transport current of 18.6 [kA], the nominal design parameter for fraction of non–Copper is $f_{\text{nonCu}} = 55\%$, and the nominal design parameter for pinning properties of the superconductor is 47 [kA T$^{0.5}$ mm^{-2}].

In figure 4.30 the coil resistance development is shown for the varying pinning coefficients, at the nominal fraction of non–Copper. As seen, the resistances in the coil grow very similarly, with the difference being that the initial quench sets in later for a better SC, and the growth is slower, since all parts of the coil now need more energy input to breach the critical surface.

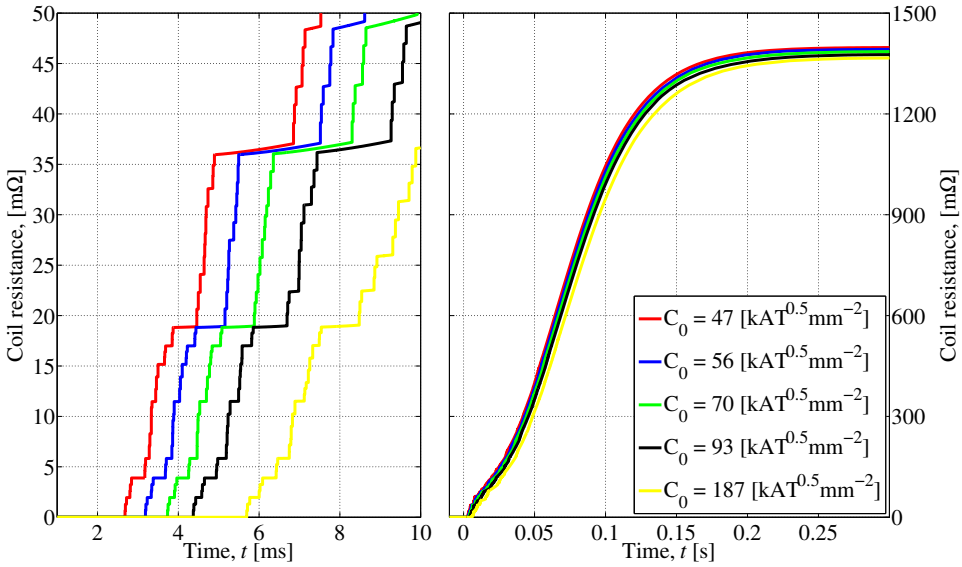

Figure 4.30: Coil resistance development in the block–coil for varying fraction of non–Copper and pinning properties of the superconductor. Note that all simulations were run at the same initial transport current, 18.6 [kA], and that the fraction of non–Copper is at its nominal value of $f_{\mathrm{nonCu}} = 55\%$. The nominal design parameter for pinning properties of the superconductor is 47 [kA $\mathrm{T}^{0.5}$ mm^{-2}].

With a better superconductor it is also, of course, possible to keep the fraction of non–Copper the same, and by that aiming at increasing the operating margin instead of reducing the hot–spot temperature[12]. Figure 4.31 shows how the short sample current of the block–coil changes with improvements in the superconductor's pinning properties. At its nominal value, the margin between the needed operating current and the short sample current is about 6%, while a superconductor with pinning properties given by a quadrupling of the scaling factor C_0 to 186 [kA $\mathrm{T}^{0.5}$ mm^{-2}], gives a margin of almost 24%.

[12]Remember that this improvement does raise the hot–spot temperature, so a balance must be struck.

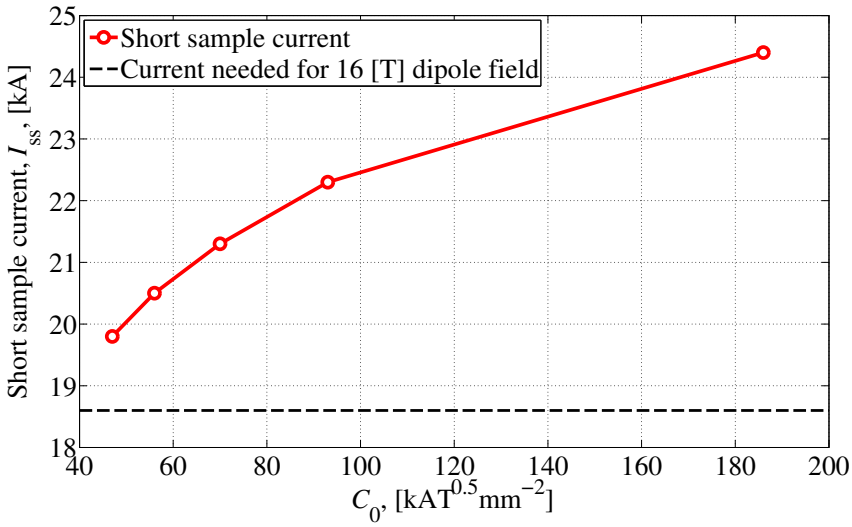

Figure 4.31: Short sample current in the block–coil for varying pinning properties of the superconductor. Note that the fraction of non–Copper is at its nominal value of $f_{\text{nonCu}} = 55\%$. The nominal design parameter for pinning properties of the superconductor is 47 [kA T$^{0.5}$ mm^{-2}].

4.9 Conclusions

With this, the initial study of the 16 [T] block–coil dipole magnet is done, and the conclusions are quite clear — by changing the charging voltage of the CLIQ unit, it is possible to achieve the desired level of protection at nominal transport current, with a hot–spot around 325 [K] for a charging voltage of 2 [kV]. However, during magnet commissioning, when training will be necessary, the protection is insufficient for currents approaching the short–sample current, as the hot–spot reaches 350 [K], even for a charging voltage of 2 [kV].

If employing the LLrev configuration the hot–spot temperature is kept well within the desired limits for all relevant current levels, with 300 [K] at short–sample current, and falling monotonously with transport current. Both LL and CL are viable but reach somewhat higher hot–spot temperatures than LLrev, with 325 [K] for both at short–sample current, and falling with initial transport current. The PP can only protect the magnet if other parameters are changed as well.

Increasing the copper content of the strands gives a similar gain in protection performance as changing the CLIQ configuration, but comes with the elevated risk of premature quench, such as during ramp–up of the magnet; increasing the amount of copper by 5 percentage points reduces the hot–spot temperature approximately 40 [K] for the PP CLIQ configuration and 30 [K] for the LL and CL, and 20 [K] for the LLrev.

Choosing the RRR or filament twist pitch differently only improves the performance notably for values very far from the nominal design parameters, and as such does not seem very promising to pursue at this stage in the coil design. At a later stage in the R& D process of the block–coil dipole magnet these parameters might be considered again, but results here indicate that, if so, it will be for other reasons than that of protection with CLIQ.

Altering the superconducting material itself, by improving its pinning characteristics, gives the option of increasing the margin to quench at normal operating conditions, while sacrificing somewhat in terms of hot–spot temperature. Combining this with increased frac-

tion of copper in the strands makes this a possible path for designing a magnet viable in a real machine where stability against external disturbances as well as reliable protection will be important.

There are, however, other ways to improve the performance of the protection system; changing the very design of the coil itself. The following chapter will investigate some variations on the initial design of the 16 [T] block–coil dipole magnet.

Chapter 5

Alternative Coil Designs

In this chapter I present results for several alternative coil geometries referred to as "variants". They include reducing the inductance as compared to the base–line variant, increasing the inductance, introducing a coil grading and finally, scaling up the coil to increase the aperture size.

All these coil variants are simulated for all CLIQ configurations, varying fractions of non–Copper and initial transport current.

Due to a special interest in the graded coil and the larger aperture coil variants, I investigate them more thoroughly towards the end of the chapter.

Given that the magnet under investigation in this thesis is still in the design phase, it is pertinent to determine way in which to improve the protection performance of the entire system (magnet with CLIQ) by ways of changing the coil geometry. Figure 5.1 shows the upper right quadrant of each of the four design variants investigated (essentially variations on the reference design presented in chapter 3).

Reducing the number of cables in the coil, as shown in figure 5.1a, will reduce its inductance, influencing the oscillation frequency during a CLIQ discharge. Figure 5.1b shows a variant of the coil design with more cables than the reference. This gives the opposite effect as compared to variant B. The main idea behind the variation given in 5.1c is that an insert (parts of the coil made of larger cables) at a lower current density than the rest of the coil's cables will allow an overall higher magnet current (or a larger operating margin, if the field is kept at the same level), as the margin to quench is increased for the larger cables[1]. Lastly, scaling up the entire coil geometry as shown in figure 5.1d will bring the whole coil to a larger margin to quench at the reference field of 16 [T], achieved with a larger current[2].

For the remainder of the thesis, the reference coil variant, presented in chapter 3 and for which simulation results were presented in chapter 4, will be referred to as *variant A*.

[1] Keep in mind that since the cables ultimately are in series, the current must be the same, regardless of the individual cable's cross section.

[2] By keeping the number of ampere–turns constant.

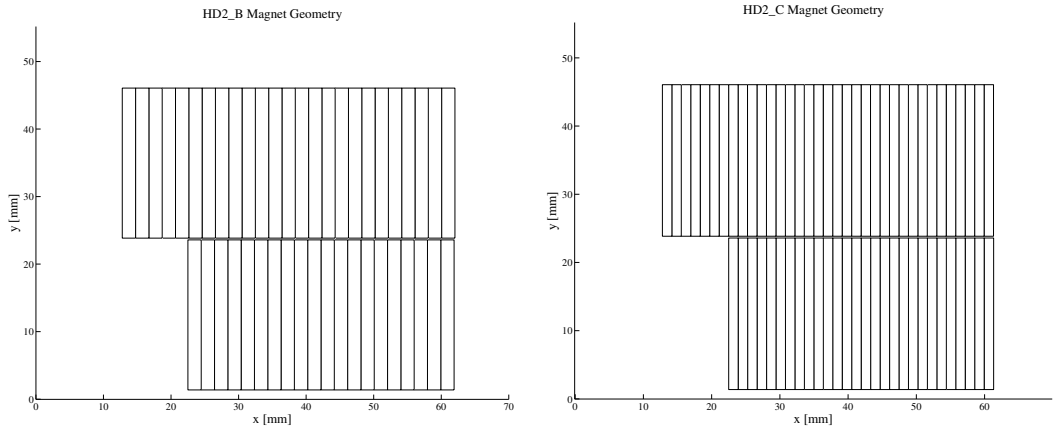

(a) HD2 variant B — Fewer cables

(b) HD2 variant C — More cables

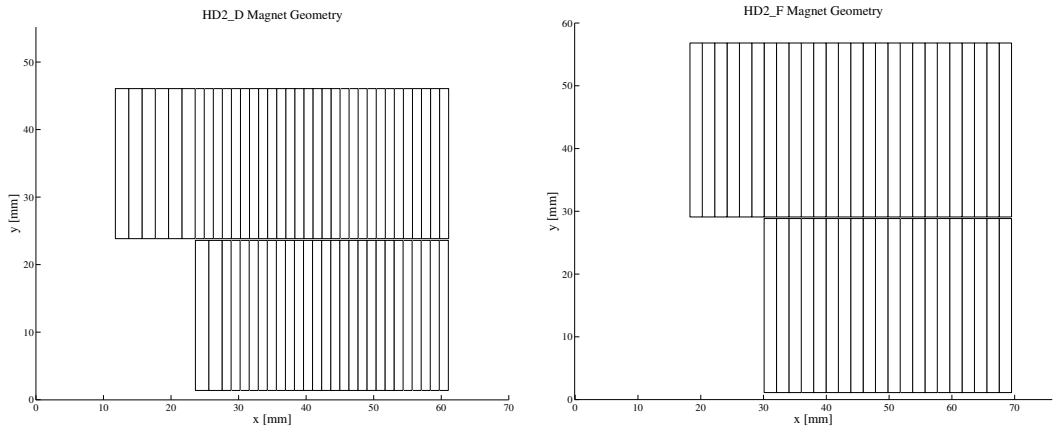

(c) HD2 variant D — Graded coil

(d) HD2 variant F — Scaled up coil

Figure 5.1: The variations on the reference block–coil variant considered in this thesis.

Differential Inductance

Figure 5.2 shows how the differential inductance varies with current for the different coil variants. For the A, B and C variants the differential inductance is, in relative terms, practically identical; this is because the inductance is only scaled by modifying the number of cables, but not the coil envelope, nor introducing any grading. The D and F variants, then, see substantial alterations with respects to the reference variant, and as such the inductance varies very differently. Note particularly for the F variant that the reduction of inductance is very large for larger currents due to the coils proximity to the iron yoke as discussed in sections 2.5 and 3.2.2.

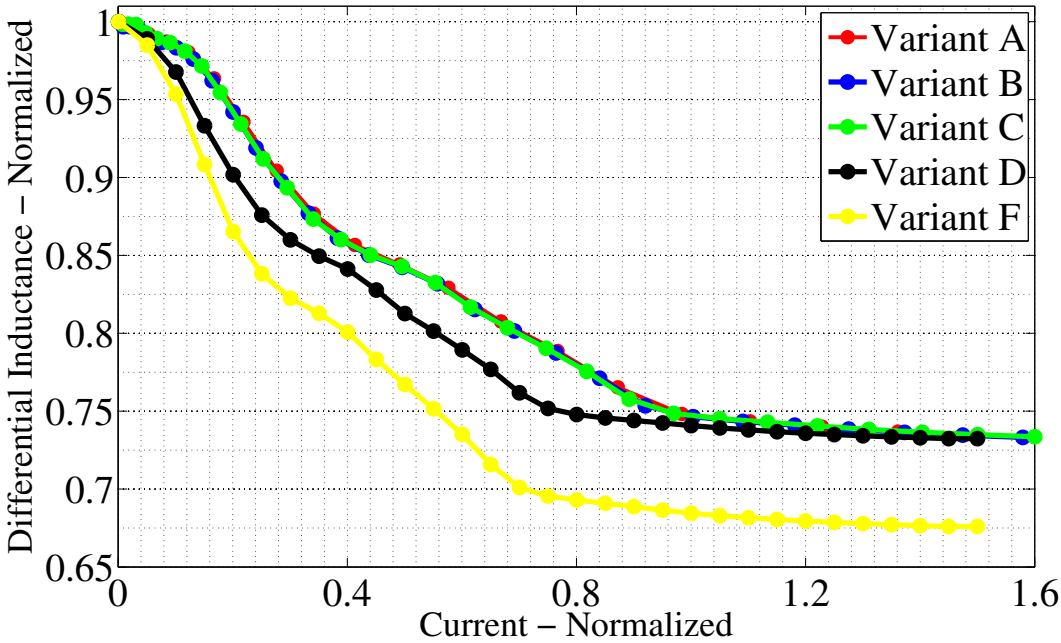

Figure 5.2: Differential inductance plotted in relative terms for comparison between the different coil geometries.

Instability Issues

For variant *D* and *F* the software used to simulate the transients in the magnets encountered stability issues when the differential inductance fell below a certain value.

For variant *D*, the severity of the problem depends on what coil sections are used as individual electrical parts; the different ways to label electrical parts for the *D* variant are discussed in–depth in section 5.6. Simulations that are labelled *variant D v2* in the thesis have been run with a constant differential inductance; this constant value, however, has been changed depending on what initial transport current was used in a given simulation. Table 5.1 gives these values. The value is always taken as the smallest value that will allow the algebraic system to remain stable (with a 5% safety margin).

Table 5.1: Constant values of the differential inductance used in simulations for the *D* variant coil only.

Current level	Differential inductance
I_{SS}[3]	0.76
I_{nom}	0.76
75% of I_{nom}	0.76
50% of I_{nom}	0.81
25% of I_{nom}	0.87

Simulations labelled *variant D* (which pertain to most of the simulations regarding the *D* coil variant) in the thesis are using a different electrical parting than the *D v2*, while using the same geometry, as referred to the variant *D* as given in figure 5.1c. This alternative electrical structure gives a different coupling between parts, and allows for a differential inductance closer to the "true" value. Figure 5.3 shows the differential inductance curve used for these simulations.

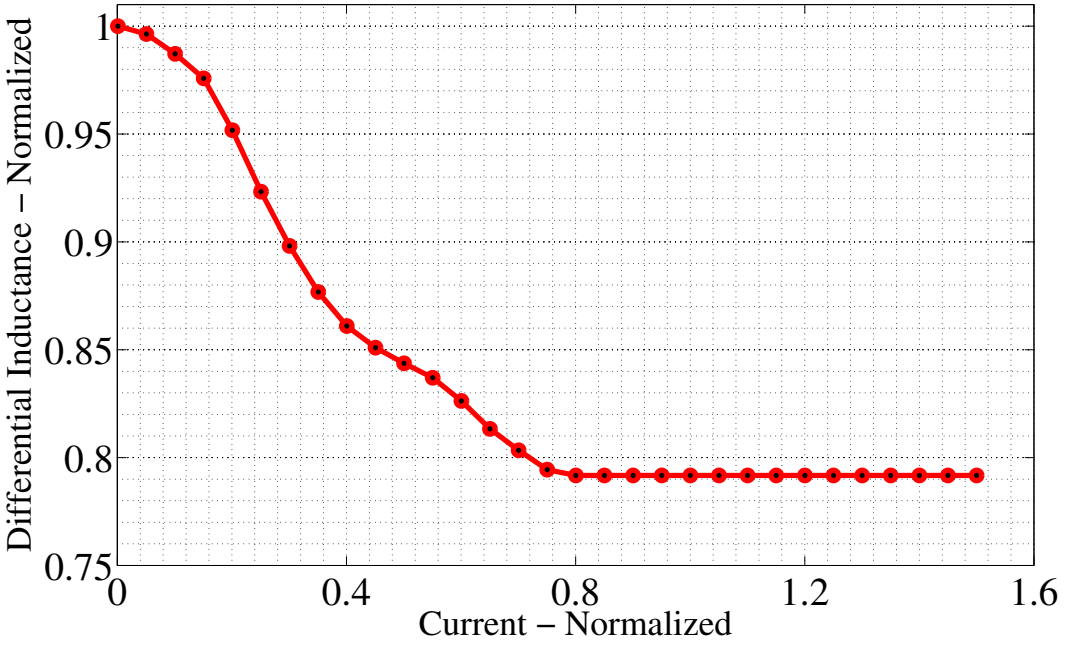

Figure 5.3: Differential inductance plotted in relative terms for the *D* variant.

All simulations run for the *F* variant have had to use a constant value for the differential inductance, given in table 5.2.

Table 5.2: Constant values of the differential inductance used in simulations for the *F* variant coil only.

Current level	Differential inductance
I_{SS}[4]	0.73
I_{nom}	0.73
75% of I_{nom}	0.73
50% of I_{nom}	0.77
25% of I_{nom}	0.84

This, obviously, takes away from the accuracy of the simulations. However, the initial few tens of milliseconds are not very influenced by the varying differential inductance — this time–span is the one typically most important for a CLIQ discharge. This means that while

[3]This is actually taken as 100 [A] below the short–sample current.
[4]This is actually taken as 100 [A] below the short–sample current.

the later part of the transient in a magnet where the constant inductance has been employed is oscillating too fast, the hot–spot temperature is not very influenced by this error, as the coil will likely have been quenched long before. Note that this means that for smaller initial transport currents, the error will be larger, seeing as the quench sets in later, meaning that a larger part of the transient current (from the CLIQ discharge) will be of importance.

5.1 Protection Performance of the Pole–Pole CLIQ Configuration

The initial CLIQ current polarities in the coil's electrical parts, for the PP CLIQ configuration, are shown in figure 5.4 for the *B*, *C*, *D* and *F* coil variants[5].

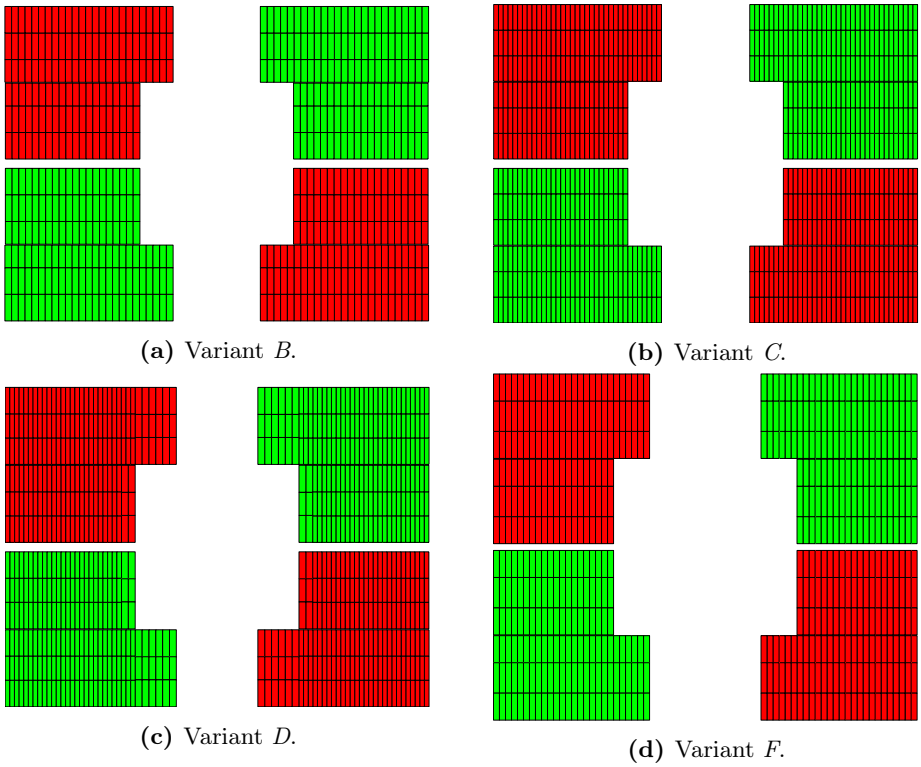

(a) Variant *B*. **(b)** Variant *C*. **(c)** Variant *D*. **(d)** Variant *F*.

Figure 5.4: Initial CLIQ current polarity in coil variants *B*, *C*, *D* and *F*, for the PP CLIQ configuration.

These current patterns give the equivalent inductances shown in table 5.3, and the CLIQ effectiveness shown in figure 5.5. From this, it is expected that the *B* variant will perform better than the base line *A* variant, while *C* will be worse. *C* and *D* seem very similar from the inductance point of view, while *F* is closer to the reference coil. Taking onto account the grading of the *D* variant makes it hard to predict the performance a priori, but seeing as the effectiveness in the insert region (larger cables) is poor while larger cables at the same time require more energy input to quench, it will probably perform worse than case *C*. Variant *F* has the possibility to be the best; while the larger cables need more energy to quench, there is no grading that will skew the enthalpy margin to quench, which means that the larger cables only give a larger tolerance to heat input — lower temperature rise, given the lower

[5]The equivalent figure for the base line, *A* variant, is figure 3.8 in chapter 3.

energy density in the larger volume, and as such it is expected to outperform the base line variant significantly.

Table 5.3: Inductance values for the PP discharge path on the *B*, *C*, *D* and *F* coil variants.

Variant	L_1 [mH m^{-1}]	L_2 [mH m^{-1}]	M_{12} [mH m^{-1}]	L_{eq} [mH m^{-1}]
A	2.20	2.20	1.01	0.59
B	1.51	1.51	0.70	0.41
C	3.00	3.00	1.37	0.81
D	2.91	2.91	1.34	0.79
F	1.78	1.78	0.79	0.50

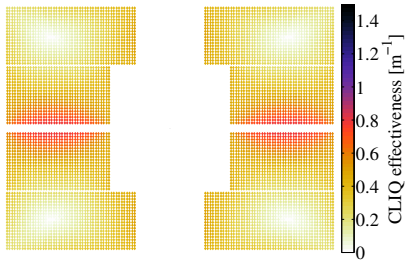

(a) Variant *B*.

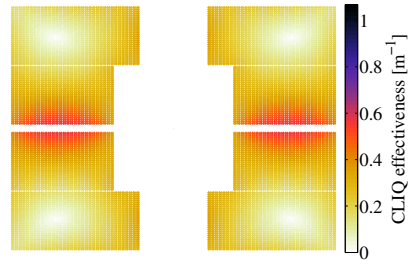

(b) Variant *C*.

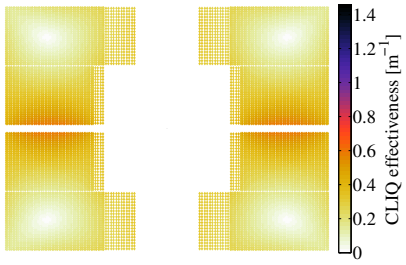

(c) Variant *D*.

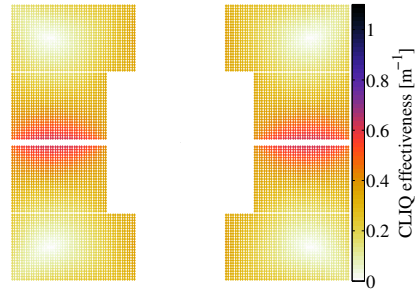

(d) Variant *F*.

Figure 5.5: CLIQ effectiveness in coil variants *B*, *C*, *D* and *F*, for the PP CLIQ configuration. Note that the scales are not identical.

Figure 5.6 shows the discharge currents in the coil plotted together with hot–spot temperature for the various coil variants. As expected, the *B* and *F* coils perform the best, with hot–spots of about 325 [K], seeing as they benefit from a combination of better inductive properties, and for the *F* variant, also a large overall volume in which to deposit the stored magnetic energy. The results also suggest that the graded coil design as implemented in variant *D* is very challenging from a protection point of view; the hot–spot reaches above 450 [K]. The *A* and *C* variants end up around 350 [K].

Note that the quench load is not a good predictor of final hot–spot temperature *across* coil variants, given the altered thermal properties combined with the plot of discharge current being normalised in order to facilitate the qualitative comparison.

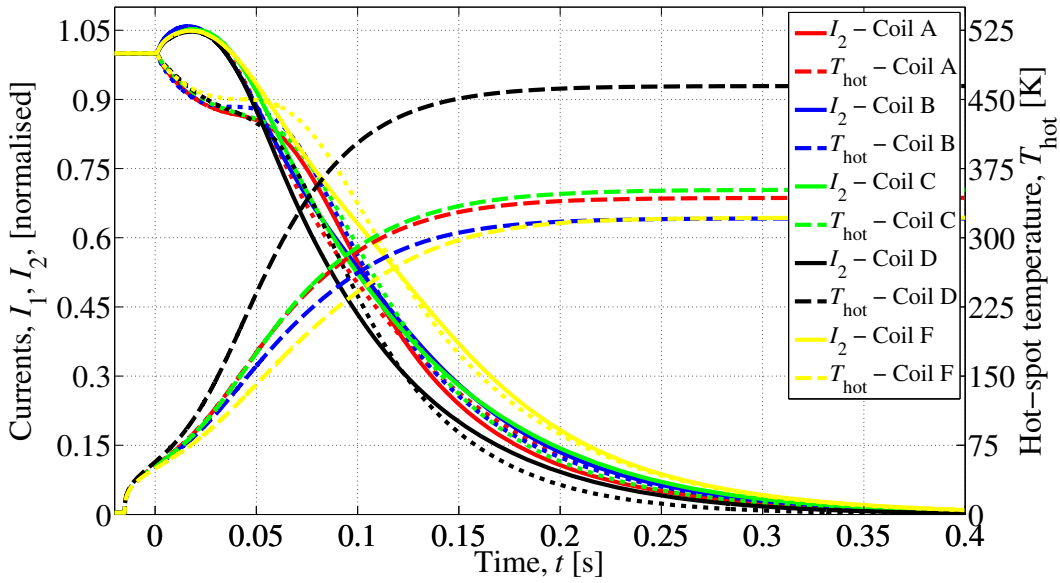

Figure 5.6: Hot–spot temperature and discharge currents for a PP CLIQ discharge, into the different coil variants. Note that all simulations were run at their respective nominal initial transport current, and then normalised for the comparison. The CLIQ used has the nominal parameters, $C_{\mathrm{CLIQ}} = 100$ [mF], $U_0 = 1000$ [V].

In figure 5.7 the currents in the CLIQ leads are plotted together for all the studied variations. Looking at the curves for variants A, B and C, the effect of varying inductance is quite clear. Increasing the number of turns (going from variant A to C), gives a larger inductance, translating into a smaller initial $\mathrm{d}I/\mathrm{d}t$ and peak current[6]. The opposite is true for the reduced inductance variant (going from variant A to B); the lower inductance makes it easier to generate a large initial $\mathrm{d}I/\mathrm{d}t$, and a larger peak current. The reason why the CLIQ current for variants B and F initially are very similar, but then separate in terms of frequency with time, is the inductance; initially the two coil variants have a fairly similar inductance, but as discussed in the beginning of this chapter, the F variant sees instability issues due to the proximity of the iron yoke to the coil edge. So, as the current falls, the inductance of the B variant increases as indicated in figure 5.2, while for the F it maintains its lowered value, as given in table 5.2.

[6]The frequency goes down for a larger inductance, which lowers the peak current, as predicted by equation 2.7.

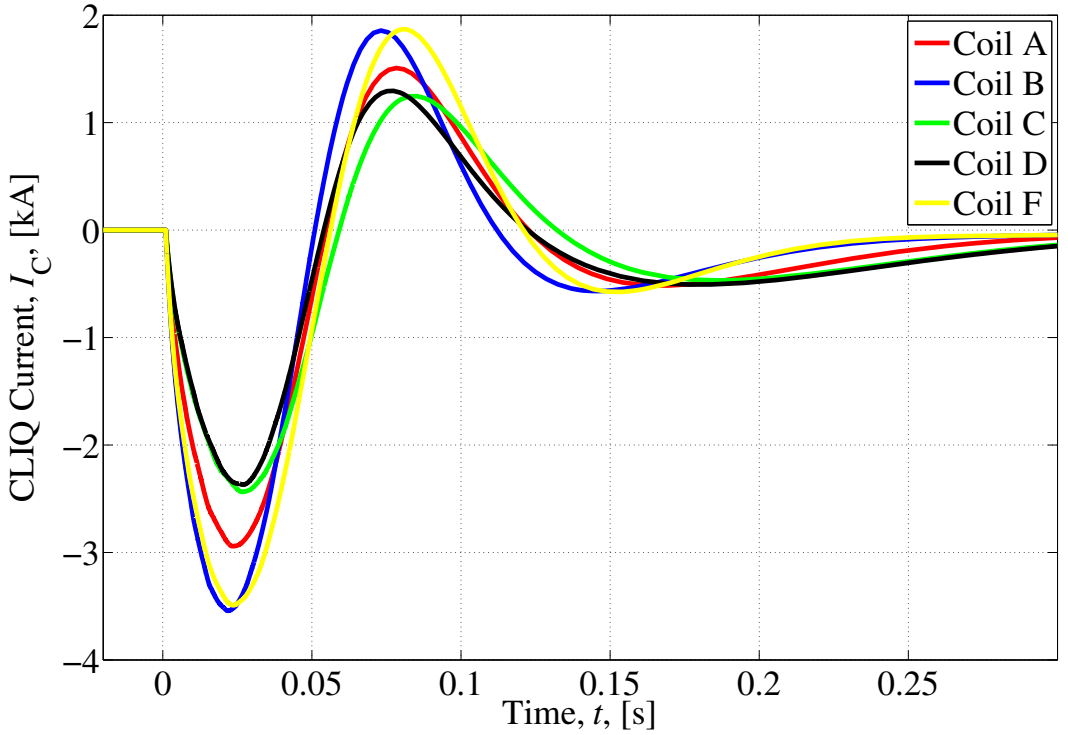

Figure 5.7: Current in the CLIQ leads during the PP CLIQ discharge into the different coil variants. Note that all simulations were run at their respective nominal initial transport current. The CLIQ used has the nominal parameters, $C_{\mathrm{CLIQ}} = 100$ [mF], $U_0 = 1000$ [V].

By normalising the coil resistance to the value the copper would have if it all was at 20 [K] and at its nominal magnetic field value, one gets a description of about how much of the coil has quenched at a given time, and also such a representation makes it possible to compare the performance of the different coil variants. Figure 5.8 plots the normalised coil resistance for the five variants protected by the PP CLIQ configuration. Note that the plateaus indicate periods of time when no new blocks quench; the slight increase in resistance comes only from the resistivity's dependence on temperature[7]. As seen, the resistance for the B and F variants develop quite similarly in the initial stages, while variant A follows quite closely. Variant C is notably slower.

The figure clearly highlights the performance issue of the D variant. The initial quench sets in much later than for the other variants (when employing this CLIQ configuration)[8], and even if the resistance rise, once the quench has started, is faster than the C variant, it comes too late to maintain an acceptable hot–spot temperature. The reason for this is to be found in how the enthalpy margin to quench.

[7] As the quench develops, the magnetic field will start falling, giving a reduction to this, but in the first few tens of milliseconds, the magnetic field is practically constant on average, in the coil.

[8] Much later is in the context of this thesis still very fast as compared to QH, as indicated in section 4.2.

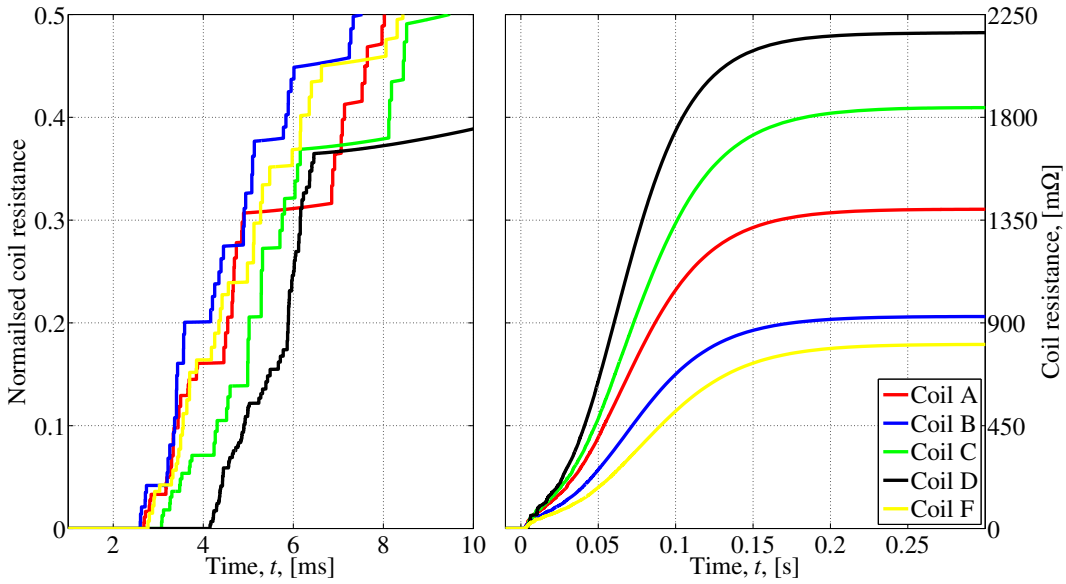

Figure 5.8: Coil resistance development in the different coil variants for the PP CLIQ configuration. Note that all simulations were run at their respective nominal initial transport current, and the resistance values in the left hand figure are normalised for the comparison. The nominal design parameters for the CLIQ unit are $C_{\mathrm{CLIQ}} = 100$ [mF], $U_0 = 1000$ [V].

Figure 5.9 shows the enthalpy margin to quench in the D coil variant, for the upper right quadrant, and adjusting the scale so that all values above 30 [mJ cm^{-3}] are equal, in order to better discern the important values closer to the bore.

The inserts have, as they are designed to, a higher margin than the cables immediately outside of them. This, coupled with the PP CLIQ configuration depositing loss mostly in the midplane region, means that it will take longer to quench the coil[9].

[9]Full enthalpy and temperature margin plots for the D variant coil are found in figures B.7 and B.8.

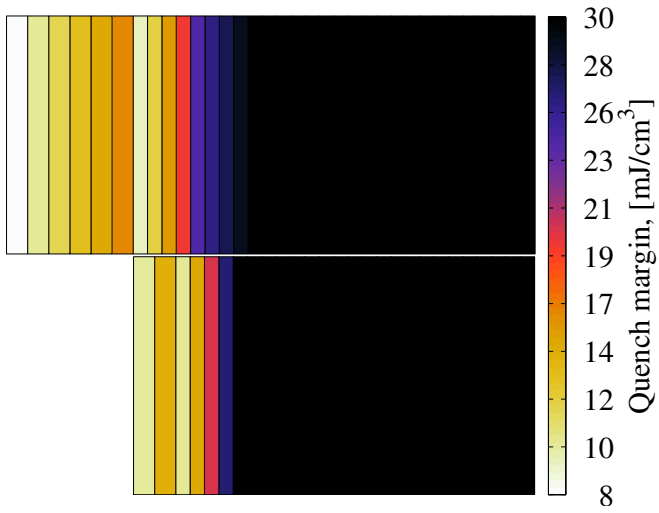

Figure 5.9: Enthalpy margin to quench, at nominal initial transport current, for the *D* coil variant. Note that any value above 30 [mJ cm^{-3}] has been set to 30, in order to better resolve the lowest values.

5.2 Protection Performance of the Crossed–Layer CLIQ configuration

The initial CLIQ current polarities in the coil's electrical parts, for the CL CLIQ configuration, are shown in figure 5.10 for the *B*, *C*, *D* and *F* coil variants.

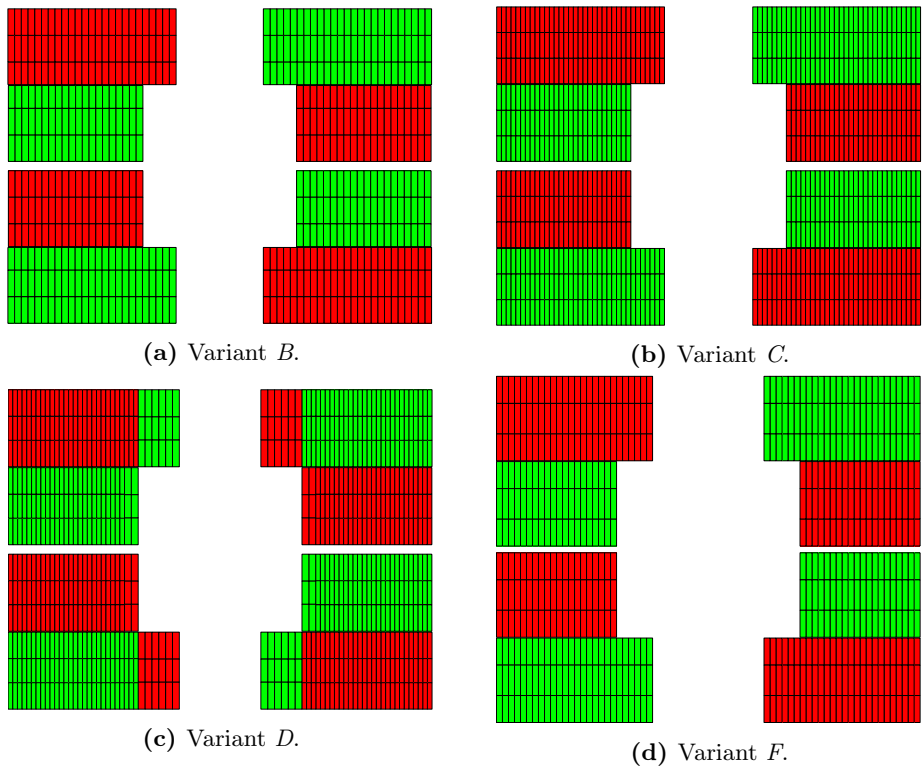

(a) Variant *B*. **(b)** Variant *C*. **(c)** Variant *D*. **(d)** Variant *F*.

Figure 5.10: Initial CLIQ current polarity in coil variants *B*, *C*, *D* and *F*, for the CL CLIQ configuration.

These current patterns give the equivalent inductances shown in table 5.4, and the CLIQ effectiveness shown in figure 5.11. As for the PP CLIQ configuration, the *B* and *F* coil variants will probably perform the best, while the *C* variant should be on par or worse than the base line *A* variant. The *D* variant is now more interesting than before, seeing as the CLIQ effectiveness plot predicts a fairly large loss to be deposited at the interface between the regular cables and the insert — this should decrease the time to initiate a quench, and depending on the resistance growth, may reduce the hot–spot temperature considerably.

Table 5.4: Inductance values for the CL discharge path on the *B*, *C*, *D* and *F* coil variants.

Variant	L_1 **[mH m^{-1}]**	L_2 **[mH m^{-1}]**	M_{12} **[mH m^{-1}]**	L_{eq} **[mH m^{-1}]**
A	1.81	1.81	1.40	0.20
B	1.24	1.24	0.96	0.14
C	2.46	2.46	1.91	0.28
D	2.32	2.32	1.93	0.19
F	1.47	1.47	1.10	0.18

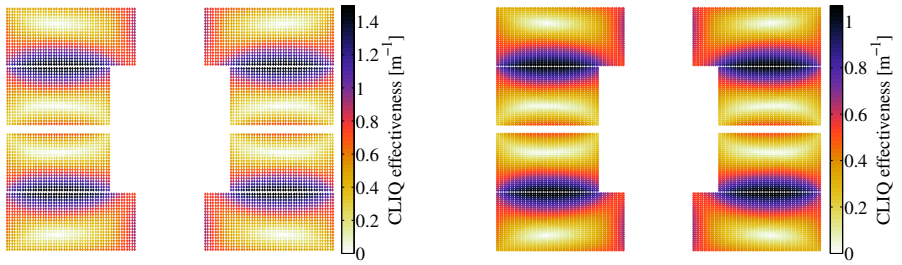

(a) Variant *B*.

(b) Variant *C*.

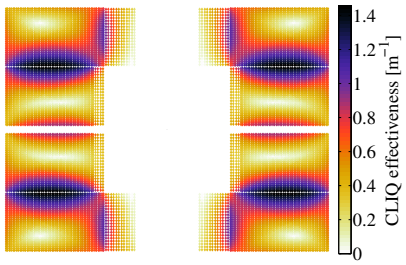

(c) Variant *D*.

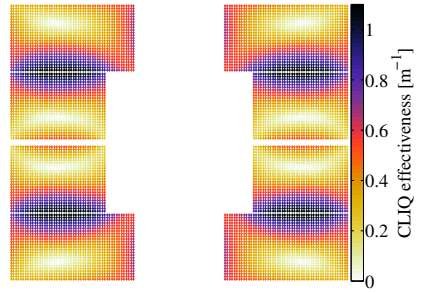

(d) Variant *F*.

Figure 5.11: CLIQ effectiveness in coil variants *B*, *C*, *D* and *F*, for the CL CLIQ configuration. Note that the scales are not identical.

Hot–spot temperatures and discharge currents in all coil variants are shown together in figure 5.12. Compared to the results for the PP CLIQ configuration, the hot–spot temperatures are now about 50 [K] lower for all variants, apart from the *D* variant, that sees a larger reduction of about 100 [K]; The *B* and *F* variants reach about 290 [K], while the *A* and *C* have hot–spots of about 300 [K]. The *D* variant is still unprotected at 360 [K].

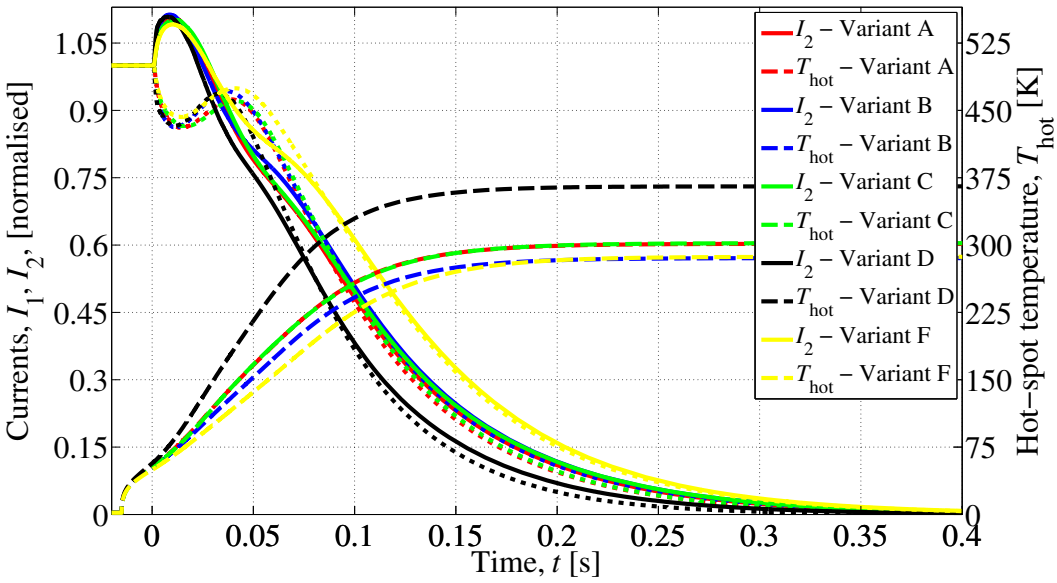

Figure 5.12: Hot–spot temperature and discharge currents for a CL CLIQ discharge, into the different coil variants. Note that all simulations were run at their respective nominal initial transport current, and then normalised for the comparison. The CLIQ used has the nominal parameters, $C_{\mathrm{CLIQ}} = 100$ [mF], $U_0 = 1000$ [V].

Looking at the coil resistances for the variants, it is no longer as apparent why the D coil performs as poorly as it does, compared to the other variants, as in figure 5.13, it is clear that the quench sets in the fastest for the D variant, and also grows rapidly. This is revisited in the next section, when discussing the LL CLIQ configuration. Isolated from the other variants, the substantial improvement in hot–spot temperature is explained by the large improvement in resistance growth.

The other variants follow the same general pattern as for the PP CLIQ configuration; variant B and F are quite close, and on average grow the fastest, while the A variant is a little better than the C variant.

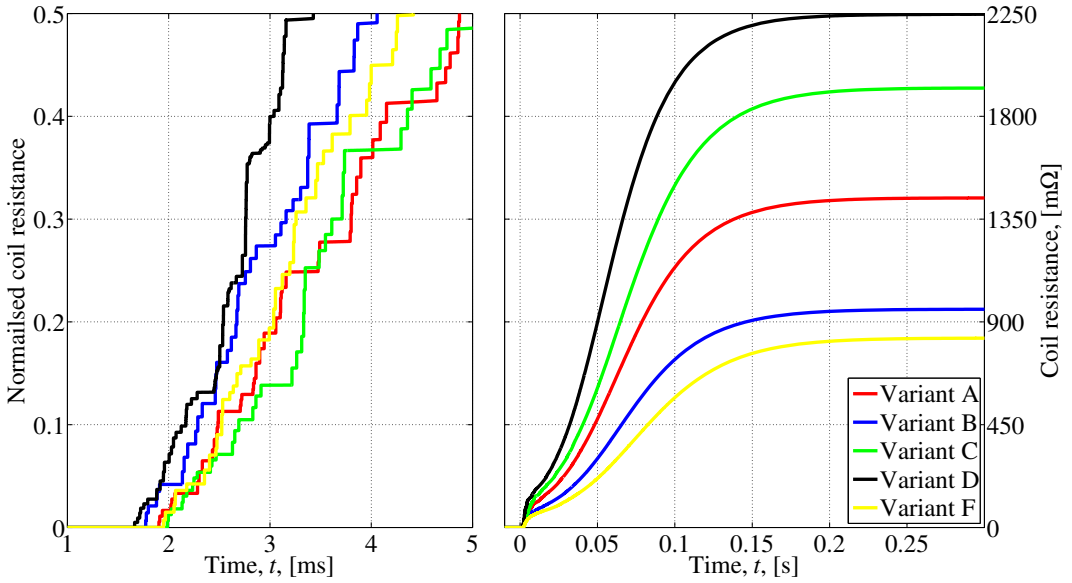

Figure 5.13: Coil resistance development in the different coil variants for the CL CLIQ configuration. Note that all simulations were run at their respective nominal initial transport current, and the resistance values in the left hand figure are normalised for the comparison. The nominal design parameters for the CLIQ unit are $C_{\mathrm{CLIQ}} = 100$ [mF], $U_0 = 1000$ [V].

5.3 Protection Performance of the Layer–Layer CLIQ configuration

Figure 5.14 shows the initial CLIQ current polarities in the different electrical parts of the coil for the *B*, *C*, *D* and *F* coil variants.

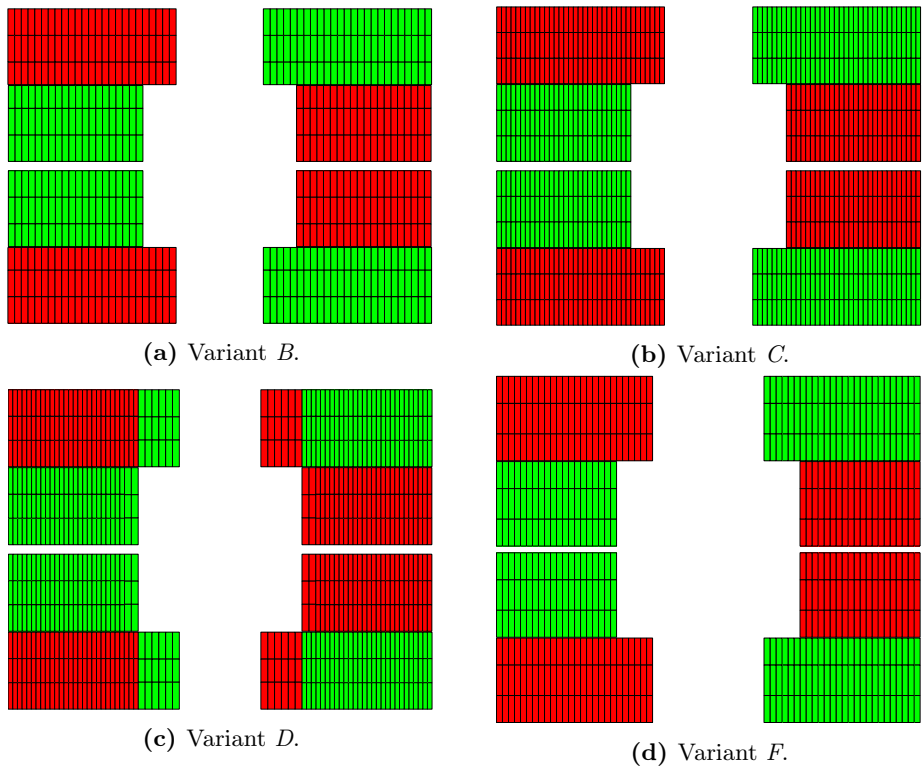

(a) Variant *B*.

(b) Variant *C*.

(c) Variant *D*.

(d) Variant *F*.

Figure 5.14: Initial CLIQ current polarity in coil variants *B*, *C*, *D* and *F*, for the CL CLIQ configuration.

These current patterns give the equivalent inductances shown in table 5.5, and the CLIQ effectiveness shown in figure 5.15. Looking at the *D* coil variant, it is notable that the interface region between the insert and outer cables still receive some IFCL, seeing as, from the current polarity plot, the way the electrical parts are structured now allow for such an interface to arise, also for the LL. From this, it seems likely that the LL and CL will perform similarly for the *D* coil variant.

As mentioned in section 3.4, the notion that there is an intrinsic balance between the outer and inner layers of a block–coil, seen as similar values for L_1 and L_2, of the general geometries given by variants *A*, *B*, *C* and *F*, is lent some credence by the numbers in table 5.5. While the *D* variant has the same envelope as the reference variant, the inner and outer layers are not structured as single electrical parts, thus disrupting the inductive balance, while the other variations, *B*, *C* and *F*, benefit from this. It is still not possible to conclude that any block–coil geometry will show the same characteristics, but it also seems that within quite a large parameter space, the property remains.

Table 5.5: Inductance values for the LL discharge path on the *B*, *C*, *D* and *F* coil variants.

Variant	L_1 [mH m^{-1}]	L_2 [mH m^{-1}]	M_{12} [mH m^{-1}]	L_{eq} [mH m^{-1}]
A	1.85	1.87	1.35	0.25
B	1.27	1.28	0.93	0.17
C	2.52	2.54	1.84	0.35
D	1.98	2.87	1.82	0.28
F	1.55	1.46	1.06	0.22

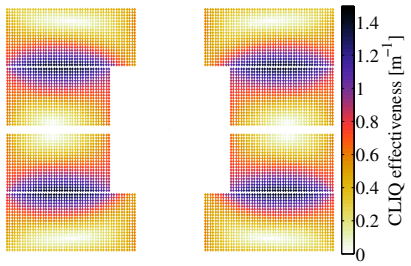

(a) Variant *B*.

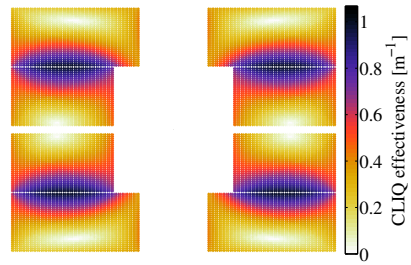

(b) Variant *C*.

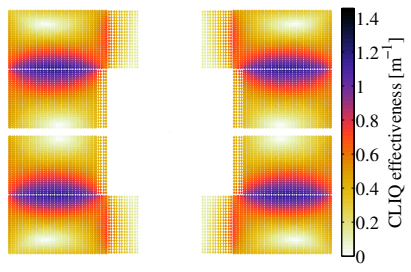

(c) Variant *D*.

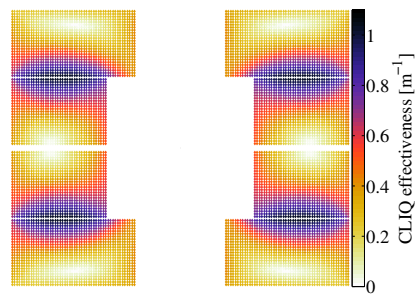

(d) Variant *F*.

Figure 5.15: CLIQ effectiveness in coil variants *B*, *C*, *D* and *F*, for the CL CLIQ configuration. Note that the scales are not identical.

Hot–spot temperatures and discharge currents in all coil variants are shown together in figure 5.16. For variants *A*, *B*, *C* and *F*, the LL and CL perform very similarly, as predicted by the similar CLIQ effectiveness values, with *B* and *F* at about 280 [K], and the *A* and *C* around 300 [K]; the *D* variant, however, sees somewhat of a performance drop, because the initial quench now takes longer to arise, given that the deposited loss in the interface towards the insert is now lower than for the CL discharge, and now reaches about 400 [K]. The reason for this difference in effectiveness, even if the current polarities across this interface are the same for CL and LL discharges (as seen in figures 5.10 versus 5.14), is that the equivalent inductance of the CL discharge path is lower than for the LL.

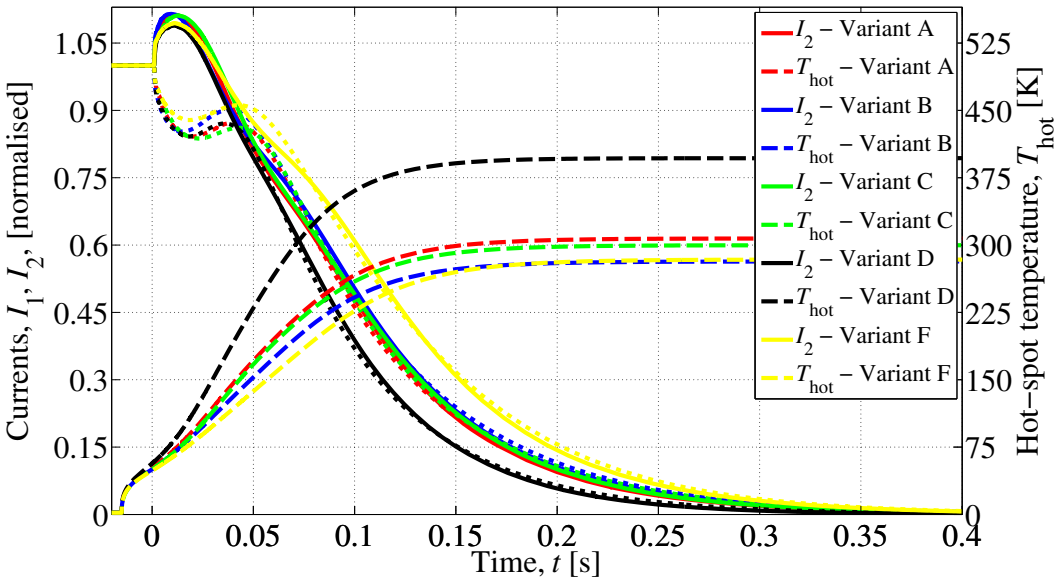

Figure 5.16: Hot–spot temperature and discharge currents in for a LL CLIQ discharge into the different coil variants. Note that all simulations were run at their respective nominal initial transport current, and then normalised for the comparison. The nominal design parameters for the CLIQ unit are $C_{\mathrm{CLIQ}} = 100$ [mF], $U_0 = 1000$ [V].

Looking at the coil resistances for the variants in figure 5.17, some of the reason for why the performance of the CL configuration on the D variant seems surprisingly poor given the resistance development becomes apparent; even when substantially improving the resistance increase when going from the PP to the CL configuration, the coil is still very difficult to protect, given the grading — the resistance development for the LL CLIQ configuration is practically the same for the D variant, while the other four see large improvements in initial onset.

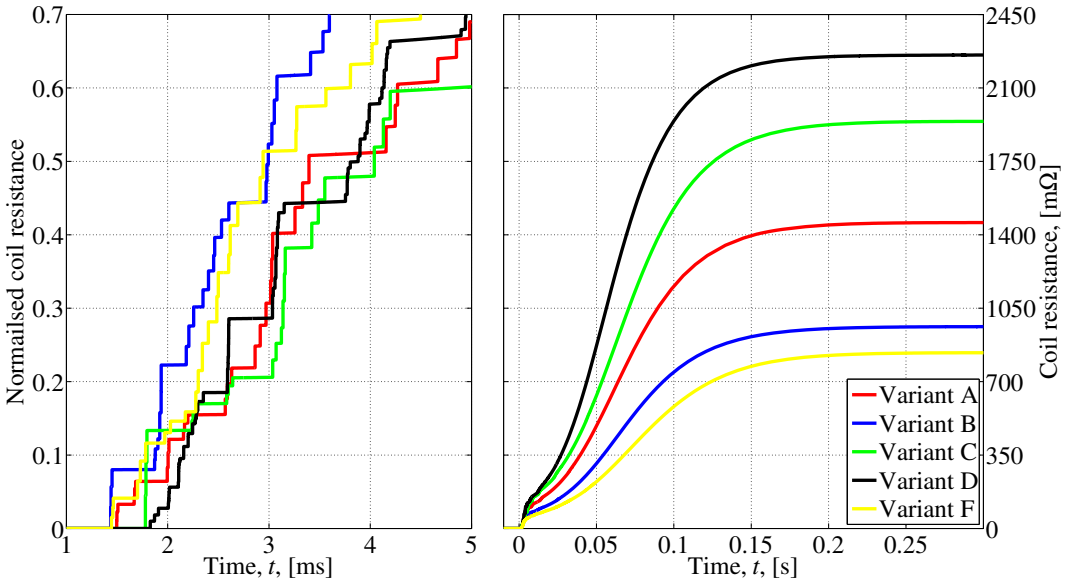

Figure 5.17: Coil resistance development in the different coil variants for the LL CLIQ configuration. Note that all simulations were run at their respective nominal initial transport current, and the resistance values in the left hand figure are normalised for the comparison. The nominal design parameters for the CLIQ unit are $C_{\mathrm{CLIQ}} = 100$ [mF], $U_0 = 1000$ [V].

Another way to look at the poorer performance of the *D* variant is highlighted in figure 5.18. Here, the time to quench each individual block of the *D* variant coil is represented. Note that any time above 15 [ms] is set to 15 [ms] in order to increase the resolution of the development in the blocks closer to the bore/inserts.

The quench propagation is almost the same for the two CLIQ configurations, and as such, the performance is also quite similar. The plots here serve to illustrate how the performance could be better — the cables in the inserts are very quick to quench, but require quite a large amount of energy from the CLIQ unit to do so, as seen in the plot of enthalpy margin to quench given back in figure 5.9. This will slow down the speed of quench in the rest of the coil, as during the very first few milliseconds heat propagation is fairly small, given that the temperature gradient in the coil is still small (adjacent cables will typically see no more than a few kelvin difference between them), and quenching of cables is mostly determined by the IFCL generated by CLIQ.

The only way to change the coil geometry while keeping the grading is to increase the grading — an investigation down this avenue is not done here, but a first guess would be that a larger insert (larger fraction of the total coil) will mean that quenching the inserts early will prove less of a slow–down to the over–all development, while also reducing the difference in margin to quench the cables in the interface between insert and regular cables, thus giving a somewhat more homogeneous quench propagation as opposed to the current one where the quench starts at this interface and propagates outwards.

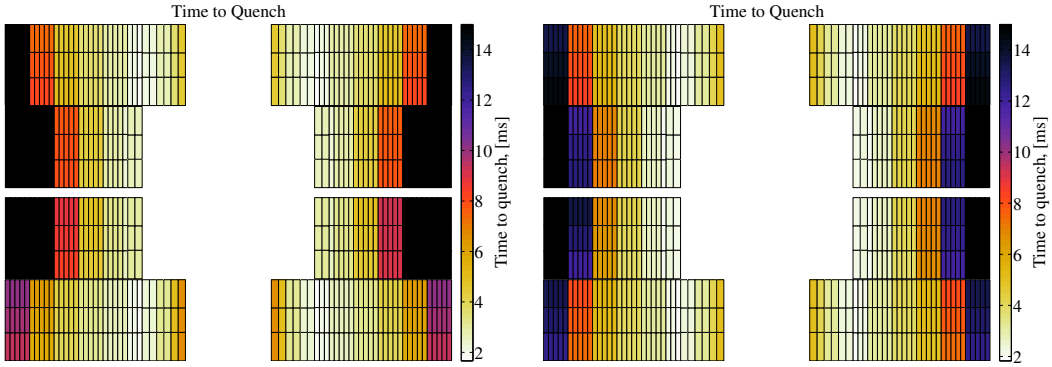

(a) CL CLIQ configuration.

(b) LL CLIQ configuration.

Figure 5.18: Time it takes to quench each individual block of the D variant coil for both CL and LL CLIQ configurations. Note that all times above 15 [ms] have been set equal to 15 [ms] in order to better resolve the development close to the inserts.

5.4 Protection Performance of the Layer–Layer Reverse CLIQ configuration

In terms of hot–spot temperature, the LLrev gives a small improvement over the LL, as seen in figure 5.19. For variants A, B, C and F, the LLrev out–performs both the LL and CL CLIQ configurations, with B and F reaching about 270 [K], and the A and C variants about 280 [K]. For the D variant, however, the LLrev is on par with the CL, with a hot–spot of around 350. When going from CL to LL, the D variant sees a loss of CLIQ effectiveness, while going from LL to LLrev, there is the aforementioned gain in enthalpy margin to quench that makes up for the loss of peak energy deposition (lower CLIQ effectiveness).

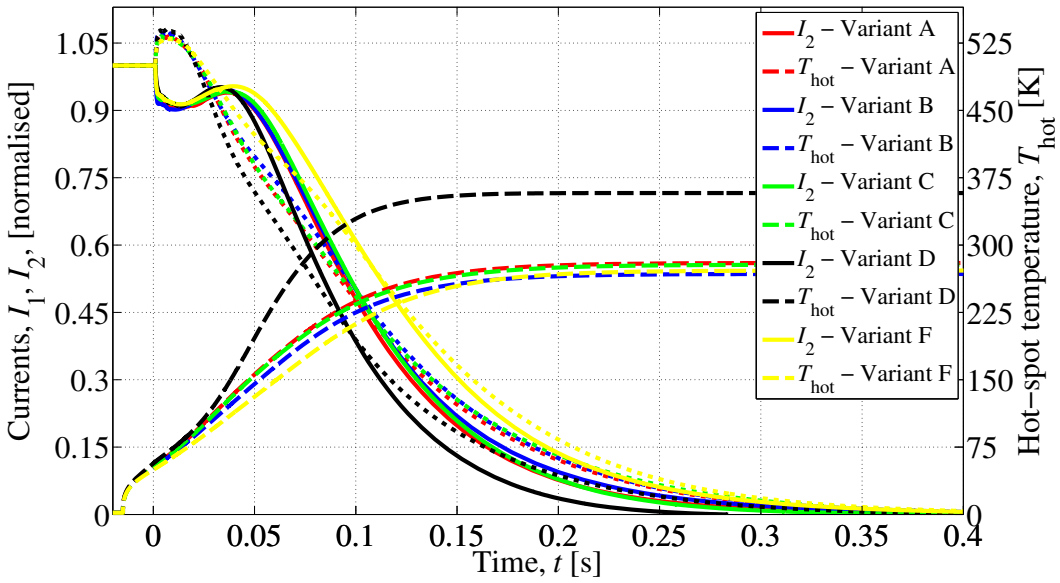

Figure 5.19: Hot–spot temperature and discharge currents in for a LLrev CLIQ discharge into the different coil variants. Note that all simulations were run at their respective nominal initial transport current, and then normalised for the comparison. The nominal design parameters for the CLIQ unit are $C_{\mathrm{CLIQ}} = 100$ [mF], $U_0 = 1000$ [V].

Looking at the coil resistances for the variants in figure 5.17, some of the reason for why the performance of the CL configuration on the D variant seems surprisingly poor given the resistance development becomes apparent; even when substantially improving the resistance increase when going from the PP to the CL configuration, the coil is still very difficult to protect, given the grading — the resistance development for the LL CLIQ configuration is practically the same for the D variant, while the other four see large improvements in initial onset.

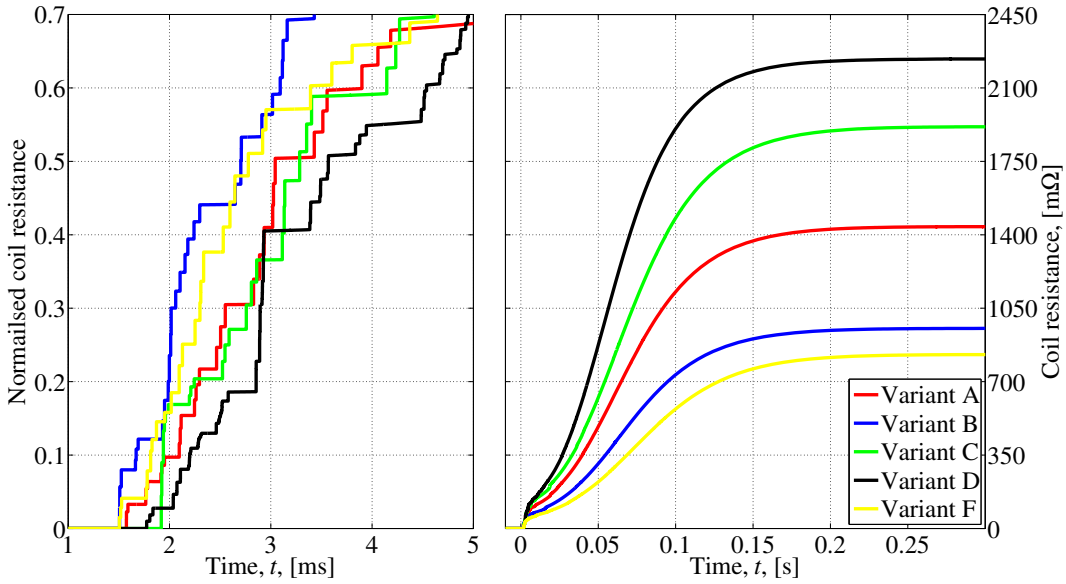

Figure 5.20: Coil resistance development in the different coil variants for the LLrev CLIQ configuration. Note that all simulations were run at their respective nominal initial transport current, and the resistance values in the left hand figure are normalised for the comparison. The nominal design parameters for the CLIQ unit are $C_{\mathrm{CLIQ}} = 100$ [mF], $U_0 = 1000$ [V].

5.5 Summary of All Coil Variants and CLIQ configurations

Figure 5.21 shows how the hot–spot temperature in the reference coil variant, A, varies with CLIQ configuration and fraction of non–Copper in the strands of the cables[10].

Figure 5.22 summarises how the hot–spot in the four other coil variants change with fraction of non–Copper and CLIQ configuration. Note that the same way as for variant A, variant C is not stable for fractions of non–Copper lower than about 45%, because the enthalpy margin to quench becomes too small to allow for safe operation (as discussed in section 4.7).

[10]Note that this is the exact same figure as figure 4.28.

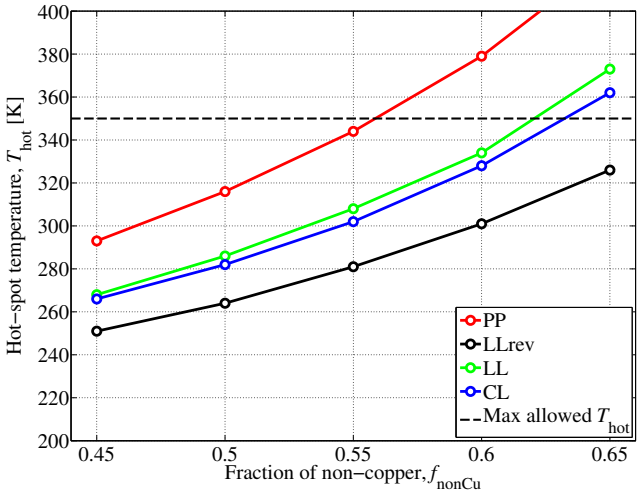

Figure 5.21: Hot–spot temperature in the block–coil, variant A, for all four CLIQ configurations and varying fraction of non–Copper. Note that all simulations were run at the same initial transport current, and that the nominal design parameter is $f_{\mathrm{nonCu}} = 55\%$.

It is clear that the D coil variant is impossible to protect with the PP CLIQ configuration, and even the LLrev can only protect it after sacrificing the over–all operating stability of the coil by reducing the fraction of non–Copper. Variants B and F are practically identical from the protection point of view, and using the PP configuration allows for a small margin also at the short–sample current (shown explicitly in figure 5.27). Variant C is easily protected by the CLIQ configurations other than PP, and the same goes for the base line coil variant as discussed before.

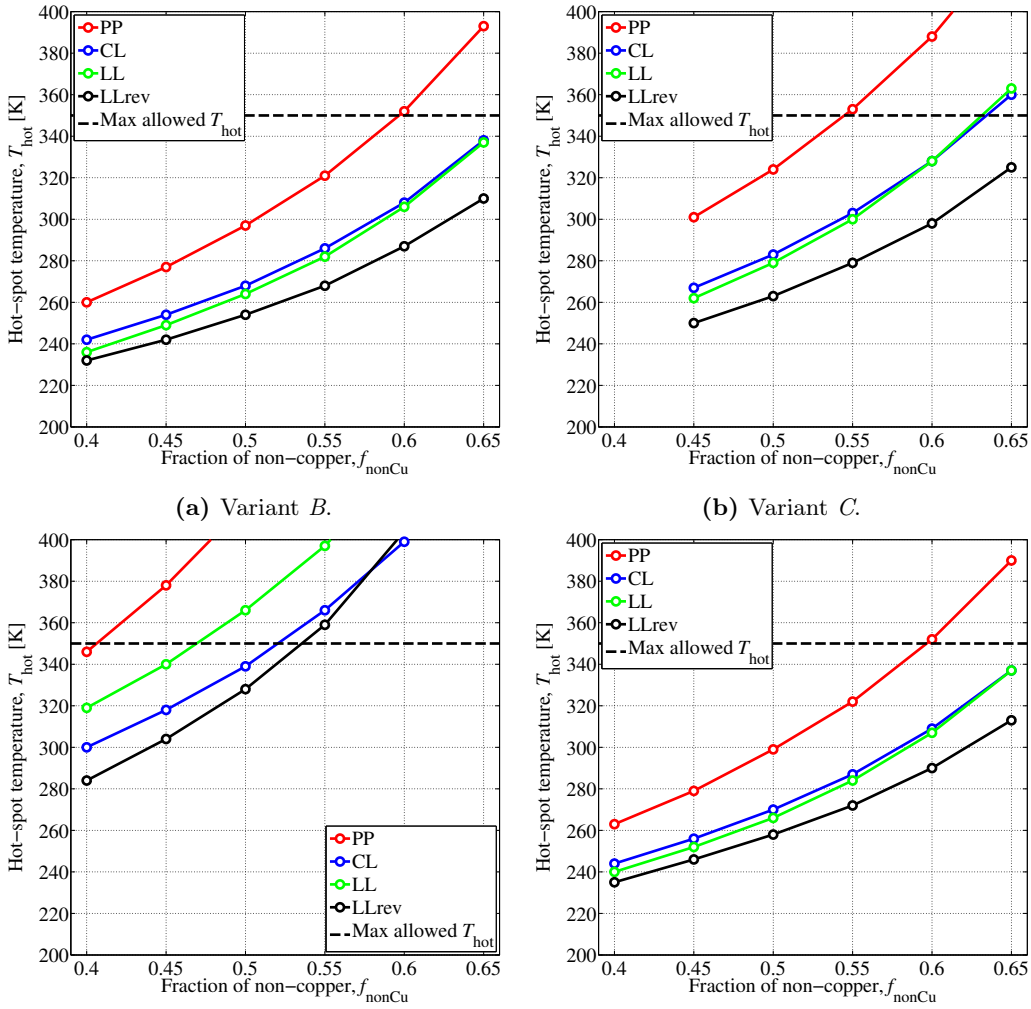

(a) Variant *B*.

(b) Variant *C*.

(c) Variant *D*.

(d) Variant *F*.

Figure 5.22: Hot–spot temperature as a function of the copper fraction in the strands for all non–reference coil variants. Note that the CLIQ unit used in all simulations use the nominal parameters, $C_{\mathrm{CLIQ}} = 100$ [mF], $U_0 = 1000$ [V].

5.6 Protecting Coil Variant *D*

The graded coil is of particular interest seeing as it would allow a sufficient operating margin in the eventual accelerator without altering the properties of the superconducting material itself [3]. The challenge, as seen, has been the protection of the coil, as the larger margin makes this task harder.

This section will explore the possibility to significantly alter the CLIQ parameters, and also a completely different connection scheme for the coil.

5.6.1 Altering the CLIQ Parameters

Figure 5.23 shows, compactly, the effect of varying the CLIQ parameters and configuration on the *D* variant with the connection scheme shown before. A smaller capacitance with a larger charging voltage is clearly the best option for all CLIQ configurations. The plot of the LLrev indicates that a capacitance of 75 [mF] charged to 1500 [V] will give the best performance, with a hot–spot reaching about 320 [K], and such a configuration is the only one able to protect the coil with any appreciable margin — it seems impossible to find parameters allowing the PP to sufficiently protect the coil. The LL might still benefit from an even smaller capacitance and larger charging voltage, however, a smaller capacitance means less energy available in the unit as a whole, which then jeopardises the performance at smaller transport currents; for the nominal CLIQ unit, with a 100 [mF] capacitor, this has not been an issue, and no further investigation has been done on this problem, however it is a distinct possibility. Lowering the capacitance seems the only way to possibly improve the performance of the CL as well, as the gain in increased voltage seems to have saturated for the 75 [mF] tested.

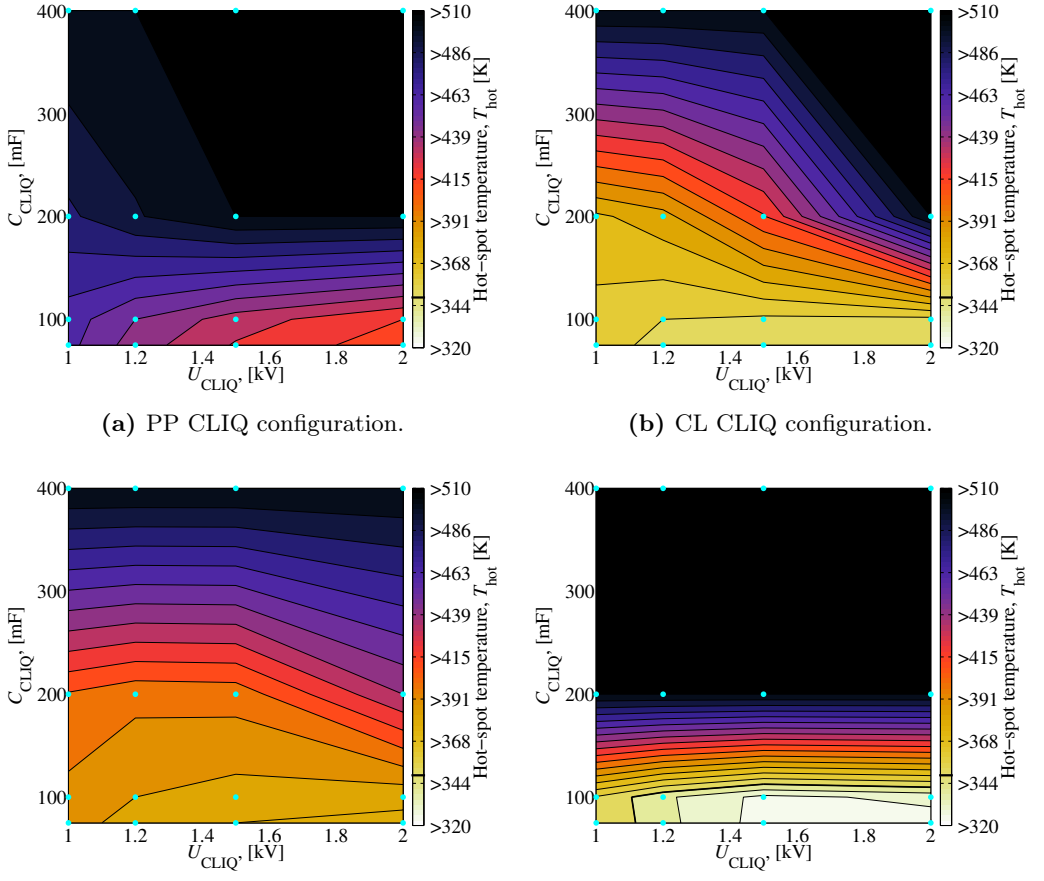

(a) PP CLIQ configuration.

(b) CL CLIQ configuration.

(c) LL CLIQ configuration.

(d) LLrev CLIQ configuration.

Figure 5.23: Hot–spot temperature in the *D* coil variant for different CLIQ capacitances, voltages and configurations.

5.6.2 Changing the Connection Scheme

Figure 5.24 shows a very different way to group the electrical parts of the coil, where the inserts in the inner and outer layers of a pole are considered separately, while the other cables within the same pole are another electrical part. The PP configuration for this connection scheme is the same as the one for the previously examined one, and in order to separate the two, the new one will be referred to as *D v2*.

The equivalent inductances of the discharge paths are shown in table 5.6 — the CL and PP are here very similar, while the LL, and thus, LLrev, are vastly different from the other two. This translates into the clear disadvantage of the PP and CL CLIQ effectiveness plots in figure 5.25.

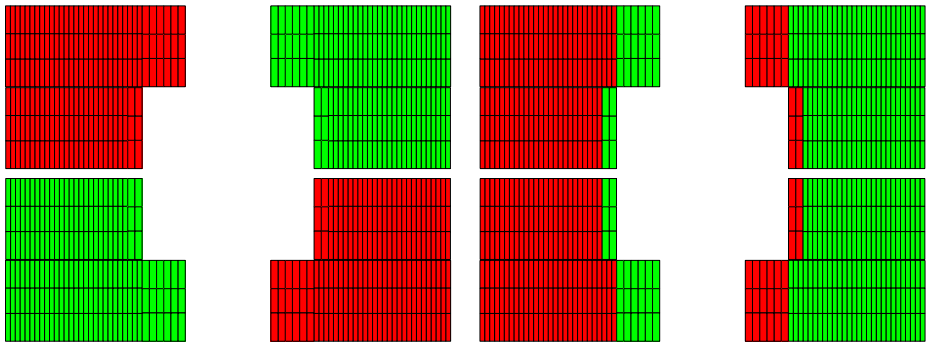

(a) PP CLIQ configuration.

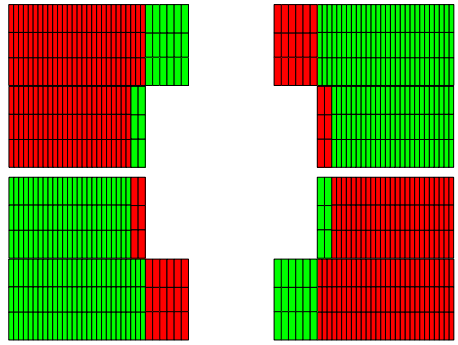

(b) LL CLIQ configuration.

(c) CL CLIQ configuration.

Figure 5.24: Current polarity of the initial CLIQ discharge with the alternative connection scheme into the *D v2* coil variant.

Table 5.6: Inductance values for the discharge paths in the alternative connection scheme of the *D v2* coil variant.

Variant	L_1 **[mH m^{-1}]**	L_2 **[mH m^{-1}]**	M_{12} **[mH m^{-1}]**	L_{eq} **[mH m^{-1}]**
PP	2.90	2.90	1.33	0.78
LL	7.19	0.11	0.58	0.05
CL	2.67	2.67	1.56	0.55

Since the equivalent inductance of the LL CLIQ configuration is as low as it is, the Ψ

takes on a very large value in the interface between the inserts and the rest of the pole (both upper and lower). This should translate into an extremely fast quench in that region. The PP and CL on the other hand, should behave quite similarly to each other, with poorer performance.

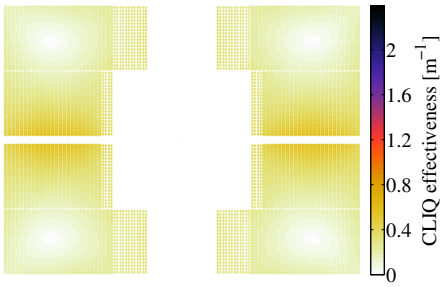

(a) PP CLIQ configuration.

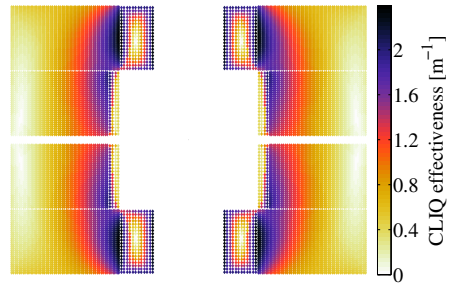

(b) LL CLIQ configuration.

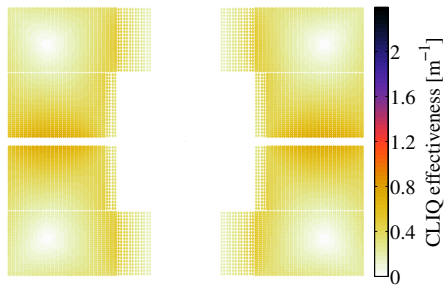

(c) CL CLIQ configuration.

Figure 5.25: CLIQ effectiveness for the CLIQ configurations on the *D v2* coil variant.

The effect of varying the CLIQ parameters and configuration on the *D v2* coil variant is shown in figure 5.26. Note that the red crosses mark data points that do not exist — when running simulations for this very unbalanced set of electrical parts, the numerical solver became unstable when the total current in any electrical part fell below zero. As this problem only arose for a very small number of simulations, namely the ten indicated with red crosses in the figure, finding a solution to the problem was never a priority. As such, the data presented is of somewhat reduced value.

That said, it is clear that the combination of small capacitance and high voltage is the most desirable from the protection point of view. It is possible to provide the desired level of protection with both the LL and LLrev CLIQ configurations without significantly increasing the charging voltage of the CLIQ unit, with the LL being somewhat more sensitive than the LLrev.

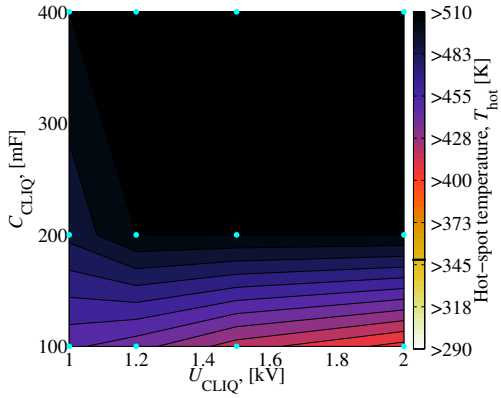

(a) PP CLIQ configuration.

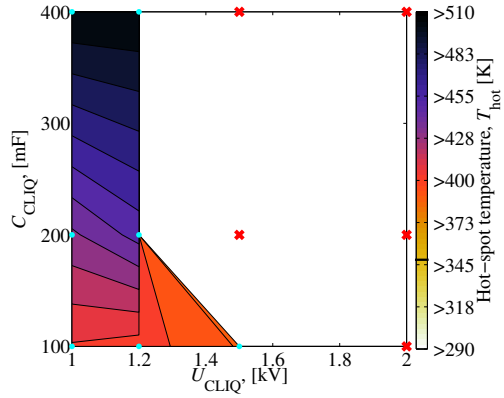

(b) CL CLIQ configuration.

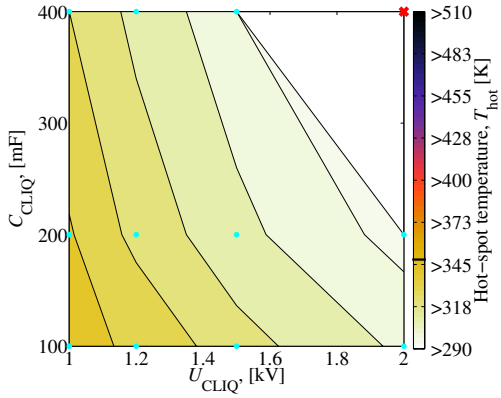

(c) LL CLIQ configuration.

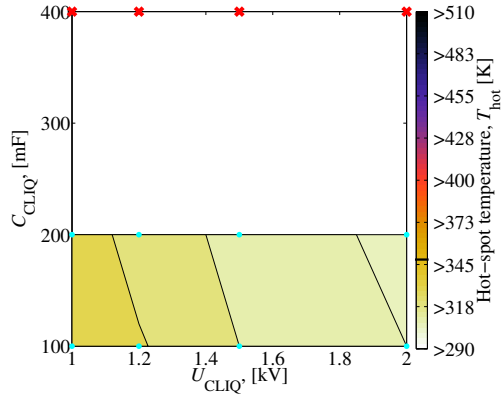

(d) LLrev CLIQ configuration.

Figure 5.26: Hot–spot temperature in the *D v2* coil variant for different CLIQ capacitances, voltages and configurations.

Note that comparing the plots of hot–spot with the two different connection schemes of the *D* variant, for the PP only, the results are very similar. This is to be expected from comparing the CLIQ effectiveness and current polarity plots of the two configurations; however, as mentioned in the beginning of this chapter, the *D v2* simulations were all run with a constant differential inductance value, while the *D* simulations were run with one closer to the complete (simulated) differential inductance (shown in figure 5.3), and thus, comparing the PP plots for the two connection schemes will serve to quantify the error incurred by using a completely static value for the inductance.

Table 5.7 shows the simulation results for the PP CLIQ configuration on the two ways to connect the *D* coil variant. As seen, the difference is about 10–15 [K] across the four different voltage levels. Although the differential inductance used for the *D* scheme does have a flat section, around the nominal current, the comparison serves to support the results for both the *D v2* and the F variants, as error seems to be quite small.

Table 5.7: Hot–spot temperature in the D coil variant for the *D* and *D v2* connection scheme. Not that only numbers for $C_{\mathrm{CLIQ}} = 100$ [mF] and the PP CLIQ configuration are shown.

Connection Scheme	**1000 [V]**	**1200 [V]**	**1500 [V]**	**2000 [V]**
D	465	450	435	420
D v2	452	444	425	406

Finally, the reason why the LL and LLrev are so similar for the *D v2* variant is that the inserts are so small in volume, compared to the rest of the coil that the effect of grading mentioned back in section 5.1 vastly overpowers any difference due to the initial current being positive or negative.

5.7 Summary of CLIQ Performance on All Coil variants

In figure 5.27 the hot–spot temperatures for varying initial transport currents are plotted — one figure for each CLIQ configuration. All these simulations are for the nominal CLIQ unit and nominal fraction of non–Copper.

On the large scale, the *D* coil variant, both in its *D* and *D v2* connection scheme, is the hardest to protect by a large margin. It is possible to keep the hot–spot below 350 [K] with the *D v2* scheme, when employing the LL or LLrev CLIQ configuration, for the nominal transport current. At close to short–sample current the nominal CLIQ unit applied to nominal conductor properties fail.

Disregarding the *D* coil variant, the typical picture shows the base line *A* coil variant together with *C* as one group, and the *B* and *F* coil variants as another. The PP CLIQ configuration is insufficient at nominal parameters to protect any of the coil variants (*A* and *C* at both nominal and short–sample, *B* and *F* only at short–sample), while the other three configurations have the necessary performance, with the LLrev coming out with the lowest hot–spot temperatures for all variants.

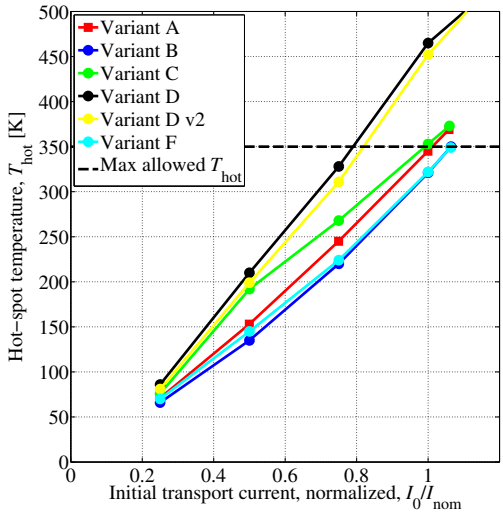

(a) PP CLIQ configuration.

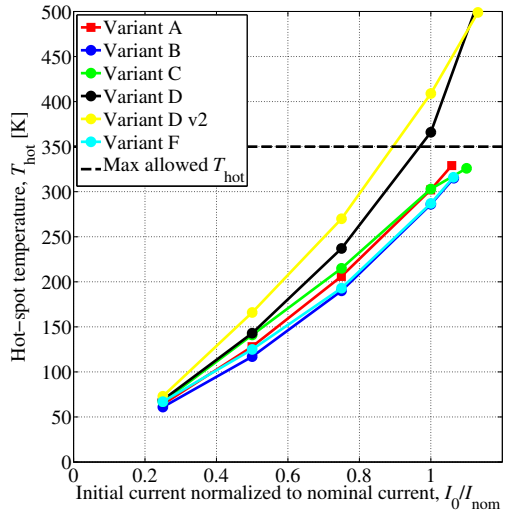

(b) CL CLIQ configuration.

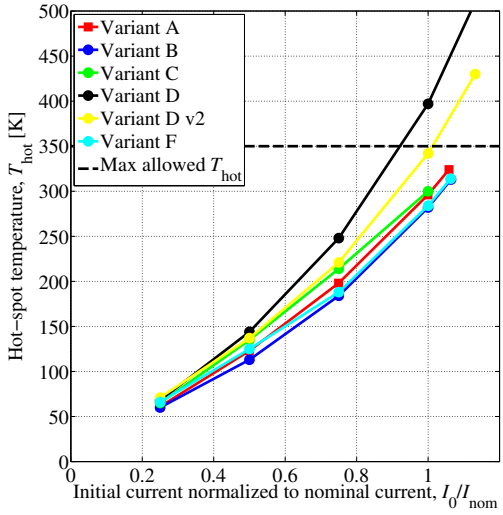

(c) LL CLIQ configuration.

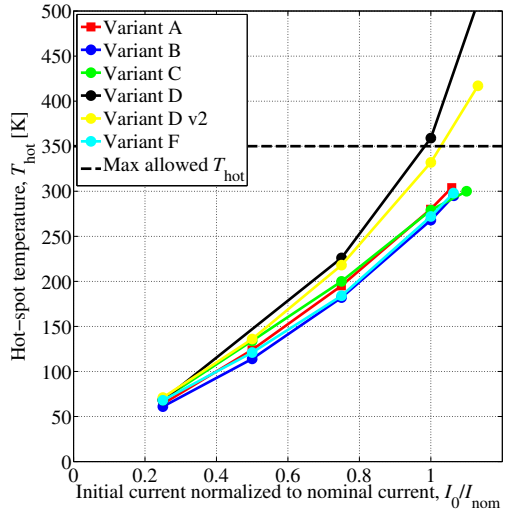

(d) LLrev CLIQ configuration.

Figure 5.27: Hot–spot temperature as a function of the initial transport current for all coil variants and CLIQ configurations. Note that the CLIQ unit used in all simulations use the nominal parameters, $C_{\mathrm{CLIQ}} = 100$ [mF], $U_0 = 1000$ [V].

5.8 Improved Operating Margin in Variant F

The F coil variant seems very promising from the protection point of view, easily keeping hot–spots below even 300 [K]. For this reason, it is interesting to look into trading some of the temperature margin for a gain in the field margin.

Figure 5.28 shows the dipole field in the coil as a function of the non–Copper fraction in the strands, at the short sample current of the coil. Thus, the value in the plot indicates the operating margin at nominal current — increasing the current gives a higher field, but at the short–sample current, the critical surface of the material is breached, and the magnet

quenches.

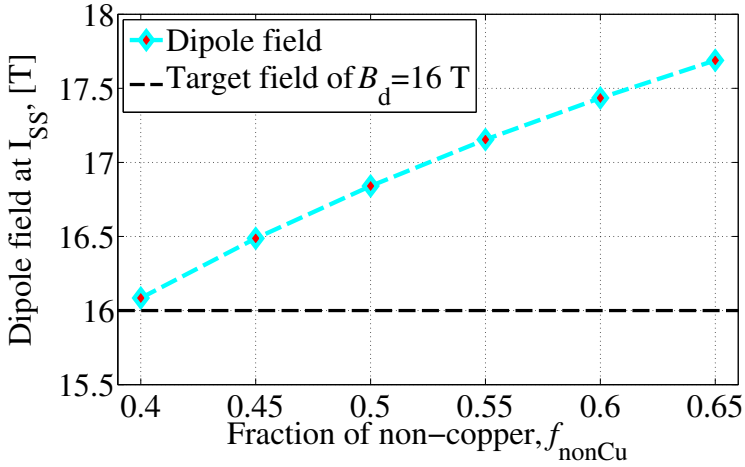

Figure 5.28: Dipole field at short–sample current for the nominal superconductor, at different fractions of non–Copper, in the F coil variant.

Figure 5.29 shows the same plot of the field at short–sample current, now including the hot–spot temperatures at the various fractions of non–Copper as well.

At the nominal value of non–Copper content, 55%, the field margin is about 7%, while the temperature margin for the PP CLIQ configuration is about the same[11]. Changing the CLIQ configuration will allow a larger faction of non–Copper, and thus a larger field margin, while also improving the temperature margin moderately. However, the best possible situation still leaves only a 9% field margin and 10% temperature margin. The field margin in the LHC dipoles is about 14% [11, Sec. 7.2.7], and so, it would be desirable to achieve the same in the block–coil dipole.

[11] The operating field is 16 [T], while the short–sample field is about 17.2 [T]; the final hot–spot temperature is about 325 [K], while the limit is 350 [K].

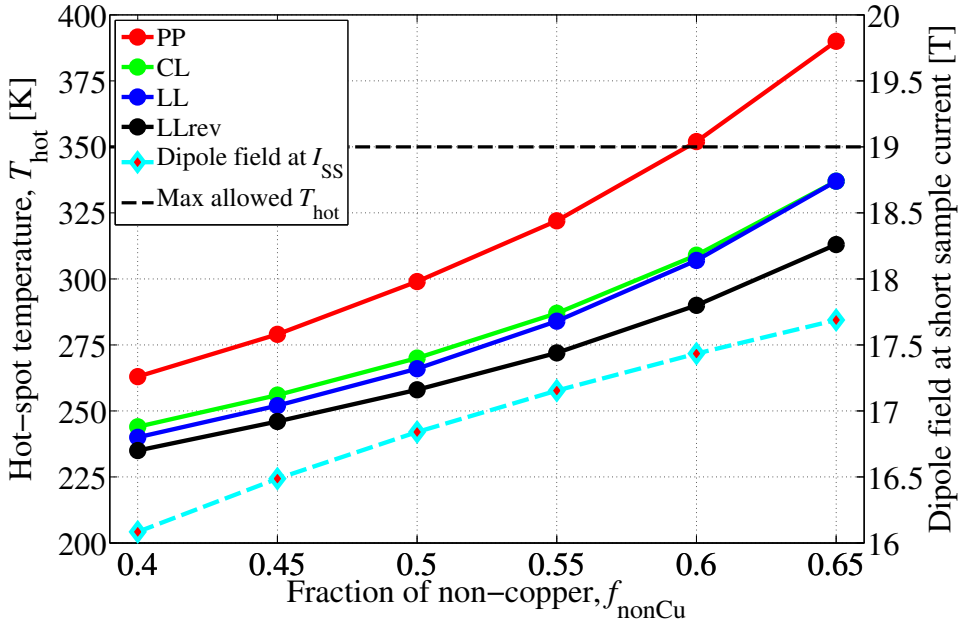

Figure 5.29: Hot–spot temperatures and dipole field at short–sample current for the nominal superconductor, at different fractions of non–Copper, in the F coil variant.

By improving the superconductors pinning properties, as discussed in section 4.8, it is possible to increase the short–sample current, and thus field margin, at the expense of a higher hot–spot temperature.

In figure 5.30, the short–sample dipole field is plotted for a superconductor that has exactly 15% field margin at the nominal fraction of non–Copper. Additionally, the figure plots the new, heightened, hot–spot temperatures. The sacrifice in temperature margin is only modest; typically any given point has moved between 10 and 25 [K], while the field margin is doubled at the nominal non–Copper fraction. The figure also shows that the coil, variant F, is still fully able to remain protected with only the PP CLIQ configuration needing a reduction of non–Copper content to become viable (and thus going back on the field margin, counter to the desire of the exercise); the other configurations able to maintain hot–spots mostly below 300 [K].

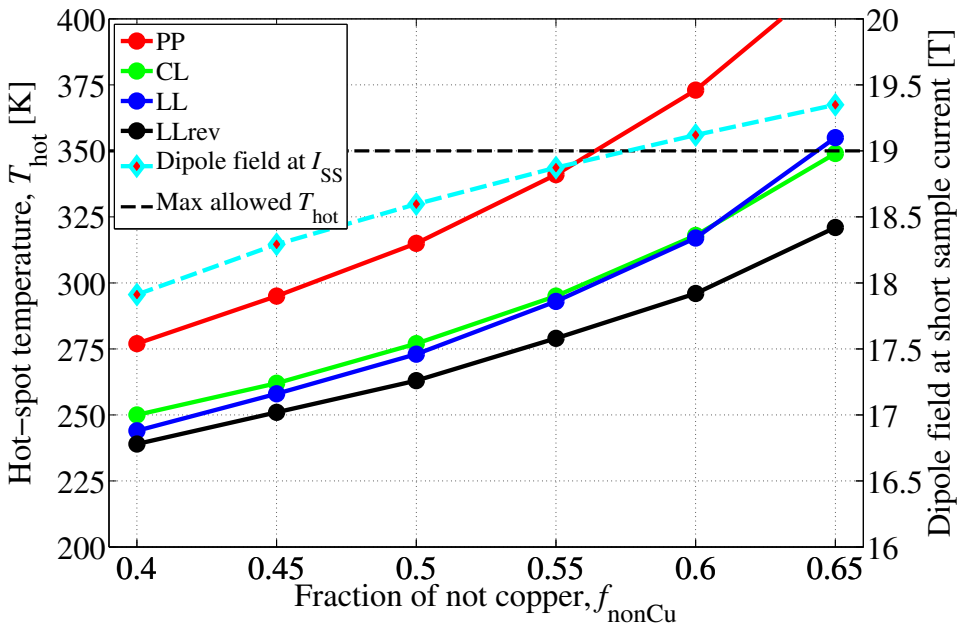

Figure 5.30: Hot–spot temperatures and dipole field at short–sample current for the improved superconductor, at different fractions of non–Copper, in the F coil variant.

5.9 Conclusions

After this study of the various propositions for alternative coil geometries, it is apparent that, thermally, the reduced inductance coil (variant B) and the scaled up coil (variant F) outperform the other alternatives with substantial margin measured by the hot–spot temperature for all CLIQ configurations — both coils lie, depending on the CLIQ configuration used, between 275 and 325 [K] at their respective nominal currents.

The increased inductance coil (variant C) is worse than the reference, variant A, coil, but with other configurations than PP it is possible to provide the desired protection level with a hot–spot between 275 and 300 [K], LLrev being the best, leaving the fraction of copper unaltered. For the PP to sufficiently protect the magnet, the copper fraction must become so large that the coil will suffer unstable operation due to a lack of superconductor.

The D variant is almost impossible to protect, and only the LLrev CLIQ configuration with *reduced* capacitance and *increased* voltage compared to the nominal CLIQ parameters, is able to protect it with any appreciable margin to the limit — with a charging voltage of 1.5 [kV] and a capacitance of 75 [mF], the hot–spot reaches around 320 [K] at nominal initial transport current.

The D *v2* variant, identical to the D, but with different electrical parting, proves somewhat more promising, where the LL and LLrev CLIQ configurations are able to keep the hot–spot right under 350 [K] for nominal CLIQ parameters and can be further improved with increases in capacitance and charging voltage. The increasing the voltage, however, increases the risk of voltage breakdown, either to ground or within the coil, and the graded coil, no matter the structure, seems too large a challenge from a protection point of view.

When increasing the operating margin of the F variant, by improving the pinning characteristics of the superconductor, it is possible to both have a 15% field margin and a temperature margin of more than 20%, making the F variant a very interesting proposition. While

it is not investigated directly, the properties of the B variant seem so similar to the F, that it is safe to assume that also the B variant would benefit in a similar way in terms of improved field margin.

Chapter 6

Analysis of the Internal Voltages in the Coil

This final chapter I use to analyse the voltages in all the coil variants during a CLIQ discharge — they can become very large, and care must be taken to select the optimal balance between voltage and hot–spot characteristics.

All CLIQ configurations are taken into account and also the possibility of connecting the coil's cables in various orders. The same, more thorough, description of the graded and larger aperture coil variants from chapter 5 is also continued for the voltage considerations.

6.1 Coil Variant *A* — Pole–Pole CLIQ Configuration

The voltage across each electrical part of the A coil variant is shown in figure 6.1. This is for a discharge at nominal initial transport current, with a PP connected CLIQ unit, of nominal parameters $C_{\text{CLIQ}} = 100$ [mF], $U_0 = 1000$ [V].

At time $t = 1$ [ms], when the CLIQ unit is triggered, the voltages across the parts are purely inductive, and balanced, caused by the initial current change introduced by the CLIQ current. The amplitude of the current derivative then starts to fall, with the upper pole seeing a positive $\mathrm{d}I/\mathrm{d}t$ (parts 1 and 2), and the lower pole a negative $\mathrm{d}I/\mathrm{d}t$[1]. After a short time the coil starts to quench, and the total current in the magnet begins to decay by the resistance arising in the coil. Now, the voltage over the electrical part is a combination of the inductive voltage due to the oscillations in the CLIQ current as well as the decay in the over–all current, and the resistive voltage that builds up across quenched parts of the coil while the magnet current is still non–zero.

[1] See, for instance, figure 4.1 for a plot of the current during this discharge.

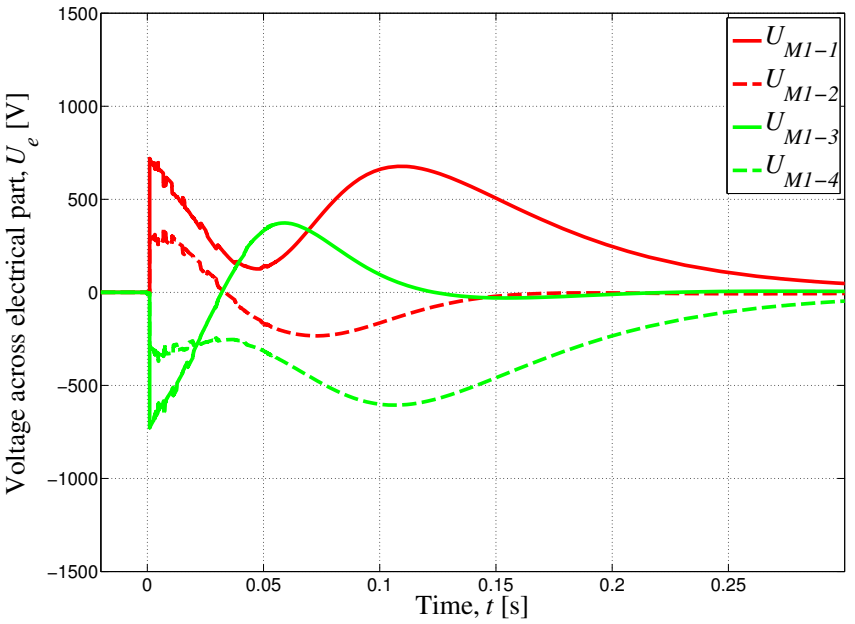

Figure 6.1: Voltages across each electrical part during the discharge of a nominal CLIQ unit, into the A variant block–coil dipole.

Starting from the end of the chain of series connected electrical parts, and labelling the node right before an electrical part A, B, C and D, as shown in figure 6.2, the voltage right before any electrical part can be expressed as in figure 6.3.

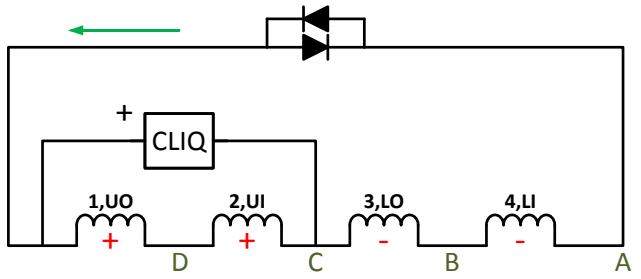

Figure 6.2: Voltages across each electrical part during the discharge of a nominal CLIQ unit, into the A variant coil.

Point A is the ground of the system, and the voltage is zero at all times in this point[2]. Looking at the time of triggering, point C sees the full, negative, charging voltage of the CLIQ unit, while points B and D are steps up towards zero according to the size of the electrical part in question[3].

[2]Disregarding voltages over the diodes in the power converter or small resistive components in the circuit outside the coil.

[3]A larger number of half–turns in the part means larger self–inductance, which means a larger inductive voltage given the same $\mathrm{d}I/\mathrm{d}t$.

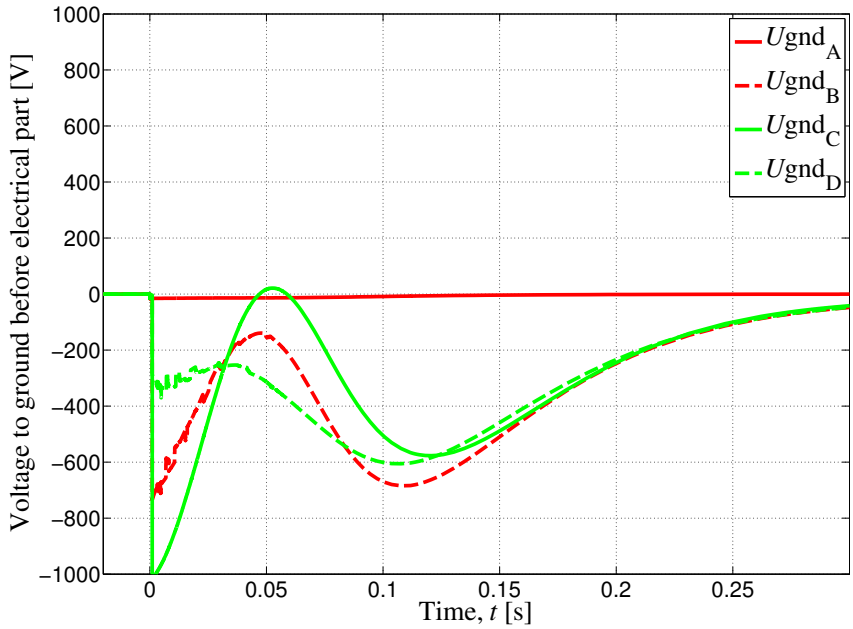

Figure 6.3: Voltages across each electrical part during the discharge of a nominal CLIQ unit, into the A variant coil.

6.1.1 Voltage Distribution Across the Coil's Half–Turns

Figure 6.4 shows the order of the turns in the A variant coil, for the connection order of parts as such: 1–2–3–4. Note that the inner most turns, the ones facing the bore, are connected together within the same pole. This is a consequence of how the coil is wound — from the bore and out.

While the half–turn order does not influence the over–all voltage across the coil, it does change what half–turns see the highest voltages, which means that one connection order could result in a large voltage difference across the inter–layer interface, while another would give the large voltage difference across the midplane (pole–to–pole), which is clearly a better situation from an electric breakdown point of view.

Throughout this chapter, the four possible connection orders are named by what order the electrical parts have. Order 1–2–3–4 (**A**) is the one shown here. Order 1–2–4–3 (**B**) is the order shown in the circuits of figures 2.10c and 2.10d. The two last orders swap the place of the inner and outer layer in the upper pole; 2–1–3–4 (**C**) and 2–1–4–3 (**D**). The other three orders are given as in figure 6.4 in appendix C. Other technically feasible connection orders exist, but they are symmetric to the four given, and as such need not be considered separately.

The PP CLIQ configuration can be used with any connection order, while the LL and LLrev only work with orders 1–2–4–3 and 2–1–3–4. The CL, likewise, is restricted to the 1–2–3–4 and 2–1–4–3.

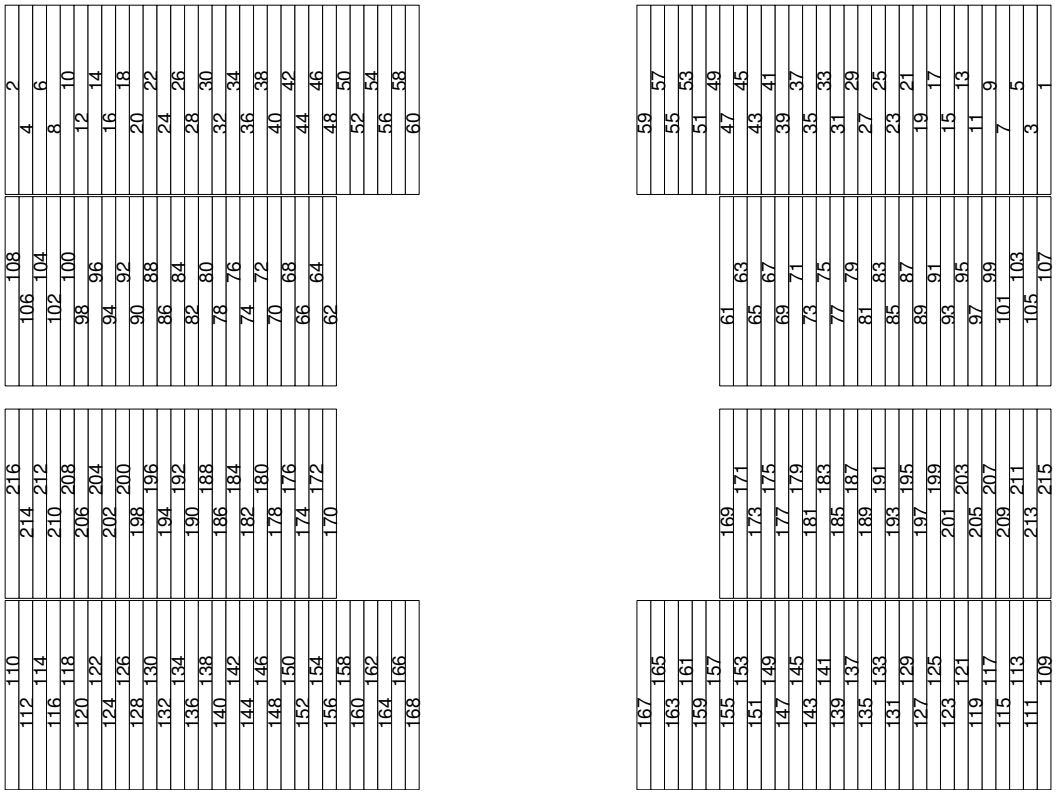

Figure 6.4: The 1–2–3–4 half–turn connection order, for the *A* variant coil, named after the order of electrical parts.

To obtain a fast and acceptably accurate estimate of the voltage across each half–turn it is assumed that the inductive voltage is linearly distributed over the conductors within a given electrical part, while the resistive voltage is given for each block, depending on temperature and time of quench.

With this assumption, the voltage over each half–turn of the coil is plotted in figure 6.5. The colours of the curves follow the order within an electrical part as given in figure 6.4 — in parts 1 and 3, black is the outer–most half–turn (number 1 in part 1, number 109 in part 3), while white is the inner–most (number 60 in part 1, and 168 in part 3). In parts 2 and 4, black is the inner–most (number 61 in part 2, number 169 in part 4) while white is the outer–most half–turn (number 108 in part 2, number 216 in part 4). Orange indicates a half–turn towards the middle, regardless of part (for instance number 30 in part 1).

Two important features are clear; the peak voltages may very well surpass the initial charging voltage of the CLIQ unit, and the peaks typically occur in the middle of an electrical part (orange–ish curves). Looking at electrical part 1 and 2, the two layers of the upper pole, the voltage across this inter–layer interface reaches around 2 [kV] around 100 [ms] into the discharge. The voltage across the midplane (part 2 to 4) is fairly small over the whole transient, while the inter–layer voltage in the lower pole (part 3 to 4) reaches about 1.5 [kV].

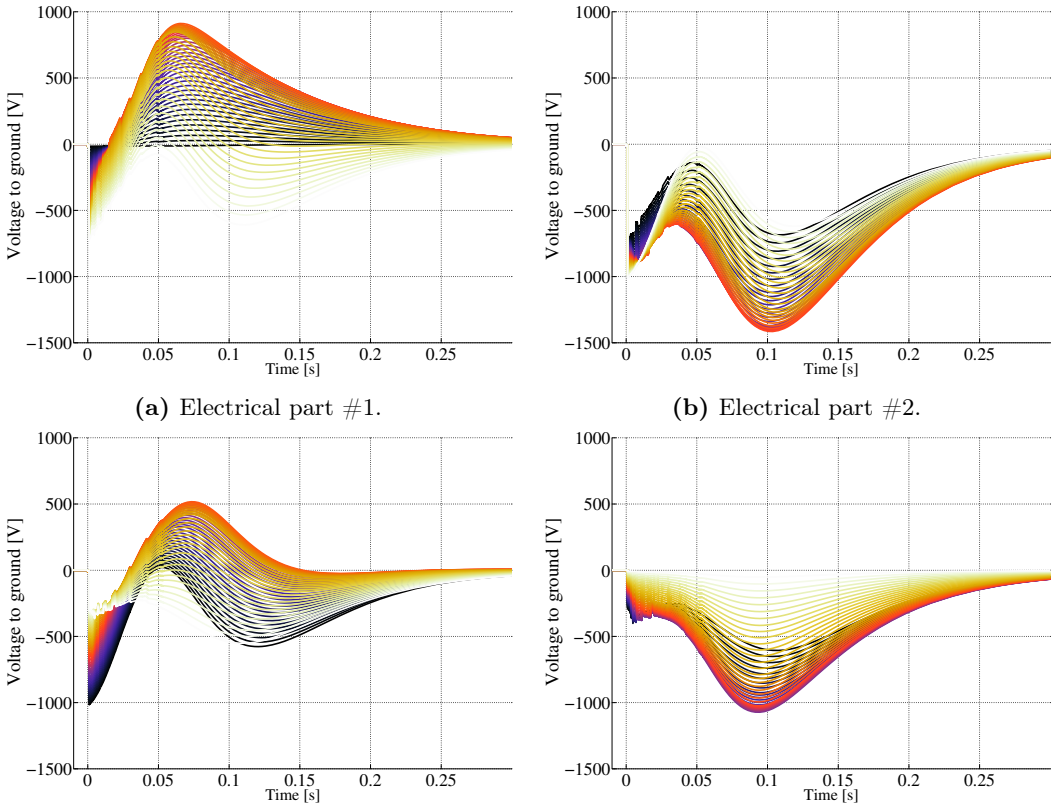

(a) Electrical part #1.

(b) Electrical part #2.

(c) Electrical part #3.

(d) Electrical part #4.

Figure 6.5: Voltage to ground for each half turn of the A variant coil as it develops in time during a PP CLIQ discharge, with connection order; 1–2–3–4. Dark corresponds to half–turns at the beginning of the electrical part, while light corresponds to half–turns at the end of the electrical part.

Figure 6.6 plots the data from figure 6.5 as a 2D representation over the coil's cross section, only at certain times, to represent the voltage distribution in the coil as it develops during the discharge. With this representation it is clear that a large voltage difference in the midplane poses far lower a risk than a high voltage in the inter–layer interface within a pole, given the large difference in distance between the two electrodes.

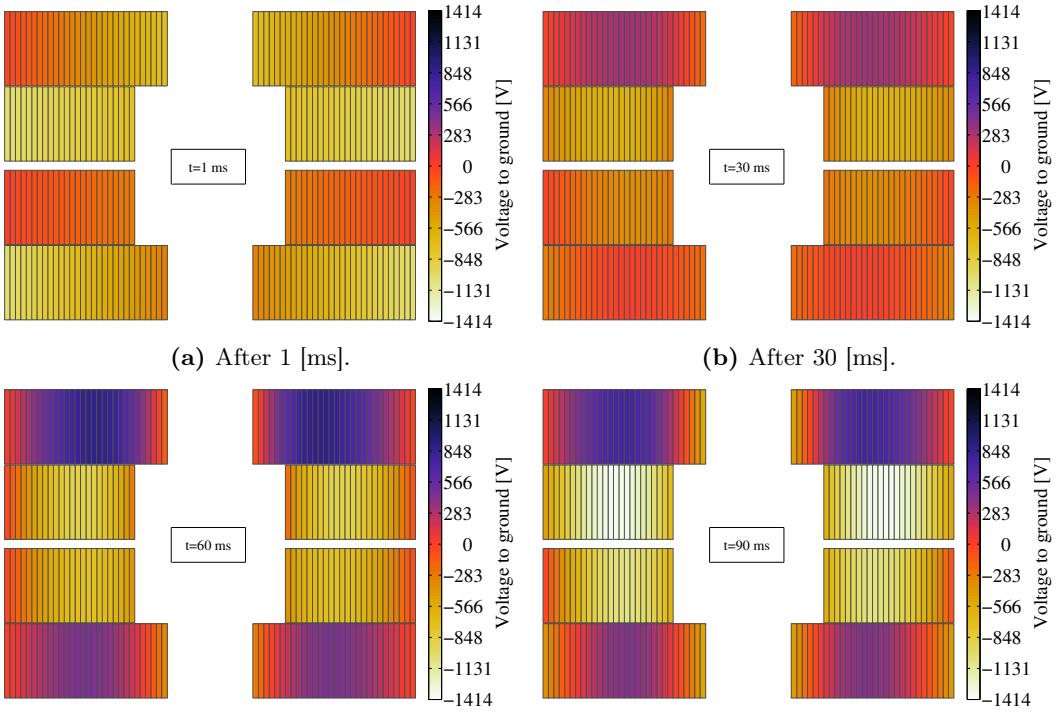

(a) After 1 [ms]. **(b)** After 30 [ms].

(c) After 60 [ms]. **(d)** After 90 [ms].

Figure 6.6: Voltage to ground for each half turn of the *A* variant coil as it develops in time. Pole–pole CLIQ configuration, with connection order; 1–2–3–4.

6.1.2 Significant Voltage Values

Several voltage values of significance relate to different locations in the coil. Figure 6.7 shows the four areas where large voltages may be particularly problematic.

Area *a* indicates all the eight half–turns closest to the grounded bore/beam pipe. Although the distance from the coil to the bore is quite large, this area is still of interest. Voltages in this area will be referred to as Coil–to–bore (CtoB) voltages.

Area *b* indicates the midplane interface (both sides of the coil), where large voltage differences may cause breakdown from one pole to the other. Also here, the distance is quite significant, and the risk is not large. Voltages in this area will be referred to as Midplane (Mid) voltages.

Area *c* indicates the inter–layer interfaces (four of them in a block–coil dipole magnet). A large voltage difference across the very thin layer of insulation here is critical for the operational safety of the CLIQ system. Voltages in this area will be referred to as Inter–layer (IL) voltages.

Area *d* indicates the entire perimeter of the coil, and is of interest due to the grounded steel collar that envelops the entire coil for the sake of mechanical stability. Also here, the distance between the high voltage and low voltage side (half–turn–collar) is very small, and the risk of breakdown is higher than for *a* and *b*. Voltages in this area will be referred to as Coil–to–collar (CtoC) voltages.

In addition to this, the peak Turn–to–turn (TtoT) voltage is of interest, seeing as voltage breakdown within the coil is just as detrimental as breakdown directly to ground.

For the discharge discussed now, a nominal CLIQ unit connected to the reference, variant A, coil, at nominal initial transport current, the four critical voltages are summarised in table 6.1. It is particularly worrying that the inter–layer voltage reaches above 2 [kV]. The peak coil–to–collar voltage occurs in the outer–most half–turns of electrical part 2, while the peak coil–to–bore voltage is for the inner–most half–turns of the same electrical part. Note also that the peaks do not occur at the same time.

Table 6.1: The peak voltages in the four key areas during the discharge of a nominal CLIQ unit into the reference, variant A, block–coil dipole.

Peak voltages, [kV]				
IL	**Mid**	**CtoC**	**CtoB**	**TtoT [V]**
2.1	1.0	-1.0	0.8	85

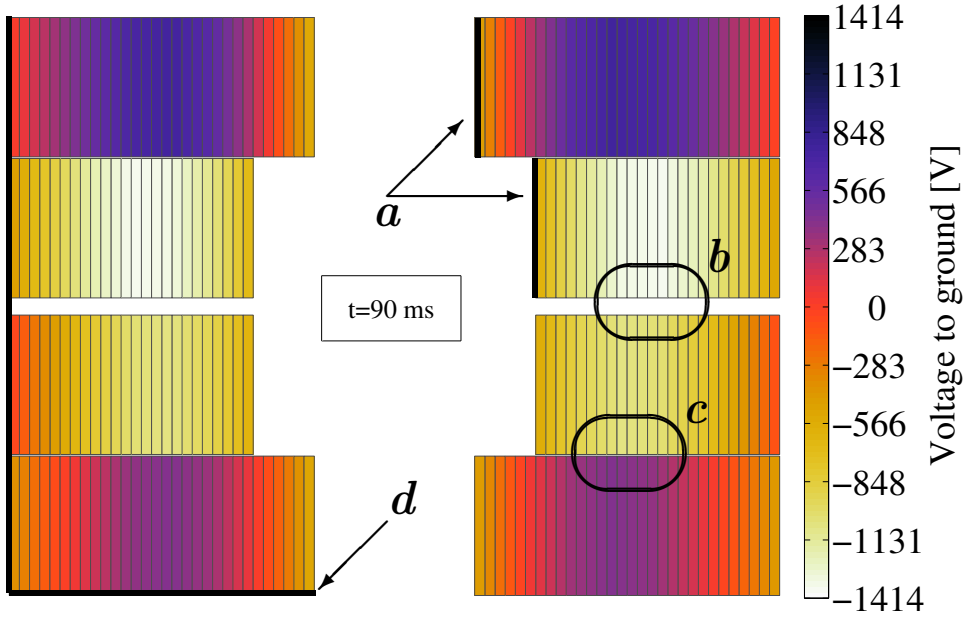

Figure 6.7: Four key areas where voltages are of particular interest.

As for the hot–spot temperature, it is convenient to select a voltage limit, above which a given configuration is deemed unsatisfactory. In the LHC Design Report specifications for different sorts of insulation are given; for the turn–to–turn insulation, the requirement is 100 [V] [11, Sec. 7.3.4], while the insulation used between the quench heaters and the coil is selected for an operating voltage of 1 [kV], and tested for 5 [kV][4] [11, Sec. 7.3.11], likewise for the insulation of the corrector magnets [11, Sec. 7.6.1]. The internal insulation of the LHC dipoles is tested at 3.5 [kV] [11, Sec. 7.7.1]. Magnet designers consider 1 [kV] the all–purpose rule of thumb, and as such, it seems pertinent to set this as the voltage limit also here, although improved insulation is not impossible to achieve if the need outweighs the cost [47, 48]. Both the 1 [kV] high–voltage limit and the 100 [V] low–voltage limit will be considered somewhat softer than that of the 350 [K] in the hot–spot.

[4]Dry air, room temperature.

It is, then, apparent that the PP CLIQ configuration with the 1–2–3–4 half–turn connection order supersedes the voltage limit for the insulation material by a very large margin, and thus must be discarded as a protection option. Recalling chapter 4, the hot–spot temperature is also too high for this scheme, and changes had to be made — increasing either the capacitance or the charging voltage — both changes will further increase the voltage in the coil, and so, this initial CLIQ system must be discarded.

6.1.3 Effect of Changing the Half–Turn Connection Order

By altering the connection order of the half–turns it is possible to change the location and amplitude of the peak voltage in the coil. Figure 6.8 shows how the choice of half–turn connection order influences the voltage distribution on the coil. As seen, using orders **C** and **D** slightly reduces the largest voltage to ground of any specific half–turn, but the peak inter–layer voltage stays the same regardless.

The difference comes from changing the location of ground. The relative voltage differences are the same as before, but ground has been lowered by about 200 [V]. Seeing as both the inductive and resistive voltages must remain the same over–all, as the connection order does not alter the way the coil quenches (and thus how the current decays), the inductive voltage across the first part of the coil sets the ground level — when the inner layer of the upper pole is connected first, this lowers the absolute voltage of the entire system, as the self–inductance of this electrical part is smaller than the outer layer; a smaller voltage falls across it.

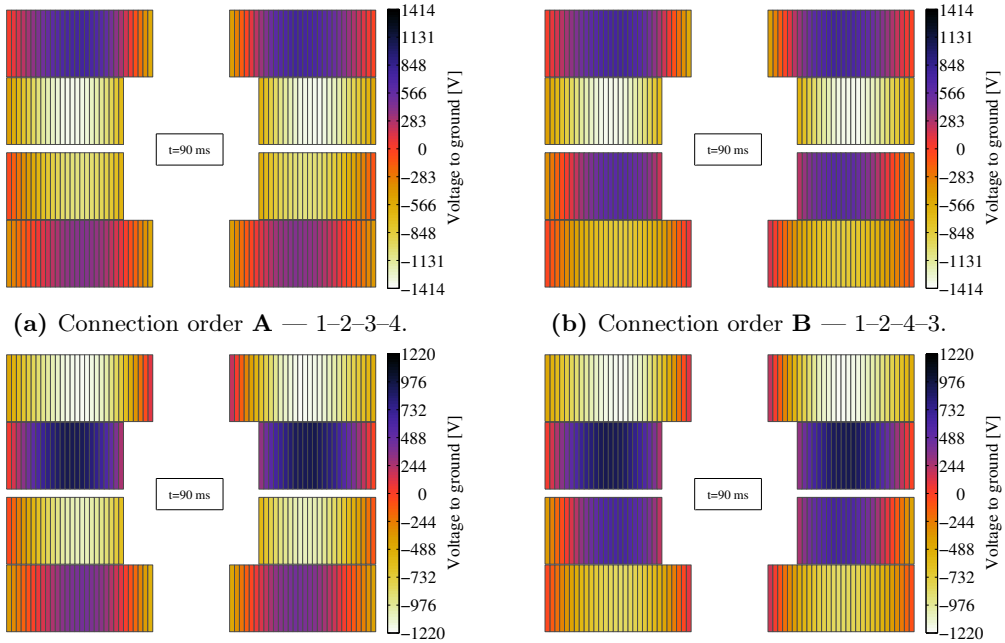

(a) Connection order **A** — 1–2–3–4.

(b) Connection order **B** — 1–2–4–3.

(c) Connection order **C** — 2–1–3–4.

(d) Connection order **D** — 2–1–4–3.

Figure 6.8: Voltage to ground for each half turn of the coil at time $t = 90$ [ms], during a PP CLIQ configuration discharge into the variant A, reference coil, with all four possible connection orders of the half–turns.

Table 6.2 summarises the effect of altering the connection order of the half–turns. None of the connection orders change the peak inter–layer voltage, and only small changes are seen

in the coil–to–collar voltage. From this, it is clear that protecting the A coil variant with a PP CLIQ unit is not possible. For comparison purposes, connection order B is chosen as optimal for the PP, seeing as it keeps both the CtoC and CtoB voltages minimal, at the expense of a large Mid voltage — the voltage here is less critical than elsewhere, given the large separation between poles in the block–coil dipole.

Table 6.2: Peak voltages for all four half–turn connection orders, during a CLIQ discharge of a nominal CLIQ unit, into the reference, variant A, coil, at nominal initial transport current.

	Peak voltages, [kV]				
Half–turn order	**IL**	**Mid**	**CtoC**	**CtoB**	**TtoT [V]**
A: 1–2–3–4	2.1	1.0	-1.0	0.8	85
B: 1–2–4–3	2.1	2.0	-1.0	-0.7	85
C: 2–1–3–4	2.1	2.0	-1.2	-0.6	85
D: 2–1–4–3	2.1	0.9	-1.2	-0.7	85

6.1.4 Effect of Varying Fraction of non–Copper

When varying the fraction of non–Copper, the coil resistance changes substantially, as seen in section 4.7, and this will influence the resistive voltage in the coil just as much, and also alter the inductive voltage seeing as the current will decay differently; the $\mathrm{d}I/\mathrm{d}t$ in the later stages of the discharge will change.

When the fraction of non–Copper increases, the resistance in the coil increases, giving both a higher resistive voltage and also a faster current decay — both the resistive and the inductive components of the voltage will grow.

Table 6.3 summarises the influence of the non–Copper fraction on the peak voltages in the A variant coil. As is clear, the non–Copper content significantly alters the IL, Mid and TtoT voltages, but only barely change the CtoC and CtoB. Note that the change in sign of the CtoC voltage between 55 and 60% non–Copper fraction is due to a change in location of the peak — the negative peak is given by the inductive voltage early in the discharge, at the end of electrical part 2, while the positive voltage for higher non–Copper content is resistance dominated and located in the middle of electrical part 3.

It is clear, with almost a 50% increase, going from 2.1 [kV] at nominal to 2.9 [kV] at 65% non–Copper fraction, in IL voltage, that altering the non–Copper content must be done with care, so as to not exceed the insulation restrictions.

Table 6.3: Peak voltages for varying fractions of non–Copper, during a CLIQ discharge of a nominal CLIQ unit, into the reference, variant A, coil, at nominal initial transport current.

	Peak voltages, [kV]				
Half–turn order	**IL**	**Mid**	**CtoC**	**CtoB**	**TtoT [V]**
$f_{\text{nonCu}} = 45\%$	1.6	1.6	-1.0	-0.7	60
$f_{\text{nonCu}} = 50\%$	1.8	1.8	-1.0	-0.7	70
$f_{\text{nonCu}} = 55\%$	2.1	2.0	-1.0	-0.7	85
$f_{\text{nonCu}} = 60\%$	2.5	2.5	1.1	-0.8	100
$f_{\text{nonCu}} = 65\%$	2.9	2.9	1.3	-0.8	125

6.2 Effect of the CLIQ Configuration — Variant *A*

Changing the CLIQ configuration substantially alters the voltage characteristics of the discharge. The location of peaks as well as the point in time they occur are different from the PP discharge. Figure 6.9 how the voltage from the same capacitor (same charging value and capacitance) distributes itself over the coil when altering the connection points. Particularly the CL looks strange, given that it reaches voltages above the charging voltage of the CLIQ unit when only the inductive voltage is considered — this is explained as such: between the beginning of electrical part 2 (the inner most half–turns of the inner layer of the upper pole) and the end of electrical part 3 (the inner most half–turns of the outer layer of the lower pole) there has to be 1 [kV], given by the charging voltage of the CLIQ unit. The beginning of electrical part 1 (outer half–turns of the outer layer of the upper pole) and the end of electrical part 4 (outer half–turns of the inner layer of the lower pole) must both be at ground potential. Recalling, then, figure 2.10b, the voltage at the beginning of electrical part 2 must be positive, and thus it falls towards the end of electrical part 3. As part 2 and 4 are symmetric, the voltage across them is symmetric, and thus, across part 4 the voltage must *fall* to zero. This explains why the voltage in the initial stage of the discharge supersedes the charging voltage of the CLIQ unit; the end of part 1 must be at 1 [kV], but the end of part 2 has to exceed this value to allow for the end of part 4 to be at ground potential.

The LL and LLrev are identical at the beginning apart from the polarity. The difference in the scale comes about from the later development of the voltage, and so, the initial state can be explained as such: recalling figure 2.10c, the points where part 1 connects to part 2, and where part 3 connects to part 4, are at symmetric potentials, because with regards to these two points, the layer–layer configuration is symmetric about the ground potential[5]. As the CLIQ unit in this configuration is completely floating, the midpoint will reach exactly 500 [V] in the positive point and -500 [V] in the negative. For the LLrev it is simply the opposite.

[5]Think of it as such: part 1 and 3 are on the "outside" while parts 2 and 4 are on the "inside" of the circuit. So from the connection point itself, it is irrelevant what direction one looks — there will be a low–inductance part on your inside hand and a high–inductance part on your outside hand.

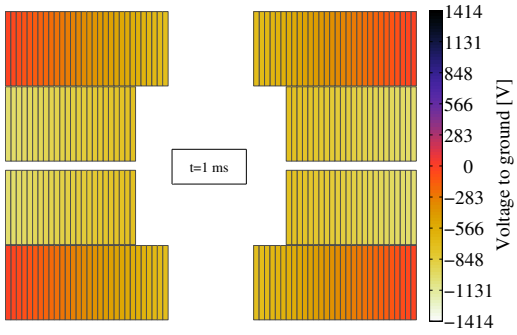

(a) PP CLIQ configuration with connection order **A** — 1–2–3–4, at $t = 1$ [ms].

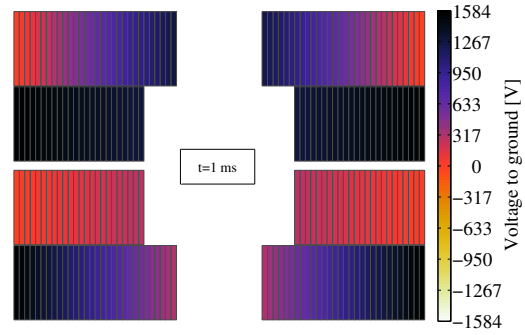

(b) CL CLIQ configuration with connection order **A** — 1–2–3–4, at $t = 1$ [ms].

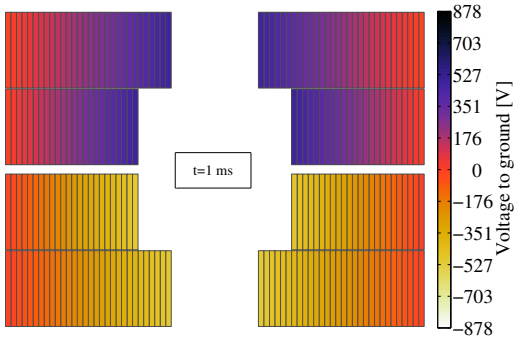

(c) LL CLIQ configuration with connection order **B** — 1–2–4–3, at $t = 1$ [ms].

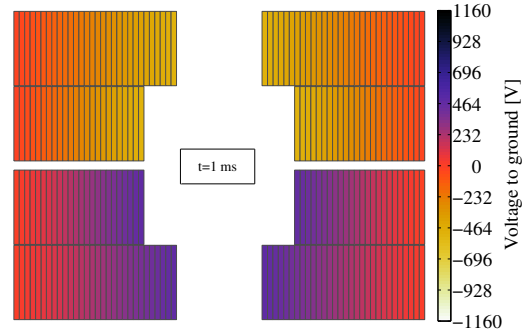

(d) LLrev CLIQ configuration with connection order **B** — 1–2–4–3, at $t = 1$ [ms].

Figure 6.9: Voltage to ground in all half–turns of the *A* variant coil, at time $t = 1$ [ms], during discharges with all four CLIQ configurations.

Plotting the voltage to ground of the half–turns with the largest positive and negative peaks within each individual electrical part for all four CLIQ configurations further highlights the differences; the maximum voltage in electrical part 1 for the PP discharge is in half–turn 33 — the middle of the part, while the peak negative voltage in electrical part 2 for the same discharge is in half–turn 25 — also in the middle (part 2 has fewer turns than part 1). These peaks occur around 70 to 100 [ms] in both parts, and gives the 2.1 [kV] inter–layer voltage from before.

Note that these figures only serve to give a general overview of the voltages, seeing as only the local peaks are considered, not peak differences across the four key areas.

Looking at the CL figure, it is clear that the largest positive peaks are the ones immediately after the CLIQ is triggered. The negative peaks are also substantial, but are reached far later, and also in different areas of the coil (typically in the middle). That half–turn 60 in part 1 has both the negative and the positive peak does not imply anything in particular — the resistive (positive) voltage at the end of the part is not sufficiently large to exceed the inductive (negative) voltage as the current decays (for this part), and so, the end of the part sees both the positive and negative peaks.

For the LL, half–turn number 55 in electrical part 1 is indicated as the peak — this is due to the voltage spike that arises when a large part of the coil quenches while the inductive voltage is still large; disregarding this voltage spike, the last half–turn of the part has the highest voltage (500 [V], being half the CLIQ charging voltage). In parts 2 and 4, giving the midplane area, half–turns 25 see their positive and negative peaks at the same time in both

parts — the peak midplane voltage is then about 1.6 [kV].

Both the midplane and inter–layer peaks can be identified in the LLrev plot, as the inductive voltage stays very similar as for the LL, but the resistive voltage changes due to faster quench; half–turn 25 in part 1 (max) and half–turn 17 in part 2 (min) are quite close, indicating a peak inter–layer voltage of about 1.5 [kV], while the same half–turn in part 2 is also close to half–turn 33 in part 4, giving a midplane voltage as high as 2.5 [kV]. These estimates are not very accurate, though, as the half–turns highlighted are not exactly opposite each other over the interfaces.

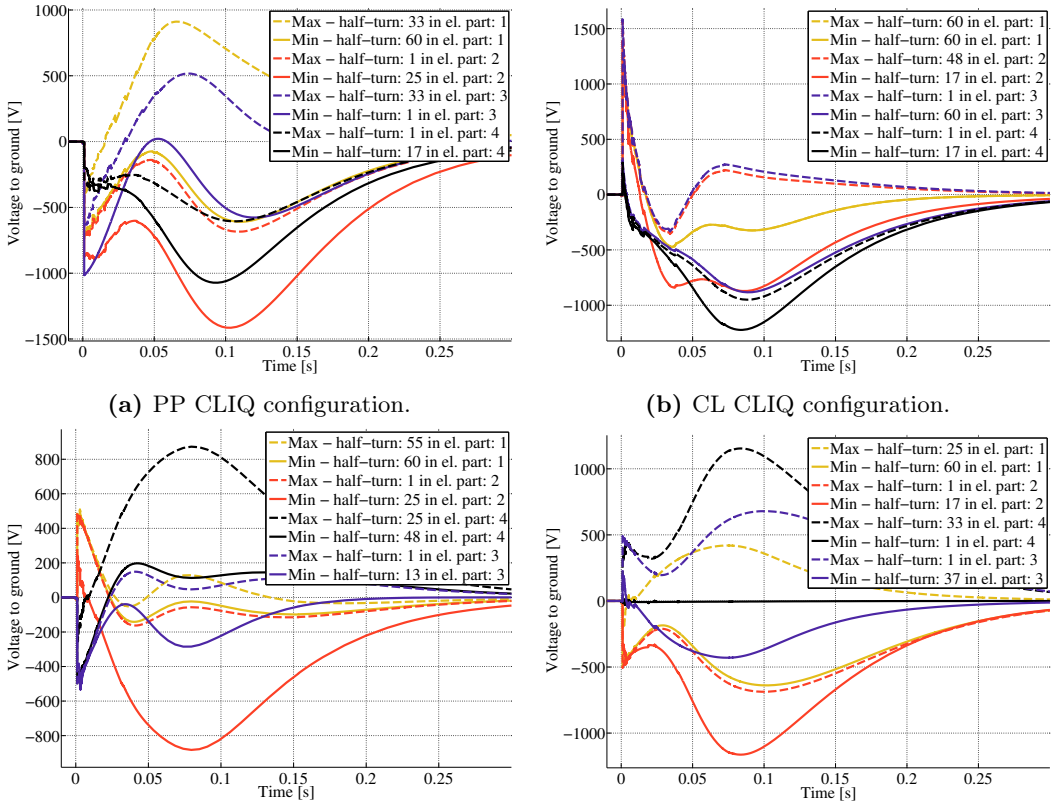

(a) PP CLIQ configuration.

(b) CL CLIQ configuration.

(c) LL CLIQ configuration.

(d) LLrev CLIQ configuration.

Figure 6.10: Voltage to ground in the half–turn with the positive and negative peak values in each electrical part for discharges with all four CLIQ configurations into coil variant A, at nominal initial transport current.

Figure 6.11 shows how the voltages to ground look for all half–turns in the variant A coil at a time $t = 90$ [ms] during discharges with the four CLIQ configurations.

The most important difference lies in the general location of peak voltages — for the PP and CL, the midplane voltages are quite small, while the inter–layer voltages reach very high values in comparison. For the LL and LLrev the midplane voltages go up substantially, but the inter–layer voltages are reduced compared to the PP and CL. The LL is clearly the better choice between the LL and the LLrev, seeing as voltage distribution itself is very similar, but the amplitude is lower. This is because the LL quenches the coil a little later and a little slower than the LLrev; the current decays slower, meaning a smaller inductive voltage during the later stages of the discharge, while the resistance in the coil is a little slower to

rise, meaning that the resistive part of the voltage is kept a little lower than for the LLrev. From previous chapters it is clear that the LLrev performs better in terms of hot–spot, with a typical difference of about 20 [K] in favour of the LLrev.

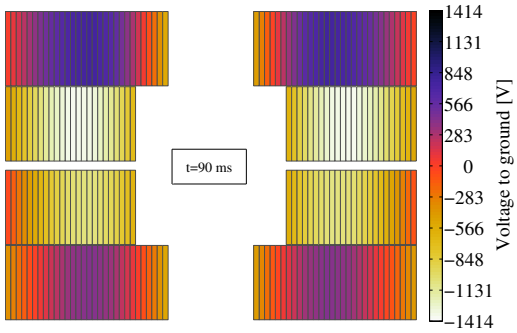

(a) PP CLIQ configuration with connection order **A** — 1–2–3–4, at $t = 90$ [ms].

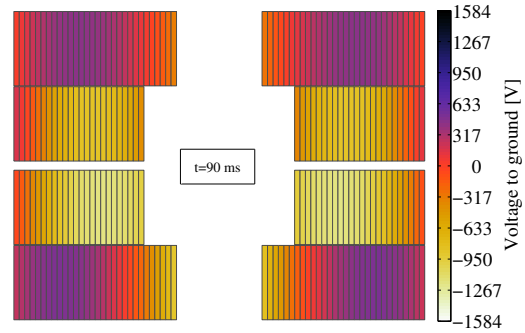

(b) CL CLIQ configuration with connection order **A** — 1–2–3–4, at $t = 90$ [ms].

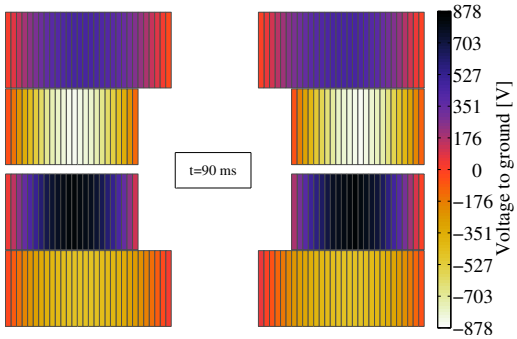

(c) LL CLIQ configuration with connection order **B** — 1–2–4–3, at $t = 90$ [ms].

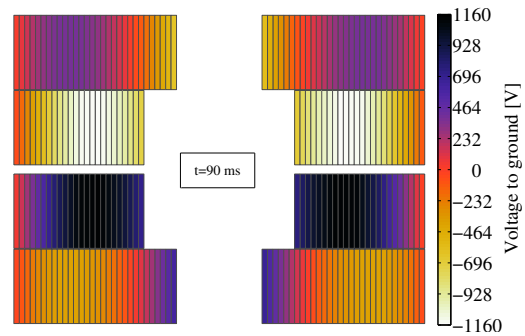

(d) LLrev CLIQ configuration with connection order **B** — 1–2–4–3, at $t = 90$ [ms].

Figure 6.11: Voltage to ground in all half–turns of the *A* variant coil, at time $t = 90$ [ms], during discharges with all four CLIQ configurations.

Table 6.4 shows the key voltage values for all combinations of CLIQ configuration and half–turn connection order. Note that there is no real difference between the **A** and **D** connections for the CL CLIQ configuration — connecting the half–turns as 1–2–3–4 or 2–1–4–3 is entirely symmetric for the CL in the sense that the figures 6.9b and 6.11b would be mirrored over the midplane, but keep the distributions and values.

All other configurations perform better than the PP in terms of both IL and TtoT voltage; as they also give significant improvements in hot–spot temperature over the PP, there is no longer any reason to keep the PP as an option.

For the LLrev, connection order **C** is by far the best option, with the peak CtoC voltage being almost half of the value with the **B** connection order. Both orders have the same IL and Mid voltages; while the Mid voltage might be acceptable, it certainly stretches the softness of the 1 [kV] limit set before, the IL is too high, given the challenging insulation situation between layers.

With this in mind, only the LL CLIQ configuration manages to obtain acceptable voltage levels — the IL does exceed the limit, but not by so much that it must be deemed impossible to overcome, while the same goes for the Mid voltage level. For a $\cos(\theta)$ coil this Mid voltage would be far more detrimental, as the distance between the upper and lower pole is much

smaller than in the block–coil geometry[6].

As for the LLrev, one connection order has substantially better CtoC voltage — the **B** connection order has this voltage lower than half the value of the **C** connection order, and is clearly preferred.

Table 6.4: Important peak voltages in the coil for nominal CLIQ parameters. The connection scheme for PP and CL connections is 1–2–3–4, while for LL and LL rev it is 1–2–4–3.

	Peak voltages, [kV]				
CLIQ configuration	**IL**	**Mid**	**CtoC**	**CtoB**	**TtoT [V]**
PP — Order **B**	2.1	2.0	0.9	-0.7	85
CL — Order **A**/**D**	1.6	1.5	1.6	1.3	70
LL — Order **B**	1.3	1.7	-0.5	-0.5	65
LL — Order **C**	1.3	1.7	-1.3	-0.6	65
LLrev — Order **B**	1.6	2.3	1.2	0.8	55
LLrev — Order **C**	1.6	2.3	0.7	0.7	55

6.2.1 Note on Varying the non–Copper Content for the LL CLIQ Configuration

Table 6.5 summarises the voltage peaks for the LL CLIQ configuration and shows the same trend as for the PP shown back in section 6.1.4; the IL, Mid and TtoT voltages all grow swiftly with larger fractions of non–Copper, while the CtoC and CtoB barely changes at all.

Note that the voltage and hot–spot temperature (as presented in section 4.7) respond in the same way to a change in the non–Copper content: they both go up for larger and down for smaller fractions.

In isolation, the non–Copper content can be changed so as to make the LL CLIQ configuration compatible with the 1 [kV] requirement in the IL. However, as mentioned back in section 4.7, this jeopardises the operational stability of the coil, and so cannot be done without other considerations in mind as well.

[6]See figure 2.11 for an example of a $\cos(\theta)$ coil.

Table 6.5: Peak voltages for varying fractions of non–Copper, during a CLIQ discharge of a nominal CLIQ unit, into the reference, variant A, coil, at nominal initial transport current, in the LL CLIQ configuration.

	Peak voltages, [kV]				
Half–turn order	**IL**	**Mid**	**CtoC**	**CtoB**	**TtoT [V]**
$f_{\text{nonCu}} = 45\%$	1.0	1.3	-0.5	-0.5	45
$f_{\text{nonCu}} = 50\%$	1.2	1.5	-0.5	-0.5	55
$f_{\text{nonCu}} = 55\%$	1.3	1.7	-0.5	-0.5	65
$f_{\text{nonCu}} = 60\%$	1.6	2.0	-0.6	-0.5	80
$f_{\text{nonCu}} = 65\%$	2.0	2.4	-0.7	-0.5	100

6.3 Voltages in the Alternative Coil Variants

From the conclusions in the previous section, the PP and LL CLIQ configurations will only be discussed with their **B** half–turn connection orders, and the LLrev only with the **C** half–turn connection order. The exception to this is the D coil variant, where the order of half–turns is not entirely equivalent to the other variants'. The CL only has one effective order, and will be discussed with the **A** order.

6.3.1 Coil Variant B — Reduced Inductance

When reducing the inductance of the coil, the inductive component of the voltage is reduced, as the voltage across an inductor is proportional to the inductance. With this reduced inductance, the CLIQ unit is more effective, as explored in chapter 5, and thus, the current decays faster than for the reference, variant A, coil. This faster decay means that the $\mathrm{d}I/\mathrm{d}t$ in the later part of the transient is somewhat higher, countering some of the lost inductance in terms of keeping the voltage higher[7]. Seeing, then, as the cable used in the B coil variant have a larger cross section than the reference ones, the resistive voltage will also be reduced, and so, the over–all effect; reduced inductance, somewhat increased $\mathrm{d}I/\mathrm{d}t$, and reduced resistance, is a marked reduction of the voltage in the coil, as compared to the reference, variant A, coil.

Table 6.6 summarises the important peak voltage values. Just like for variant A, the LL stands out as the best performer — the inter–layer voltage is within the 1 [kV] limit, 300 [V] below the corresponding value of the reference variant; the midplane voltage is not very far above the limit, also 300 [V] below the reference; while both the coil–to–collar and coil–to–bore are far below safe limits, being the same as the reference. The same goes for the peak turn–to–turn voltage.

For this coil variant it is notable also that the LLrev is not completely unreasonable, assuming that almost 2 [kV] across the midplane is acceptable — this does provide a noticeable improvement in the hot–spot temperature, as shown back in figure 5.27 (approximately 20 [K] improvement from the LL).

[7] The later part is here thought of as the part of the transient where the CLIQ oscillations have been damped completely, and only the exponentially decaying magnet current remains.

Table 6.6: Important peak voltages in the B coil variant for nominal CLIQ parameters. The connection order for PP and LLrev is **B** , CL is **A** and LL is **C**.

	Peak voltages, [kV]				
CLIQ configuration	**IL**	**Mid**	**CtoC**	**CtoB**	**TtoT [V]**
PP	1.7	0.9	1.0	0.7	75
CL	1.7	1.7	1.8	1.4	65
LL	1.0	1.4	0.5	-0.5	55
LLrev	1.1	1.8	0.9	0.6	55

6.3.2 Coil Variant C — Increased Inductance

For the C variant, the exact opposite is true: the higher inductance influences the inductive voltage more than the slightly lowered $\mathrm{d}I/\mathrm{d}t$, while the smaller cable give a larger resistance, over–all resulting in voltages much higher than for the reference variant. The PP fails on almost all accounts, with the inter–layer voltage far above a safe value, and even the turn–to–turn voltage skirting the threshold of 100 [V], as the summarising table 6.7 shows.

The LL is still the best option, but with an inter–layer voltage 60% above the limit, it is not satisfactory.

Table 6.7: Important peak voltages in the C coil variant for nominal CLIQ parameters. The connection order for PP and LLrev is **B** , CL is **A** and LL is **C**.

	Peak voltages, [kV]				
CLIQ configuration	**IL**	**Mid**	**CtoC**	**CtoB**	**TtoT [V]**
PP	2.7	1.0	1.5	0.7	100
CL	2.1	1.6	1.8	1.4	75
LL	1.6	2.2	-0.6	-0.5	65
LLrev	2.0	2.9	0.6	0.8	65

6.3.3 Coil Variant D — Graded Coil

The graded coil, variant D, poses a problem, as seen in figure 6.12; the inhomogeneous quench propagation, already discussed in section 5.1, gives rise to large voltage gradients around the interface between the coil insert and the regular cable. The figure shows the voltage in all half–turns of the coil at $t = 60$ [ms]. Compared to the smooth gradient in the A variant, in figure 6.11, the D variant has far larger turn–to–turn voltages.

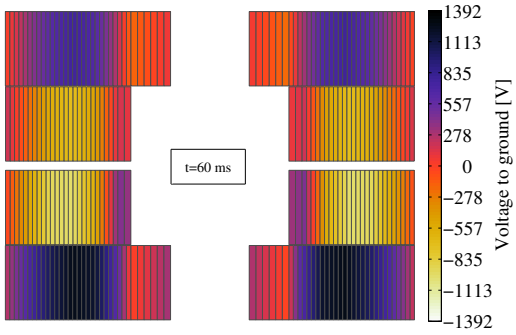

(a) PP CLIQ configuration with connection order **A** — 1–2–3–4, at $t = 60$ [ms].

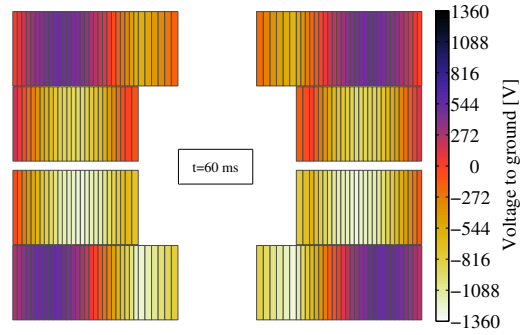

(b) CL CLIQ configuration with connection order **A** — 1–2–3–4, at $t = 60$ [ms].

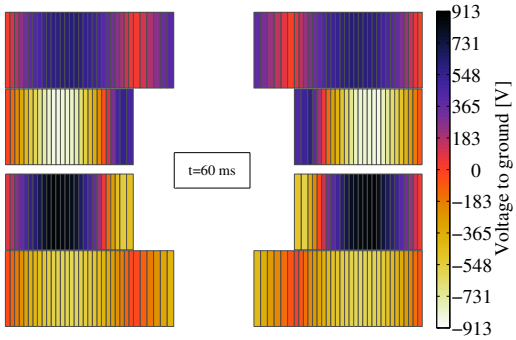

(c) LL CLIQ configuration with connection order **B** — 1–2–4–3, at $t = 60$ [ms].

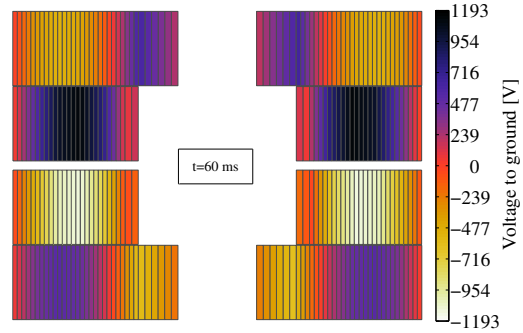

(d) LLrev CLIQ configuration with connection order **C** — 2–1–3–4, at $t = 60$ [ms].

Figure 6.12: Voltage to ground in all half–turns of the D variant coil, at time $t = 60$ [ms], during discharges with all four CLIQ configurations.

For the D variant, the small cable on the outside of the inserts quench very early, while most of the insert is still superconducting — this means that a large resistive voltage builds up in the quenched half–turn, while the inductive voltage of the insert stays the same. Table 6.8 summarises the voltage characteristics of the D variant, and it is clear that the turn–to–turn voltage is far too high, due to the difference across the insert–to–coil interface. The other key values are also on the high side, even for the LL CLIQ configuration, and the graded coil seems impossible to protect from the voltage insulation point of view.

Table 6.8: Important peak voltages in the D coil variant for nominal CLIQ parameters. The connection order for PP and LLrev is **B** , CL is **A** and LL is **C**.

	Peak voltages, [kV]				
CLIQ configuration	**IL**	**Mid**	**CtoC**	**CtoB**	**TtoT [V]**
PP	2.4	0.9	1.4	0.7	225
CL	1.6	1.3	-1.4	1.2	165
LL	1.4	1.7	0.6	0.5	195
LLrev	1.6	2.4	0.8	0.4	170

6.3.4 Coil Variant *D* — Graded Coil — Alternative Electrical Parts

The discussion of the *D v2* version of the *D* coil variant in section 5.6.2 indicates that the alternative connection scheme allows the LL and LLrev to protect the *D* coil — at nominal CLIQ parameters, the temperature margin is about 10 [K] for the LL and 20 [K] for the LLrev. Recalling the summarising figures showing how the initial transport current influences the hot–spot temperature, in the previous chapter (figure 5.27), the hot–spot rises almost 100 [K] going from nominal current to short–sample for the *D v2* — this means that protecting the coil will be near impossible at all current levels, and so, looking at the voltage in this section will be more for the sake of completeness than finding a working protection system.

From the simulation results in section 5.6.2, four cases are of interest: nominal CLIQ parameters for both LL and LLrev, and the LL with $U_0 = 1.2$ [kV], $C_{\mathrm{CLIQ}} = 400$ [mF], and the LLrev with $U_0 = 1.5$ [kV], $C_{\mathrm{CLIQ}} = 200$ [mF][8].

Figure 6.13 shows the voltage to ground of all half–turns, for the four interesting configurations, at $t = 60$ [ms]. It is obvious that the voltage gradient over the insert–to–coil interface is even worse than for the *D* variant[9].

Note that the half–turn order for the *D v2* is not as simple as the one for the other variants, and the **B** and **C** connection orders (**C** is the optimal for all four cases in the figure) are shown in appendix C[10].

[8] These two simulations give the same final hot–spot temperature of about 315 [K].

[9] The results shown here seem trustworthy when taking the success of the other simulations into account, but in their own right, the numbers seem almost sensational, and, ideally, more time should be spent investigating possible errors.

[10] Figure C.5.

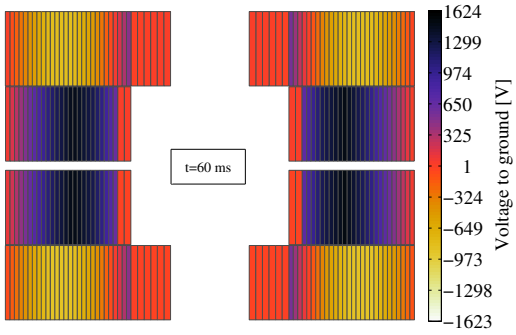

(a) PP CLIQ configuration with connection order **C** — 2–1–3–4, at $t = 60$ [ms].

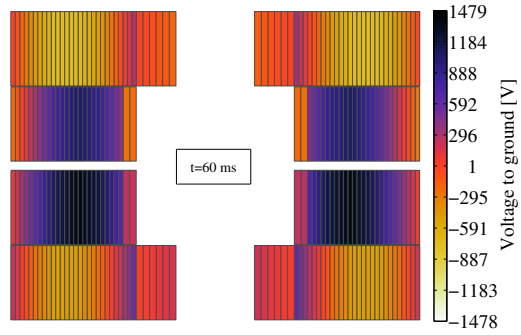

(b) CL CLIQ configuration with connection order **C** — 2–1–3–4, at $t = 60$ [ms].

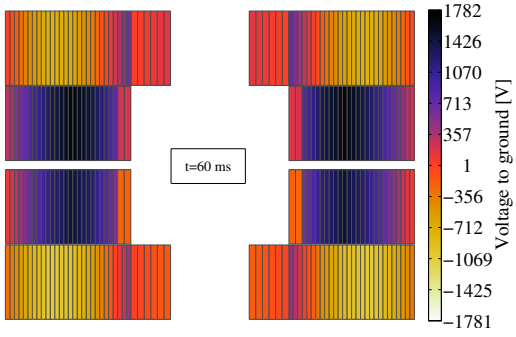

(c) LL CLIQ configuration with connection order **C** — 2–1–3–4, at $t = 60$ [ms].

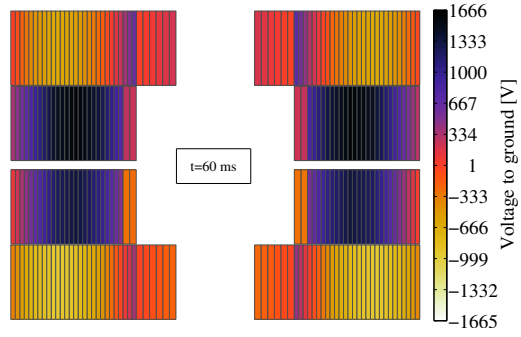

(d) LLrev CLIQ configuration with connection order **C** — 2–1–3–4, at $t = 60$ [ms].

Figure 6.13: Voltage to ground in all half–turns of the *D v2* variant coil, at time $t = 60$ [ms], during discharges with the LL and LLrev CLIQ configurations, with varying CLIQ parameters

Table 6.9 gives the most important voltage values, and the turn–to–turn voltages, with peaks always around the interface between the insert and the rest of the coil, are tremendously large, seven to nine times as large, compared to the design limit of 100 [V]. This can safely be assumed an insurmountable challenge.

Table 6.9: Important peak voltages in the *D v2* coil variant for varying CLIQ parameters. The connection scheme in all plots is the **C** half–turn order.

	Peak voltages, [kV]				
CLIQ configuration	**IL**	**Mid**	**CtoC**	**CtoB**	**TtoT [V]**
LL — nominal	2.4	1.6	1.3	0.4	900
LL — $U_0 = 1.2$ [kV], $C_{\text{CLIQ}} = 400$ [mF]	2.2	1.2	0.7	0.5	700
LLrev — nominal	2.5	1.6	1.4	0.4	900
LLrev — $U_0 = 1.5$ [kV], $C_{\text{CLIQ}} = 200$ [mF]	2.2	1.5	1.0	0.7	800

6.3.5 Coil Variant *F* — Larger Aperture

As with the hot–spot considerations, the *F* variant behaves the same as the *B* — smaller inductance gives a faster quench, and larger cable cross sections give a smaller resistance — and the voltages, as shown in table 6.10, are almost identical to those of the *B* variant.

The LL, again, is preferred, with an inter–layer voltage only slightly above the limit of 1 [kV], and very good coil–to–collar and coil–to–bore voltages.

Table 6.10: Important peak voltages in the *F* coil variant for nominal CLIQ parameters. The connection order for PP and LLrev is **B** , CL is **A** and LL is **C**.

	Peak voltages, [kV]				
CLIQ configuration	**IL**	**Mid**	**CtoC**	**CtoB**	**TtoT [V]**
Pole–pole	1.8	1.5	1.0	0.7	80
Crossed–layer	1.6	1.7	1.7	1.4	65
Layer–layer	1.1	1.5	0.5	-0.5	55
Layer–layer rev	1.3	1.9	0.6	0.7	55

6.3.6 Coil Variant *F* — Larger Aperture — Better Operating Margin

When increasing the operating margin of the *F* variant, investigated in section 5.8, it was clear that the hot–spot temperature rose as a trade off between temperature margin and field margin, where improved field margin was the goal. Table 6.11 summarises the impact this trade off has on the voltage of the coil — even if the quench initiation is slightly delayed by the improved superconductor (increased enthalpy margin to quench), there are no significant changes in the peak voltages during the CLIQ transient, and the LL CLIQ configuration remains the best choice from a voltage insulation point of view.

Table 6.11: Important peak voltages in the *F* coil variant, with improved operating margin, for nominal CLIQ parameters. The connection order for PP and LLrev is **B** , CL is **A** and LL is **C**.

	Peak voltages, [kV]				
CLIQ configuration	**IL**	**Mid**	**CtoC**	**CtoB**	**TtoT [V]**
Pole–pole	1.8	1.5	1.0	0.7	85
Crossed–layer	1.7	1.7	1.7	1.4	65
Layer–layer	1.1	1.5	-0.5	-0.5	60
Layer–layer rev	1.4	1.9	0.6	0.7	60

6.4 Conclusions

It is interesting to note from the discussion of the *D v2* variant that the voltages in the coil do not depend very largely on the charging voltage of the CLIQ unit; it is much more important how fast the quench propagates, as this reduces the large resistive part of the

voltage, as well as reduces the time of high inductive voltages. This does lend a hand to the possibility of improving the protection level of the *C* variant by increasing the charging voltage. The caveat is that the CL CLIQ configuration cannot be used — as seen, the CL has an unfortunate inductive voltage distribution at the point of triggering, and will exceed the voltage limit quite easily. No further investigation into this possibility has been made.

The LL CLIQ configuration consistently proves the best in terms of the voltages in the coil, while the PP is the worst. Only the LL applied to the *B* or *F* variants is able to keep the inter–layer voltage at an acceptable level, right around the 1 [kV] soft limit set for the high–voltage insulation. The *D* and *D v2* both have a large problem with the turn–to–turn voltages, with the *D* variant typically going 100% above the 100 [V] limit, and the *D v2* more than 9 times above. As such, it seems impossible to protect the *D* variant all–together.

The connection order of the half–turns in the coil play a large role for the LL and LLrev CLIQ configurations, typically halving the coil–to–collar voltage, and thereby making the LL a very viable protection candidate (the LLrev still struggles with large inter–layer voltages). Also the PP CLIQ configuration is impacted greatly in the midplane voltage from altering the connection order of the half–turns: for the *A* variant, the midplane voltage can be halved from 2 to 1 [kV] with the right choice of order.

In all cases, the midplane voltage is the one to see the largest strain on the 1 [kV] limit, but seeing as the distance between the poles is as large as it is in all the block–coil variants investigated it is assumed that the voltage limit can be reasonably relaxed here, with LL values for both *B* and *F* variants around 1.5 [kV].

Improving the superconductor, although altering the hot–spot temperature, is not found to have any significant impact on the voltage characteristics of the coil.

Chapter 7

Conclusions and Suggestions for Further Work

7.1 Parameter Space

The ability to protect the coil is always measured against the hard limits of hot–spot temperature at 350 [K] and turn–to–turn voltage of 100 [V], as well as the softer high–voltage limit of 1 [kV].

CLIQ parameters Changing the charging voltage or the capacitance of the CLIQ unit does alter the hot–spot temperature, but it has been found that even for a doubling of the voltage, only about 25 [K] is gained in the hot–spot, from 350 [K]. For an increase in the capacitance, the hot–spot rises due to a larger energy deposition from the CLIQ unit. Lowering the capacitance has had some success for the D variant coil, but only in conjunction with increased voltage, which reduces the electrical safety of the system.

CLIQ configurations Altering the CLIQ configuration has a tremendous impact on the hot–spot temperature; going from the PP to the CL or LL grants gains in the hot–spot on the order of 40–60 [K], depending on the coil variant. Going to the LLrev will reduce the hot–spot temperature with another 20–30 [K].

In terms of voltage, the same is clear — the CLIQ configuration is of defining significance for the inter–layer, midplane and turn–to–turn voltages, as well as the coil–to–collar and coil–to–bore; the PP and CL CLIQ configurations will typically see as much as 2 [kV] inter–layer voltage — far above the limit, while the LLrev typically manages about 500 [V] less, but still above the limit. Only the LL CLIQ configuration seems a truly promising approach, managing to reach as far down as exactly 1 [kV] inter–layer voltage, while consistently keeping the turn–to–turn voltages the lowest (or on par with the LLrev).

Initial transport current The magnet will operate at all currents between zero and nominal, and must be protected at all current levels — for all variants the CLIQ unit, regardless of configuration or system parameters, was able to adequately protect the coil.

RRR The RRR has been found to have only very little influence on the hot–spot temperature. At very high filament twist pitches the dependence grows somewhat, but other parameters have far larger importance; it will typically change the hot–spot by about 10 [K], with larger RRR giving a larger hot–spot.

Fraction of non–Copper As for the CLIQ configuration the fraction of non–Copper is very important for the hot–spot temperature, and also influences the voltages in the coil. Depending on the coil variant, changing the fraction by 5 percentage points up or down will typically increase or decrease the hot–spot temperature by 20–30 [K], with the PP CLIQ configuration being more sensitive and the LLrev being less sensitive. The same change in non–Copper content will increase or decrease the peak inter–layer voltage by 200–400 [V], with the PP being the most sensitive and the LL the least sensitive.

Filament Twist Pitch As for the RRR, the filament twist pitch is not tremendously important within the physically probable limits around 10 to 18 [mm], and reduces the hot–spot temperature by about 30 [K] when going from the smallest to the largest twist pitch. For values outside of those likely to be chosen in an actual strand for a cable, less likely due to elevated risk of flux jumps, the hot–spot can be reduced by as much as 50 [K].

Critical surface By improving the superconductor it is found that the operational margin of the coil can be improved substantially while at the same time only very small sacrifices are made in the hot–spot temperature (typically increasing by 20 [K]) and peak voltages (no significant changes).

Coil geometry Similarly to CLIQ configuration and the non–Copper fraction, the coil geometry has a large impact on whether or not the coil can be protected effectively. Reducing the inductance and increasing the cable's cross sectional area is quite effective at reducing both the hot–spot temperature and the peak voltages; going from the reference coil design to either a similar aperture with larger cables or a larger aperture with larger cables reduces the peak temperature by 30 [K] when using the PP CLIQ configuration and 20 [K] when using the LLrev. For a variant with smaller cables, giving a larger self–inductance, the hot–spot temperature rises by about 10 [K]. The graded coil seems nigh impossible to protect; not only is the hot–spot temperature very hard to bring down below 350 [K], but the peak turn–to–turn voltages are between 2 and 9 times the 100 [V] limit.

7.2 Key Considerations

Tables 7.1 and 7.2 give qualitative overviews of the protectability and effectiveness of the coil variants and CLIQ configuration respectively.

It is clear that the *D v2* variant can be disregarded completely from a voltage point of view, while the *D* variant is out also due to the very high hot–spot temperatures.

Variant *C* shows little promise both in the hot–spot and the coil voltages, while the baseline variant, *A*, has the voltages as a particular challenge while the hot–spot is acceptable.

Table 7.1: Qualitative comparison of coil variants.

Variant	Manufacture	T_{hot}	U_{ground}
A	✓		✗
B	✓	✓	✓
C	✓	✗	✗
D	✗	✗	✗
D v2	✗		✗✗
F		✓	✓

The CL CLIQ configuration can easily be dismissed; the voltages are poor, and the hot–spots are mostly on par with the LL. The PP configuration is also challenging from the voltage requirements, while also unsatisfactory in terms of hot–spot.

The LLrev CLIQ configuration has the best hot–spot characteristics, but when also voltage is taken into account, only the LL manages to safely protect the magnet, and even this configuration does push at the soft voltage limit set.

Table 7.2: Qualitative comparison of CLIQ configurations.

Configuration	Manufacture	T_{hot}	U_{ground}
PP	✓	✗	✗
CL	✗		✗
LL	✗		✓
LLrev	✗	✓	

7.3 Final Recommendation

When taking all results into account, it is quite clear that the *F* coil variant, with the slight improvement in the superconductor's pinning properties, protected by the LL CLIQ configuration is the best alternative. There is still room for tuning with the non–Copper fraction and CLIQ parameters, and the coil is protected at all current levels. Presumably, the *B* variant will behave similarly to an improved superconductor, and as such the two variants are considered on par.

Even clearer than the issue of what alternative to *promote*, the *D* (and *D v2*) variant stands out in the opposite sense — hot–spots that are, at best, right below the temperature limit, and voltages, at best, twice above theirs; the clear conclusion is to disregard the design unless far better insulation materials or fundamental changes to the degree of grading can be made.

List of Figures

Bibliography

[1] A.W. Chao. *Handbook of Accelerator Physics and Engineering*. World Scientific, 2013. ISBN: 9789814415842.

[2] CERN. *The Synchrocyclotron*. 2015. URL: `http://home.web.cern.ch/about/accelerators/synchrocyclotron` (visited on 09/21/2015).

[3] G Sabbi, Luca Bottura, Daniel W Cheng, Daniel R Dietderich, Paolo Ferracin, Arno Godeke, Stephen A Gourlay, Maxim Marchevsky, Ezio Todesco, and Xiaorong Wang. "Performance Characteristics of Block-Coil Dipoles for a 100 TeV Hadron Collider". In: *Applied Superconductivity, IEEE Transactions on* 25.3 (2015), pp. 1–7.

[4] MJ Syphers, MA Harrison, and S Peggs. "Beyond the LHC: A Conceptual Approach to a Future High Energy Hadron Collider". In: *Particle Accelerator Conference, 1995., Proceedings of the 1995*. Vol. 1. IEEE. 1995, pp. 431–433.

[5] CERN. *Future Circular Collider Study — Hadron Collider*. 2015. URL: `https://fcc.web.cern.ch/Pages/Hadron-Collider.aspx` (visited on 09/21/2015).

[6] M.N. Wilson. *Superconducting Magnets*. Monographs on Cryogenics. Clarendon Press, 1987. ISBN: 9780198548102.

[7] Y. Iwasa. *Case Studies in Superconducting Magnets: Design and Operational Issues*. Springer US, 2010. ISBN: 9781441935397.

[8] Magnet Group. *Design Report for the 1.2 Interaction Region Dipoles and the 2.1 RF Region Dipoles*. Tech. rep. `http://www.bnl.gov/magnets/APUL/pdfs/DsgnRpt99a.pdf`. Brookhaven National Laboratory, Sept. 1999.

[9] S. Russenschuck and T. Tortschanoff. "Optimization of the Coil of the LHC Main Dipole". In: *Magnetics, IEEE Transactions on* 29.2 (Mar. 1993), pp. 1795–1798. ISSN: 0018-9464. DOI: `10.1109/20.250754`.

[10] Arjan Peter Verweij. "Electrodynamics of Superconducting Cables in Accelerator Magnets". University of Twente, 1995. ISBN: 90–9008555–6.

[11] Oliver Sim Brüning, Paul Collier, P Lebrun, Stephen Myers, Ranko Ostojic, John Poole, and Paul Proudlock. *LHC Design Report — Volume 1*. Geneva: CERN, 2004. URL: https://cds.cern.ch/record/782076.

[12] Z.B. Popović and B.D. Popović. *Introductory Electromagnetics*. Prentice Hall, 2000. ISBN: 9780201326789. URL: https://books.google.no/books?id=-S9HAQAAIAAJ.

[13] Jan Erik Skog and Nils Henrik Jendal. *NorNed kabel HVDC Project*. 2006. URL: http://ewh.ieee.org/r8/norway/pe/norned/061206NorNedStatnett.pdf (visited on 09/19/2015).

[14] Wikipedia. *Current density — Wikipedia, The Free Encyclopedia*. 2015. URL: https://en.wikipedia.org/wiki/Current_density (visited on 09/19/2015).

[15] C. Kittel. *Introduction to Solid State Physics*. Wiley, 2004. ISBN: 9780471415268.

[16] J.F. Annett. *Superconductivity, Superfluids and Condensates*. Oxford Master Series in Physics. OUP Oxford, 2004. ISBN: 9780198507567.

[17] CERN. *Future Circular Collider Study: Magnets*. 2014. URL: https://espace2013.cern.ch/fcc/Pages/Magnets.aspx (visited on 01/19/2015).

[18] M. K. Wu, J. R. Ashburn, C. J. Torng, P. H. Hor, R. L. Meng, L. Gao, Z. J. Huang, Y. Q. Wang, and C. W. Chu. "Superconductivity at 93 K in a new mixed-phase Y-Ba-Cu-O compound system at ambient pressure". In: *Phys. Rev. Lett.* 58 (9 Mar. 1987), pp. 908–910. DOI: 10.1103/PhysRevLett.58.908. URL: http://link.aps.org/doi/10.1103/PhysRevLett.58.908.

[19] K. Vinod, R. G. Abhilash Kumar, and U. Syamaprasad. "Prospects for MgB_2 superconductors for magnet application". In: *Superconductor Science and Technology* 20 (1 2007), R1–R13. DOI: 10.1088/0953-2048/20/1/R01. URL: http://iopscience.iop.org/0953-2048/20/1/R01.

[20] Wikipedia. *Meissner effect — Wikipedia, The Free Encyclopedia*. 2015. URL: https://en.wikipedia.org/wiki/Meissner_effect (visited on 09/19/2015).

[21] W. Buckel and R. Kleiner. *Superconductivity: Fundamentals and Applications*. Physics textbook. Wiley, 2008. ISBN: 9783527618514.

[22] C.P. Poole, H.A. Farach, R.J. Creswick, and R. Prozorov. *Superconductivity*. Superconductivity Series. Elsevier Science, 2007. ISBN: 9780080550480.

[23] Leon N. Cooper. "Bound Electron Pairs in a Degenerate Fermi Gas". In: *Phys. Rev.* 104 (4 Nov. 1956), pp. 1189–1190. DOI: 10.1103/PhysRev.104.1189. URL: http://link.aps.org/doi/10.1103/PhysRev.104.1189.

[24] James Clerk Maxwell. "On Physical Lines of Force". In: *The London, Edinburgh and Dublin Philosophical Magazine and Journal of Science* (Mar. 1861). Relevant part is number III of April and May 1861. URL: http://upload.wikimedia.org/wikipedia/commons/b/b8/On_Physical_Lines_of_Force.pdf.

[25] L. Ya. Vinnikov, J. Karpinski, S. M. Kazakov, J. Jun, J. Anderegg, S. L. Bud'ko, and P. C. Canfield. "Vortex structure in MgB_2 single crystals observed by the Bitter decoration technique". In: *Phys. Rev. B* 67 (9 Mar. 2003), p. 092512. DOI: 10.1103/

PhysRevB.67.092512. URL: http://link.aps.org/doi/10.1103/PhysRevB.67.092512.

[26] H. F. Hess, R. B. Robinson, R. C. Dynes, J. M. Valles, and J. V. Waszczak. "Scanning–Tunneling–Microscope Observation of the Abrikosov Flux Lattice and the Density of States Near and Inside a Fluxoid". In: *Phys. Rev. Lett.* 62 (2 Jan. 1989), pp. 214–216. DOI: 10.1103/PhysRevLett.62.214. URL: http://link.aps.org/doi/10.1103/PhysRevLett.62.214.

[27] Jan Kaczmarczyk and Jozef Spałek. "Superconductivity in an almost localized Fermi liquid of quasiparticles with spin-dependent masses and effective-field induced by electron correlations". In: *Phys. Rev. B* 79 (21 June 2009), p. 214519. DOI: 10.1103/PhysRevB.79.214519. URL: http://link.aps.org/doi/10.1103/PhysRevB.79.214519.

[28] L.T. Summers, M. Guinan, J.R. Miller, and P. Hahn. "A model for the prediction of Nb 3 Sn critical current as a function of field, temperature, strain, and radiation damage". In: *Magnetics, IEEE Transactions on* 27.2 (1991), pp. 2041–2044.

[29] A.V. Narlikar. *Frontiers in Superconducting Materials*. Springer, 2005. ISBN: 9783540272946. URL: https://books.google.fr/books?id=8SIEyA-0zI8C.

[30] Ruoyi Zhou, Seungok Hong, and B. H. Kear. "Improved pinning in Nb and Nb3Sn superconductors". In: *Philosophical Magazine Part B* 71.3 (1995), pp. 427–436. DOI: 10.1080/13642819508239045. eprint: http://dx.doi.org/10.1080/13642819508239045. URL: http://dx.doi.org/10.1080/13642819508239045.

[31] CH Cheng, H Zhang, Y Zhao, Y Feng, XF Rui, P Munroe, HM Zeng, N Koshizuka, and M Murakami. "Doping effect of nano-diamond on superconductivity and flux pinning in MgB2". In: *Superconductor Science and Technology* 16.10 (2003), p. 1182.

[32] P Mikheenko, JS Abell, A Sarkar, VS Dang, MM Awang Kechik, JL Tanner, P Paturi, H Huhtinen, N Hari Babu, DA Cardwell, et al. "Self-assembled artificial pinning centres in thick YBCO superconducting films". In: *Journal of Physics: Conference Series*. Vol. 234. 2. IOP Publishing. 2010, p. 022022.

[33] L. Dresner. *Stability of Superconductors*. Selected Topics in Superconductivity. Springer US, 1995. ISBN: 9780306450303.

[34] CERN. *Taking a Closer Look at the LHC: Superconducting Cables*. URL: http://www.lhc-closer.es/1/4/8/1 (visited on 02/09/2015).

[35] Bernardo Bordini. "11T Cable Development and Procurement Strategy at CERN". In: 2nd International Review of the HL–LHC 11 T Dipole for DS Collimation — 8–10th December 2014, CERN — https://indico.cern.ch/event/354499/contribution/15/material/slides/1.pdf.

[36] D. C. Larbalestier et al. "Isotropic round-wire multifilament cuprate superconductor for generation of magnetic fields above 30 T". In: *Nature Materials* 13 (4 Mar. 2014), pp. 375–381. DOI: doi:10.1038/nmat3887. URL: http://www.nature.com/nmat/journal/v13/n4/abs/nmat3887.html.

[37] G.H. Morgan. “Theoretical Behavior of Twisted Multicore Superconducting Wire in a Time-Varying Uniform Magnetic Field”. In: *Journal of Applied Physics* 41.9 (1970), pp. 3673–3679.

[38] K Kwasnitza. “Scaling law for the ac losses of multifilament superconductors”. In: *Cryogenics* 17.11 (1977), pp. 616–620.

[39] V.I. Datskov, J.A. Demko, S.D. Augustynowicz, and R.D. Hutton. “An Experimental Evaluation of Joint Electrical Resistance on Power Lead Thermal Performance”. English. In: *Supercollider 5*. Ed. by Phyllis Hale. Springer US, 1994, pp. 563–566. ISBN: 978-1-4613-6036-0. DOI: 10.1007/978-1-4615-2439-7_131. URL: http://dx.doi.org/10.1007/978-1-4615-2439-7_131.

[40] Seog-Whan Kim. “Material properties for quench simulation (Cu, NbTi and Nb3Sn)”. In: (2000).

[41] G. Ambrosio. “Nb3Sn High Field Magnets for the High Luminosity LHC Upgrade Project”. In: *Applied Superconductivity, IEEE Transactions on* 25.3 (June 2015), pp. 1–7. ISSN: 1051-8223. DOI: 10.1109/TASC.2014.2367024.

[42] N Cheggour, LF Goodrich, TC Stauffer, JD Splett, XF Lu, AK Ghosh, and G Ambrosio. “Influence of Ti and Ta doping on the irreversible strain limit of ternary Nb3Sn superconducting wires made by the restacked-rod process”. In: *Superconductor Science and Technology* 23.5 (2010), p. 052002.

[43] E Barzi, N Andreev, M Karppinen, V Lombardo, F Nobrega, D Turrioni, R Yamada, and AV Zlobin. “Development and Fabrication of Rutherford Cable for the 11 T DS Dipole Demonstrator Model”. In: *Applied Superconductivity, IEEE Transactions on* 22.3 (2012), pp. 6000805–6000805.

[44] M Bajko et al. *Report of the Task Force on the Incident of 19th September 2008 at the LHC*. Tech. rep. LHC-PROJECT-Report-1168. CERN-LHC-PROJECT-Report-1168. Geneva: CERN, Mar. 2009.

[45] Ph Fazilleau, M Devaux, M Durante, T Lecrevisse, and J-M Rey. “Protection of the 13 T Nb3Sn Fresca II dipole”. In: *arXiv preprint arXiv:1401.3961* (2014).

[46] G Ambrosio. “Maximum allowable temperature during quench in Nb3Sn accelerator magnets”. In: *arXiv preprint arXiv:1401.3955* (2014).

[47] Emmanuele Ravaioli. *Private communication*. Continuous communication. Oct. 2014.

[48] GianLuca Sabbi. *Private communication*. Continuous communication. Oct. 2014.

[49] L Bottura. “Cable Stability”. In: arXiv:1412.5373 (2014). Comments: 51 pages, contribution to the CAS-CERN Accelerator School: Superconductivity for Accelerators, Erice, Italy, 24 April - 4 May 2013, edited by R. Bailey, 50 p.

[50] J.H. Schultz. “Protection of superconducting magnets”. In: *Applied Superconductivity, IEEE Transactions on* 12.1 (Mar. 2002), pp. 1390–1395. ISSN: 1051-8223. DOI: 10.1109/TASC.2002.1018662.

[51] Emmanuele Ravaioli. “CLIQ — A new quench protection technology for superconducting magnets”. University of Twente, 2015. ISBN: 978–90–365–3908–1.

[52] A. Vergara Fernández and F. Rodrigurez-Mateos. "Reliability of the quench protection system for the {LHC} superconducting elements". In: *Nuclear Instruments and Methods in Physics Research Section A: Accelerators, Spectrometers, Detectors and Associated Equipment* 525.3 (2004), pp. 439 –446. ISSN: 0168-9002. DOI: http://dx.doi.org/10.1016/j.nima.2004.01.081. URL: http://www.sciencedirect.com/science/article/pii/S016890020400244X.

[53] P. Cruikshank, P. Proudlock, G. Riddone, R. Saban, and R. Schmidt. "General Parameters for Equipment Installed in the LHC". In: 1999. URL: http://at-div-vac.web.cern.ch/at-div-vac/VACPAGES/MINUTES/LHC_Vacuum_Design_Minutes/1999/118th_Meeting/parameters_for_LHC_equipment.pdf.

[54] Andrzej Siemko. *Safeguarding the superconducting magnets*. Aug. 2013. URL: http://cerncourier.com/cws/article/cern/54383 (visited on 02/16/2015).

[55] E. Todesco, L. Bottura, G. de Rijk, and L. Rossi. "Dipoles for High–Energy LHC". In: *Applied Superconductivity, IEEE Transactions on* 24.3 (June 2014), pp. 1–6. ISSN: 1051–8223. DOI: 10.1109/TASC.2013.2286002.

[56] L Rossi and E Todesco. "Conceptual design of 20 T dipoles for High-Energy LHC". In: *arXiv preprint arXiv:1108.1619* (2011).

[57] L. Bottura, G. de Rijk, L. Rossi, and E. Todesco. "Advanced Accelerator Magnets for Upgrading the LHC". In: *Applied Superconductivity, IEEE Transactions on* 22.3 (June 2012), pp. 4002008–4002008. ISSN: 1051-8223. DOI: 10.1109/TASC.2012.2186109.

[58] L. Coull, D. Hagedorn, V. Remondino, and F. Rodriguez-Mateos. "LHC magnet quench protection system". In: *Magnetics, IEEE Transactions on* 30.4 (July 1994), pp. 1742–1745. ISSN: 0018-9464. DOI: 10.1109/20.305593.

[59] K Dahlerup-Petersen, R Denz, JL Gomez-Costa, D Hagedorn, P Proudlock, F Rodriguez-Mateos, R Schmidt, and F Sonnemann. "The protection system for the superconducting elements of the Large Hadron Collider at CERN". In: *18th IEEE Particle Accelerator Conference*. Vol. 1. 1999, pp. 3200–3202.

[60] K. Dahlerup-Petersen, A. Medvedko, A. Erokhin, B. Kazmin, V. Sytchev, and L. Vassiliev. "Energy extraction in the CERN Large Hadron Collider: a project overview". In: *Pulsed Power Plasma Science, 2001. PPPS-2001. Digest of Technical Papers*. Vol. 2. June 2001, 1473–1476 vol.2. DOI: 10.1109/PPPS.2001.1001835.

[61] F Rodríguez-Mateos, R Schmidt, A Siemko, and F Sonnemann. *Quench Process and Protection of LHC Dipole Magnets*. Tech. rep. LHC-PROJECT-NOTE-184. Geneva: CERN, July 1999.

[62] Balázs Szeless, F Rodríguez-Mateos, and F Calvone. *Development of Industrially Produced Composite Quench Heaters for the LHC Superconducting Lattice Magnets*. Tech. rep. LHC-Project-Report-48. CERN-LHC-Project-Report-48. Geneva: CERN, Sept. 1996.

[63] F. Rodriguez-Mateos and F. Sonnemann. "Quench heater studies for the LHC magnets". In: *Particle Accelerator Conference, 2001. PAC 2001. Proceedings of the 2001*. Vol. 5. 2001, 3451–3453 vol.5. DOI: 10.1109/PAC.2001.988141.

[64] Felix Rodriguez Mateos. *REVIEW OF QUENCH HEATERS FOR LHC*. Apr. 2014. URL: https://indico.cern.ch/event/311824/contribution/10/material/slides/1.pdf.

[65] V. Maroussov, S. Sanfilippo, and A. Siemko. "Temperature profiles during quenches in LHC superconducting dipole magnets protected by quench heaters". In: *Applied Superconductivity, IEEE Transactions on* 10.1 (Mar. 2000), pp. 661–664. ISSN: 1051-8223. DOI: 10.1109/77.828320.

[66] E Todesco. "Quench limits in the next generation of magnets". In: arXiv:1401.3931 (Jan. 2014). Comments: 7 pages, Contribution to WAMSDO 2013: Workshop on Accelerator Magnet, Superconductor, Design and Optimization; 15 - 16 Jan 2013, CERN, Geneva, Switzerland, 7 p.

[67] G. Chlachidze et al. "Performance of HQ02, an Optimized Version of the 120 mm Nb_3Sn LARP Quadrupole". In: *Applied Superconductivity, IEEE Transactions on* 24.3 (June 2014), pp. 1–5. ISSN: 1051-8223. DOI: 10.1109/TASC.2013.2285885.

[68] G. Chlachidze, I. Novitski, A.V. Zlobin, B. Auchmann, and M. Karppinen. "Experimental results and analysis from the 11 T Nb3Sn DS dipole". In: (2014), pp. 47–56. DOI: 10.5170/CERN-2013-006.47. arXiv: 1401.3958 [physics.acc-ph].

[69] A.V. Zlobin et al. "11-T Twin-Aperture Nb_3Sn Dipole Development for LHC Upgrades". In: *Applied Superconductivity, IEEE Transactions on* 25.3 (June 2015), pp. 1–9. ISSN: 1051-8223. DOI: 10.1109/TASC.2014.2367312.

[70] M. Bajko, G. Berard, G. Rolando, and G. Molinari. *Report on Quench Heater Failures*. Tech. rep. Technical Note 2008–02 – EDMS no: 889445. Geneva: CERN, Jan. 2008.

[71] Gerard Willering. *MP3 Recommendation Fatigue Testing of MB Quench Heaters Using the new LHC Monitoring System*. Tech. rep. LHC–MP3–EN–0014 – EDMS no: 1423341. Geneva: CERN, Feb. 2014.

[72] L.R. Evans. *The Large Hadron Collider: A Marvel of Technology*. Fundamental sciences. EPFL Press, 2009. ISBN: 9782940222346.

[73] Emmanuele Ravaioli, Arjan P Verweij, and Herman HJ ten Kate. "Unbalanced Impedance of the Aperture Coils of Some LHC Main Dipole Magnets". In: *Applied Superconductivity, IEEE Transactions on* 23.3 (2013), pp. 4000104–4000104.

[74] E. Ravaioli, V.I. Datskov, C. Giloux, G. Kirby, H.H.J. ten Kate, and A.P. Verweij. "New, Coupling Loss Induced, Quench Protection System for Superconducting Accelerator Magnets". In: *Applied Superconductivity, IEEE Transactions on* 24.3 (June 2014), pp. 1–5. ISSN: 1051-8223. DOI: 10.1109/TASC.2013.2281223.

[75] G Chlachidze, Giorgio Ambrosio, Michael Anerella, F Borgnolutti, R Bossert, S Caspi, DW Cheng, Daniel Dietderich, H Felice, P Ferracin, et al. "Performance of HQ02, an Optimized Version of the 120 mm LARP Quadrupole". In: *Applied Superconductivity, IEEE Transactions on* 24.3 (2014), pp. 1–5.

[76] E Ravaioli, H Bajas, VI Datskov, V Desbiolles, J Feuvrier, G Kirby, M Maciejewski, G Sabbi, HHJ ten Kate, and AP Verweij. "Protecting a Full-Scale Magnet With CLIQ,

the New Coupling-Loss-Induced Quench System". In: *Applied Superconductivity, IEEE Transactions on* 25.3 (2015), pp. 1–5.

[77] R.M. Schöttler and H.W. Lorenzen. "Temperature and Pressure Rise in Supercritical Helium during the Quench of Indirectly Cooled SC Coils". English. In: *Advances in Cryogenic Engineering*. Ed. by Peter Kittel. Vol. 41. A Cryogenic Engineering Conference Publication. Springer US, 1996, pp. 325–334. ISBN: 978-1-4613-8022-1. DOI: 10.1007/978-1-4613-0373-2_42. URL: http://dx.doi.org/10.1007/978-1-4613-0373-2_42.

[78] J. Taylor, M. Alston-Garnjost, P. Eberhard, G. Gibson, M.A. Green, B. Pardoe, M. Pripstein, R.R. Ross, R. Smits, and P. Lecomte. "Quench protection for a 2-MJ magnet". In: *Magnetics, IEEE Transactions on* 15.1 (Jan. 1979), pp. 855–859. ISSN: 0018-9464. DOI: 10.1109/TMAG.1979.1060158.

[79] G.A. KIRBY, V. DATSKOV, and E. RAVAIOLI. *Ac-current induced quench protection system*. WO Patent App. PCT/EP2014/063,575. Dec. 2014. URL: https://encrypted.google.com/patents/WO2014207130A1?cl=zh-TW.

[80] E. Ravaioli, V.I. Datskov, A.V. Dudarev, G. Kirby, K.A. Sperin, H.H.J. ten Kate, and A.P. Verweij. "First experience with the new Coupling Loss Induced Quench system". In: *Cryogenics* 60.0 (2014), pp. 33 –43. ISSN: 0011-2275. DOI: http://dx.doi.org/10.1016/j.cryogenics.2014.01.008. URL: http://www.sciencedirect.com/science/article/pii/S0011227514000162.

[81] E. Ravaioli, B. Auchmann, M. Maciejewski, H. H. J. ten Kate, and A. P. Verweij. *Lumped–Element Dynamic Electro–Thermal Model of a Superconducting Magnet*. Cryogenics, to be published. 2015.

[82] J.W. Nilsson and S.A. Riedel. *Electric Circuits*. Pearson/Prentice Hall, 2008. ISBN: 9780135031650. URL: https://books.google.ch/books?id=FB1NPgAACAAJ.

[83] Stephan Russenschuck. "ROXIE: A Computer Code for the Integrated Design of Accelerator Magnets". In: LHC–Project–Report–276. CERN–LHC–Project–Report–276 (Feb. 1999), 4 p.

[84] V Marinozzi, M Sorbi, G Manfreda, F Bellina, H Bajas, and G Chlachidze. "Effect of coupling currents on the dynamic inductance during fast transient in superconducting magnets". In: *Physical Review Special Topics-Accelerators and Beams* 18.3 (2015), p. 032401.

[85] Frederic Savary. "The 11T Dipole Project Motivation and Challenges". In: 2nd International Review of the HL–LHC 11 T Dipole for DS Collimation — 8–10th December 2014, CERN — https://indico.cern.ch/event/354499/contribution/4/material/slides/1.pdf.

[86] Herbert De Gersem. *Numerical Simulation of Eddy Currents in the Superconductive Rutherford Cable of a Fast-Pulsed Dipole Magnet*. https://www-alt.gsi.de/documents/DOC-2003-Sep-1.html, [TU Darmstadt, Computational Electromagnetics Laboratory]. Mar. 2003.

[87] Herbert De Gersem and Thomas Weiland. "Finite-element models for superconductive cables with finite interwire resistance". In: *Magnetics, IEEE Transactions on* 40.2 (2004), pp. 667–670.

[88] S. Russenschuck. *Field Computation for Accelerator Magnets: Analytical and Numerical Methods for Electromagnetic Design and Optimization*. Wiley, 2011. ISBN: 9783527635474. URL: https://books.google.ch/books?id=tA4VxZvoiJUC.

[89] Alain Laprade, Scott Pearson, Stan Benczkowski, Gary Dolny, and Frank Wheatley. "A new PSPICE electro-thermal subcircuit for power MOSFETs". In: (2004).

[90] G Sabbi, SE Bartlett, S Caspi, DR Dietderich, P Ferracin, SA Gourlay, AR Hafalia, CR Hannaford, AF Lietzke, S Mattafirri, et al. "Design of HD2: a 15 tesla Nb 3 Sn dipole with a 35 mm bore". In: *Applied Superconductivity, IEEE Transactions on* 15.2 (2005), pp. 1128–1131.

[91] P Ferracin, SE Bartlett, S Caspi, DR Dietderich, SA Gourlay, AR Hafalia, CR Hannaford, AF Lietzke, S Mattafirri, AD McInturff, et al. "Mechanical Design of HD2, a 15 T Nb_3Sn Dipole Magnet with a 35 mm Bore". In: *Applied Superconductivity, IEEE Transactions on* 16.2 (2006), pp. 378–381.

[92] P Ferracin, S Caspi, DW Cheng, DR Dietderich, AR Hafalia, CR Hannaford, H Higley, AF Lietzke, J Lizarazo, AD McInturff, et al. "Development of the 15 T Dipole HD2". In: *Applied Superconductivity, IEEE Transactions on* 18.2 (2008), pp. 277–280.

[93] Paolo Ferracin, Brad Bingham, Shlomo Caspi, DW Cheng, Daniel R Dietderich, Helene Felice, Arno Godeke, AR Hafalia, CR Hannaford, JM Joseph, et al. "Assembly and test of HD2, a 36 mm bore high field dipole magnet". In: *Applied Superconductivity, IEEE Transactions on* 19.3 (2009), pp. 1240–1243.

[94] P Ferracin, B Bingham, S Caspi, DW Cheng, DR Dietderich, H Felice, AR Hafalia, CR Hannaford, J Joseph, AF Lietzke, et al. "Recent test results of the high field dipole magnet HD2". In: *Applied Superconductivity, IEEE Transactions on* 20.3 (2010), pp. 292–295.

[95] H Felice, F Borgnolutti, S Caspi, DW Cheng, DR Dietderich, P Ferracin, A Godeke, AR Hafalia, Jan Moritz Joseph, J Lizarazo, et al. "Challenges in the Support Structure Design and Assembly of HD3, a Block-Type Dipole Magnet". In: *Applied Superconductivity, IEEE Transactions on* 23.3 (2013), pp. 4001705–4001705.

[96] DW Cheng, S Caspi, DR Dietderich, H Felice, P Ferracin, AR Hafalia, M Marchevsky, S Prestemon, and G Sabbi. "Design and Fabrication Experience With Block-Type Coils for High Field Accelerator Dipoles". In: *Applied Superconductivity, IEEE Transactions on* 23.3 (2013), pp. 4002504–4002504.

[97] M Marchevsky, S Caspi, DW Cheng, DR Dietderich, J DiMarco, H Felice, P Ferracin, A Godeke, AR Hafalia, Jayaraj Joseph, et al. "Test of the High-Field Dipole Magnet HD3b". In: *Applied Superconductivity, IEEE Transactions on* 24.3 (2014), pp. 1–6.

[98] E. Ravaioli, V.I. Datskov, J.B. Ghini, G. Kirby, M. Maciejewski, G. Sabbi, H. H. J. ten Kate, and A. P. Verweij. *Quench protection of a 16 T block–coil dipole magnet for a 100 TeV Hadron Collider using CLIQ*. IEEE Transactions on Applied Superconductivity, to be published. 2015.

[99] G. Manfreda. *Nb3Sn Specific Heat Fit Function for Quench Simulation*. CERN TE–MSC internal note 2011-22, EDMS number: 1177998 v.2. Dec. 2011.

[100] E.D. Marquardt, J.P. Le, and Ray Radebaugh. "Cryogenic Material Properties Database". In: 11th International Cryocooler Conference, June 20, 2000.

[101] Michal Maciejewski. *Automated Object–Oriented Simulation Framework for Modelling of Superconducting Magnets at CERN*. Sept. 2014.

[102] *MATLAB and Simulink Release R2013b*. The MathWorks, Inc., Natick, Massachusetts, United States.

Appendix A

Example of cos(θ) Coil Dipole Field

Figure A.1 shows the dipole field of the proposed 11 T HL–LHC magnet. The inner layer, closest to the bore, is clearly seeing a higher field than the outer layer, and the region of high field is quite evenly distributed across all the cables of these inner layers. This means that the margin to quench for all the cables in the inner layers is low and similar. This is a very good feature from a CLIQ protection point of view, given its uniform energy deposition in the coil.

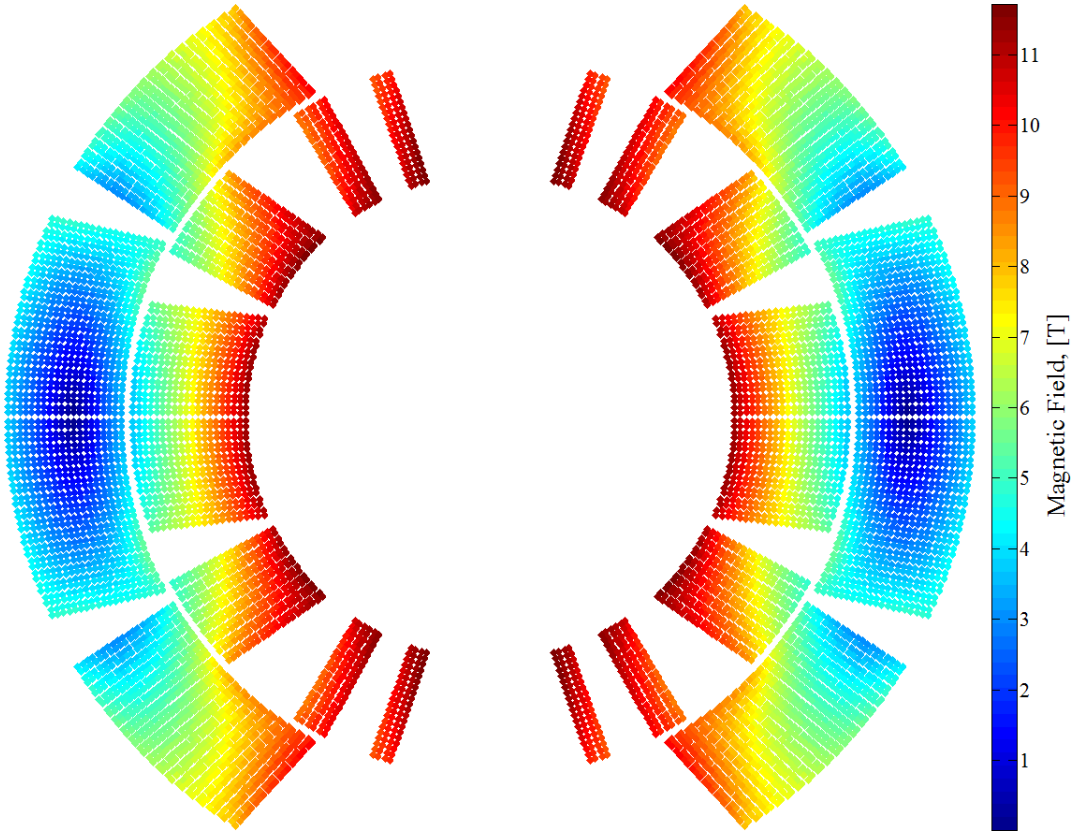

Figure A.1: Field distribution in the 11 T HL–LHC dipole, for the nominal transport current of 11.85 [kA].

Appendix B

Quench Margins

B.1 Enthalpy and Temperature Margins for the Block–Coil Dipole Magnet

75% of Nominal Transport Current — Enthalpy Margin to Quench

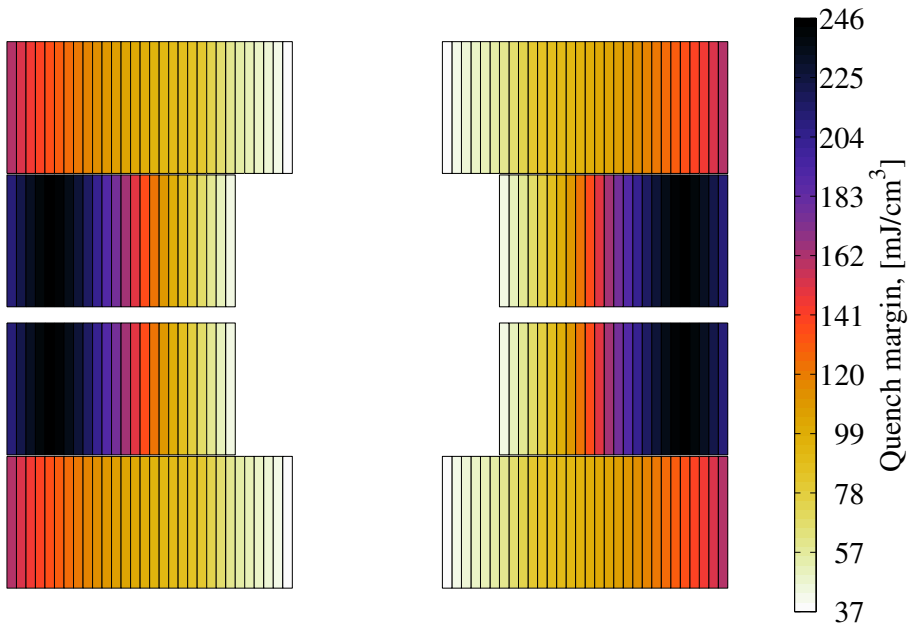

Figure B.1: Enthalpy margin to quench in the different cables of the coil for an initial transport current of 13950 [A] (75% of the nominal current).

75% of Nominal Transport Current — Temperature Margin

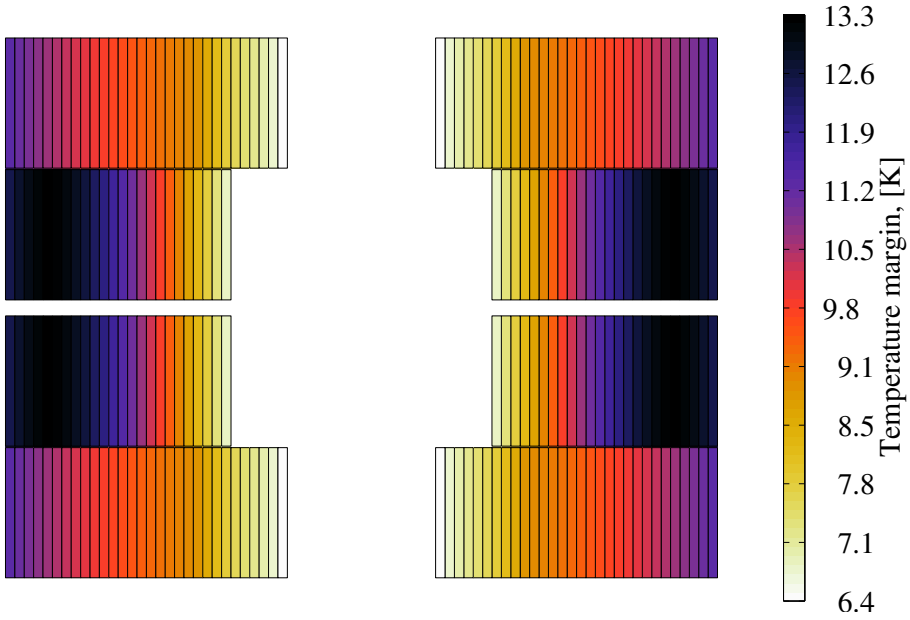

Figure B.2: Temperature margin in the different cables of the coil for an initial transport current of 13950 [A] (75% of the nominal current).

50% of Nominal Transport Current — Enthalpy Margin to Quench

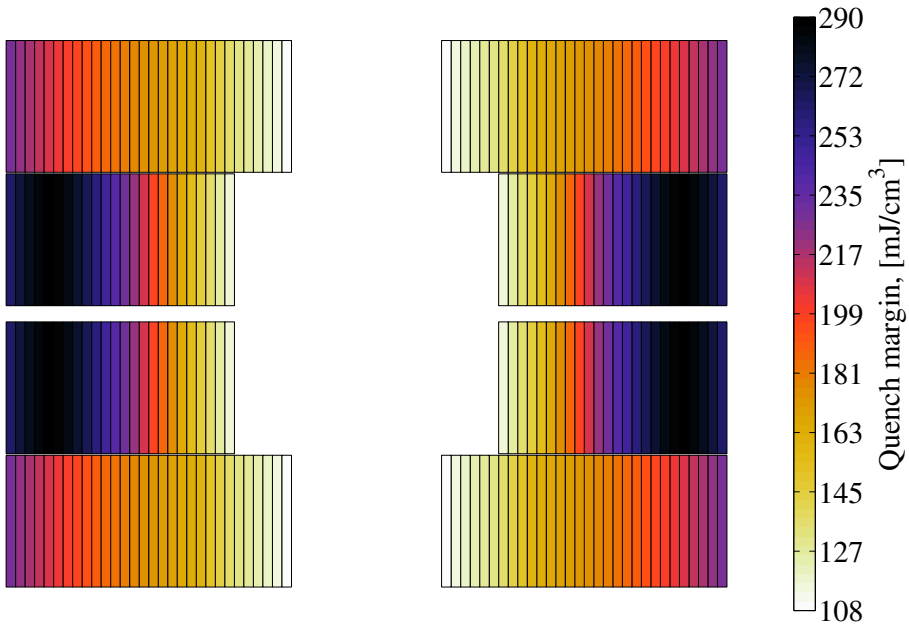

Figure B.3: Enthalpy margin to quench in the different cables of the coil for an initial transport current of 9300 [A] (50% of the nominal current).

50% of Nominal Transport Current — Temperature Margin

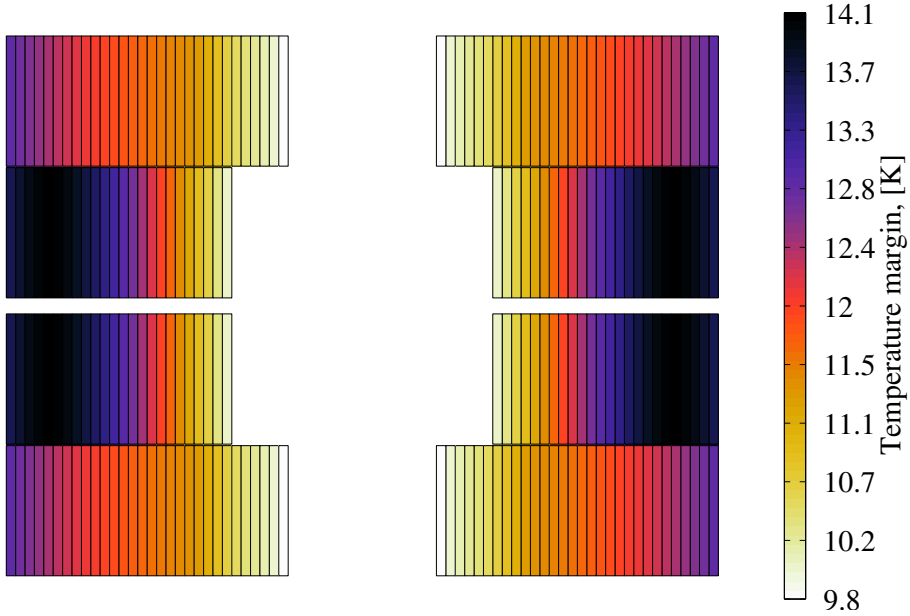

Figure B.4: Temperature margin in the different cables of the coil for an initial transport current of 9300 [A] (50% of the nominal current).

25% of Nominal Transport Current — Enthalpy Margin to Quench

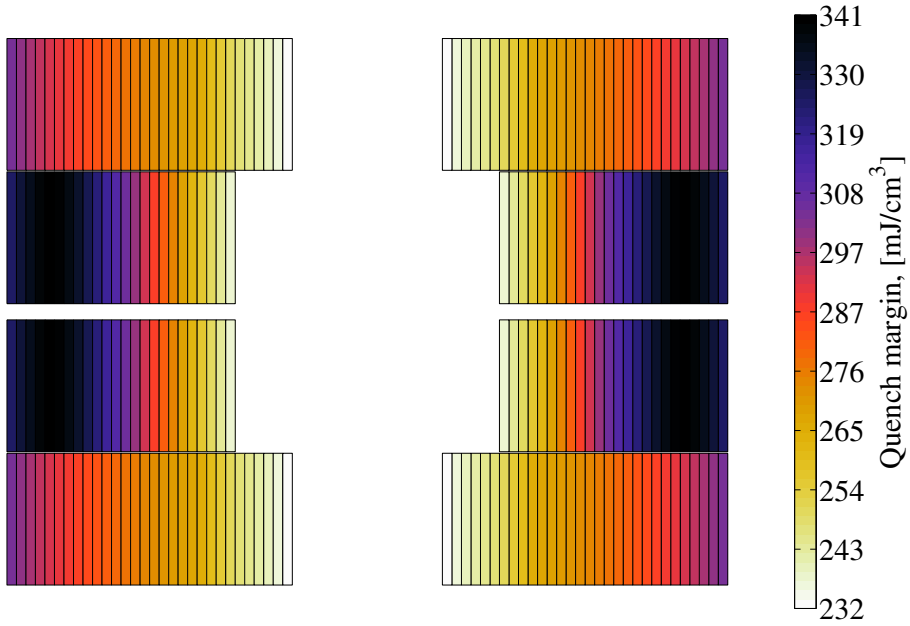

Figure B.5: Enthalpy margin to quench in the different cables of the coil for an initial transport current of 4650 [A] (25% of the nominal current).

25% of Nominal Transport Current — Temperature Margin

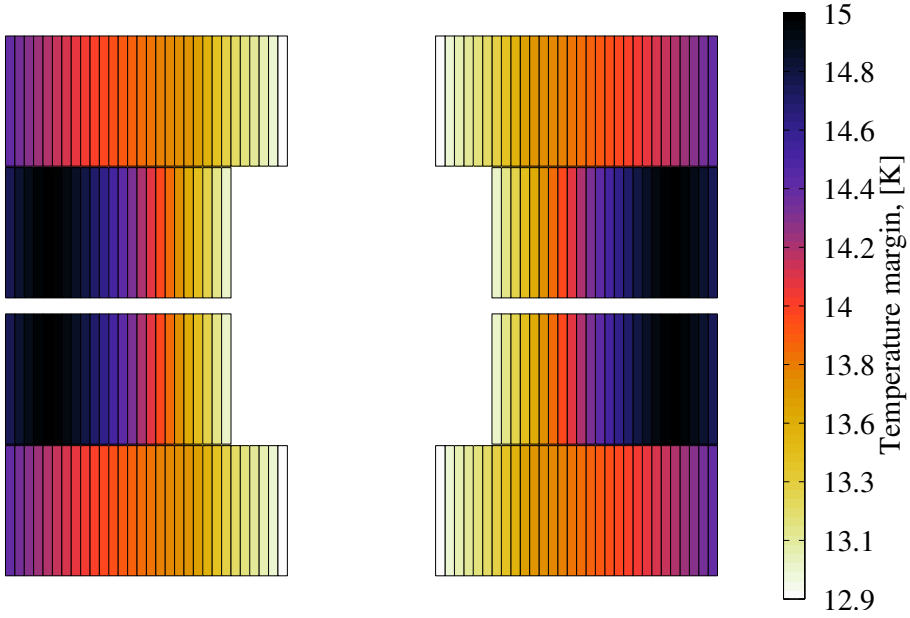

Figure B.6: Temperature margin in the different cables of the coil for an initial transport current of 4650 [A] (25% of the nominal current).

B.2 Enthalpy and Temperature Margins for the *D* Variant Block–Coil Dipole Magnet

Nominal Transport Current — Enthalpy Margin to Quench

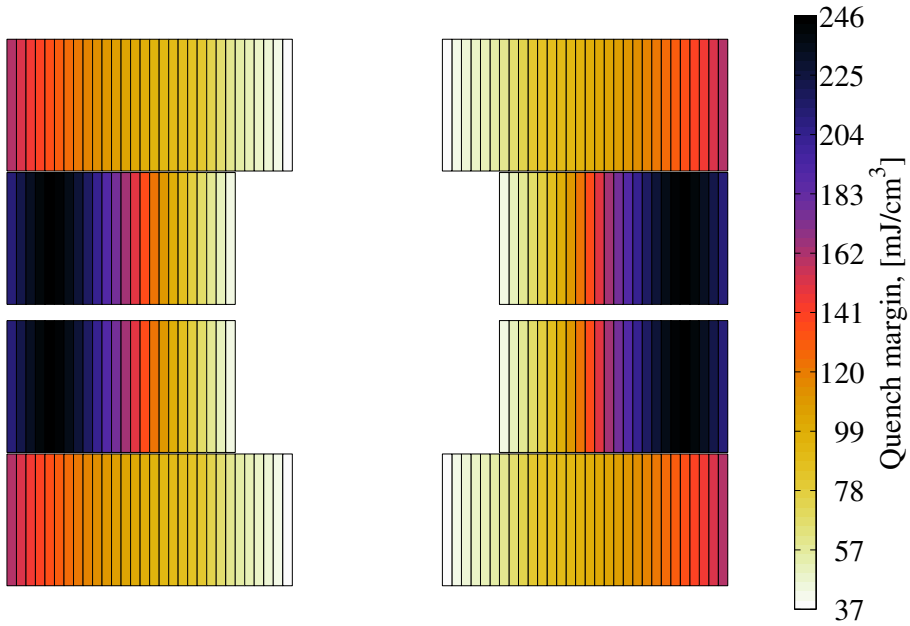

Figure B.7: Enthalpy margin to quench in the different cables of the *D* variant coil for the nominal initial transport current.

Nominal Transport Current — Temperature Margin

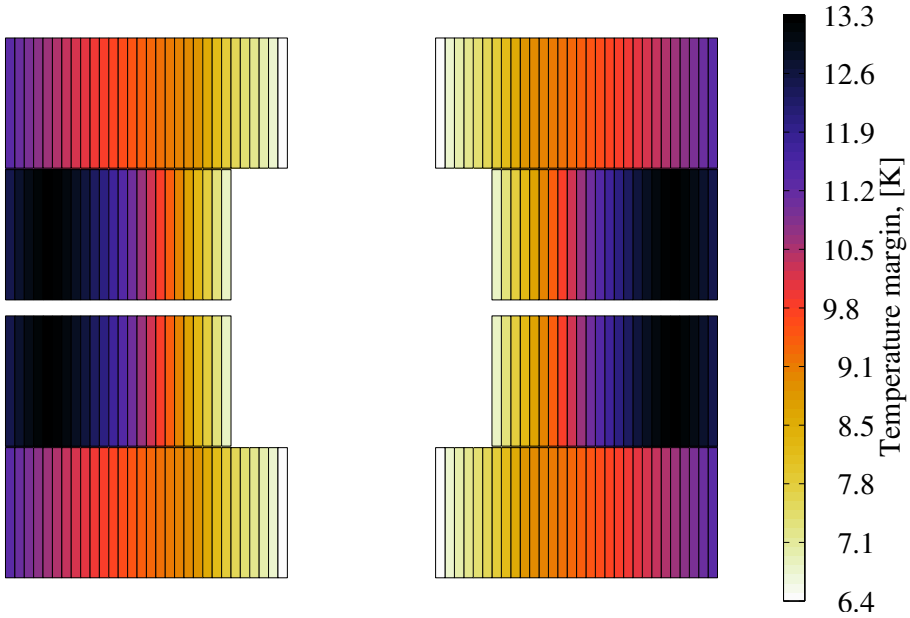

Figure B.8: Enthalpy Margin to Quench in the different cables of the *D* variant coil for the nominal initial transport current.

Appendix C

Connection Orders

C.1 Half–turn Order for the *A* Coil Variant

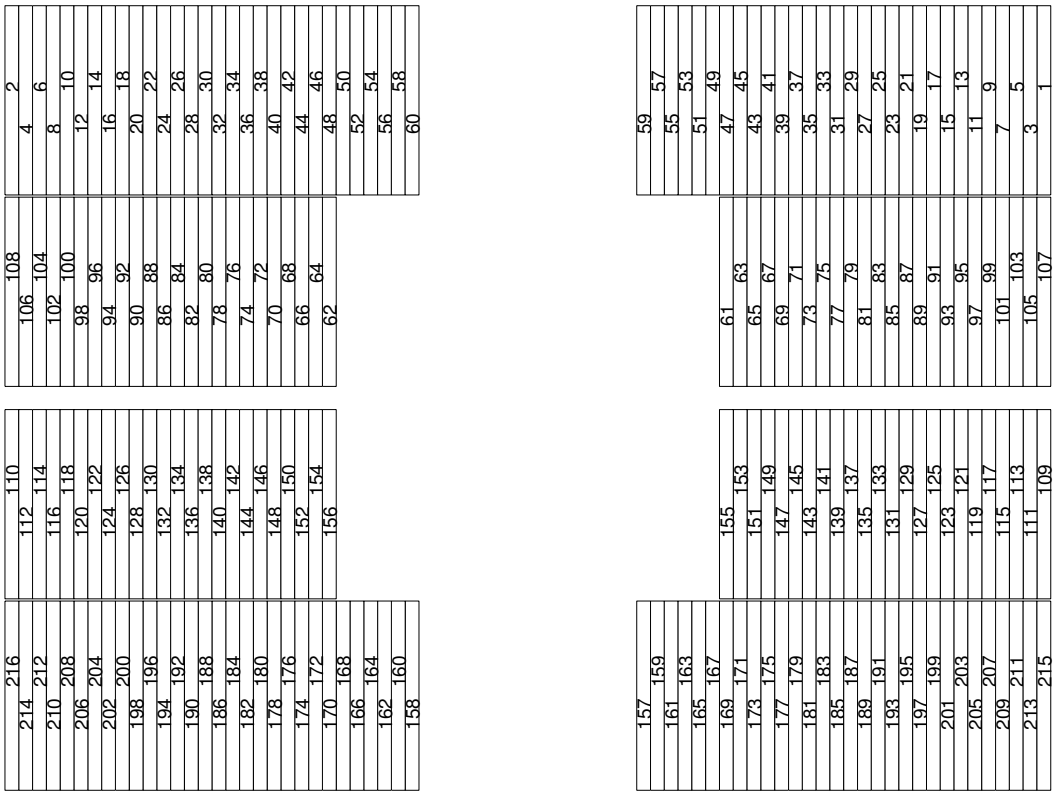

Figure C.1: The 1–2–4–3 cable connection order, named after the order of electrical parts, for variant *A*.

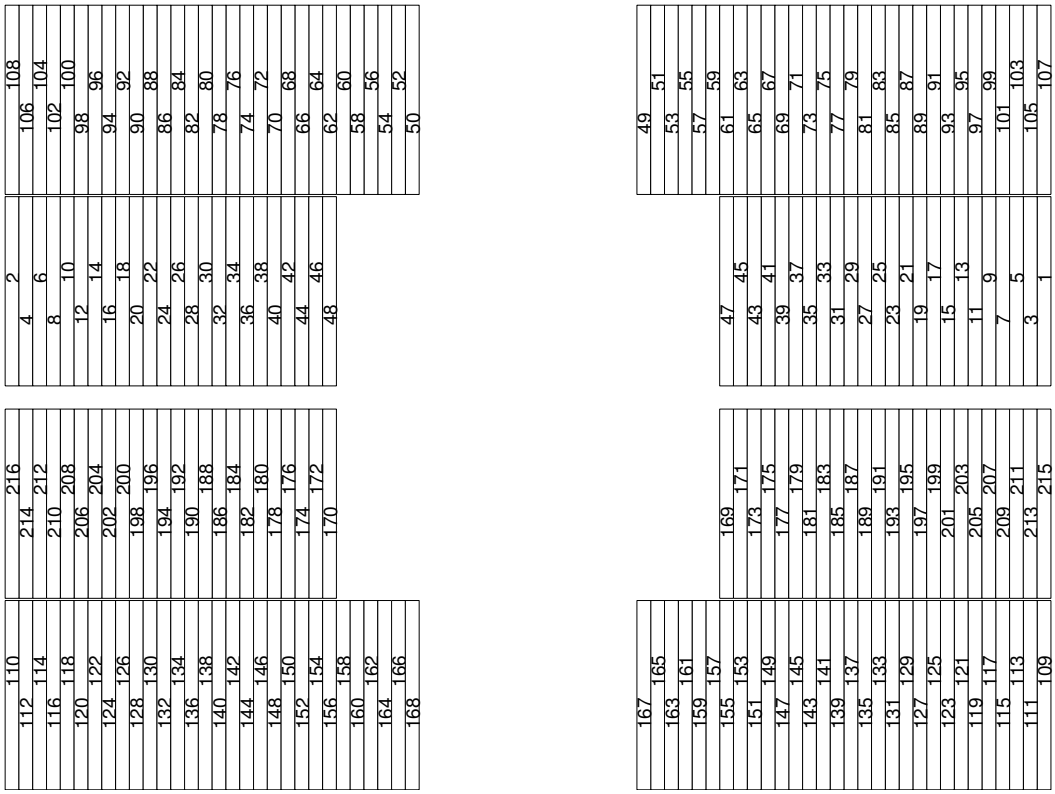

Figure C.2: The 2–1–3–4 cable connection order, named after the order of electrical parts, for variant *A*.

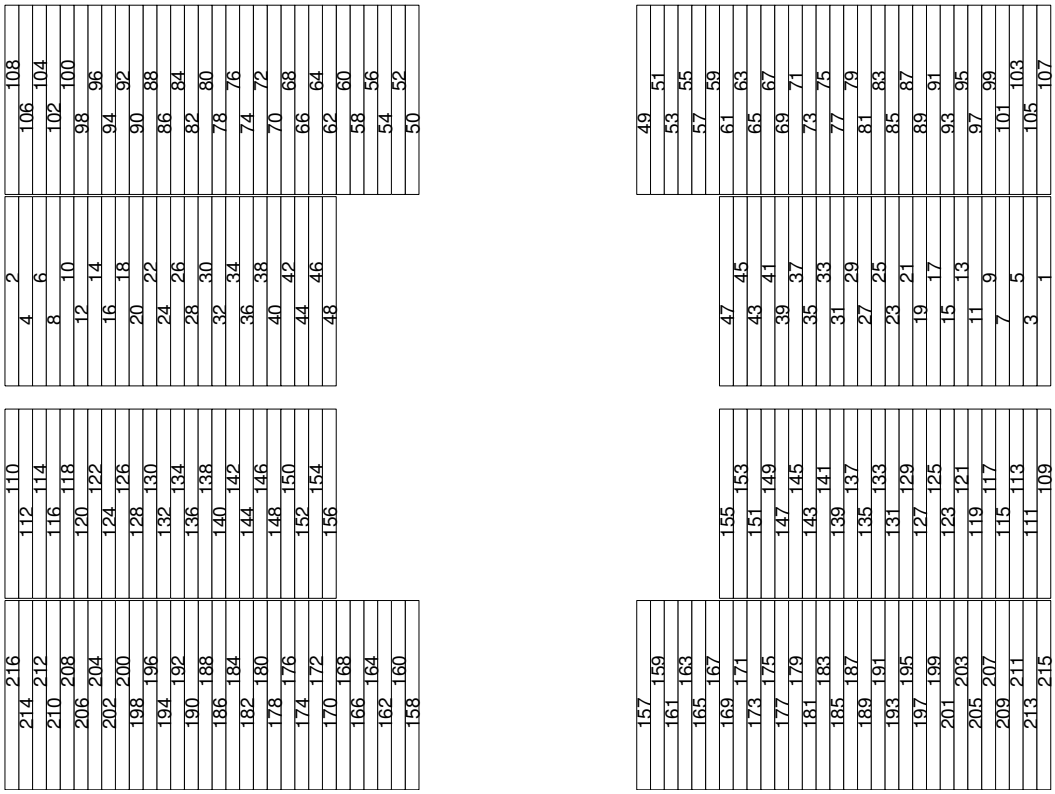

Figure C.3: The 2–1–4–3 cable connection order, named after the order of electrical parts, for variant *A*.

C.2 Half–turn Order for Alternative *D v2* Connection Scheme

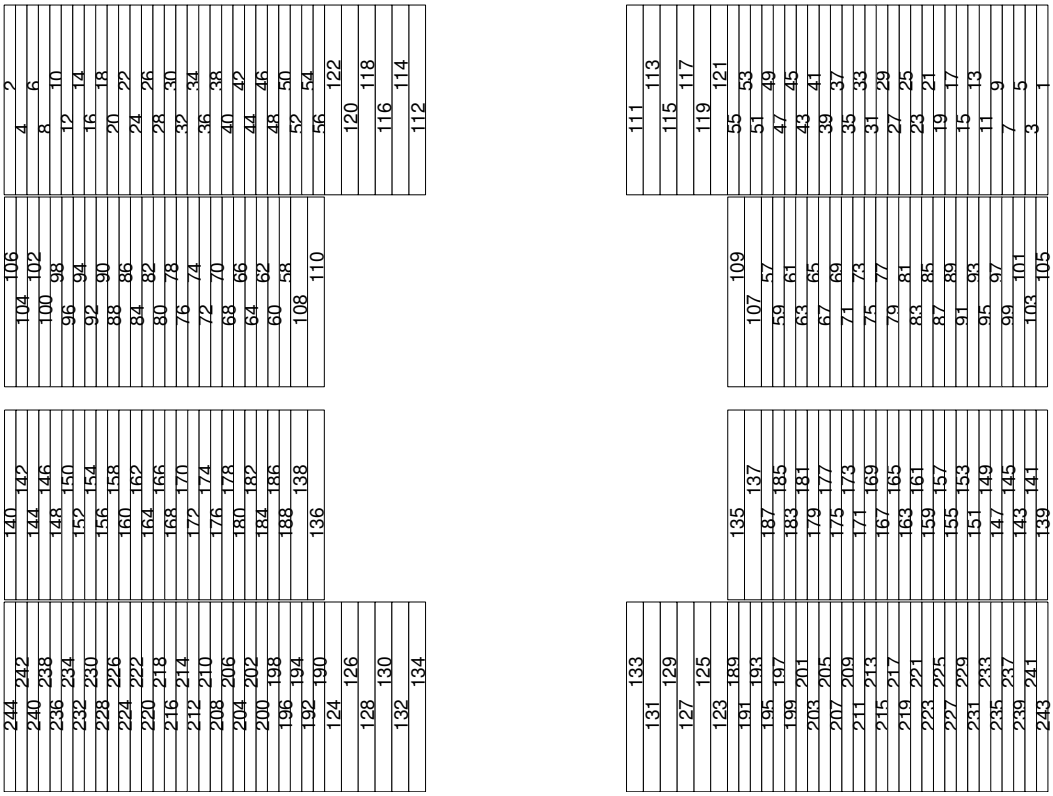

Figure C.4: The 1–2–4–3 cable connection order, named after the order of electrical parts.

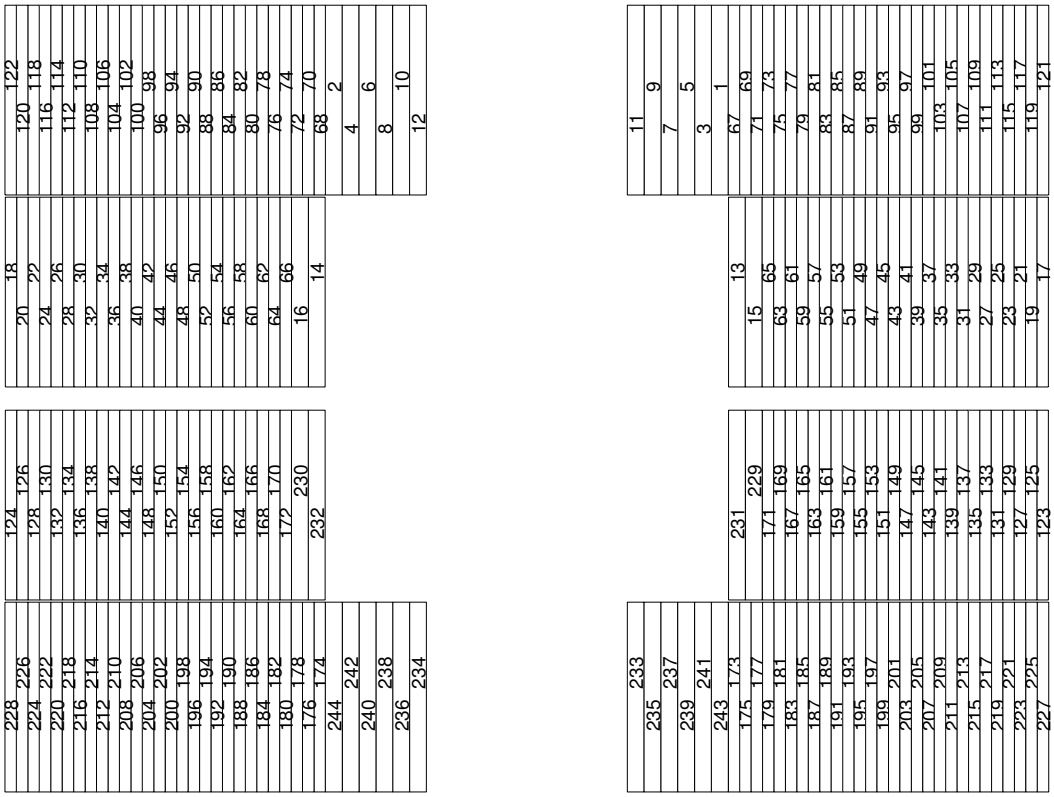

Figure C.5: The 2–1–3–4 cable connection order, named after the order of electrical parts, for variant *D v2*.